



HAL
open science

Study of early transition metal carbides for energy storage applications

Yohan Dall'Agnese

► **To cite this version:**

Yohan Dall'Agnese. Study of early transition metal carbides for energy storage applications. Mechanics of materials [physics.class-ph]. Université Paul Sabatier - Toulouse III, 2016. English. NNT : 2016TOU30025 . tel-01452608

HAL Id: tel-01452608

<https://theses.hal.science/tel-01452608>

Submitted on 2 Feb 2017

HAL is a multi-disciplinary open access archive for the deposit and dissemination of scientific research documents, whether they are published or not. The documents may come from teaching and research institutions in France or abroad, or from public or private research centers.

L'archive ouverte pluridisciplinaire **HAL**, est destinée au dépôt et à la diffusion de documents scientifiques de niveau recherche, publiés ou non, émanant des établissements d'enseignement et de recherche français ou étrangers, des laboratoires publics ou privés.

Université Fédérale



Toulouse Midi-Pyrénées

THÈSE

En vue de l'obtention du

DOCTORAT DE L'UNIVERSITE DE TOULOUSE

Délivré par :

Université Toulouse 3 Paul Sabatier (UT3 Paul Sabatier)

Présentée et soutenue par **Yohan DALL'AGNESE**

Le 9 Mars 2016

Study of early transition metal carbides for energy storage applications

Ecole doctorale et discipline ou spécialité :

ED SDM : Sciences et Génie des Matériaux

Unité de recherche :

UMR 5085 Institut Carnot CIRIMAT

Directeurs de thèse :

Pr. Patrice SIMON et Dr. Pierre-Louis TABERNA

Jury :

Frédéric FAVIER	Directeur de Recherche – ICGM	Rapporteur
Liliane GUERLOU-DEMOURGUES	Professeur – ICMCB	Rapporteur
Christophe LETHIEN	Maître de Conférences – IEMN	Examineur
Encarnacion RAYMUNDO-PINERO	Chargé de recherche – CEMHTI	Examineur
Théodore TZEDAKIS	Professeur – LGC	Examineur
Patrice SIMON	Professeur – CIRIMAT	Directeur de thèse
Pierre-Louis TABERNA	Chargé de recherche – CIRIMAT	Co-directeur de thèse

Acknowledgments

Acknowledgments

First of all, I would like to thank my PhD thesis advisors Dr. Patrice Simon and Dr. Pierre-Louis Taberna for providing me all the opportunities to do this research, their continuous support, and good advices throughout the projects. I was sincerely honored to meet and work with them. I would like to express the deepest gratitude to Prof. Yury Gogotsi for his guidance and enthusiasm, and for hosting me in his laboratory at Drexel University (Philadelphia, USA) where I was trained on MXene synthesis and characterization.

I would like to sincerely thank my committee members: Prof. Théodore Tzedakis (LGC), Dr. Frédéric Favier (ICGM), Prof. Liliane Guerlou-Demourgues (ICMCB), Dr. Christophe Lethien (IEMN) and Dr. Encarnacion Raymundo-Pinero (CEMHTI) for their time, useful comments and interest in my work.

I would like to acknowledge the financial support from the European Research Council (ERC, Advanced Grant, ERC-2011-AdG, Project 291543 — IONACES) and the Partnership Universities Fund (PUF) of French Embassy (PUF2012, "New twodimensional ceramics for better batteries").

I would like to thank all my collaborators, , Olya Masthalir, Evelyn Chang Ren, Vadym Mochalin, Min Heon, Kevin Cook (Drexel University), Patrick Rozier, Barbara Daffos, and Benjamin Duployer (Université Paul Sabatier) with whom I had many useful and stimulating discussions. Separate thanks to Dr. Michel Barsoum, Dr. Michael Naguib and Dr. Maria Lukatskaya for their constructive feedbacks on my work.

I give special thanks to my labmate in CIRIMAT: Jeremy Come, Peihua Huang, Wan-yu Tsai, Etsuro Iwama, Koki Urita, Thomas Desaunay, Laurent Bazin, Zifeng Lin, Alagar Raj Paulraj, Léo Nègre, Kévin Brousse, Yinghui Yin and Dasha Iermakova. I am also grateful to Noé, Hélène, Jean-Baptiste, Papy, Fréd, Florent, Elodie, Nicolas, Souphiane, Sébastien, Kévin, Romain, Claire, Jessica, Dalya, Imane, Vincent, Charles, Abdé, Guillaume, Alexis and

Benjamin for making my working experience fun and unforgettable. I would like to thank administrative help from Soraya Berkouk, Laetitia Lale and Sandra Geminiano, Nicole Luga, Nabila Smahi, Sandrine Cerny, Christiane Bonino, Murielle Soleillant and Maryse Bellanger. I would like to thank all the research engineers, PhD students, Master students, postdoctoral researchers and professors from CIRIMAT whom I have not mentioned but were part of this adventure.

Additionally I'm also grateful to all my group mates in Drexel who have helped in many ways, in particular: Kristy Jost, Carlos Pérez, Boris Dyatkin, Riju Singhal, John McDonough, Amanda Pentecost, Kelsey Hatzell, Katie van Aken, Chuanfang (John) Zhang, Joseph Halim, Mengqiang Zhao, Jonathan Campos, Vadym Borysiuk, Majid Beidaghi and Muhammad Boota. I particularly thank Babak Anasori and Michael Ghidui for help with the synthesis of both MAX phases and MXenes. Special thanks to Tyler Mathis for helpful corrections. I would like to thank the Drexel Nanomaterials Institute staff; Wendy Thurman, Michelle Sipics and Danielle Tadros Kopicko for their indispensable administrative support.

Last but not least, my deepest gratitude goes to my family for their love, patience and never-ending support. I specially thank to my wife, Sissi, for her endless support and encouragement during my Ph.D.

Contents

Table of Contents

General Introduction.....	1
Chapter I : Bibliography	5
I Electrochemical storage	5
I. 1 Batteries.....	8
I. 1-1 Lithium-ion batteries.....	10
I. 1-2 Sodium-ion batteries	12
I. 2 Supercapacitors.....	16
I. 2-1 Double –Layer Capacitance	16
I. 2-2 Pseudocapacitance	20
I. 2-3 Electrolyte	23
I. 2-4 Hybrid Capacitors.....	25
II Relevant 2D Materials for energy storage	29
II. 1 Graphene	29
II. 1-1 Graphene for supercapacitors.....	29
II. 1-2 Graphene for Lithium ion batteries.....	30
II. 2 Graphene Composites	31
II. 2-1 Graphene composites for supercapacitors.....	31
II. 2-1 Graphene composites for batteries.....	32
II. 3 Transition metal dichalcogenides	33
II. 3-1 Lithium ion battery	34

II. 3-2	Electrochemical Capacitors.....	34
III	New two dimensional material: MXene.....	36
III. 1	MAX Phase.....	36
III. 2	Synthesis of MXene	38
III. 3	Delamination.....	40
III. 4	Applications	41
IV	PhD goal.....	44
Chapter II	: Materials and Methods.....	49
I	MXene synthesis	49
I. 1	MAX Phase	49
I. 2	Etching	49
I. 3	Delamination	50
II	Electrochemical characterizations.....	52
II. 1	Electrochemical cells	52
II. 1-1	Two-electrode setup.....	52
II. 1-2	Three-electrode setup.....	53
II. 2	Cyclic voltammetry.....	53
II. 3	Galvanostatic charge-discharge measurement	55
II. 4	Electrochemical Impedance Spectroscopy.....	57
III	Materials Characterization Techniques	59
III. 1	X-ray diffraction.....	59

III. 1-1	Principle.....	59
III. 1-2	Equipment.....	61
III. 2	Scanning electron microscopy	62
III. 2-1	Principle.....	62
III. 2-1	Equipment.....	62
III. 3	Energy dispersive X-ray spectroscopy	62
III. 4	Gas Sorption Analysis	63
III. 5	X-ray photoelectron spectroscopy.....	63
Chapter III : MXene as a Supercapacitor electrode in aqueous electrolytes		67
I	Introduction	67
II	Spontaneous intercalation of cation	68
II. 1	Study by X-ray diffraction	68
II. 2	Delamination	73
III	Surface modification	74
III. 1	Observation by scanning electron microscopy	75
III. 2	X-ray photoelectron spectroscopy.....	77
IV	Electrochemical characterization.....	79
IV. 1	Results in various aqueous electrolytes	79
IV. 2	Mechanism study by in situ X-ray diffraction	83
IV. 3	Surface-modified $Ti_3C_2T_x$ performance	86
V	Conclusion	89

Chapter IV : MXene for Na-ion capacitors	93
I Introduction	93
II Selection of suitable MXene electrode.....	94
II. 1 Comparison of cyclic voltammograms	94
III $Ti_3C_2T_x$	97
III. 1 Energy storage mechanism	97
III. 2 Modification of $Ti_3C_2T_x$	99
III. 2-1 Delaminated $Ti_3C_2T_x$	101
III. 2-2 Clay $Ti_3C_2T_x$	102
IV V_2CT_x as positive electrode.....	106
IV. 1 V_2CT_x vs Na.....	106
IV. 1-1 Electrode preparation	106
IV. 1-2 Cyclic voltammetry	106
IV. 1-3 Galvanostatic charge discharge.....	107
IV. 1-4 Mechanism.....	108
IV. 1-5 Electrochemical impedance spectroscopy	108
IV. 1-6 X-ray diffraction	109
IV. 2 Full cell	110
IV. 2-1 Negative electrode Hard Carbon.....	110
IV. 2-2 Full cell testing.....	111
V Conclusion	114

Chapter V : MXene as a Supercapacitor electrode in organic electrolyte	117
I Introduction	117
I. 1 Recent development in MXene electrode preparation.....	117
I. 1-1 MXene composite	117
I. 1-2 Clay MXene	119
I. 2 Objectives.....	120
II Electrode preparation.....	121
III Materials characterization	121
IV Electrochemical behavior	124
IV. 1 Characterization of carbon nanotube.....	124
IV. 2 Cyclic voltammetry	125
IV. 3 Electrochemical impedance spectroscopy	127
IV. 4 Galvanostatic charge-discharge measurement.....	127
V Charge storage mechanism.....	129
V. 1 In-situ X-ray diffraction	129
V. 2 Cyclic voltammetry.....	131
VI Other organic electrolytes	132
VII Conclusions	134
General Conclusion	137
Future Work.....	139
Annexes	143

List of Figures	147
List of Tables	155
References	159
Résumé de Thèse	171

General Introduction

General Introduction

Since the last century, the main energy sources have been fossil fuels (oil, gas and coal) which have led to economic concerns (limited resources) and ecological issues (global warming). With the rise of renewable energy sources (wind, sun, hydropower...), one of today's challenges has been to create cheaper and more efficient technologies to store this intermittent energy (1, 2). Recently, another challenge has emerged with the popularization of rechargeable portable electronic devices (laptop, smart phone, etc.) that require increasing energy and power densities. Electrochemical energy storage solutions such as batteries and supercapacitors are environmentally friendly and have the advantage of excellent efficiency and adaptable scale (3-5). Batteries store the energy through electrochemical reduction and oxidation reactions while supercapacitors, also called electrochemical capacitors, store energy through double layer electrostatic interactions (6).

The demand for higher energy and power densities is continuously increasing. Unfortunately, current commercial batteries and supercapacitors are not suitable to face future needs (5, 7). To be economically sustainable, electrode materials need to provide better performances at the same cost or lower. Indeed, commercial electrochemical capacitors suffer from low energy densities because they use activated carbon electrodes which store the energy only through double layer capacitance (4). In recent years it has been proposed that a promising method to reach higher energy densities with supercapacitors is to use pseudocapacitive materials that store energy through fast redox reactions. In a different manner, hybrid capacitors based on lithium ion battery technology are another solution proposed to increase the energy density.

The work reported herein focuses on the electrochemical performances of a new family of material called MXene. MXenes are a family of two-dimensional transition metal carbides

which have shown promising results in the field of lithium ion battery application (8, 9). The motivation to study these materials is that their chemical composition are more diverse than carbon and contain transition metals that can allow redox reaction and higher energy density. In this work, we investigated a few members of this family; Ti_3C_2 , Ti_2C , Ti_3CN , Nb_2C , V_2C , $\text{Ti}_{1.5}\text{V}_{1.5}\text{C}_2$ and TiVC , in 3 different electrochemical storage devices; supercapacitors, sodium-ion batteries and sodium-ion capacitors.

The first chapter is a bibliographic review. We explain the principle of lithium ion batteries before focusing on the state of the art sodium ion batteries and electrochemical capacitors. Finally, a summary of the performance of various two-dimensional materials used for energy storage are given in the last part, before concluding with an introduction about the new family of MXene.

The second chapter describes the experimental methods used. In particular, the MXene synthesis from the MAX phase is presented, as well as its delamination treatment. The basic principles of the electrochemical and material characterizations are also given.

The third chapter focuses on the electrochemical performance of Ti_3C_2 as an electrode material for electrochemical capacitors in aqueous electrolytes. The spontaneous intercalation mechanism from aqueous electrolyte ion into MXene is described.

The fourth chapter starts with an overview of all synthesized MXene materials behavior upon sodium ion intercalation in half cell batteries. We identified V_2C as a promising electrode for sodium-ion capacitor and further used V_2C as a positive electrode in a full cell with hard carbon as the negative electrode.

In the fifth chapter, MXene electrochemical behavior is investigated in organic electrolytes. The electrochemical storage mechanism is analyzed by in-situ X-ray diffraction.

In the final part, the general conclusion and perspective of this work are presented.

Chapter I: Bibliography

Chapter I : Bibliography

I Electrochemical storage

The first reported electrochemical storage device was a battery created by Alessandro Volta in 1800 (10). It consisted of a zinc electrode and a copper electrode separated by a paper soaked with NaCl electrolyte. The mechanism taking place (oxidation of Zn and oxygen reduction at the Cu electrode) was not understood until 1834 when Michael Faraday demonstrated that the oxidation state of the Zn metal changed during the reaction. This discovery contributed to the creation of a new scientific field called Electrochemistry. The 19th and 20th centuries saw the development of electrochemical energy storage technologies such as batteries and supercapacitors.

Among the numerous great improvements of batteries, some of the most notable are the development of the lead acid battery by Gaston Planté in 1859 , the Zn-MnO₂ dry cell in 1887, the first Nickel-Cadmium battery in 1899, the commercial success of alkaline battery in 1959 and finally, after the discovery in 1980 of LiCoO₂ as cathode material from J. Goodenough (11) and graphite as anode from B.Scrosati and others (12), SONY introduced the lithium ion battery to the market in 1991. The latter has revolutionized portable electronic devices (phone, laptop, etc.) and electric vehicles (Tesla).

The research on supercapacitors is more recent with the first patent in 1957 from H. Becker at General Electric, consisting of stainless steel electrodes in sulfuric acid electrolyte (13). However the charge mechanisms were not yet understood. Research done between 1966 and 1970 at Sohio Corporation (Standard Oil Company Of Ohio) using graphite electrodes in organic electrolyte (14) revealed that the charge storage mechanism is due to the formation of double layer, the interphase of which was studied by Helmholtz in 1879 (15). Commercial

applications waited until 1982 by the Nippon Electric Company. The first devices had low capacitances and low energy densities (0.5 Wh/kg) limiting their applications. Nevertheless, better products based on activated carbons were quickly commercialized by several companies that invested in the research, such as Panasonic, Elna, ECONO, Maxwell and Batscap. Different commercial electrochemical capacitors were produced for various applications, from transport (stop and go) to large scale stationary storage. Electrochemical capacitors based on another principle, called pseudocapacitance, have been studied as well (16). Conway was the first to describe oxide materials that store energy through fast faradaic reactions. Pseudocapacitor materials are typically transition metal oxides (RuO_2 , MnO_2 , V_2O_5 , etc.) and electronically conducting polymers (polyaniline, polypyrrole, etc.) but no commercial application has emerged so far (4, 17).

Nowadays, many different chemistries can be used for electrochemical energy storage devices that broaden the range of energy and power densities available, as shown Figure I.1. The energy and power stored are calculated according to:

$$E = \frac{1}{2} C \times \Delta V^2 \quad \text{Eq.1}$$

$$P = \frac{\Delta V^2}{4R} \quad \text{Eq.2}$$

Where: C is the capacitance of the cell (F), ΔV is the potential window (V) and R is equivalent series resistance (Ω).

It appears that energy storage through faradaic oxidation-reduction reactions in batteries provides higher energy densities but lower power densities than devices that store energy through electrostatic interaction such as electrochemical capacitors. In the following, the scientific principles of lithium ion battery, sodium ion battery, electrochemical capacitors and hybrid capacitors are introduced.

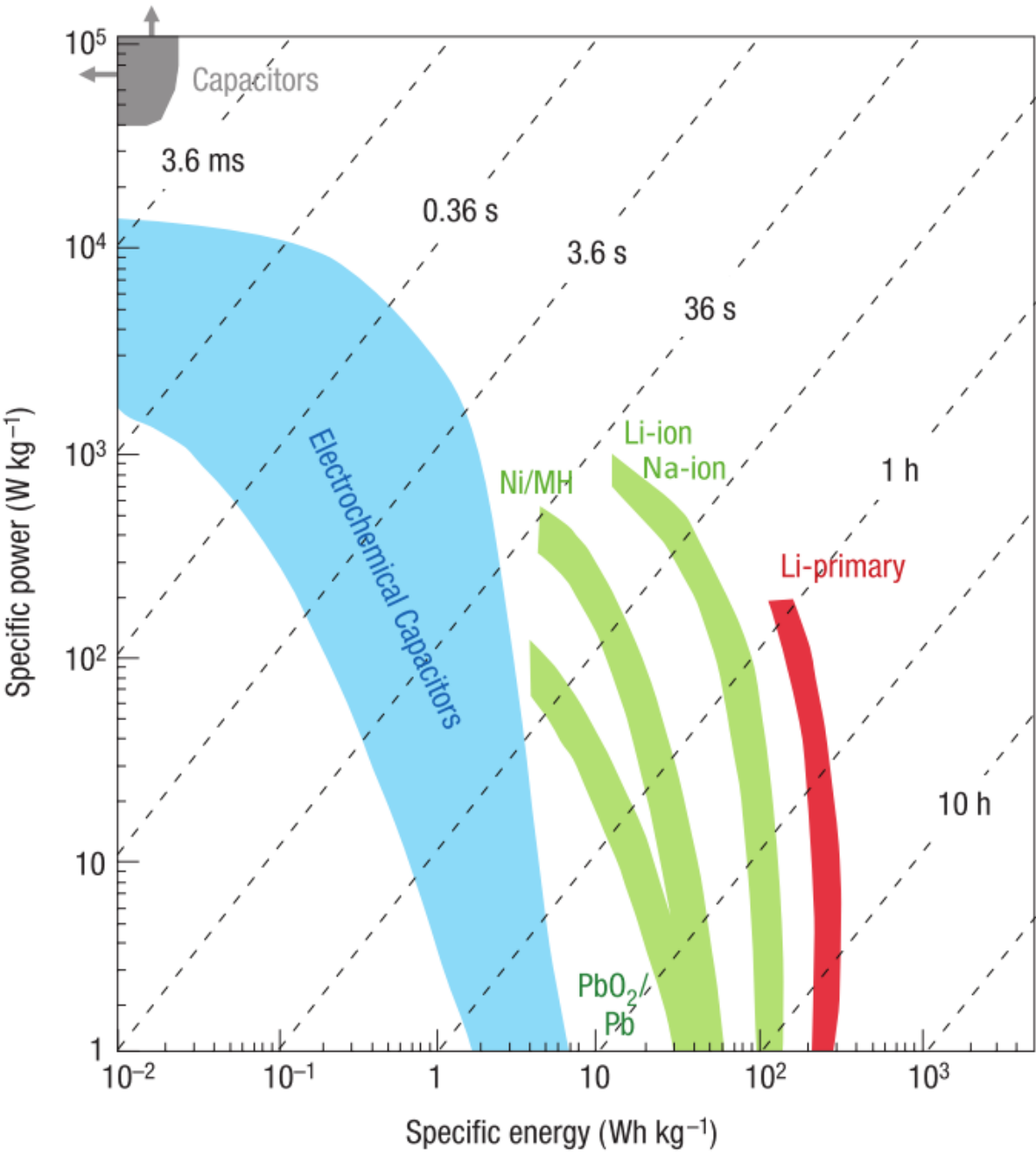


Figure I.1: Ragone plot (specific power vs. specific energy) (adapted from (4)).

I. 1 Batteries

As previously mentioned, there are many different types of batteries but all batteries store energy through faradaic oxidation-reduction reactions at the electrodes, as described in Figure I.2. In these devices two electrodes, negative and positive, are separated by an ion-conducting and electronic-insulating electrolyte. The oxidation states of the electrode active materials are modified by charge transfer during battery charge and discharge. When the two electrodes are connected, electricity is spontaneously generated (discharge). Oxidation of the active material occurs at the anode during discharge which generates electrons while reduction occurs at the cathode which consumes electrons. The reaction occurs until one electrode has totally reacted. The battery can be recharged by applying an external current. (18)

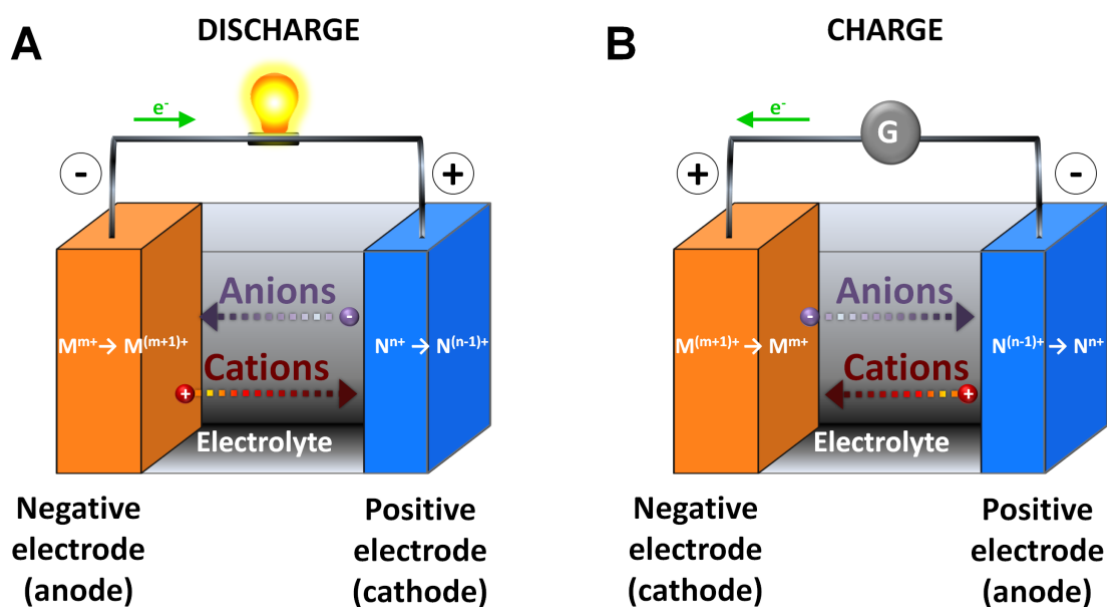


Figure I.2: Schematic representation of a battery during discharge (A) and charge (B).

Each electrodes material has characteristic electrode potential (noted E , expressed in V vs. SHE) and capacity (noted Q , expressed in mAh/g) determined according to the following equations (18) :

$$E = E'^{\circ} - 2,3 \times \frac{RT}{nF} \log\left(\frac{\theta}{1-\theta}\right) \quad \text{Eq. 3}$$

$$Q = \frac{nF}{3.6 \times M} \quad \text{Eq. 4}$$

Where: E'° is the standard potential of the redox couple (V vs. SHE), F is the Faraday constant (96485 C/mol), θ is the extent of fractional coverage of the surface of inner structure, R is the universal gas constant (8.314 J/K.mol), T is the absolute temperature (K), M is the molar mass (g/mol) and n is the number of moles of electrons transferred.

In terms of electrochemical characterization, the behavior of a battery-type material is illustrated Figure I.3. The cyclic voltammetry and galvanostatic charge-discharge principles are extensively described in chapter 2. There are well defined potentials where the oxidation and reduction occurs that are identified by peaks in the cyclic voltammetry and by plateaus in the galvanostatic charge-discharge.

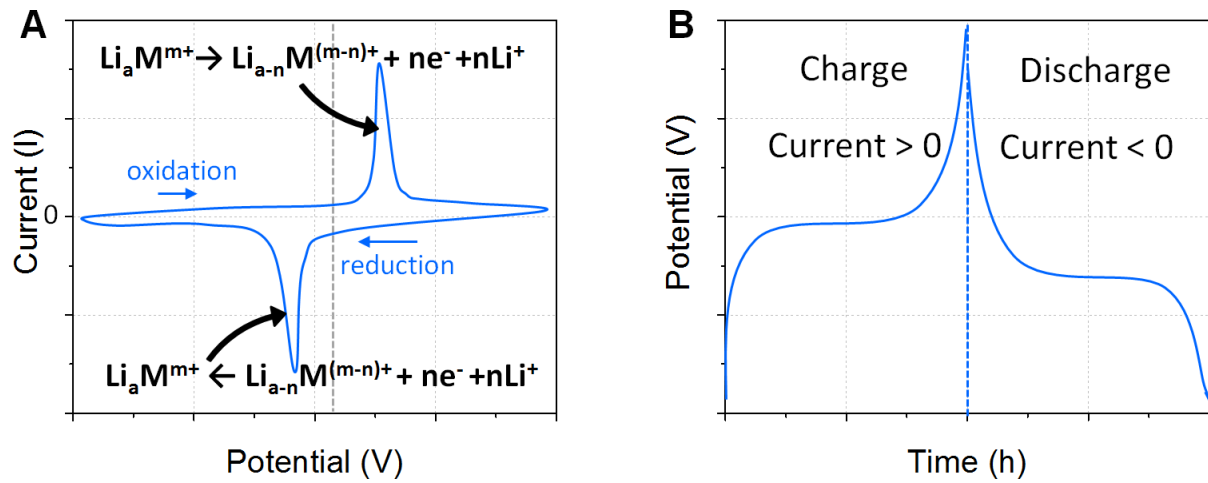
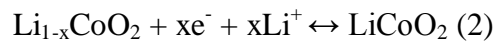
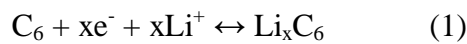


Figure I.3: Typical behavior of a lithium-ion battery material during cyclic voltammetry (A) and galvanostatic charge-discharge measurement (B).

Although various commercial battery systems exist based on various chemistries, we will only describe lithium ion and sodium ion batteries, the latter being under development.

I. 1-1 Lithium-ion batteries

Lithium-ion batteries are the most advanced electrochemical energy storage technology in terms of performance (5). The advantage of this technology is its low cost, high energy density (>550Wh/L) and long cycle life (~ 1000 cycle). Figure I.4 is a schematic representation of a commercial lithium ion battery. It is composed of graphite as negative electrode, LiCoO₂ (LCO) positive electrode and 1M LiPF₆ as electrolyte. The reactions occurring at the electrodes are respectively (19):



Where x is the mole number.

These Li⁺ intercalation reactions lead to specific capacity up to 165 mAh/g and a voltage of 4.1V. Seen from (1) and (2) both electrodes can host lithium ions. This mechanism is called the rocking chair because the active Li ions are “transported” back and forth between the two electrodes during charge and discharge, as illustrated in Figure I.4. This mechanism is specific to ion battery technology that we will also observe in sodium ion batteries (19-21).

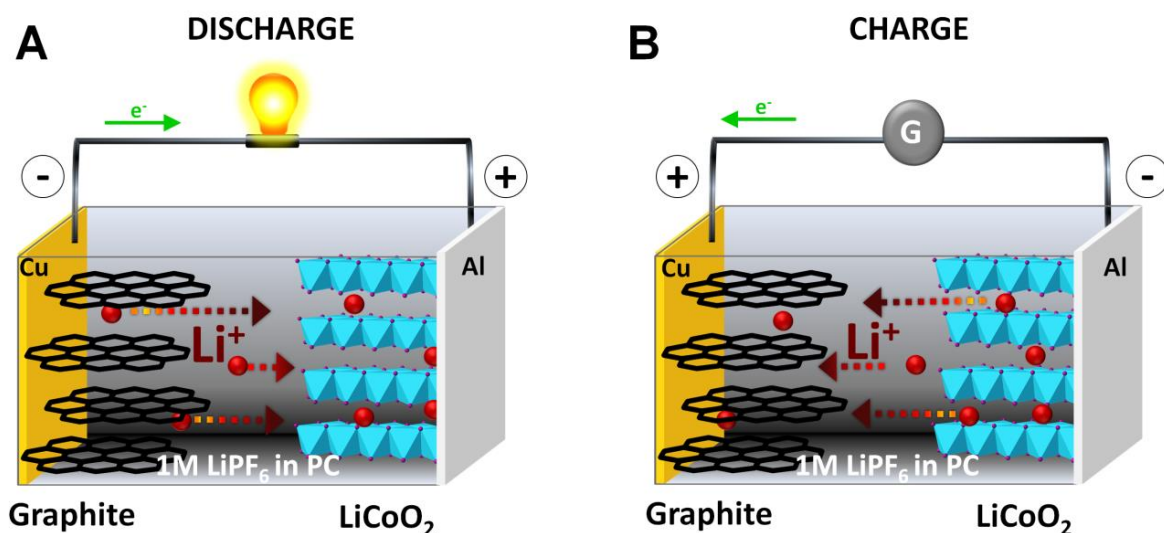


Figure I.4: Schematic representation of a Li-ion battery during discharge (A) and charge (B).

For the past few decades, extensive efforts have been focused on the improvement of materials' capacities. The graphite anode in Li ion batteries suffers from irreversible capacity loss due to solid electrolyte interphase formation during cycling and has limited energy and power density. In addition, the LCO cathode is expensive, not thermally safe, and has short cycle life and low power density. Figure I.5 presents various electrodes proposed in the literature to replace current electrode materials. The main alternatives are; LiMn_2O_4 (LMO), LiNiMnCoO_2 (NMC) and LiFePO_4 (LFP) (22, 23). LMO is safer and has better power density than LCO but lower energy density and cycle life. NMC has high energy and high power densities however LFP is safer, has longer cycle life and possesses higher power density than all other Li-ion systems, but lower voltage and higher self-discharge (24). Materials for lithium ion battery are not the main focus here but other relevant materials will be presented in the second part of this chapter.

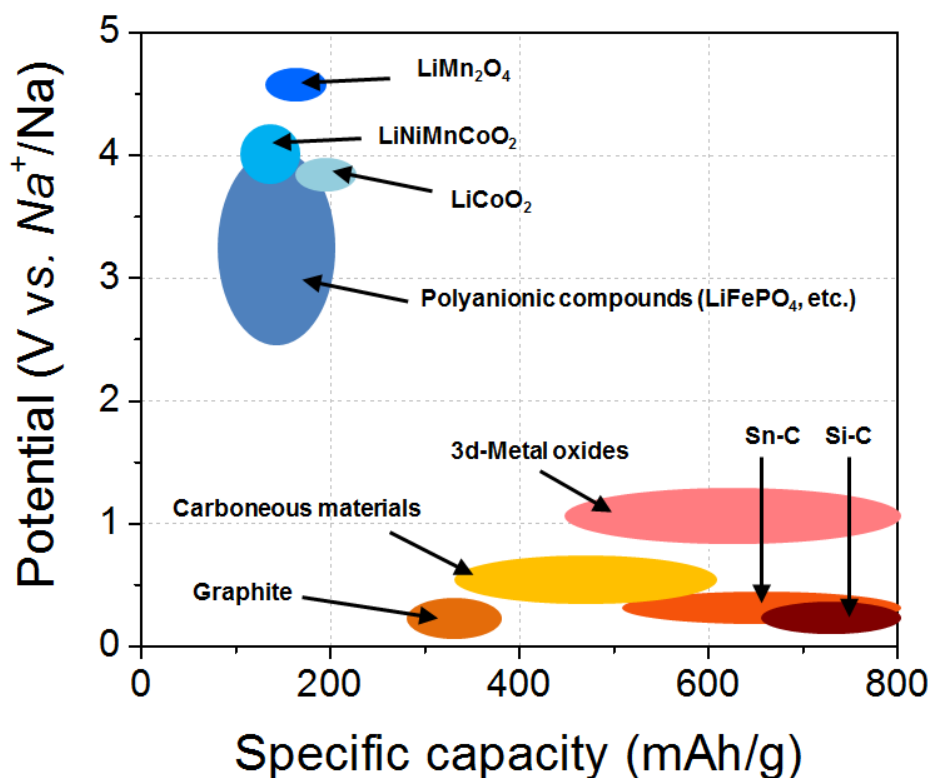


Figure I.5: Voltage vs. Capacity of relevant positive and negative electrodes materials for lithium-ion battery (adapted from (1)).

I. 1-2 *Sodium-ion batteries*

In recent years, there has been speculation concerning lithium reserves and its price (25, 26). The main producers are Talison in Australia, FMC in Argentina, SQM and Rockwood Lithium ion in Chile and Tianqi Lithium in China. An increase demand in lithium is predicted for the next few decades, especially driven with the need of large scale energy storage facilities and electric vehicles. Because lithium is not abundant and the resources are mainly located in emerging countries, it could create political tensions and increase the cost of metallic lithium and lithium salts. Even if it is uncertain that a lithium economic crisis will occur, these concerns have driven the researchers to study more sustainable alternative energy storage technologies.

Since sodium is one of the most abundant elements on earth and homogeneously distributed (see Table 1), it will not suffer from geopolitical issues (25-29). Moreover, the copper current collector that is required in lithium ion battery anode technology can be replaced by cheaper aluminum current collectors. Beside these advantages, it is important to know that the technology used in Li-ion batteries and Na-ion batteries are very similar. This has renewed the interest in the development of Na-ion technology (30-34). The advancement of Na-ion batteries faces several intrinsic challenges. First, the redox potential of Na^+/Na is higher than Li^+/Li , reducing the operating voltage. Then, the ionic radius is larger, meaning that many materials cannot reversibly host it (for example graphite), it can cause higher volumetric change, and reduce the ionic conductivity and diffusion. Because of these drawbacks, the firsts Na based systems that was developed in the 90's had been disregarded, until recently (20, 21, 35-38).

Table 1: Comparison of lithium and sodium properties.

	Li	Na
Abundance in Earth crust	20 ppm	23 000 ppm
Average world production	24 600 tons	281 800 000 tons
Specific capacity	3860 mAh/g	1160 mAh/g
Redox potential	-3.045 V vs. SHE	-2.714 V vs. SHE
Ionic radius	0.76 Å	1.02 Å

One of the challenges that sodium-ion batteries are facing is the limited number of suitable negative materials. Graphite is the most commonly used negative electrode in Lithium-ion batteries. It has numerous advantages, such as a very competitive cost and reasonable capacity of 372 mAh/g. Although Na-ion technology is similar to that of Li-ion, unfortunately Na-ion do not intercalate into graphite (27-29). Several alternatives have been studied from carbon materials to alloys. The most notable anode materials, hard carbon and NaTiO₂, are discussed here. A comparison between the different electrodes is shown at the end of this part, Figure I.7.

Hard carbon, amorphous carbon synthesized by oxidation then carbonization under neutral flow, has been proposed as a negative electrode for sodium-ion batteries as early as in 2000 by Dahn *et al.* (39). It has been later studied and improved by several independent groups, notably in 2002 by Thomas *et al.* (40), by Komaba in 2011 (41) and finally by Ponrouch *et al.* in 2013 (42). The later investigated the effect of the synthesis method to optimize the surface area, the porosity, the particle size and the degree of graphitization in order to obtain the best electrochemical performance, as shown in Figure I.6. Specific capacity up to 326 mAh/g at C/10 rate with excellent capacity retention (>100 cycles) and excellent rate capability (230 mAh/g at 1C rate) were achieved by hard carbon prepared through a relatively cheap pyrolysis of sugar. These results are comparable to graphite in lithium ion battery.

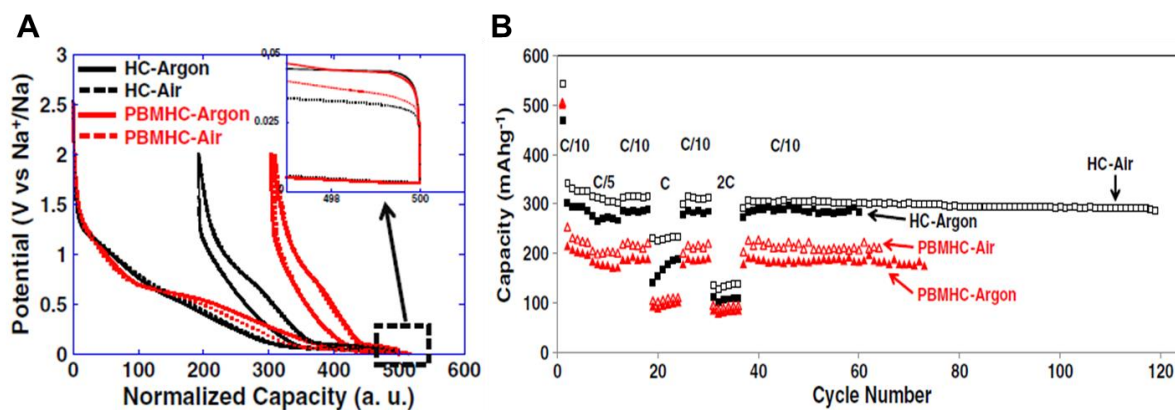


Figure I.6: Electrochemical performance of hard carbon with different synthesis methods cycled in 1M NaClO₄ in EC:PC vs. metallic Na: first cycle galvanostatic charge-discharge curves (A) and capacities vs. cycle number (B) (adapted from (42)).

The other relevant negative electrode materials are early transition metal oxides, in particular Ti-based intercalation compounds, such as NaTiO₂ and Na₂Ti₃O₇. Xiong *et al.* showed promising results obtained from large NaTiO₂ nanotube (lateral dimension >80 nm) (43). Capacity improved from 70 to 150 mAh/g after 15 cycles at C/3 rate when cycled between 1V and 2.5V vs Na⁺/Na. This was attributed to the fact that Na ion concentration on the surface is increasing upon cycling and suggests the need for pre-cycling a cell in some cases limiting commercial interest. Senguttuvan *et al.* reported on Na₂Ti₃O₇ which is a very low voltage insertion compound (between 0.2 and 0.4 V vs. Na⁺/Na) (44). Capacity about 200 mAh/g at low rate (C/25 rate) was measured, corresponding to the insertion of 2 Na ions. But suffer from low rate capability and cycle life.

Numerous studies have been done on cathode materials for lithium-ion battery and this is the reason most of the cathode materials proposed for sodium-ion batteries are the sodiated counterpart of the well-studied layered transition metal oxides, olivines and compounds with the NASICON framework.

Early research on transition metal oxides containing sodium, Na_xMO₂, were done in the 80's by Delmas *et al.* (45). It was demonstrated that reversible insertion/deinsertion is feasible and

therefore extensive research on such structure has been done. The most studied metal oxides are Na_xMnO_2 and Na_xCoO_2 based materials (46-53). In these systems, capacities up to 140 mAh/g at slow rates were obtained but on a large 2-3.8V potential range numerous two-phase transition steps are observable which is undesirable for real devices.

Olivine structured-materials have been extensively studied for lithium ion batteries, most notably LiFePO_4 (54). Its sodium based analog, NaFePO_4 , has logically been proposed (55-58). Although the capacities obtained, 125 mAh/g at C/20 rate, are comparable to the capacity obtained with LiFePO_4 in lithium-ion battery (150 mAh/g) the same drawback associated with low potential is present.

The NASICON, or Sodium super ion conductor, is a family of 3D structure with good structural stability and fast ion conduction. Several member of this family have been investigated, such as $\text{NaTi}_2(\text{PO}_4)_3$, $\text{NaNbFe}(\text{PO}_4)_3$, $\text{Na}_2\text{TiFe}(\text{PO}_4)_3$, $\text{Na}_2\text{TiCr}(\text{PO}_4)_3$ and $\text{Na}_3\text{V}_2(\text{PO}_4)_3$ (35, 59-61). Recently the effort focused on carbon-coated $\text{Na}_3\text{V}_2(\text{PO}_4)_3$ demonstrated capacity up to 240 mAh/g when cycled between 3.8V and 1.5V at C/12.5 rate but a potential plateau at 1.6V vs Na^+/Na was observed, which is neither cathodic nor anodic (61-65).

Another important part of a battery is the electrolyte (41, 47, 66, 67). The most common electrolyte formulations found in the literature are similar to those used in lithium ion battery, replacing Li^+ ions with Na^+ : NaPF_6 or NaClO_4 salts are dissolved in carbonate ester solvents such as propylene carbonate, ethylene carbonate or diethyl carbonate. The formation of the solid electrolyte interphase (SEI) in sodium-ion batteries has been less investigated than in Lithium-ion battery. It appeared that the SEI is not stable and homogeneous in these electrolytes causing coulombic inefficiency. Here also research efforts on electrolyte additives to stabilize the SEI have been inspired from Li-ion battery field. Ponrouch *et al.*, proposed the addition of fluoroethylene (FEC) to stabilized the SEI film at the negative electrode and

results showed an improved cycling capacity (66). Deeper understanding of the SEI formation and solvent formulation will have to be performed to further improve the performance of sodium-ion batteries, however it is not the focus of this thesis.

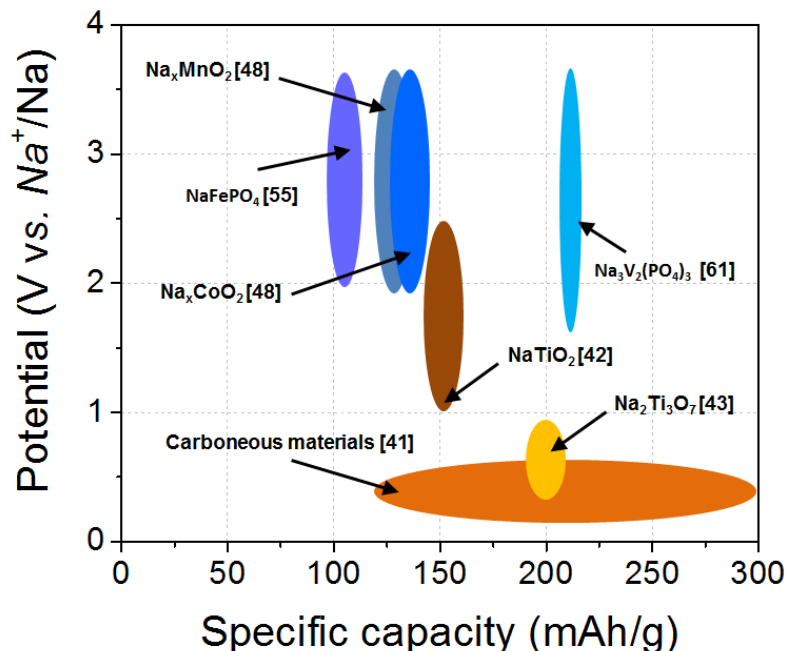


Figure I.7: Voltage vs. Capacity of relevant positive and negative electrodes materials for sodium ion battery. All materials can be found in the text.

I. 2 Supercapacitors

Supercapacitors, also called electrochemical capacitors or electrical double layer capacitors, consist of two electrodes separated by a separator soaked with electrolyte (68). Different from batteries, supercapacitors have high power densities, excellent rate capability and almost infinite cycle life. Supercapacitors can store energy through two fast-kinetic charge storage mechanisms: double layer capacitance and pseudocapacitance (3, 4, 69). The difference between these two mechanisms will be described in the following sections.

I. 2-1 Double –Layer Capacitance

The double-layer capacitance is caused by electrostatic separation of the charges at the electrode / electrolyte interface when a potential is imposed, as described in the simplified

schematic Figure I.8. Several models have been developed to describe the double layer successively by Helmholtz (1853) (15), Gouy and Chapman (1913)(70), Stern (1924), Grahame (1947) (71), Bockris, Devanathan and Muller (1963).

The Helmholtz model describes the double layer as two layers of opposite charge accumulated at the electrode/electrolyte interface and separated by the radius of the solvated ion. The Gouy-Chapman model describes a diffuse model of the double layer, due to thermodynamic distribution of counter-ions from the electrolyte. The Stern model represented in Figure I.8.B combines both model and considers that the charge compensation occurs within a volume of electrolyte defined by the thickness d of the diffusive layer. The layer of charges in the electrolyte near the interface is in fact composed of several layers. Right next to the negative electrode there is the compact layers or Helmholtz layers at the distance of the partially desolvated and solvated cations radius and then the Gouy-Chapman diffusive layer.

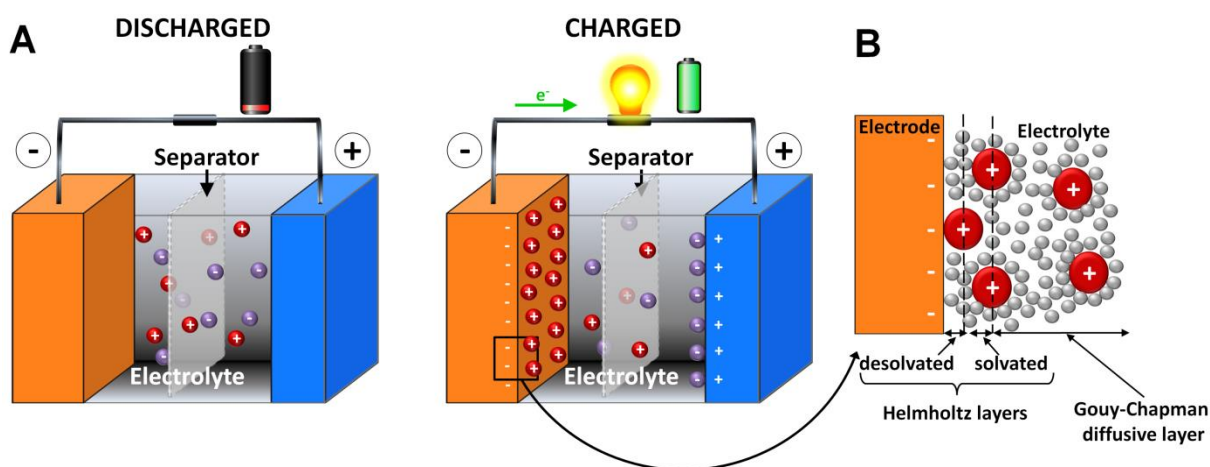


Figure I.8: Schematic representation of an electrochemical double layer capacitor (A) and the Stern model (B).

The capacitance can be described as the association of the Helmholtz capacitance and Gouy-Chapman capacitance in serie:

$$\frac{1}{C_{dl}} = \frac{1}{C_{Helmoltz}} + \frac{1}{C_{Gouy-Chapman}} = \frac{d}{A\varepsilon_r\varepsilon_0} + \frac{1}{A\varepsilon_r\varepsilon_0\kappa_D} \quad \text{Eq.5}$$

Where: C_{dl} is the double layer capacitance (F) of the electrode, A is the electrode surface area (m^2), ε_r is the relative dielectric constant, ε_0 is the permittivity of the vacuum ($8.85 \cdot 10^{-12}$ F/m), d is the approaching distance of the ions (m) and κ_D is the Debye length or $1/\kappa_D$ is the diffusion length of the Gouy-Chapman layer.

In concentrated electrolyte, like in our work, $1/\kappa_D$ tends to 0. Thus, the double layer capacitance is defined by the Helmholtz capacitance.

As described in Figure I.8.A, there are two electrodes facing each other. Therefore the total capacitance of the cell can be described as the combination of the two electrodes capacitances in series and is given by the following equation:

$$\frac{1}{C_{cell}} = \frac{1}{C_+} + \frac{1}{C_-} \quad \text{Eq.6}$$

The electrochemical responses of an ideal supercapacitor are shown Figure I.9. In contrast to batteries, the storage mechanism do not occurs at a specific potential, thus no plateaus or peaks are present. The current response to linear voltage sweep in cyclic voltammetry has a rectangular shape corresponding to equation 7.

$$I = C \frac{dV}{dt} \quad \text{Eq.7}$$

Where, I is the current (A), C is the capacitance (F), V is the potential (V) and t is the time (s). Further characteristic of the electrochemical measurement methods will be described in Chapter 2.

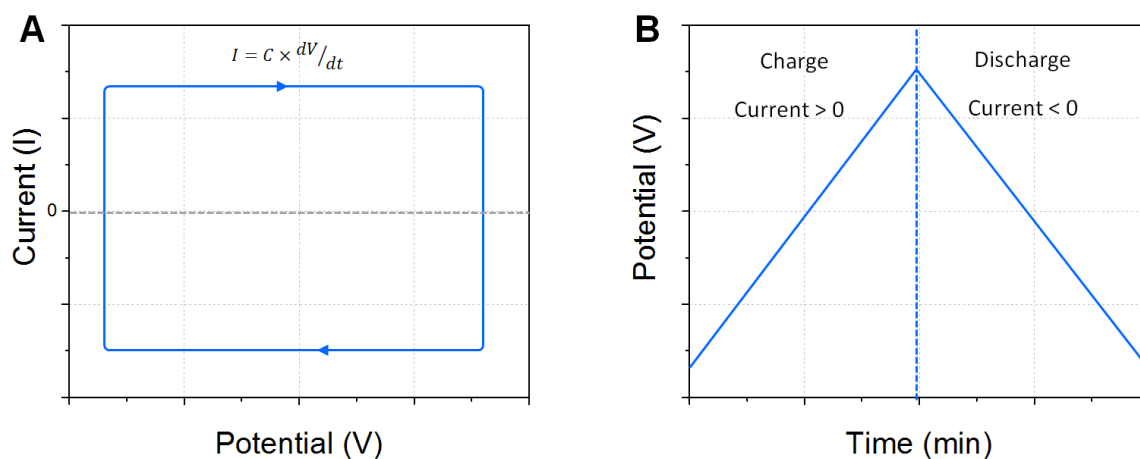


Figure I.9: Typical behavior of electrochemical double layer capacitors during cyclic voltammetry (A) and galvanostatic charge-discharge measurement (B).

The electrode materials must exhibit high electric conductivity and high specific surface area. The best candidates are carbon materials, such as carbon nanotubes, graphene sheets and activated carbon (72-75). They have a large electrochemical stability voltage window in addition to their high electric conductivity and their high specific surface area. The most conventional materials used are activated carbons thanks to their good properties and low cost. Activated carbons are synthesized from biomass (coconut shell, wood, etc.) by carbonization at temperatures lower than 800°C in inert atmosphere, then treated in a process called activation, consisting of physical method (steam, etc.) and/or chemical treatment (strong bases, etc.), in order to enhance the porosity (76). Table 2 summarizes the properties of these materials:

Table 2: Comparison of different carbon materials electrochemical performances (75).

	Specific surface area (m ² /g)	Specific Capacitance (F/g)	
		In 1M H ₂ SO ₄	In organic electrolyte
Activated carbon	2000 - 3000	300	240
Carbide derived carbon	1300 - 2500	200	170
Carbon nanotubes	300 - 1000	150	90
Onion-like carbon	550	40	38
Graphene	300 - 3000	280	170
Carbon aerogels	400 – 1000	100	80

Kotz demonstrated that when increasing the specific surface area above 1500 m²/g, the capacitance reached a limit of about 100 F/g (77). Another significant parameter is the pore size distribution and the electrode-electrolyte interface. Chmiola *et al.* (78) controlled the pore size distribution of a CDC by controlling the synthesis temperature and demonstrated the importance of these parameters on the electrochemical performance. An unprecedented increase in capacitance was observed for pore size smaller than 1 nm, which was attributed to ion de-solvation observed when the average pore size corresponds to the ion size (79, 80).

I. 2-2 Pseudocapacitance

The electrochemical behavior, such as the current response of a potential change, of a pseudocapacitor is similar to double layer capacitors. The distinction comes from the energy storage mechanism as double layer capacitance occurs through electrostatic interaction whereas pseudocapacitance is due to electron-transfer reactions (16, 17, 81). Therefore, higher energy density can be achieved using pseudocapacitive materials. However, it can also be distinguished from faradaic reaction occurring in batteries for two main reasons: the faster charging time and the linear dependence of the charge stored with the potential window.

Conway described pseudocapacitance as one of the three faradaic mechanisms described in Figure I.10 that can exhibit capacitive electrochemical behavior. The first case is underpotential deposition, which is metal ions forming an adsorbed monolayer at a different metal's surface above their redox potential. The second case is redox capacitance, which is the electrochemical adsorption of ion onto the surface or near surface of a material with a concomitant faradaic charge-transfer. The third case is intercalation capacitance, which is the faradaic intercalation of ions into tunnels or layers of electrode materials. It is worth noting that some battery-type materials can exhibit this behavior thanks to tuning the engineering of the electrodes; usually using thin film technology or nanometric particles synthesis to achieve pseudocapacitive behavior (16, 82). These materials are called extrinsic pseudocapacitive materials because their bulk counterparts do not behave as supercapacitor type materials, as opposed to intrinsic pseudocapacitive materials that behave similar to a double layer capacitors regardless of the particle size.

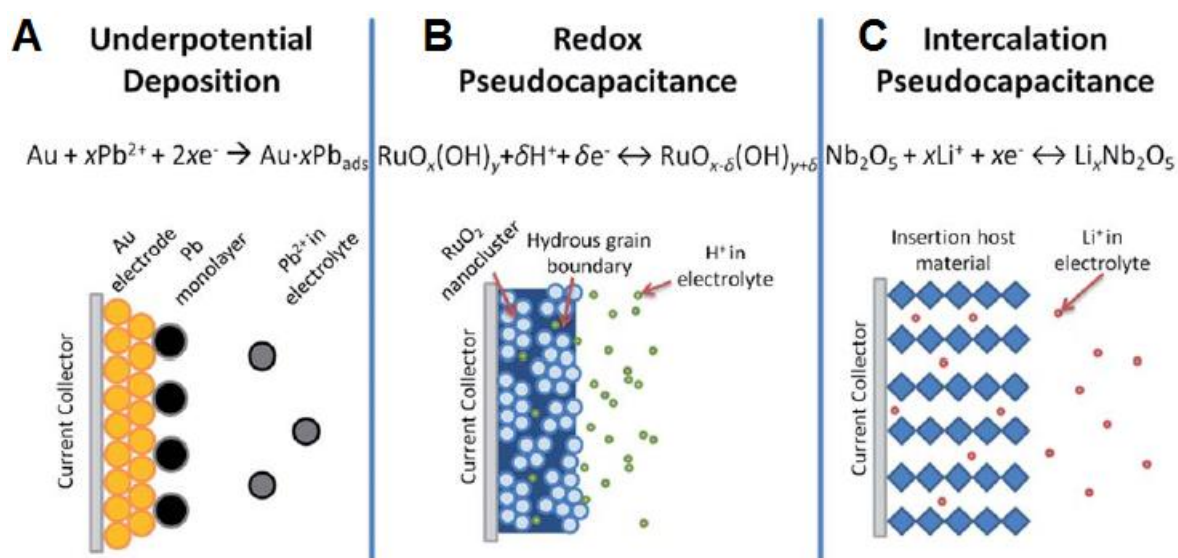


Figure I.10: Different types of reversible redox mechanisms that give rise to pseudocapacitance: underpotential deposition (A), redox pseudocapacitance (B) and intercalation pseudocapacitance (C) (adapted from (16)).

Since pseudocapacitive electrodes store energy through faradaic reactions, the capacitance (C) can be expressed by equation 8.

$$C = \left(\frac{nF}{M}\right) \frac{\theta}{E} \quad \text{Eq. 8}$$

Where, C is the specific capacitance (F/g), n is the number of electron, F is the Faraday constant (96 485 C/mol) and M is the molecular weight of the active material (mol/g). This induces an infinite apparent redox potential next to each other and the potential (E) responds linearly with the extent of fractional coverage of the surface of inner structure or the advancement of the reaction (θ).

This translates as mirror image voltammograms and a triangular shaped galvanostatic charge-discharge curve, as illustrated in Figure I.11. In other words, the capacitive behavior of pseudocapacitive electrodes results from fast, successive, indistinguishable, and reversible redox reactions occurring at the surface, which are not limited by diffusion (83).

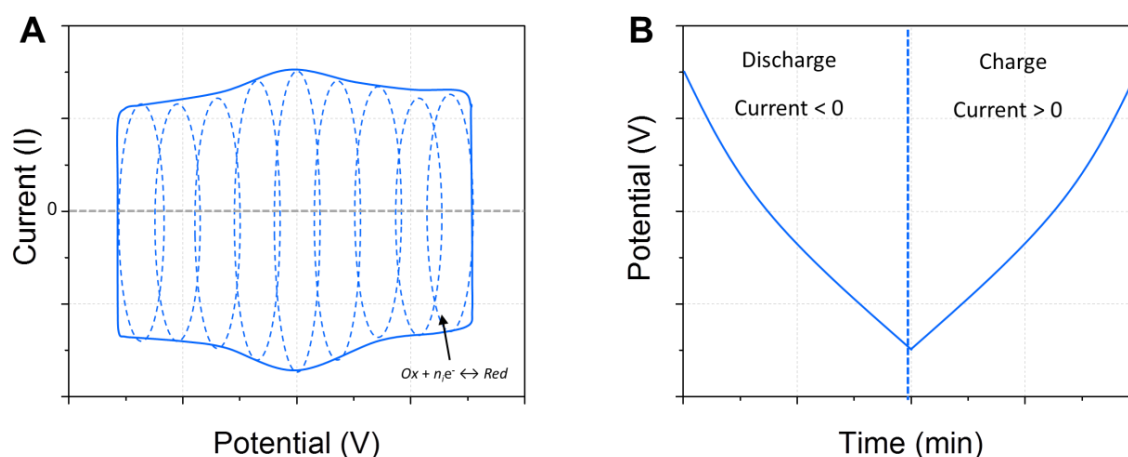


Figure I.11: Typical behavior of pseudocapacitive material during cyclic voltammetry (A) and galvanostatic charge-discharge measurement (B).

Transition metal oxides, such as MnO_2 , RuO_2 , TiO_2 and V_2O_5 were the first materials investigated for pseudocapacitor (16). The most studied is RuO_2 because regardless of its high cost it present the highest conductivity and three stable oxidation state occurring on a 1.2V potential range (84-88). When cycled in sulfuric acid the reaction noted in Figure I.10.B occurs. Figure I.12 shows the voltammograms obtained for different potential ranges and highlights the pseudocapacitive behavior of RuO_2 as the broad anodic and cathodic peaks are symmetric. First results using RuO_2 showed capacitance up to 720 F/g (88, 89).

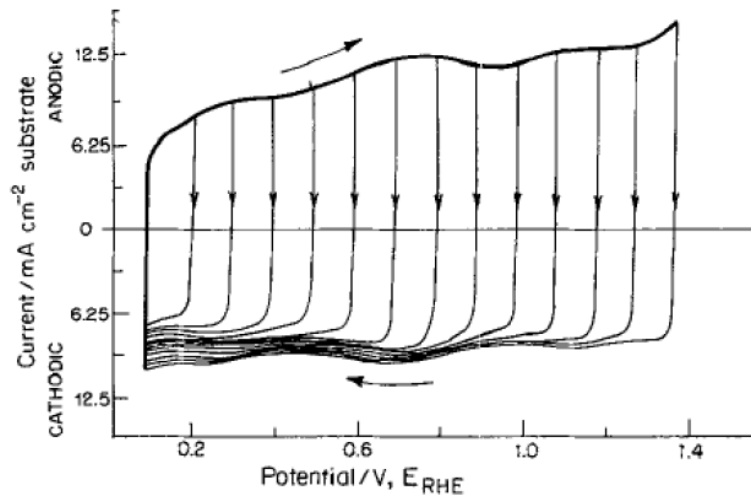


Figure I.12: Cycle voltammetry of RuO₂ in H₂SO₄ at 50 mV/s (adapted from (3)).

Other metal oxides have been studied, in particular MnO₂ because of its low cost, resource abundance, environmental friendliness and high theoretical capacitance (90). Capacitance up to 260 F/g was obtained in 0.5M K₂SO₄ (91). Because of the low electronic conductivity of oxide materials, the preparation of composites using a carbon matrix was proposed to benefit from better electric conductivity as well as higher specific surface area. In the second part of this chapter we will investigate some composites with graphene.

I. 2-3 *Electrolyte*

The electrolyte is a key factor in the electrochemical performance of a supercapacitor (92). The energy and power are proportional to the square of the potential window (equations 1 and 2). Therefore research has been focused on formulating electrolytes with large potential window stability. There are three types of liquid electrolytes: aqueous electrolytes, organic electrolytes and ionic liquids. The ionic conductivity, the temperature stability and the compatibility with the electrode are also important factors. Table 3 summarizes the properties of these electrolytes and it falls to the engineer to select the best electrolyte corresponding to the desired application.

Table 3: Properties of electrolytes (72, 92, 93).

	Potential window stability (V)	Conductivity (mS/cm)	Temperature stability (°C)
Aqueous	< 1.2	>400	-20 to +50
Organic	< 3	<100	-40 to +80
Ionic Liquid	< 6	<15	-100 to +400

Ionic liquids, which are room-temperature solvent-free electrolytes, show the largest potential window and temperature stability. However they have lower conductivity which reduces power density. Two of the most conventional ionic liquids used are EMITFSI (1-ethyl-3-methylimidazolium bis(trifluoromethylsulfonyl)imide) and EMIBF₄ (1-ethyl-3-methylimidazolium tetrafluoroborate).

Organic electrolytes are typically solutions of tetraethyl ammonium salts dissolved in acetonitrile (ACN) or propylene carbonate (PC).

Aqueous electrolytes suffer from reduced potential window limited by the electrolysis potentials of water. Nevertheless, they are the most used electrolytes thanks to safety, convenience, high conductivity, low cost and good compatibility with most electrode materials, in particular with pseudocapacitive electrodes. Figure I.13 shows example of the behavior of an activated carbon in various electrolytes. In all cases, rectangular shaped cyclic voltammograms are obtained; however the operating potential ranges and resistances are different and will be explained later.

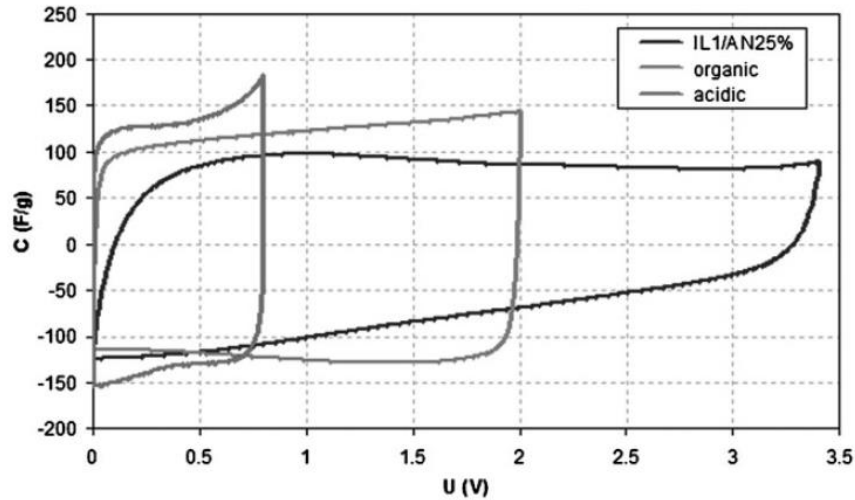


Figure I.13: Cycle voltammetry of activated carbon at 5 mV/s in different electrolytes (adapted from (94)).

I. 2-4 Hybrid Capacitors

The principle of a hybrid between electrochemical capacitors and batteries was first introduced by John Miller (95). Hybrid capacitors combine an electrochemical capacitor electrode with a battery electrode. As the battery-type electrode potential is mostly constant during the charge-discharge (plateau), the total cell potential behaves like the electrochemical capacitor electrode that is the cell potential changes linearly with time during constant charge-discharge cycles, as described in Figure I.14. The objectives of these systems are to deliver higher energy than supercapacitors at higher power density than batteries (96, 97), by increasing the average discharge voltage and the cell capacity. In other words, hybrid capacitors are promising energy storage devices that bridge the gap between batteries and supercapacitors on the Ragone plot (Figure I.1).

The capacitance of a hybrid cell is described by equation 6. In the case of a symmetric EC the cell capacitance can be expressed as half the capacitance of an electrode ($C_{cell} = C_{EC+,-}/2$). Whereas in the case of an asymmetric hybrid capacitor, the capacitance of the faradaic electrode ($C_{Faradaic}$) is greatly superior to the capacitance of the capacitive electrode (C_{EC}) and the total cell capacitance is expressed as follow:

$$\frac{1}{C_{cell}} = \frac{1}{C_{EC}} + \frac{1}{C_{Faradaic}} \quad \Leftrightarrow C_{total} \approx C_{EC}$$

Therefore the total capacitance in a hybrid capacitor cell is twice the capacitance of a symmetric EC. Depending of the choice of the faradaic electrode, the cell voltage can be greatly improved. However, using a faradaic electrode also comes with a limitation in the rate capability and cycle life because of the presence of a battery-like electrode.

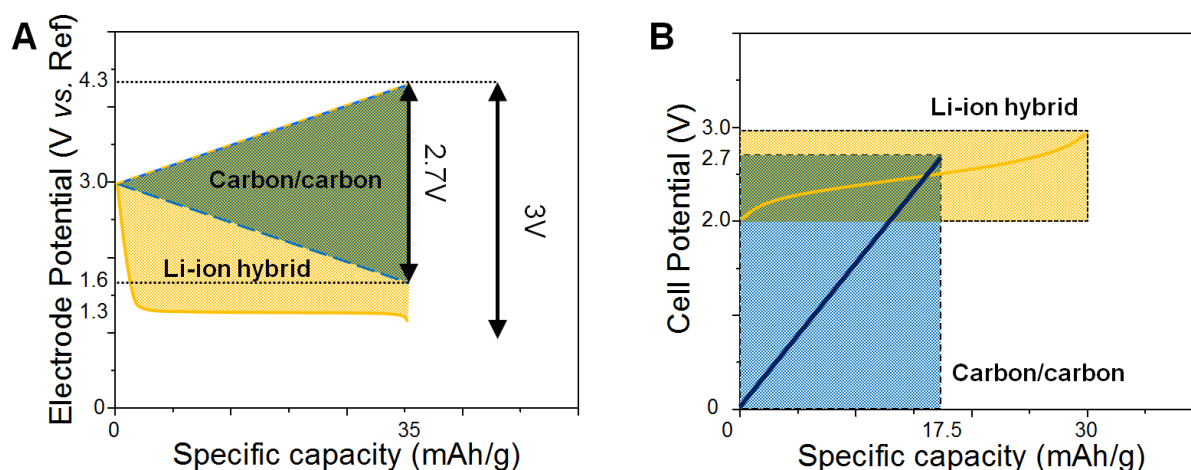


Figure I.14: Electrode potentials vs. specific capacity of each electrode in a symmetric carbon/carbon supercapacitor and an asymmetric Li-ion hybrid during charge (A). Cell potential vs. specific capacity based on the total mass of the two electrodes (B).

Several hybrid systems have been investigated. In aqueous electrolytes the most extensively systems studied are: Carbon/NiOOH in KOH (98), Carbon/PbO₂ in H₂SO₄ (commercial)(99) and MnO₂/Carbon in K₂SO₄ (100). Although these systems are interesting, this thesis will focus only on hybrid capacitor in organic electrolytes that are lithium ion capacitors and sodium ion capacitors since these systems have larger voltage window and show the best performances in terms of power and energy densities.

Li-ion capacitor systems combine high energy density from the lithium ion intercalation electrode of batteries and high power of supercapacitors electrode. The electrolytes used are lithium salts in carbonate-based organic solvents, similar to electrolytes used in Lithium-ion batteries. Due to their high energy and power densities, they are intended for use in a wide variety of applications, such as transportation (electric and hybrid cars), electronics

(telephones and laptops), and storage of renewable energy. Several companies have started to commercialize their devices, such as ACT, JM Energy Corp, Ioxus, Asahi Kasei FDK Energy, Aowei and TAIYO YUDEN Co (97).

Amatucci *et al.* were the first to propose a non-aqueous hybrid device in 2001 (101), with two systems: activated carbon/ $\text{Li}_4\text{Ti}_5\text{O}_{12}$ (LTO) and activated carbon/ WO_2 in a 1M LiBF_4 in acetonitrile. The most interesting is the former because LTO has several advantages including high coulombic efficiency ($\approx 100\%$), high theoretical capacity (175 mAh/g), safe cycling with redox plateau potential at 1.55 V vs. Li^+/Li (above solid electrolyte interphase formation), small volumetric changes and low cost. Such devices reached up to 18 Wh/kg (102). Figure I.15 shows the first results published by Amatucci *et al.* Later this system's power performance has been greatly improved by Naoi *et al.* using a nanocomposite between carbon nanofibers and nano-crystal of LTO synthesized by ultracentrifugation (103, 104). This process solved the problem of the low conductivity of LTO. Excellent high rate performances were obtained with up to 40 mAh/g at 1200C rate as well as excellent cycle life. Activated carbon is still used as positive electrode thanks to its suitable properties already discussed earlier and counter anion of the electrolyte can form double layer capacitance at its surface.

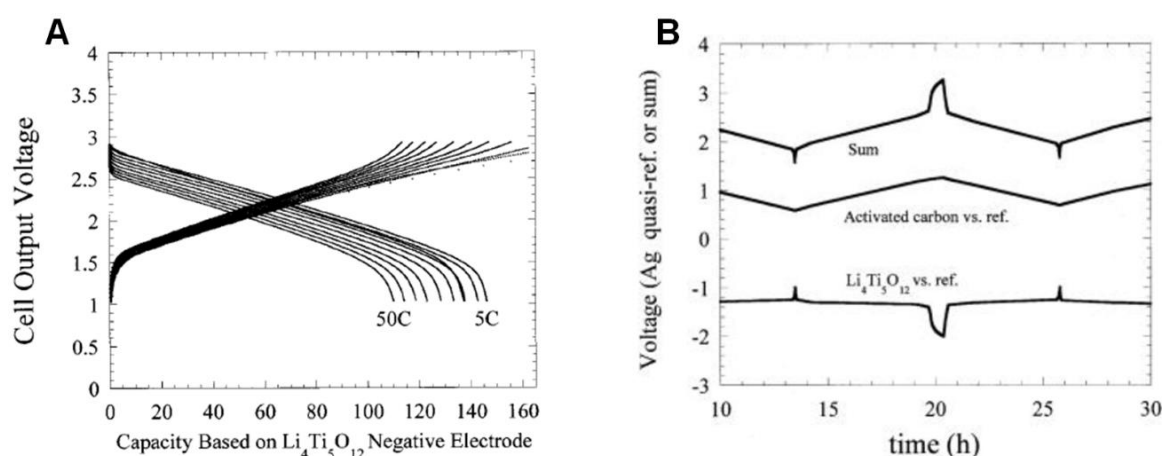


Figure I.15: Discharge profile as function of rate (A) and three-electrode measurement (B) of an asymmetric hybrid cell utilizing an activated carbon positive electrode and $\text{Li}_4\text{Ti}_5\text{O}_{12}$ negative electrode in LiPF_6 EC/DMC electrolyte (adapted from (101)).

With graphite and activated carbon being respectively the most used electrodes in batteries and supercapacitors, asymmetric hybrid devices combining these two materials were proposed (105). The graphite needs to be pre-lithiated because of the formation of the solid electrolyte interphase and lithium-ion consumption that decrease the conductivity during the first lithiation. The advantage of pre-lithiated graphite/activated carbon system compared to LTO/AC is that graphite as a higher specific capacity and low intercalation/deintercalation potential (0.1V vs Li^+/Li) extending the cell operating voltage range. This system has been commercialized by JMEnergy since 2008, with cells that claim capacities of 2200F and power densities up to 10 kW/kg but energy densities limited at 10Wh/kg (106).

However, the limited supply of lithium and quickly widening use of energy storage devices justify replacement of lithium with a cheap and abundant element. For the same reason that sodium ion-batteries emerged as an alternative to Li-ion batteries, sodium-ion capacitors, where the Li intercalation electrode is replaced with a low cost Na ion electrode were proposed (107-110). In 2012, Kuratani *et al.* investigated HC/activated carbon Na-IC and showed the feasibility of such systems (108). Similar to lithium-ion capacitors and sodium-ion batteries, most of the on-going work on Na-ion capacitors is focused on the development of negative electrodes and several anodes have been proposed, such as hard carbon, carbon nanotubes, NiCo_2O_4 and sodium titanate nanotubes.

II Relevant 2D Materials for energy storage

High power densities can only be reached if the energy storage mechanism is either an electrostatic interaction at the electrode / electrolyte interface or fast surface redox reaction. Therefore, bulk materials containing inactive volume that does not participate in charge storage are inappropriate candidates. In a 2D material, all the active material is directly in contact with the electrolyte as the single sheets of the material are only a few nanometers thick. Moreover, 2D materials have also attracted attention as promising electrode materials since graphene has excellent conductivity, has similar surface area to activated carbon and can be used without insulating binder (III). This thesis focuses on a new family of 2D materials called MXene. Before describing the state-of-the-art MXene, other relevant 2D materials for energy storage will be introduced.

II. 1 Graphene

Among 2D materials, Graphene is by far the most famous (Nobel Prize 2010) and the most extensively studied. It consists of a few layers of carbon with a graphitic structure that has an excellent theoretical electric conductivity, high charge carrier mobility, high specific surface area, high transparency, high flexibility and great mechanical strength (112-115). These properties are very interesting for many applications, including energy storage. Recently, graphene electrodes were prepared for ECs and Lithium-ion battery.

II. 1-1 Graphene for supercapacitors

As mentioned, graphene has a very high specific surface area ($SSA_{\text{theoretical}} = 2630 \text{ m}^2/\text{g}$) corresponding to a maximum theoretical capacitance of 550 F/g, one of the highest among carbon materials. Therefore many attempts to use graphene as electrode material in EC have been attempted that have been more or less successful (116-123). Zhu *et al.* used microwaved

exfoliation of graphene oxide activated in KOH with an apparent specific surface area of 3100 m²/g. Performances in several electrolytes were investigated and capacitance up to 166 F/g were obtained in organic electrolyte (BMIMBF₄) with good cycle life but resistive voltammograms compared to activated carbons (120). El-Kady *et al*, developed a laser scribing technique to prepare few micrometer thick graphene, obtaining a graphene specific surface area of 1520 m²/g. The authors used a polymer gel electrolyte (PVA-H₃PO₄) to assemble an all solid supercapacitor and tested the flexibility of the cell, as described in Figure I.16. The performance at different angles demonstrates the feasibility of flexible supercapacitors that have many new applications such as wearable electronic. Other electrolytes were used to increase the potential range and capacitance up to 276 F/g were obtained in EMIMBF₄ ionic liquid with a potential range of 3.5V. The limitation here lies in the small areal capacitance (mF/cm²) due to the use of thin film.

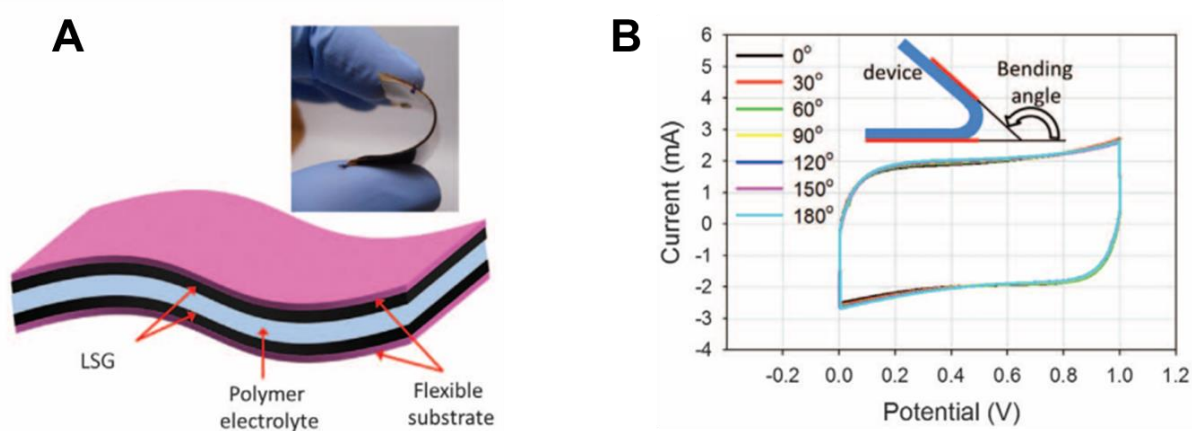


Figure I.16: Design of a flexible supercapacitor based on laser-scribed graphene. (inset) A digital photograph showing the flexibility of the device (A) Cyclic voltammograms and the effect of the bending at 1000 mV/s (adapted from (121)).

II. 1-2 Graphene for Lithium ion batteries

Keeping in mind that graphite is the most commonly used negative electrode in lithium ion batteries, graphene has still attracted a great deal of attention for Lithium-ion batteries. The

theoretical capacity of graphene is 744 mAh/g (twice that of graphite) corresponding to two layers of lithium on both sides of the graphene sheet. Many research teams currently investigate graphene for Lithium-ion batteries, both experimentally and theoretically (122, 124-131). However the storage mechanism is still not understood, in particular the diffusion of lithium and the effect of defects on performances.

The first investigations by Yoo *et al.* showed a capacity of 540 mAh/g for graphene sheets prepared by reduction of graphene oxide and later improved to 650 mAh/g with thinner graphene. These capacities are higher than for graphite and support the hypothesis that lithium can be adsorbed at the graphene surface. The authors added C60 to further increase the capacity up to 784 mAh/g. Graphene prepared by other synthesis route lead to different results highlighting the effects of the synthesis method used.

However, graphene is facing major obstacles of it is to be used as the negative electrode for Lithium-ion batteries (122). First, there are no plateaus during galvanostatic charge-discharge which are required for stable discharge voltage. Second, the solid electrolyte interphase formation and reaction with functional groups during the first cycle are responsible for a significant degree of irreversibility in the first cycle (126). Third, the rate capability is poor because of the limited lithium diffusion in stacked graphene layers.

II. 2 Graphene Composites

II. 2-1 Graphene composites for supercapacitors

Metal oxides, presented earlier as materials for supercapacitors, store the energy through pseudocapacitance (fast reversible redox reactions). The low conductivity of most oxides and of doped polymers limits their electrochemical performances. Composite materials using good electric conductors such as CNTs or carbon black were investigated early on and recently

graphene composites have been proposed. Another factor to improve the performance is the use of nanomaterials, because the fast redox reaction occurs at the surface of the electrode and the inner part is not active. Therefore, nanomaterials benefit from increased specific surface area, shorter diffusion and reduced charge transfer length (125).

Metal oxide/graphene composites have also been proposed (125, 132-134). MnO₂/graphene nanosheet composites were synthesized and exhibited good conductivity, good capacitance (310 F/g), good cycle life (95% retention after 15000 cycles) and good rate capability. Ni(OH)₂ was synthesized in situ on graphene sheets and showed capacitances up to 935 F/g. Similar techniques were used for the synthesis of Co(OH)₂/graphene composite and leads to 972 F/g.

However, despite graphene composites showing higher capacitance than graphene thanks to redox reactions, insulating materials reduces the conductivity and the composite has lower cycle life and rate capability than its pure graphene counterpart. More work is on-going to find new synthesis routes and balance between these different factors.

II. 2-1 *Graphene composites for batteries*

As mentioned earlier, many other electrodes with higher capacity than graphite have been proposed. Some have intrinsic drawbacks such as a huge volume change during cycling (Sb, Sn and Si) or a poor electrical conductivity (metal oxides). Therefore, mixing these materials with carbon materials (including graphene) is considered to be a solution.

The electrode materials commonly used in Lithium-ion battery (Co₃O₄, Fe₂O₃, TiO₂, SnO₂, LiFePO₄, etc.) were investigated for graphene composites in order to improve their conductivity and rate capability with more or less success in laboratory scale (135-145). Negative electrode using metal alloy reaction to stores energy such as Si, Sb or Sn have excellent theoretical capacity but have problems such as huge volume change, short cycle life,

low rate capability and aggregation of particles. It is reported that graphene composites partially solve these issues (146-148). For example Chou *et al.* showed a graphene/Si composite with capacity up to 1168 mAh/g, whereas graphene showed less than 200 mAh/g and silicon nanoparticle showed 346 mAh/g, but the issue of short cycle life persists (148).

II. 3 Transition metal dichalcogenides

Transition metal dichalcogenides are a family of two dimensional materials that are composed of MX_2 layer, with M a transition metal element (Mo, W, etc.) and X a chalcogen element (S, Se, etc.) (149). The most common member of this large family are MoS_2 , WS_2 , and SnS_2 as represented in Figure I.17. Multilayered transition metal dichalcogenides are structurally similar to graphite. Like graphite, the layers of transition metal dichalcogenides are bound to each other by weak Van-der-Waals interaction that can be broken to obtain single sheets that have different physical and chemical properties. These materials have been considered for different applications, including energy storage (150).

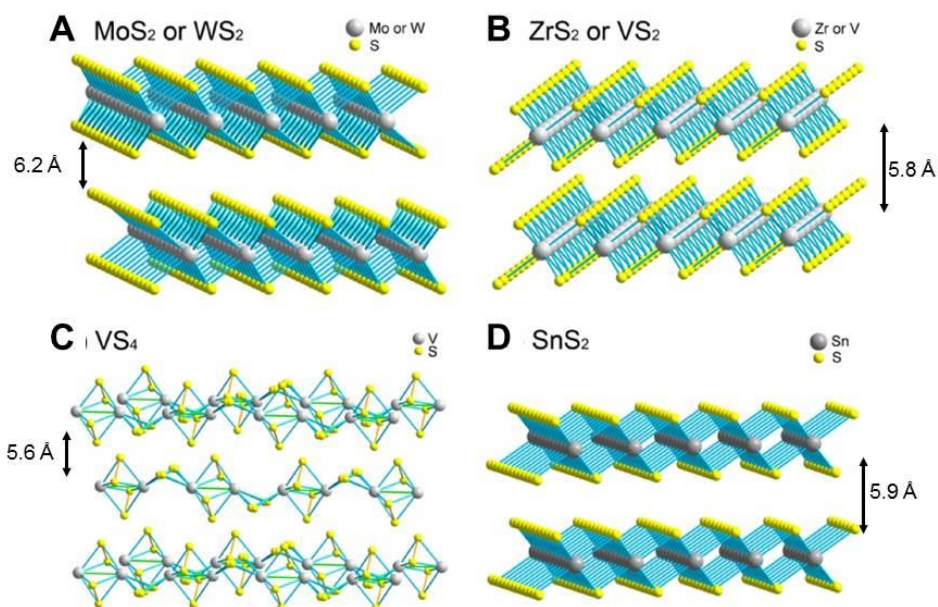


Figure I.17: Structure of several typical layered transition metal sulfides: (A) MoS_2 or WS_2 , (B) ZrS_2 or VS_2 , (C) VS_4 and (D) SnS_2 (adapted from (149)).

II. 3-1 *Lithium ion battery*

Among the transition metal dichalcogenide family, the layered transition metal sulfides have attracted attention as potential electrode for lithium ion battery for different reasons. They store energy through complex mechanism such as conversion or alloying reactions. They have theoretical capacity higher than graphite (from 432 mAh/g for WS₂ to 1196 mAh/g for VS₄), show less volume change compared to silicon and metal oxides, and better rate capability and cycle life thanks to their layered structure.

The most investigated transition metal dichalcogenides for Lithium-ion battery are MoS₂ (151, 152) and Sn₂S (149, 150, 153). Many MoS₂ synthesis routes have been investigated but the capacity, up to 1183 mAh/g, has short cycle life. Moreover, the lithium storage mechanism in MoS₂ and several other metal sulfides is a 3 steps process which is not practical for commercial applications. Although the first cycle is irreversible, the interest of this system relies on the reversible lithiation/delithiation of sulfur. A systematic study by Kim and Goodenough demonstrated that the position of the potential plateau of this reaction increased with the heavier transition metal used (154).

II. 3-2 *Electrochemical Capacitors*

Relatively few studies have been focused on transition metal dichalcogenide for supercapacitor applications. Feng *et al.* investigated two dimensional VS₂ nanosheets for an in-plane supercapacitor (155). They succeeded in synthesizing VS₂ thin film with a high specific surface area and high conductivity. They fabricated the in-plane supercapacitors by a mechanical shaping process and a solid electrolyte (BMIMBF₄-PVA gel) was used. Capacitance was measured from galvanostatic charge discharge and volumetric capacitance values up to 317 F/cm³ were obtained with good cyclability. However, the cyclic

voltammogram shown in Figure I.18 is very resistive and far from the rectangular shape expected for supercapacitors.

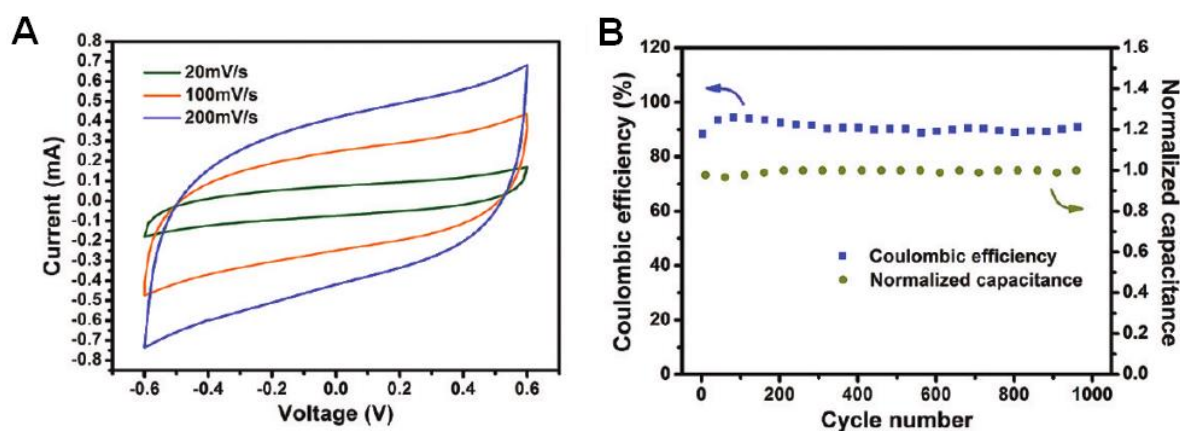


Figure I.18: Performances of the in-plan supercapacitor based on VS_2 ; cyclic voltammetry (A) and cycle life (B) (adapted from (155)).

TiS_2 was suggested to have a pseudocapacitive behavior by Conway. Recently, Muller *et al.* investigated the electrochemical performance of TiS_2 as electrode for Li-ion capacitors (156). The authors observed and analyzed the storage mechanism, separating the capacitive and pseudocapacitive behavior. Figure I.19 shows the electrochemical performance. Impressive capacitances up to 540 F/g at 4C and 320 F/g at 120C were obtained but a potential drop occurs between 3V and 2.5V, reducing the real voltage window.

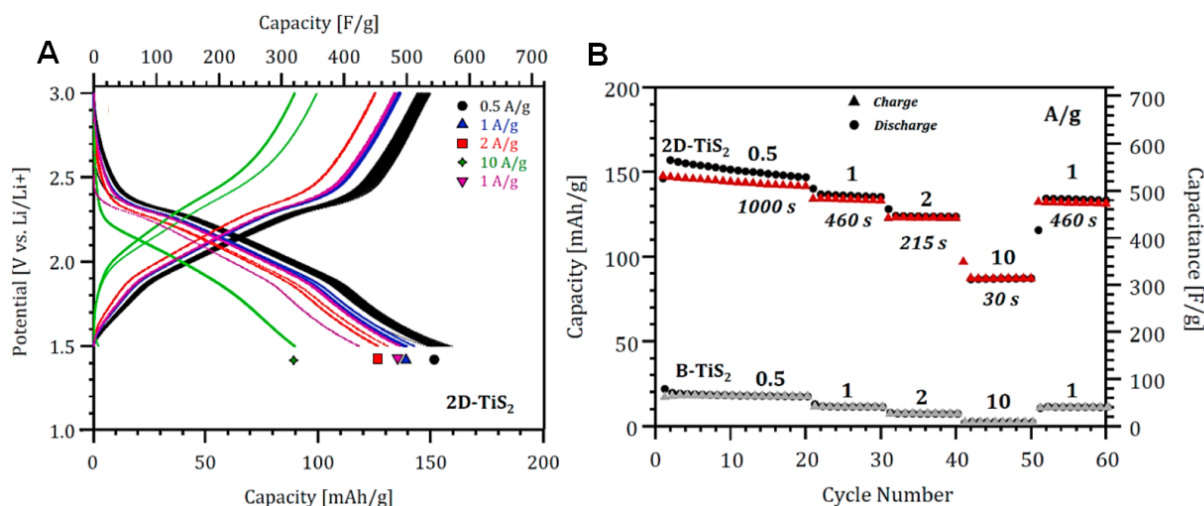


Figure I.19: Charge-discharge curves (A) and rate capability (B) of TiS_2 (adapted from (156)).

III New two dimensional material: MXene

A new family of 2D materials has been discovered in 2011 by Y. Gogotsi' and M. Barsoum's groups at Drexel University; a whole family of exfoliated materials derived from MAX phases and called MXene (8, 157). These materials have a layered structure composed of more than one element. Ti_3C_2 , Ti_2C , Ta_4C_3 and $TiNbC$ were the first synthesized compounds (158). The main interest in MXenes for energy storage applications is that these materials contain a carbide core that guarantees good conductivity and tunable transition metal oxides at the surface that can undergo redox reaction. Its potential for lithium ion battery and lithium ion capacitor applications has been previously demonstrated.

III. 1 MAX Phase

MAX phases are a class of layered ternary carbide or nitride composed of an early transition metal element M, an A-group element A and carbon or nitrogen represented by X. Figure I.20 shows a classification of the MAX phases on periodic table (159).

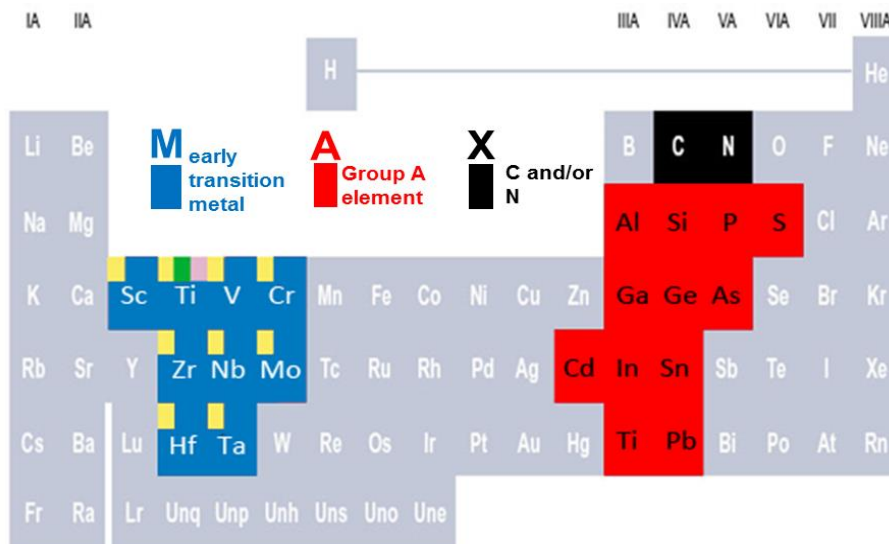


Figure I.20: Repartition of M, A and X elements on the periodic table (adapted from (159)).

These phases are layered hexagonal (space group $D_{6h}^4-P6_3/mmc$) with two formula units per cell, as represented in Figure I.21. They are organized in a $M_{n+1}AX_n$ chemistry, where n is 1,

2, or 3. They are commonly called by their respective chemistry, for example Ti_3AlC_2 belongs to the 312's group.

Regardless of the chemistry, a MAX phase structure can be described as close-packed layers of M layers which are interleaved with A layers in the center of trigonal prism and where X atoms occupy the octahedral site in M_6X . The main difference between the three structures shown in Figure I.21 is the number of M-layers separating the A-layers; in the 211's there are two, in the 312's three and in the 413's four.

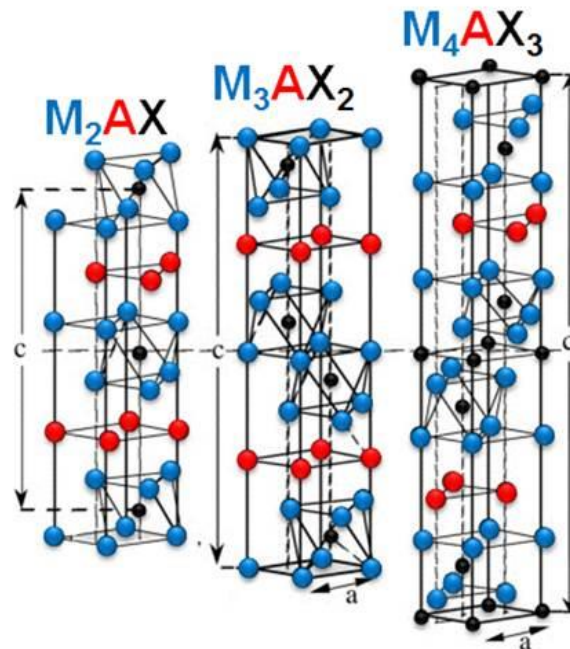


Figure I.21: Crystalline structure of MAX phases M_2AX , M_3AX_2 and M_4AX_3 (adapted from (159)).

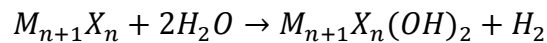
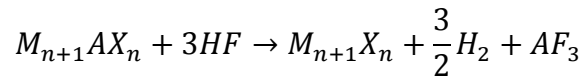
MAX phases are highly damage tolerant, resistant to chemical attack, thermal shock resistant, and machinable. In other terms, they have some properties found in metals and some found in ceramics. Anomalously, they are soft for transition metal carbides and nitrides.

The Vickers hardness values are between 2-8 GPa, which is high for transition metal. In some MAX phases it has been shown that they have plastic-brittle transition at temperature above 1000°C , while retaining decent mechanical properties. At elevated temperature, these phases decompose incongruently into MX-based compound and A-rich liquids in inert atmosphere

whereas they are oxidized in air. Some display formation of protective oxide layer, and therefore have excellent oxidation resistance.

III. 2 Synthesis of MXene

A family of MAX derived compounds has been discovered: MXene. More precisely it is exfoliated layers of MAX phases where the A layer is removed. Developed in 2011, the first synthesis route consists of wet HF treatment of the MAX phases previously described. Figure I.22 shows a schematic representation of the MXene synthesis. The reaction occurring are the following:



After etching, MXene surface is not M-terminated but covered with oxygen-containing groups and fluorine. Considering that there are more than 60 MAX phases known, with different properties, MXene family is already believed to be as diverse and complex as its precursor. Previous studies already show the successful synthesis of several member of this family: Ti_3C_2 , Ta_4C_3 , $TiNbC$, and $(V_{0.5}Cr_{0.5})_3C$. Figure I.23 shows scanning electron microscopy images of MAX phases and exfoliated MXene. Electric conductivities of cold pressed MXene disks were found to be comparable to multilayer graphene. The specific surface area was found to be about 20 m²/g.

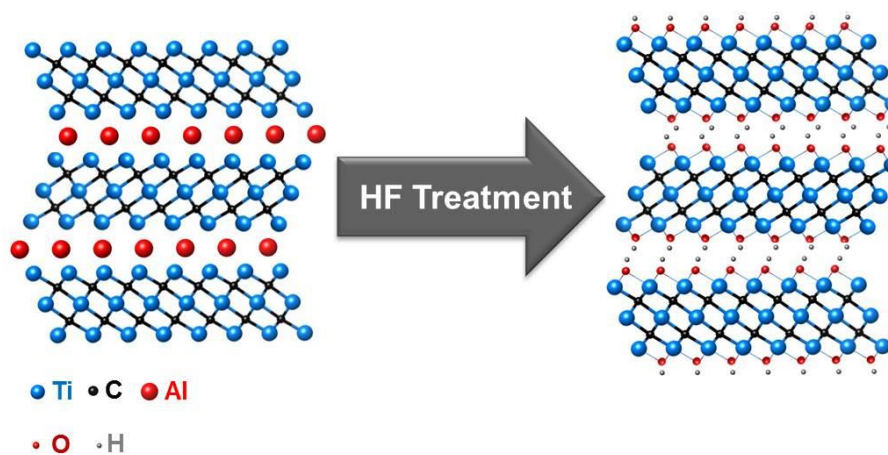


Figure I.22: Schematic synthesis of MXene from MAX phases.

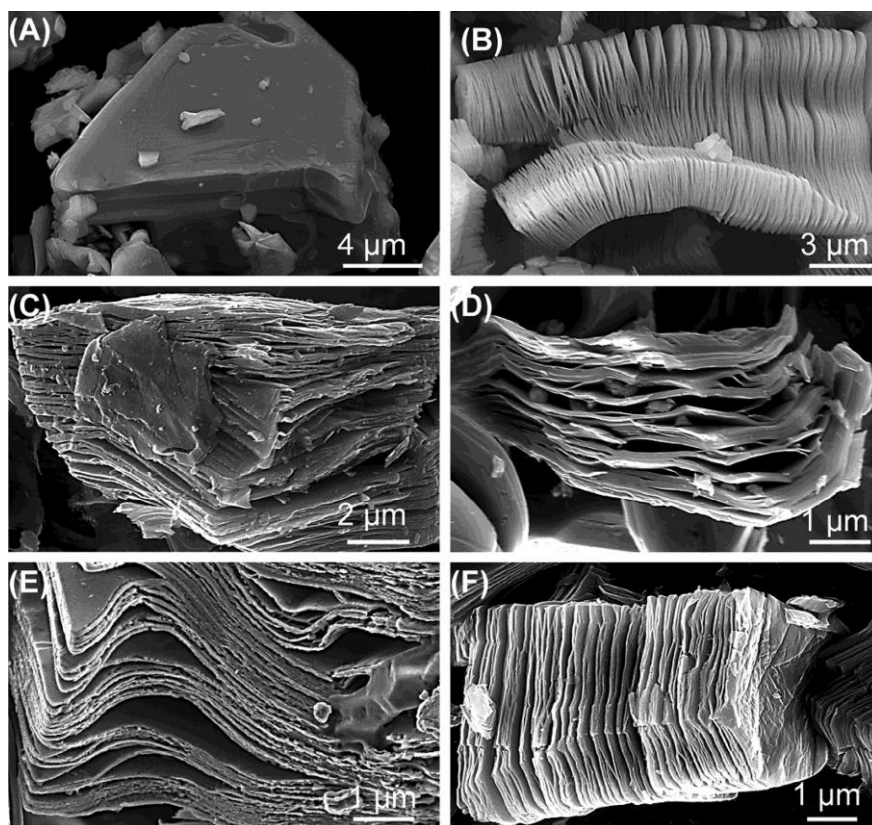


Figure I.23: Secondary electron micrographs for (A) Ti_3AlC_2 particle before treatment. Particles after HF treatment of (B) Ti_3AlC_2 , (C) Ti_2C , (D) Ta_4AlC_3 , (E) TiNbAlC and (F) Ti_3AlCN (adapted from (158))

III. 3 Delamination

Intercalation and delamination of two-dimensional solids is a requisite step in many cases for exploiting the enhanced properties of two-dimensional materials. In 2012, Mashtalir *et al.* demonstrated that MXene can be intercalated by Urea, hydrazine and N,N-dimethylformamide (160). The increase of the c-lattice parameter of surface functionalized Ti_3C_2 was observed by X-ray diffraction (from 19.5 to 25.5 and 26.8 Å). Figure 24.A shows a schematic representation of intercalated MXene. When dimethyl sulphoxide (DMSO) was intercalated into Ti_3C_2 , followed by sonication in water, the Ti_3C_2 was delaminated ($d-Ti_3C_2T_x$) forming a stable colloidal solution (Figure 24.B) that was in turn filtered to produce single sheet MXene (Figure 24.C).

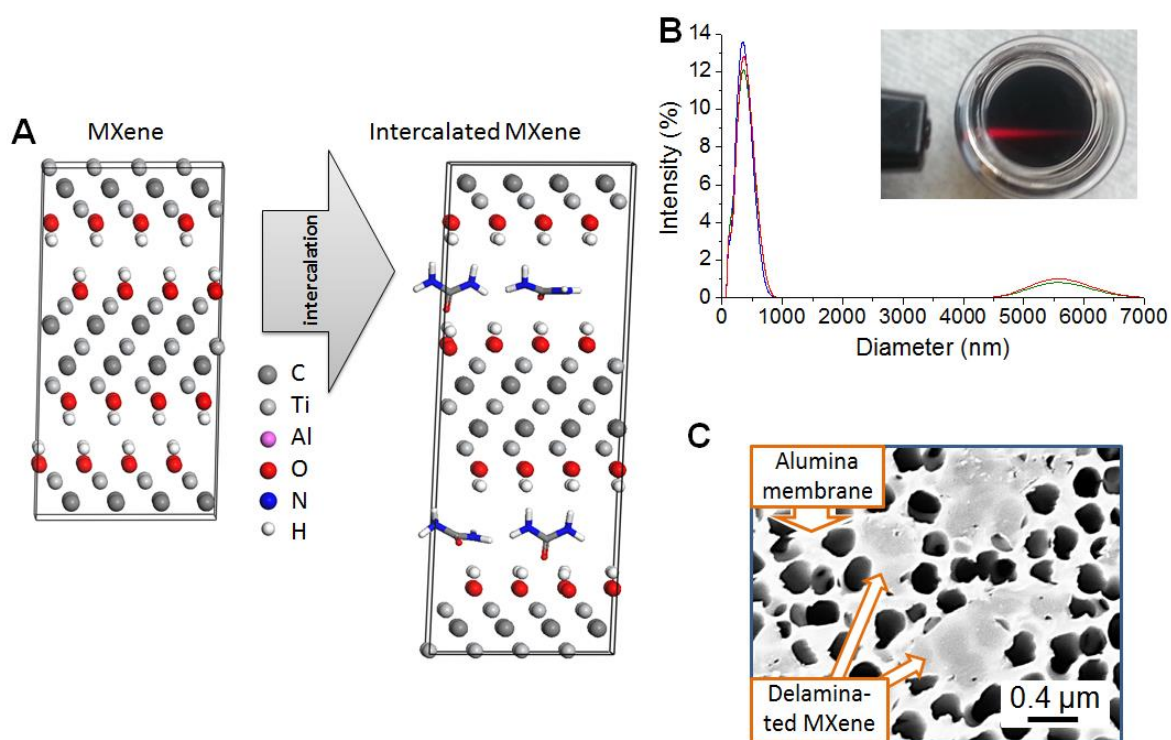
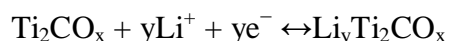


Figure I.24: Schematic representation of the intercalation mechanism (A). Particle size distribution in aqueous colloidal solution; inset shows Tyndall scattering effect in the solution (B). Scanning electron microscope image of $d-Ti_3C_2$ single flake on alumina membrane (C) (adapted from (160)).

III. 4 Applications

Ti₂C was the first member of the family to be analyzed for lithium ion battery application. The reason is that Ti₂AlC is one of the most common and cheapest MAX phases. Powders with particles smaller than 45 μm (– 325 mesh) are commercially available. It is also an excellent electronic conductor and its associated MXene is the lightest (158).

Figure I.25.A shows the cyclic voltammogram of the Ti₂C electrode. A broad irreversible peak was observed around 0.6 V, during the first lithiation (9). It was attributed to the formation of a solid electrolyte interphase and to an irreversible reaction with the electrode material. Authors assigned these peaks with TiO₂ and lithiated titania. Thanks to the similarities, the following redox reaction was proposed:



It is suggested by the authors that because the electrode is dried at 200°C prior to assembling the coin cell, all absorbed water and OH species are removed. Figure 25.B shows capacity values vs. cycle number. A stable capacity of 225 mAh/g at a C/25 rate was reported corresponding to about one Li per Ti₂C formula unit. A promising reversible cycling capacity of 80 mAh g⁻¹ at 3C rate and 70 mAh g⁻¹ after 200 cycles at a 10C rate were reported.

Moreover, Ti₂C was investigated as negative electrode in non-aqueous asymmetric cell in lithium ion capacitors (161). Authors investigated the lithiation/delithiation mechanism. Figure I.26.A shows in-situ X-ray diffraction measurement. A shift was observed, coherent with the lithium insertion process. Figure I.26.B shows charge and discharge specific capacity at 10C rate. The capacity decreased from 70 mAh/g to 60 mAh/g after 1000 cycle.

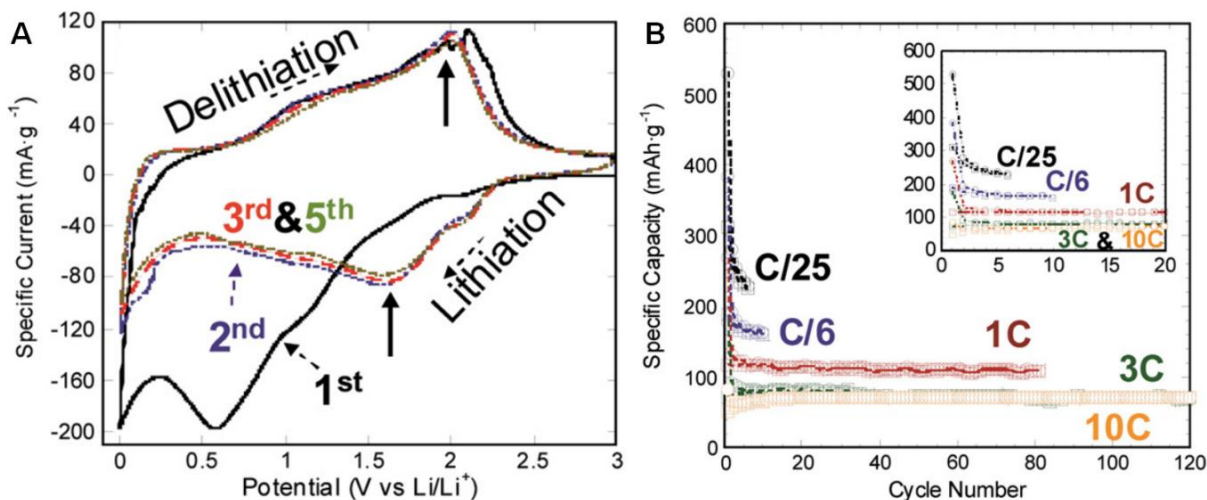


Figure I.25: Cyclic voltammetry at a constant scan rate of 0.2 mV/s. The solid arrows refer to main peaks positions during lithiation and delithiation cycles (A) and capacities vs cycle number at different scan rates (B) (adapted from (9)).

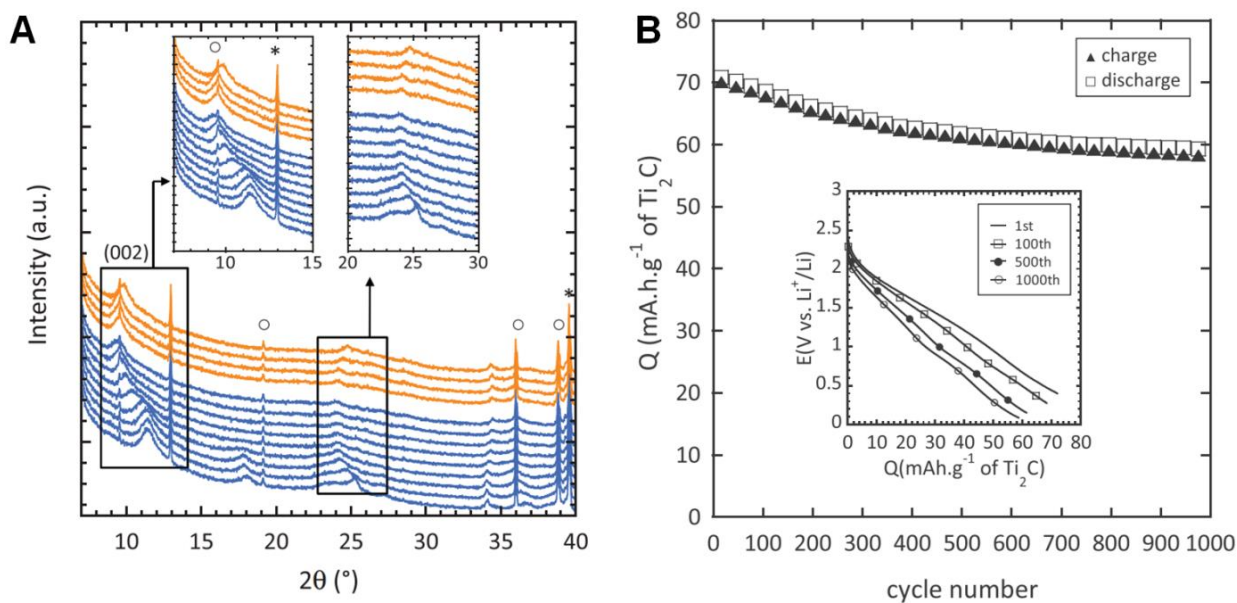


Figure I.26: In-situ X-ray diffraction patterns during charge and discharge of Ti₂C (A) Charge and discharge specific capacity vs. cycle number of a Ti₂C/activated carbon asymmetric cell at 10C rate. Inset: corresponding curves at different cycles (B) (adapted from (161)).

The delamination process of Ti_3C_2 recently discovered was used to assemble a binder-free MXene ‘paper’ (inset Figure. I.27.A) by filtering the aforementioned colloidal solution through a membrane. The breakthrough in terms of Lithium-ion battery applications is the Li-ion uptake on d- Ti_3C_2 free-standing paper. As shown in Fig. I.27.A the capacity of d- Ti_3C_2 is a factor of 4 higher than that of as-synthesized Ti_3C_2 . The paper showed a capacity of 410 mAh/g at a 1C cycling rate and 110 mAh/g at 36C. As shown in Fig I.27.B, the 410 mAh/g represents three Li per $\text{Ti}_3\text{C}_2(\text{OH})_2$. The capacity obtained at 1C was higher than the maximum theoretical capacity of Ti_3C_2 MXene predicted (320 mAh/g (162)). The results at 1C rate are better than graphite and MXene exhibits excellent rate capability promising for high power applications. Nevertheless no plateau was observed during cycling thus limiting the interest for this material as a lithium ion battery electrode. The good rate capability obtained was not the objective of this preliminary work, but it raised the interest of these materials toward high power applications. It is essential to further study this large family of material to improve its power densities.

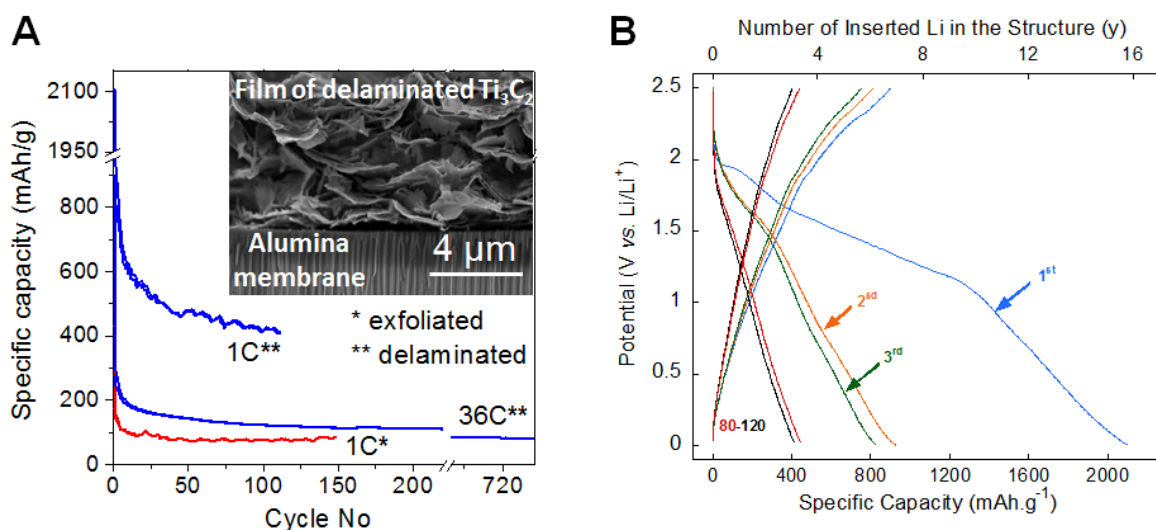


Figure I.27: Comparison of the performance of exfoliated and delaminated Ti_3C_2 as anode material in Li-ion batteries. Inset shows scanning electron microscope image of an additive-free film of delaminated f- Ti_3C_2 filtered through the membrane. (A) The galvanostatic charge/discharge curves at a 1C rate. The “y” value shown on top x-axis was calculated assuming a MXene chemistry of $\text{Ti}_3\text{C}_2(\text{OH})_2$ (B) (adapted from (160))

IV PhD goal

This PhD thesis started just after the demonstration by O. Mashtalir *et al.* (160) of the intercalation of large organic molecule into MXene and elaborated the procedure to obtain delaminated MXene. I co-authored this article and my contribution consisted in the electrochemical testing of the delaminated paper as electrode materials for lithium ion batteries and demonstrated the impressive rate capability of this material.

Herein, the primary objective of this PhD thesis is to investigate MXene performance for high power applications. The challenges are to select the right MXene for each application, to optimize the selected MXene by preparing composites or by chemically modifying its surface and to investigate the energy storage mechanism. Energy storage applications and two-dimensional materials are among the hottest research topics. Since the initial discovery of MXene in 2011, scientific activities on this topic started worldwide.

The high rate performance demonstrated in Lithium-ion batteries led to the investigation of the electrochemical performance of MXene for ECs. Chapter III is focused on multilayered MXene and delaminated MXene electrodes tests in various aqueous electrolytes. The effect of the surface chemistry is extensively discussed. The results demonstrated the intercalation of large cation into Ti_3C_2 , including Na^+ . This encourages the exploration of MXene for beyond-lithium ion batteries.

Chapter IV is focused on the systematic investigation of all synthesized MXene for negative and positive electrodes for either sodium ion batteries or sodium ion capacitors. The behavior during charge-discharge lacked a potential plateau, which is extremely important for practical battery type electrodes. Therefore the research shifted toward Na-ion capacitor. However around the same time, Wang *et al.* released an article about Ti_2C as negative electrode for Na-

ion capacitor. In order to propose innovative research, V_2C has been proposed as positive electrode and a full cell with hard carbon was assembled.

The results obtained in 2014 by Ghidui *et al.* (163) concerning a new synthesis method and the results obtained by Zhao *et al.* (164) concerning CNT/MXene composite modified the direction of the end of the thesis. From the study of HF synthesized MXene, we changed to the study of CNT/'clay'MXene. Chapter V investigates the electrochemical behavior as supercapacitors electrodes in organic electrolyte in order to increase the potential window and increase the power density.

Chapter II: Materials and Methods

Chapter II : Materials and Methods

I MXene synthesis

Two-dimensional transition metal carbides and nitrides, called MXene, studied in this thesis were prepared in collaboration with Professor M. Barsoum's group at Drexel University.

I. 1 MAX Phase

MXenes are derived from MAX phases that are a class of layered ternary carbide and/or nitride that has been introduced in the previous chapter (Figure I.20 and I.21). The MAX phases used are either commercial or were prepared at Drexel University by ball milling raw precursor in a specific ratio then heating in a tube furnace under argon. The following seven different MAX phases were prepared for the study; Ti_3AlC_2 , Ti_2AlC , Nb_2AlC , V_2AlC , $TiVAAlC$, $Ti_{1.5}V_{1.5}AlC_2$ and Ti_3AlCN .

The Ti_3AlC_2 MAX phase was synthesized by mixing commercial Ti_2AlC powders (> 92 wt%, 3-ONE-2, Voorhees, NJ) with TiC (99%, Johnson Matthey Electronic, NY) in a 1:1 molar ratio, followed by ball milling for 24 h using zirconia balls. The mixture was then heated at 5 °C/min, under flowing argon in a tube furnace for 2 h at 1,350 °C. The resulting lightly sintered brick was ground with a TiN-coated milling bit and sieved through a 400 mesh sieve producing powder with particle size less than 38 μm (8).

I. 2 Etching

Wet hydrofluoric acid (HF) treatment of MAX phases was the first efficient method to synthesize MXenes discovered. It allows selective extraction of the aluminum layers from the MAX phases.

To synthesize a given MXene, 10 g of the corresponding MAX phase is immersed in 100 mL of a HF solution (Fisher Scientific, Fair Lawn, NJ) at room temperature. The reactions between HF and the MAX phase were previously discussed in chapter I. The resulting suspension was then washed several times using deionized water and centrifuged to separate the powders. The resulting layers are terminated with mostly oxygenated and fluorinated groups, which are weakly bonded together. In regards to the functional groups, T_x is added to the MXene formula, where “ T_x ” stand for terminated-surface groups such as in $Ti_3C_2T_x$. Table 4 gives the detailed synthesis conditions for each MXene.

Table 4: Synthesis condition of MXene.

MAX Phase	HF concentration	time	MXene
Ti_3AlC_2	50%	18h	$Ti_3C_2T_x$
Ti_2AlC	10%	10h	Ti_2CT_x
Nb_2AlC	50%	90h	Nb_2CT_x
V_2AlC	50%	8h	V_2CT_x
$TiVAIC$	50%	1h	$TiVCT_x$
$Ti_{1.5}V_{1.5}AlC_2$	50%	18h	$Ti_{1.5}V_{1.5}C_2T_x$
Ti_3AlCN	30%	18h	Ti_3CNT_x

I. 3 Delamination

The delamination process, described in chapter I and illustrated Figure II.1, consists of intercalating a large organic molecule to weaken the bond between layers and using ultrasound to completely separate the layers (165). After mixing $Ti_3C_2T_x$ with dimethyl sulfoxide (DMSO) for 18 h at room temperature, the colloidal MXene suspension was centrifuged to

separate the intercalated powder from the liquid DMSO. After decantation of the DMSO, deionized water was added to the residue in a weight ratio of MXene to water of 1:500. After bath sonication of the suspension for 6 h, centrifuging was carried out and the colloidal solution was filtered using a porous anodic aluminium oxide membrane filter (47 mm diameter, 0.2 mm pore size, Whatman Anodisc, Maidstone, UK) and dried in the oven at 70°C overnight, resulting in d-MXene ‘paper’ that detach easily from the membrane (160).

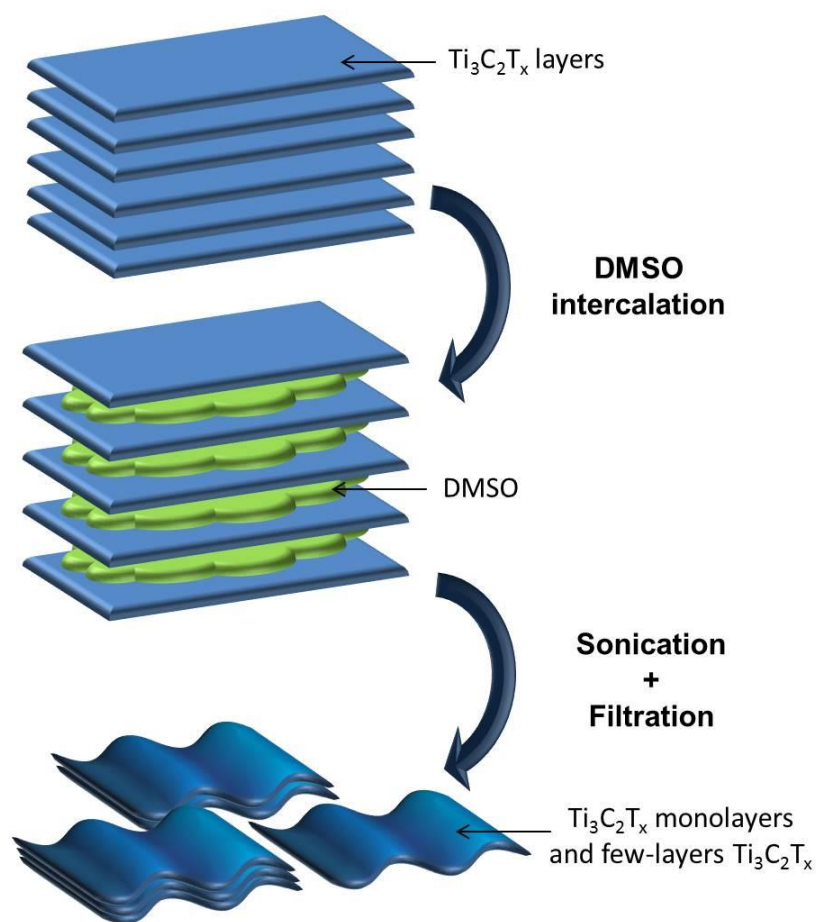


Figure II.1: Schematic illustration of the delamination process.

II Electrochemical characterizations

Electrochemical characterizations of the materials were done using two types of swagelok cells (2- and 3-electrode). Three main electrochemical techniques were used (cyclic voltammetry, galvanostatic charge-discharge and electrochemical impedance spectroscopy) at room temperature using a VMP3 potentiostat (Bio-logic S.A, France).

II. 1 Electrochemical cells

II. 1-1 *Two-electrode setup*

Figure II.2 shows the two electrode Swagelok cell used for assessing the electrochemical performances of the different MXenes synthesized.

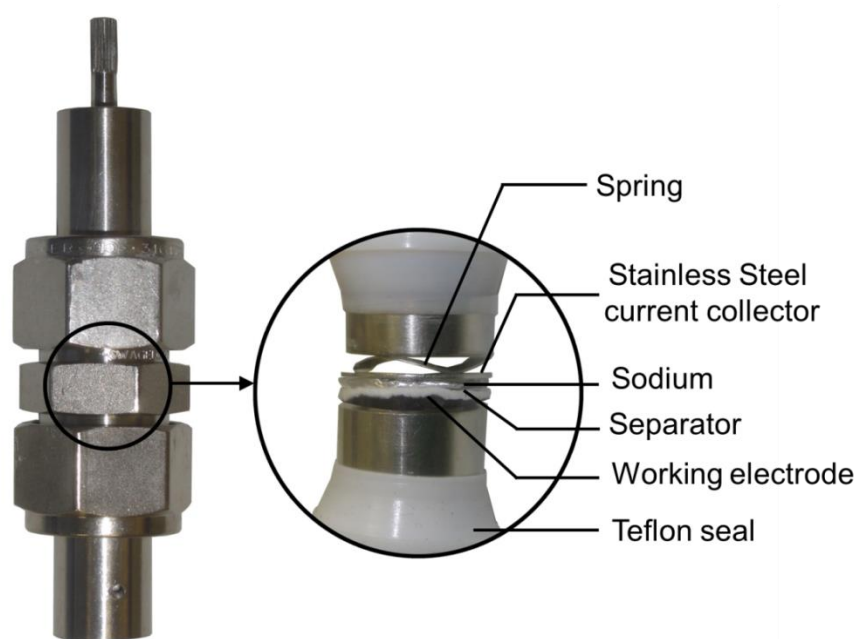


Figure II.2: Picture of a 2-electrode Swagelok cell.

This configuration was mainly used for cyclic voltammetry tests in a half-cell sodium ion battery configuration. In this case, the working electrode is set as the positive electrode and metallic sodium is the negative electrode. The cell was assembled in an argon-filled glovebox because both the electrolyte and metallic sodium are oxygen and water sensitive.

II. 1-2 Three-electrode setup

In a three electrode configuration, a reference electrode is added and placed near the two others. Therefore, it is possible to control the potential of the working (positive) electrode and while simultaneously measuring the potential of the negative electrode vs. the Reference. Silver wire was selected to be the quasi-reference electrode thanks to its electrochemical stability in all the electrolytes studied. Figure II.3 shows the three electrode Swagelok cell used for this setup.

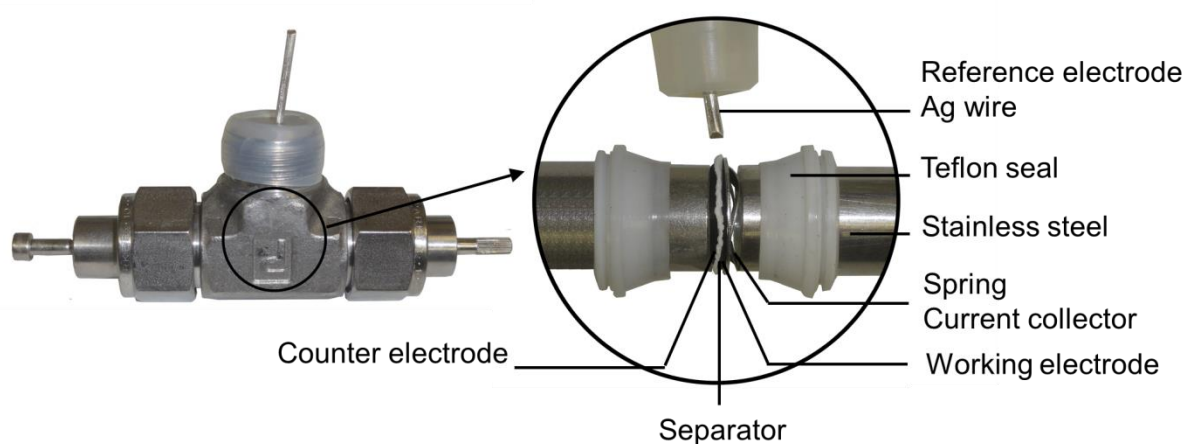


Figure II.3: Picture of a 3-electrode Swagelok cell.

With this cell, two types of setup are possible. In the first case, the potential is controlled and/or measured between the working electrode and the reference electrode. This configuration was used in chapters 3 and 5, where an overcapacitive activated carbon was used as a counter electrode. In the second case, the potential is controlled and/or measured between the working electrode and the counter electrode. This configuration was used in chapter 4 for the full cell study using hard carbon negative counter electrode and positive V_2CT_x electrode.

II. 2 Cyclic voltammetry

Cyclic voltammetry measurement consists of measuring the current response when imposing a potential change at a constant scan rate (v in V/s) between two set potentials according to the following equation:

$$E(t) = E_0 \pm vt \quad \text{Eq. 9}$$

Where, E_0 is the initial potential (V), generally the open circuit potential, v is the scan rate (V/s), t is time (s).

When the cell's potential reaches a set potential, the linear potential sweep is reversed. During cycling, a current is generated due to the potential variation. Herein, the current is mainly driven by various electrochemical phenomena occurring at the electrode/electrolyte interface. The two main phenomena are charge storage through redox reactions and double layer capacitance. Their corresponding I vs. E voltammograms are shown Figure II.4.

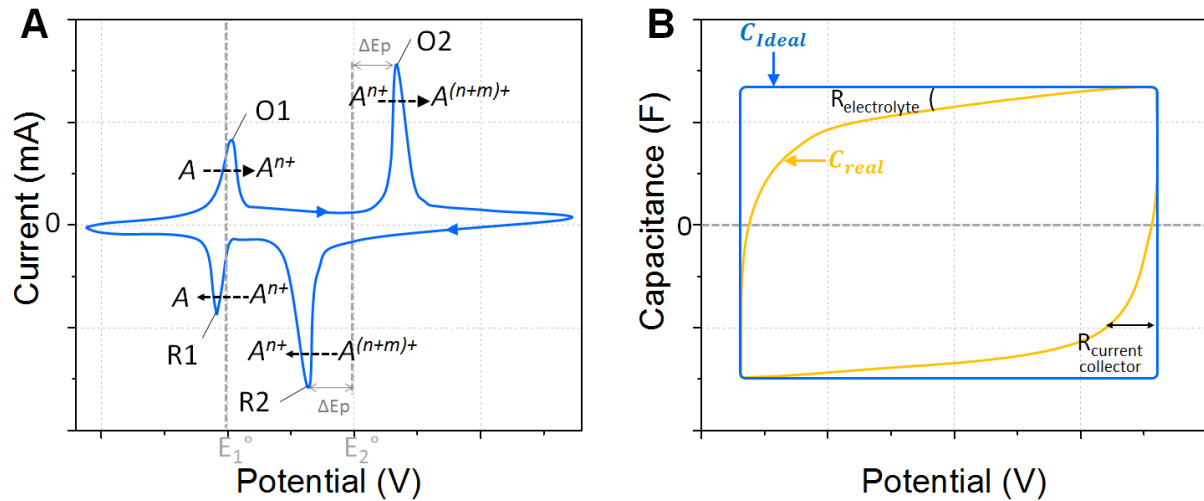
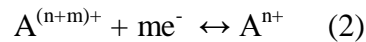
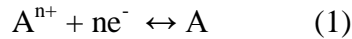


Figure II.4: Typical cyclic voltammograms of redox (A) and double layer (B) materials.

In the first example (Figure II.4.A) the presence of two set of peaks (O1;R1 and O2;R2) that could be attributed to two redox reactions.



In this example, the oxidant of one reaction is the reductant of this other. The distance between the peaks, or ΔE_p , of the second reaction is larger than the first, meaning that this reaction is more irreversible (or shows a larger potential polarization). ΔE_p also increases with the scan rate and diffusion limitation can be extrapolated. In reversible redox reaction, the areas of oxidation and reduction peaks are the same. In most battery-type electrode, the

peak current intensity is proportional to the square root of the scan rate which means that the reactions are usually kinetically limited by mass transfer to the electrode.

In the second example, Figure II.4.B, rectangular shaped voltammograms characteristic of capacitive behavior is observed. The differences between an ideal double layer capacitor and a more realistic supercapacitor have many origins. An ideal double layer capacitance is constant at all scan rates and is determined from the equation 10:

$$C_{dl} = \frac{I}{\nu} \quad \text{Eq. 10}$$

Where, C_{dl} is the double layer capacitance of an electrode (F), ν is the scan rate (V/s) and I is the current (A).

Several phenomena can cause deviation from ideal rectangular voltammograms. The most common are the series resistance (mainly coming from the electrolyte resistance), electrolyte decomposition, gas evolution, irreversible surface reaction and the carbon pore size distribution that may create mass transfer limitation in smaller pores at high potential scan rate.

II. 3 Galvanostatic charge-discharge measurement

The galvanostatic charge-discharge measurement consists of passing a constant current to the cell and recording the potential evolution with time. A potential window is selected and when a potential limit is reached the current is reversed. The charge/discharge curves are usually plotted as potential vs. time or potential vs. capacity. This technique is also used to estimate the cycle life of the cell, by repeating the charge/discharge a high number of times and trace the capacity or capacitance vs. the cycle number. The cycling rate is generally noted as C/n rate where n is the time in hours for a complete charge or discharge at the corresponding current density and C the capacity (Ah). Usually the rate is lower for battery (tenth of minutes to hours) than for supercapacitors (tenth of seconds to minutes).

As shown in chapter 1, batteries and supercapacitors have different behaviors during galvanostatic cycling. Figure II. 5 summarize the main characteristic observable on a charge-discharge curves.

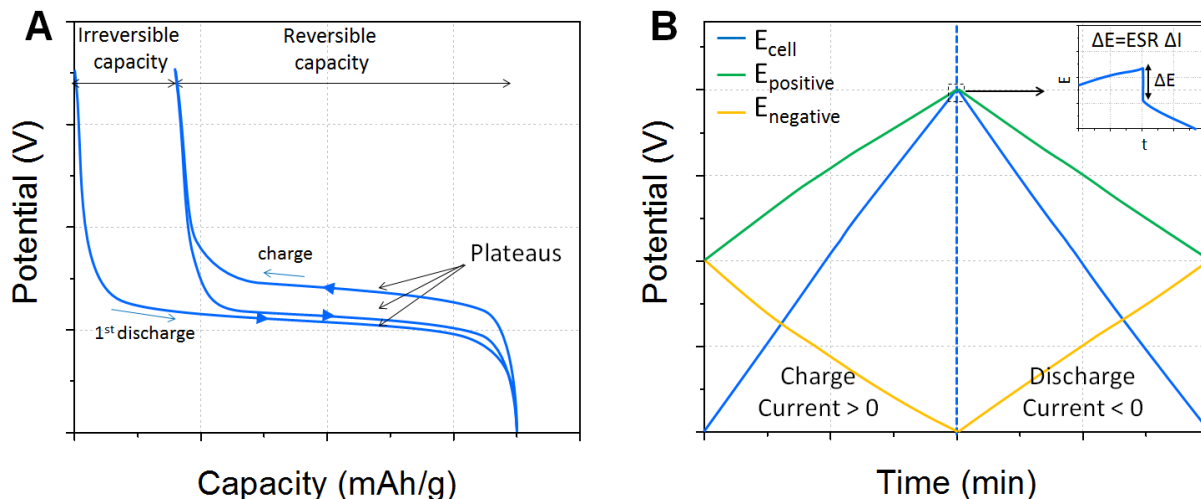


Figure II.5: Typical galvanostatic charge-discharge curves of lithium ion intercalation (A) and double layer (B) materials.

In both cases, the specific capacity is calculated from equation 11. Volumetric and areal capacities are also often calculated.

$$Q = \frac{I \times t}{m} \quad \text{Eq.11}$$

Where Q is gravimetric capacity (mAh/g), I is the current applied (A), t is the time (h) and m is the mass (g).

In the example of redox reaction Figure II.5.A, the plateau regions are characteristic of a two-phase mechanism corresponding to the insertion of cations into the host material. These redox reactions occur at a given potential. The differences of plateau potential during charge and discharge can originate from thermodynamic limitation, charge transfer kinetics limitation, ions diffusion, and electrical resistance (166). In most cases for batteries, irreversibility is observed during the first cycle. For lithium-ion batteries irreversible reactions occur, such as the formation of a solid electrolyte interphase at the anode during charging, which is responsible for the irreversibility seen in the first cycle (167).

In the case of capacitive-type electrodes, Figure II.5.B, the potential follows a quasi-straight line during galvanostatic charge-discharge measurements that correspond to the following equation:

$$\Delta E = I \times (ESR + \frac{t}{C}) \quad \text{Eq. 12}$$

Where ΔE is the potential evolution (V), I is the current applied (A), ESR is the equivalent series resistance (Ω), C is the double layer capacitance (F) and t is the time (s).

The coulombic efficiency is a factor that brings out information regarding the cycle life of a cell. It is calculated from the following equation:

$$\eta (\%) = \frac{Q_{discharge}}{Q_{charge}} \quad \text{Eq.13}$$

Double layer capacitive materials have excellent coulombic efficiency (>99%) which allow supercapacitors to reach 100,000 cycles. In contrast, electrode materials that store charge through redox reactions usually have lower coulombic efficiency. The cycle life of lithium ion batteries is approximately hundreds of cycles.

II. 4 Electrochemical Impedance Spectroscopy

This technique consists in imposing a sinusoidal potential of small amplitude (few mV) over a wide range of frequency f (from hundreds of kHz down to few mHz) according to equation 14 to a steady state. Equation 15 describes the current response to the applied potential. It is a sinusoidal current which presents a shifted angle of phase φ .

$$E = E_0 + \Delta E \sin(\omega t) \quad \text{Eq.14}$$

$$I = I_0 + \Delta I \sin(\omega t + \varphi) \quad \text{Eq.15}$$

Where E is the potential (V), E_0 is the initial steady state potential (V), ΔE is the amplitude of the signal (V), ω is the pulsation (rad.s^{-1}), t is the time (s), I is the current (A), I_0 is the initial steady state current (in this thesis $I_0 = 0$ A), ΔI is the amplitude of the current response (A) and φ is the phase shift.

In order to facilitate mathematical treatment, the potential and current during the electrochemical impedance spectroscopy are usually written with complex numbers as follow:

$$\Delta E = \Delta E_{max} e^{j(\omega t)} \quad \text{Eq.16}$$

$$\Delta I = \Delta I_{max} e^{j(\omega t + \varphi)} \quad \text{Eq.17}$$

The complex impedance is defined by the ratio between the complex potential and complex current:

$$Z = \frac{\Delta E}{\Delta I} = \frac{\Delta E_{max}}{\Delta I_{max}} e^{-j\varphi} \quad \text{Eq.18}$$

And using the Euler's formula:

$$Z = \frac{\Delta E_{max}}{\Delta I_{max}} \cdot [\cos(\varphi) - j\sin(\varphi)] = \text{Re}(Z) - j \times \text{Im}(Z) \quad \text{Eq.18}$$

Where $\text{Re}(Z)$ and $\text{Im}(Z)$ are the real part and imaginary part of the impedance.

The most common data representation method is to plot $-\text{Im}(Z)$ versus $\text{Re}(Z)$ which is called the Nyquist plot. Figure II.6 represents the Nyquist plot of the electrochemical impedance for two different electrochemical systems.

The equivalent circuit of lithium ion electrode is presented Figure II.6.A, accompanied with a typical impedance of an intercalation material $\text{Li}_x\text{Mn}_2\text{O}_4$ (168-170). When the frequency tends to ∞ , the impedance depends on the electrolyte resistance. When the frequency decreases, the first semi-circle observed corresponds to the solid electrolyte interphase and the second semi-circle describes non-ideal double layer behavior. At lower frequency, an element called Warburg impedance is present, related to diffusion limitation, then the curve tends toward a vertical line associated with intercalation capacitance (169).

The Nyquist impedance and equivalent circuit of a porous electrode in electrochemical double layer capacitors are represented in Figure II.6.B. This model, called the Transmission Line Model, was proposed by De Levie in 1963 and consists of a succession of series/parallel RC

components that account for the porosity of the carbon (171, 172). At high frequency the ions can only reach the outer surface of the electrode, thus the impedance depends on the electrolyte resistance, the current collector resistance and electronic resistance of electrodes. When the frequency decreases, schematically, ions can access deeper into the pores, thus the resistance increase due to the diffusion of ions inside the pores. As the frequency decreases, it reaches the knee frequency which corresponds to the frequency where the resistance reaches a maximum. At lower frequency, a vertical straight line is observed corresponding to a capacitive behavior (173).

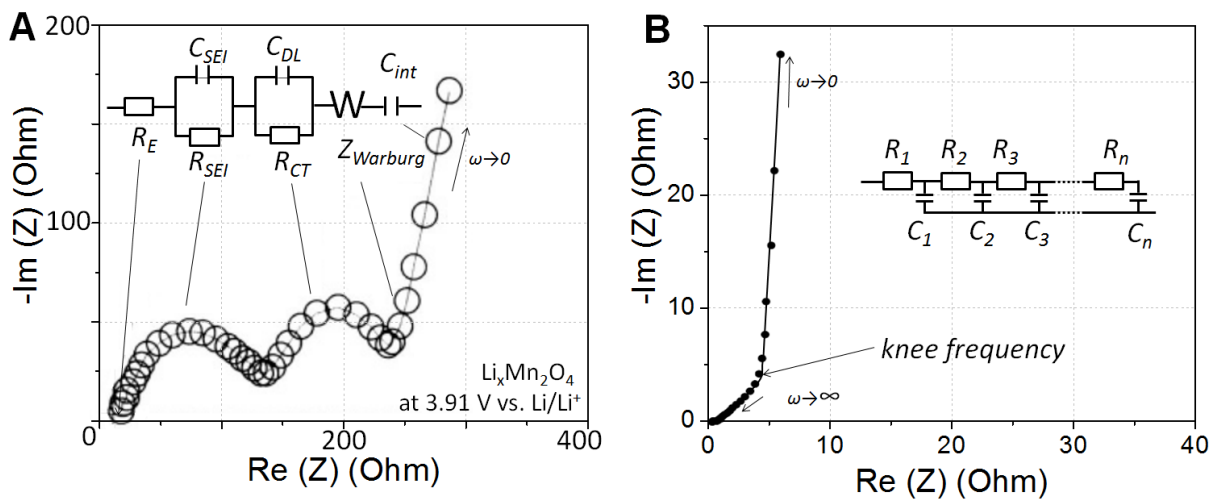


Figure II.6: Typical Nyquist plots of a battery-type materials ($\text{Li}_x\text{Mn}_2\text{O}_4$) (A) and carbon double layer material (B). Inset: equivalent circuit (adapted from (169) (173)).

III Materials Characterization Techniques

III. 1 X-ray diffraction

III. 1-1 Principle

X-ray diffraction is an analytical technique used to characterize materials atomic structure. A solid is defined as crystal when it is composed of a regular arrangement of atoms as represented in Figure II.7. The crystal is defined by a three dimensions lattice and the

interplane atomic spacing is noted d_{hkl} where h , k and l , called Miller indices, are the reciprocal of the lattice vectors.

The X-rays generated from copper excitation irradiate the solid, and are scattered from its electrons. The wavelength of copper $K\alpha$ radiation is similar in size to d_{hkl} (few Å). As a consequence, diffraction patterns can be observed due to constructive and destructive interference between x-rays and atoms. The condition for constructive interference is given by the Bragg's Law:

$$n\lambda = 2d_{hkl}\sin\theta \quad \text{Eq.19}$$

Where n is an integer corresponding to the order of the reflection, λ is the wavelength of radiation used, d_{hkl} is the interplane atomic spacing and θ is the scattering angle.

In a θ - 2θ configuration, θ corresponds to the angle between the hkl plan and the incident X-ray and the diffracted X-ray. The detector is placed at an angle 2θ to the incident X-ray. The results are usually presented as the intensity vs. 2θ . From the position of intensity peak it is possible to calculate d_{hkl} according the Bragg's Law. In the specific case of MXene the (002) plane, corresponding to $h=0$ $k=0$ and $l=2$, diffracts and is one of the most intense peaks observed. The 2θ position of this peak is therefore used to determine the c -lattice parameter.

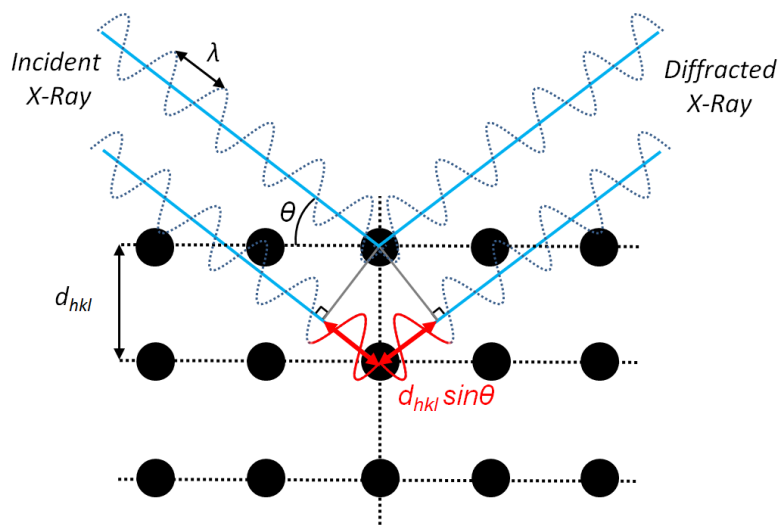


Figure II.7: Schematic representation of Bragg's diffraction.

III. 1-2 Equipment

Ex-situ X-ray diffraction patterns of the electrodes were collected using a Bruker D4 diffractometer using a Cu K α radiation ($\lambda = 1.5406 \text{ \AA}$) in the range $2\theta = 5\text{--}50^\circ$ with a step of 0.016° .

In-situ X-ray diffraction patterns of $\text{Ti}_3\text{C}_2\text{T}_x$ electrodes were collected on a Bruker D8 diffractometer using a Cu K α radiation ($\lambda=1.5406 \text{ \AA}$) with a step of 0.02° . Figure II.8 shows the special 2-electrode Swagelok-type cell designed in LRCS (Amiens University), where the samples are placed and covered with materials that are transparent to X-ray to avoid electrolyte evaporation and allow in-situ X-ray diffraction recording. With aqueous electrolytes a Mylar window was used whereas a beryllium window was used with organic electrolytes. The counter electrodes were either overcapacitive activated carbon or metallic sodium. In each chapter, the corresponding experimental details of the in-situ setup will be described.

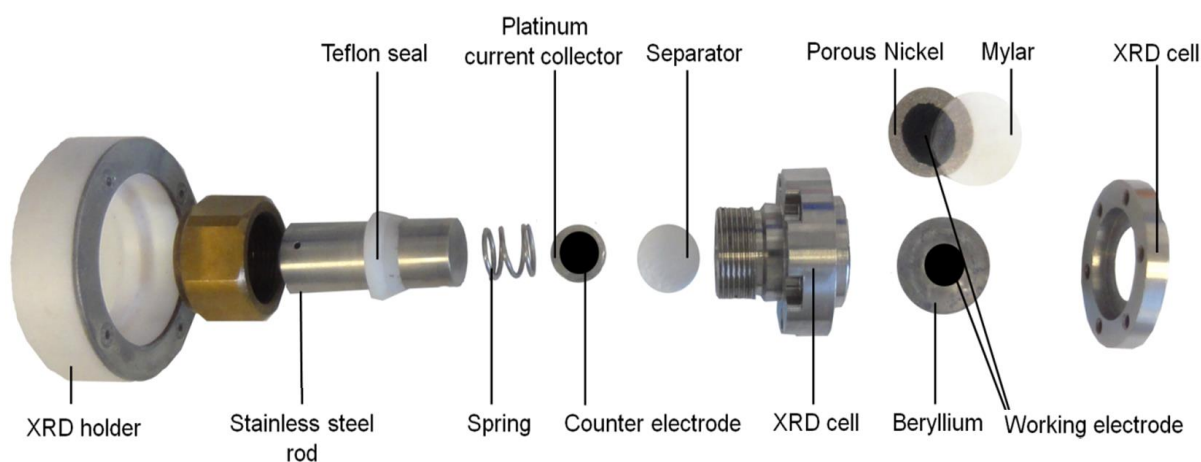


Figure II.8: Photography of the electrochemical in-situ X-ray diffraction cell.

III. 2 Scanning electron microscopy

III. 2-1 Principle

Scanning electron microscopy is a technique commonly used to observe the topography of materials at the microscopic scale based on the interaction of the material with a beam of electrons. The electron beam is produced thermionically by the tungsten filament cathode of an electron gun. The interaction between material and the electron beam produce various types of radiation (electrons, X-rays and fluorescence). Specialized detectors collect the secondary electrons which are low-energy electrons (<50 eV) ejected from the k-shell of the atoms at the surface of the material. An image is created by scanning the material surface with the electron beam and recording the number of secondary electron detected.

III. 2-1 Equipment

Two scanning electron microscopes were used to investigate the electrodes' morphology, structure and thickness. A JSM-6700F (JEOL, Japan) was used by Barbara Daffos and a Zeiss Supra 50 VP (Carl Zeiss SMT AG, Oberkochen, Germany) was used by Maria R. Lukatskaya.

III. 3 Energy dispersive X-ray spectroscopy

Energy dispersive X-ray spectroscopy is a technique used for elemental analysis and is often present in scanning electron microscopes, like in our case. A Zeiss Supra 50 VP (Carl Zeiss SMT AG, Oberkochen, Germany) was used. The principle is to use an X-ray detector to record the number and energy of X-rays produced in the sample studied during irradiation by an electron beam. The energies of the X-ray emitted are converted to measure the elemental composition of the sample.

III. 4 Gas Sorption Analysis

Gas sorption analysis consists of measuring the quantity of gas absorbed by the sample studied as a function of gas pressure at constant temperature. This data can be used to calculate the specific surface area using the Brunauer–Emmet–Teller equation. Nitrogen sorption analysis at 77 K using a Micromeritics ASAP 2020 apparatus was carried out after outgassing under vacuum at 300 °C for 12 h. The analysis was performed with the help of Barbara Daffos.

III. 5 X-ray photoelectron spectroscopy

X-ray photoelectron spectroscopy is a technique commonly used to analyze the surface chemistry of a sample based on the interaction of the material with an X-ray beam that produces photo-emitted electrons. The number and kinetic energy of these electrons can be measured using a specialized detector under ultrahigh vacuum ($<10^{-7}$ Pa). An X-ray photoelectron spectrometer (VersaProbe 5000, Physical Electronics Inc., USA) using a 100 μm monochromatic Al K α X-ray beam to irradiate the surface of the samples was used to obtain X-ray photoelectron spectra. Emitted photoelectrons were collected using a 180° hemispherical electron energy analyzer. Samples were analyzed at a 45° takeoff angle between the sample surface and the path to the analyzer. High-resolution spectra were taken at a pass energy of 23.50 eV and with a step size of 0.05 eV. The peak fitting was carried out using CasaXPS Version 2.3.16 RP 1.6. The experiment and analyses were performed by Kevin M. Cook at Drexel University.

**Chapter III: MXene as a Supercapacitor
electrode in aqueous electrolytes**

Chapter III : MXene as a Supercapacitor electrode in aqueous electrolytes

I Introduction

The primary objective of this chapter is to investigate the electrochemical performance of MXene as an electrode material for supercapacitors for high power applications.

Our strategy is to develop MXene electrodes for supercapacitors that could potentially store energy through surface redox reactions or intercalation of ions between layers. In this chapter, the study focuses exclusively on $Ti_3C_2T_x$ which was selected because it has shown the best performances in lithium ion batteries (160). The intercalation of ions between MXene layers has been previously observed. Come *et al.* demonstrated the intercalation of Li^+ into Ti_2C promoted electrochemically (161) and Mastalir *et al.* showed the spontaneous intercalation of organic molecules (DMSO, hydrazine, urea) into Ti_3C_2 (160). The purpose of this work is to investigate the spontaneous intercalation of ions from several aqueous electrolytes in between the 2D $Ti_3C_2T_x$ layers, where T_x stands for surface terminal groups containing oxygen and fluorine functional groups. The electrochemical performance of $Ti_3C_2T_x$ in a variety of electrolytes was measured by cyclic voltammetry and galvanostatic charge-discharge techniques. The surface chemistry was analyzed by X-ray photoelectron spectroscopy and the intercalation mechanism was observed by X-ray diffraction.

II Spontaneous intercalation of cation

II.1 Study by X-ray diffraction

To investigate the spontaneous reaction of $Ti_3C_2T_x$ with aqueous solutions, 0.4 g of as-synthesized $Ti_3C_2T_x$ powder was added to 50 mL of various aqueous electrolytes, stirred for an hour with a magnetic stirrer at room temperature; then the solution was decanted after powder sedimentation; this process was repeated 5 times. The final time the solution was filtered on a hydrophilic polypropylene membrane (GH polypropylene). The powders were collected and analyzed by x-ray diffraction. X-ray diffraction patterns of $Ti_3C_2T_x$ and treated $Ti_3C_2T_x$ (here in LiOH as an example) are shown in Figure III.1. As described in Chapter 2, the distance between single Ti_3C_2 sheets of $Ti_3C_2T_x$ and treated $Ti_3C_2T_x$ is proportional to the c-lattice parameter which can be calculated directly from the (00n) peaks according to equation 18: $d_{(00n)} = n \times \lambda / 2\sin(\theta) = n \times d_{c-lattice\ parameter}$. The (002) peak was always the most intense peak of the pattern, therefore calculations and discussions focus on this peak. In the case of $Ti_3C_2T_x$ the c-lattice parameter is calculated to be 20.3 Å. The intercalation of species between layers induces an increase in the c-lattice parameter, noticeable by the 2 θ downshift of the (00n) peaks position compared to the untreated $Ti_3C_2T_x$.

Figure III.2 shows the X-ray diffraction patterns of $Ti_3C_2T_x$ obtained after treatment in various electrolytes. The aqueous solutions selected were 1M sulfuric acid (H_2SO_4), 1M lithium hydroxide (LiOH), 1M sodium hydroxide (NaOH), 1M potassium hydroxide (KOH), 1M potassium acetate (KOAc), 1M potassium sulfate (K_2SO_4), 3M sodium acetate (NaOAc), 1M lithium sulfate (Li_2SO_4), 1M sodium sulfate (Na_2SO_4) and 1M magnesium sulfate ($MgSO_4$). A 2 θ downshift was observed in all cases except with $Ti_3C_2T_x$ treated by 1M H_2SO_4 . A possible explanation is that the distance between two Ti_3C_2 layers is large enough that of the intercalation of small H^+ has no effect on the c-lattice parameter. Another

explanation could be that the as-synthesized $\text{Ti}_3\text{C}_2\text{T}_x$ already contains intercalated H^+ cations that comes from the acidic environment during the synthesis with hydrofluoric acid.

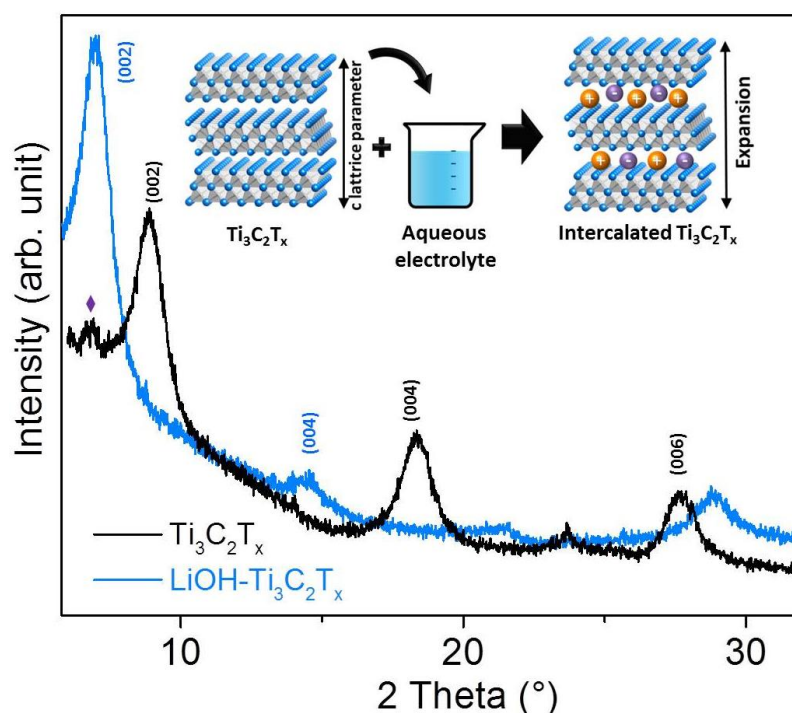


Figure III.1: X-ray diffraction pattern of $\text{Ti}_3\text{C}_2\text{T}_x$ and $\text{LiOH-Ti}_3\text{C}_2\text{T}_x$. Purple diamond indicates peak coming from measurement set-up. Inset is a schematic of the intercalation process.

Figure III.2A shows $\text{Ti}_3\text{C}_2\text{T}_x$ treated in KOH, KOAc and K_2SO_4 . The three chemicals share the same cation, thus the difference in their c-lattice parameter is related to other factors, such as pH or anion size. Yet, despite the acetate ion being larger than the hydroxide ion, KOH- $\text{Ti}_3\text{C}_2\text{T}_x$ has a larger c-lattice parameter than KOAc- $\text{Ti}_3\text{C}_2\text{T}_x$, thus the difference cannot be directly correlated with the size of the anion. The same conclusion can be deduced from the results presented in Figure III.2B where $\text{Ti}_3\text{C}_2\text{T}_x$ is treated with three chemicals that share the same Na^+ cation.

Figure III.2C shows $\text{Ti}_3\text{C}_2\text{T}_x$ treated in 1M LiOH, NaOH and KOH. In this case, the anion and the pH are the same for the three solutions; therefore the differences observed should be attributed to the cation nature. Slightly different shifts are observed but it does not correlate

with the cation size. Although the downshift of the (002) peaks is not exactly the same, they are more similar to each other than with any of the other electrolytes investigated, which demonstrates the importance of the pH.

Figure III.2D shows $\text{Ti}_3\text{C}_2\text{T}_x$ treated in 1M H_2SO_4 , Li_2SO_4 and MgSO_4 . Here, the anion is the same but the cation and pH are different. As explained before no shift was recorded after treatment in H_2SO_4 . The intercalation from Li_2SO_4 is comparable to results obtained with Na_2SO_4 and K_2SO_4 . The shift obtained in the case of the MgSO_4 treatment is the largest observed so far. As the pH of 1M Li_2SO_4 , Na_2SO_4 , K_2SO_4 and MgSO_4 is similar, it suggests that the cation valence has an effect on the lattice expansion.

To conclude, the shift depends on both pH and valence of the cation.

Energy-dispersive X-ray spectroscopy analysis of $\text{Ti}_3\text{C}_2\text{T}_x$ after treatment in a few electrolytes was performed in order to demonstrate if either the cations or the anions were intercalated into $\text{Ti}_3\text{C}_2\text{T}_x$ layers. Results are presented in Table 5 and confirmed the presence of the cations while anion (sulfur) was not detected. This implies that the cations intercalate between the $\text{Ti}_3\text{C}_2\text{T}_x$ layers.

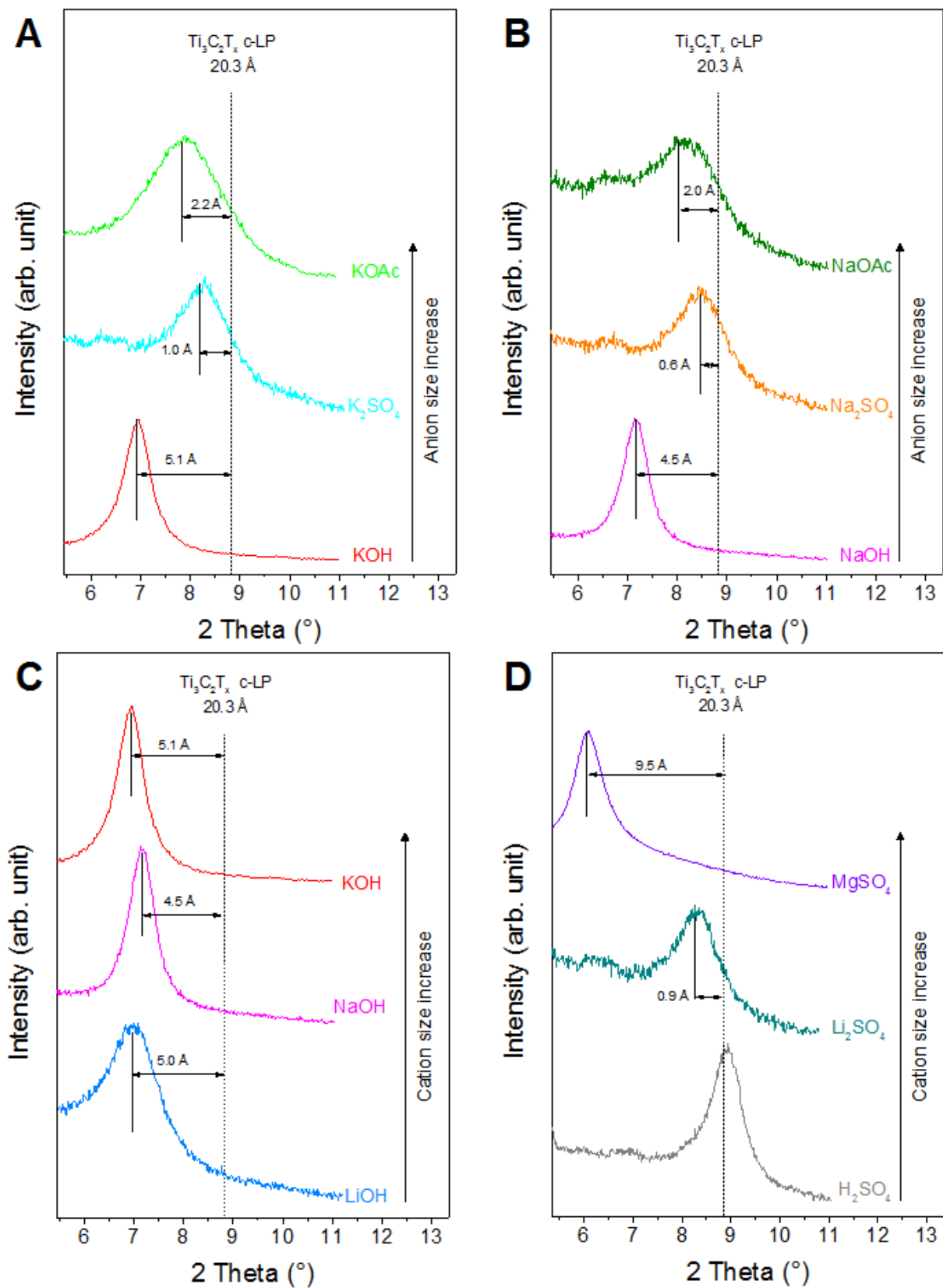


Figure III.2: X-ray diffraction patterns of $\text{Ti}_3\text{C}_2\text{T}_x$ after treatment in electrolytes with different anions (A-B) and different cations (C-D).

Table 5: Energy-dispersive X-ray spectroscopy analysis of $\text{Ti}_3\text{C}_2\text{T}_x$ -based powder.

Material	Atomic %					
	Ti	C	O	F	S	Cation of electrolyte
$\text{Ti}_3\text{C}_2\text{T}_x$	30.0	14.8	16.0	18.9	-	-
KOH- $\text{Ti}_3\text{C}_2\text{T}_x$	30.0	21.2	30.9	11.4	-	3.2
NaOAc- $\text{Ti}_3\text{C}_2\text{T}_x$	30.0	16.2	18.2	27.4	-	5.5
K_2SO_4 - $\text{Ti}_3\text{C}_2\text{T}_x$	30.0	17.8	8.4	15.4	0	1.4
Na_2SO_4 - $\text{Ti}_3\text{C}_2\text{T}_x$	30.0	17.5	12.9	15.8	0	1.0

*Values of the carbon, oxygen and fluorine content are approximate, since spectra were collected from the rolled $\text{Ti}_3\text{C}_2\text{T}_x$ -based electrode, which contained carbon additive (contributes to C and O content) and PTFE binder (contributes to C, O and F content) (adapted from (174)).

In most of 2D materials, the intercalation of ions is electrochemically driven or is limited by diffusion and kinetics (175, 176). In order to shed light on the spontaneous intercalation mechanism, X-ray diffraction spectra of $\text{Ti}_3\text{C}_2\text{T}_x$ in an in-situ cell containing a 1M MgSO_4 solution was recorded during cycling, as shown in Figure III.3. In the first pattern (yellow) there are no shifts observed but with time the peak at 9° starts to decline while a peak at lower angles emerged. In the second scan the two peaks are clearly identifiable. The emerging peak shift from 6.7° to 6° in the following scans. This suggests that the intercalation reaction of MgSO_4 into $\text{Ti}_3\text{C}_2\text{T}_x$ layers is limited by diffusion.

Similar experiments (not reported here) were attempted with $\text{Ti}_3\text{C}_2\text{T}_x$ in 1M KOH and 3M NaOAc but the (002) downshift was observed immediately. This suggests that the diffusion and kinetic parameters of the intercalation depends on the electrolyte used but further work is needed to better understand the mechanism.

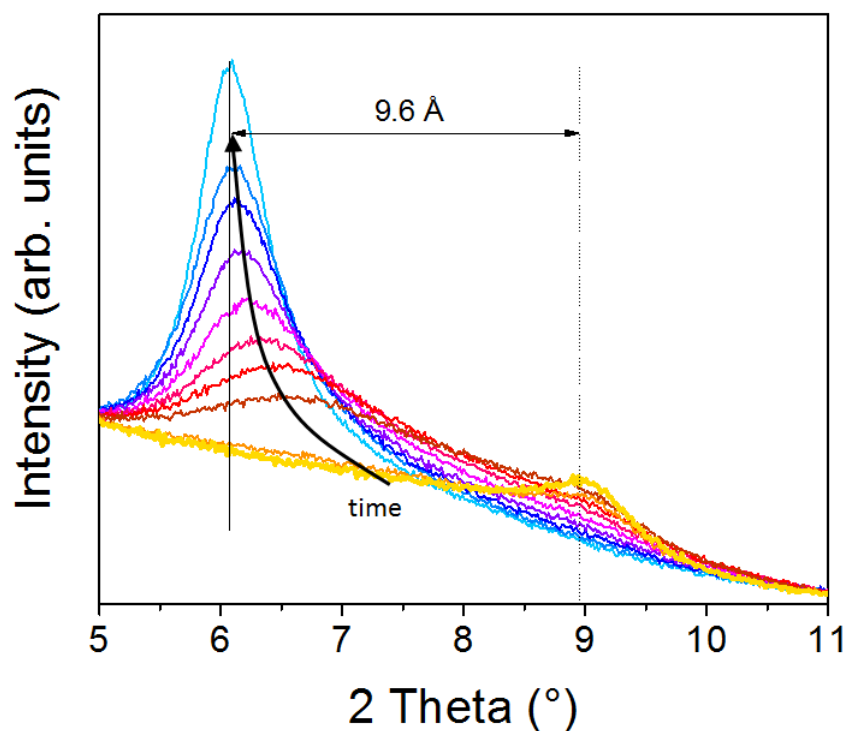


Figure III.3: X-ray diffraction patterns of $\text{Ti}_3\text{C}_2\text{T}_x$ during intercalation from 1M MgSO_4 . Each pattern took 20 min to be recorded. Vertical dashed lines indicate the original position of the (002) peak.

II. 2 Delamination

Similar to the spontaneous intercalation of aqueous electrolytes described in the previous pages, Mashtalir *et al.* demonstrated the intercalation of large organic molecules, in particular dimethyl sulfoxide (DMSO) (160). The intercalation of DMSO was demonstrated by X-ray diffraction, as shown in Figure III.4. The intercalation has the effect of weakening the bond between $\text{Ti}_3\text{C}_2\text{T}_x$ layers. Thanks to this, it is possible to separate most layers to each other by ultrasonication. This procedure, called delamination, is described in detail in chapter 2. Figure III.4 shows the X-ray diffraction pattern obtained for the freestanding delaminated Ti_3C_2 film prepared by filtration, noted d- $\text{Ti}_3\text{C}_2\text{T}_x$. A peak was observed at 6.16° meaning that the delaminated layers recombined with the same orientation. The d- $\text{Ti}_3\text{C}_2\text{T}_x$ (002) peak is at lower angle than the DMSO- $\text{Ti}_3\text{C}_2\text{T}_x$ (002) peak proving that DMSO molecules are not present between layers after the washing and ultrasonication steps.

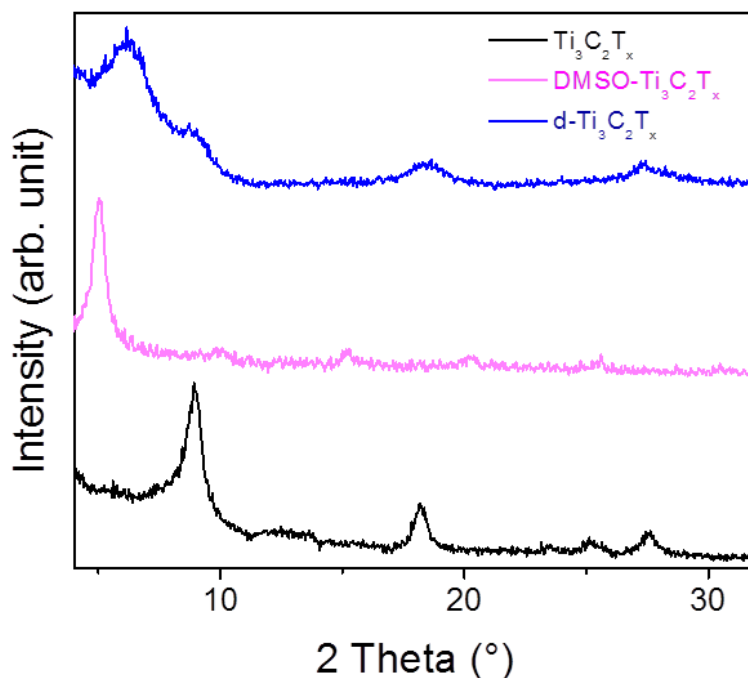


Figure III.4: X-ray diffraction patterns of $\text{Ti}_3\text{C}_2\text{T}_x$, $\text{DMSO-Ti}_3\text{C}_2\text{T}_x$ and $\text{d-Ti}_3\text{C}_2\text{T}_x$.

III Surface modification

The surface chemistry of the as-synthesized $\text{Ti}_3\text{C}_2\text{T}_x$ is rich in oxygenated and fluorinated groups (157). After $\text{Ti}_3\text{C}_2\text{T}_x$ treatment in various aqueous electrolytes, cations were found in the material but the nature of the bond between cation and the $\text{Ti}_3\text{C}_2\text{T}_x$ surface is not known. The hypothesis deduced earlier is that the intercalation of cations induces a change in the c-lattice parameter that depends on the pH and cation valence. Theoretical predictions suggested that treatment in basic aqueous solutions should replace $-\text{F}$ terminal groups with hydroxyl groups as Ti-F becomes unstable at high pH (177). Moreover the delamination process demonstrated that the morphology of MXenes can be modified.

In the following, our goal was to investigate the morphology and surface chemistry modifications of $\text{Ti}_3\text{C}_2\text{T}_x$ after two different processes: 1) the intercalation of K^+ cations between $\text{Ti}_3\text{C}_2\text{T}_x$ layers from treatment in 1M KOH and 1M KOAc as described previously;

2) the delamination of individual $Ti_3C_2T_x$ layers after the intercalation of DMSO and ultrasonication (160). To monitor these processes, the structure and chemistry of the $Ti_3C_2T_x$ electrodes were analyzed by scanning electron microscopy (Zeiss, Supra 50VP, Oberkochen, Germany) and X-ray photoelectron spectroscopy (VersaProbe 5000, Physical Electronics Inc., USA).

III. 1 Observation by scanning electron microscopy

The morphologies of $Ti_3C_2T_x$, $KOH-Ti_3C_2T_x$ and $d-Ti_3C_2T_x$ were observed using scanning electron microscopy as shown in Figure III.5. $Ti_3C_2T_x$ and $KOH-Ti_3C_2T_x$ images showed aggregates of multilayered particles. Although the K^+ intercalation preserved the exfoliated morphology, it can be noted that the layer thickness appears to be larger than before intercalation as if layers were glued together. This phenomenon is commonly observed in intercalated graphite (178, 179).

$d-Ti_3C_2T_x$ images shows layers on top of each other's forming a continuous ordered film and no multilayered $Ti_3C_2T_x$ aggregate is noticeable. This led to an increase in the specific surface area up to $100\text{ m}^2/\text{g}$ while $Ti_3C_2T_x$ and $KOH-Ti_3C_2$ specific surface areas are about $20\text{ m}^2/\text{g}$ (160). As described in chapter 2, the $d-Ti_3C_2T_x$ film electrode is prepared by filtration and does not contain any binder. The reason we obtained a free standing and flexible film is thanks to the formation of a network of layers overlapping (similarly to graphene (123)).

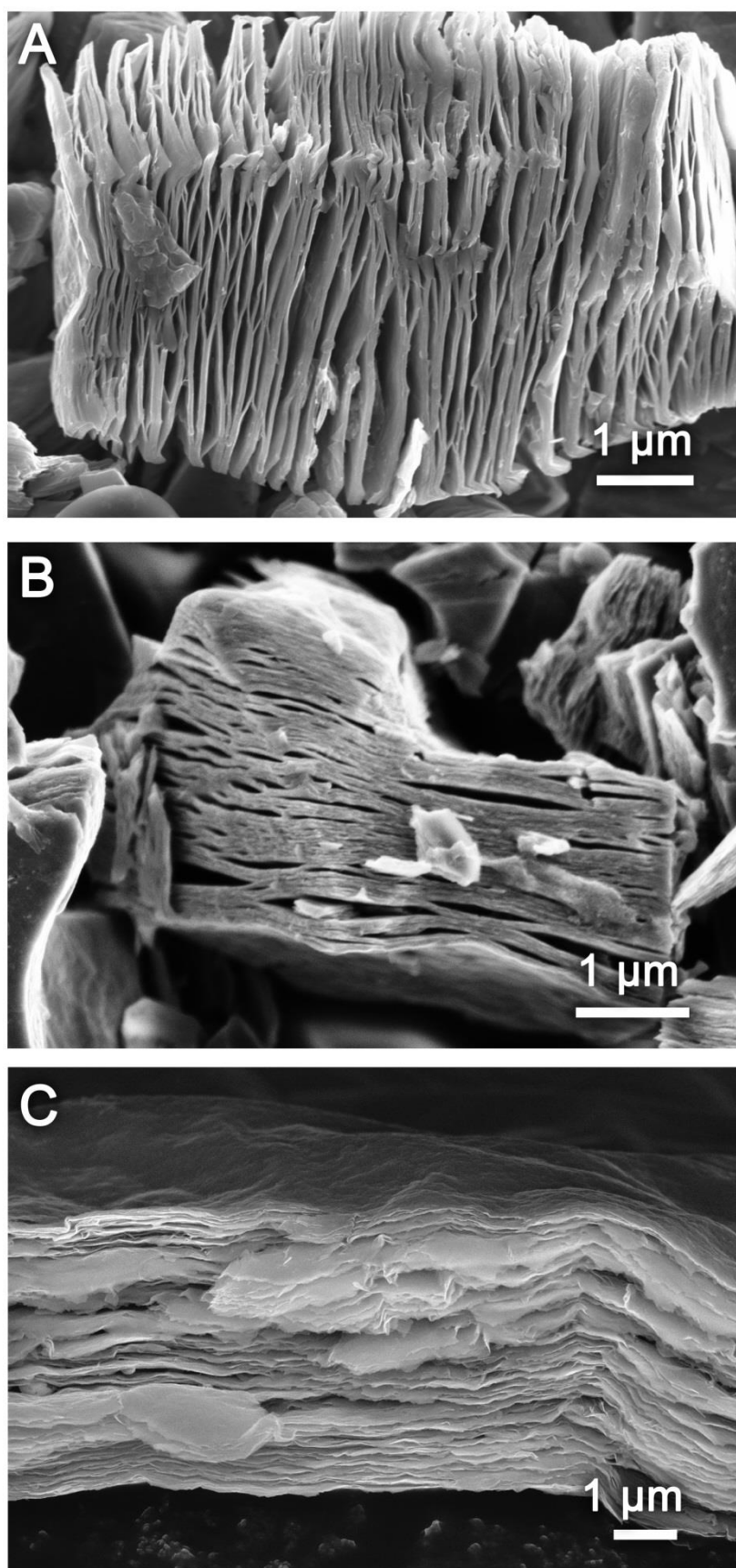


Figure III.5: Scanning-electron microscope images of $\text{Ti}_3\text{C}_2\text{T}_x$ (A), $\text{KOH-Ti}_3\text{C}_2\text{T}_x$ (B) and $\text{d-Ti}_3\text{C}_2\text{T}_x$ (C) (adapted from (180)).

III. 2 X-ray photoelectron spectroscopy

X-ray photoelectron spectroscopy was used to characterize the surface chemistry of the samples. High-resolution X-ray photoelectron spectroscopy spectra of the samples ($\text{Ti}_3\text{C}_2\text{T}_x$, $\text{KOH-Ti}_3\text{C}_2\text{T}_x$, $\text{KOAc-Ti}_3\text{C}_2\text{T}_x$ and $\text{d-Ti}_3\text{C}_2\text{T}_x$, shown in Figure III.6.A-C) in the F 1s region indicated that the $\text{Ti}_3\text{C}_2\text{T}_x$ sample contained a large amount of F-terminated Ti (Figure III.6.A). It was also noticed that AlF_3 salt residue from MAX phase etching was only present in the $\text{KOAc-Ti}_3\text{C}_2\text{T}_x$ and $\text{Ti}_3\text{C}_2\text{T}_x$ samples. It was completely removed after KOH or DMSO treatment. The intensity of the Ti-F peaks decreases in the order $\text{d-Ti}_3\text{C}_2\text{T}_x$, $\text{KOAc-Ti}_3\text{C}_2\text{T}_x$, $\text{KOH-Ti}_3\text{C}_2\text{T}_x$, being the lowest for the latter one. The signal of the Ti-F component, which was initially at 684.4 eV, shifts toward a higher-binding energy as F is removed from Ti as fluoride salt.

Due to the 2D-nature of the $\text{Ti}_3\text{C}_2\text{T}_x$, oxidation does not proceed homogeneously and likely starts from the outer edges of the $\text{Ti}_3\text{C}_2\text{T}_x$ grains, giving oxides and mixed carboxides (TiC_xO_y) at the flake edges and on the outermost surface layer of the multilayer particle, while $\text{Ti}_3\text{C}_2\text{T}_x$ remains in the center of the grain. This inhomogeneity gives rise to the broadened and convoluted spectra seen in the Ti 2p region (Figure III.6.B). In this region, the Ti-carbide photoemission arises from $\text{Ti}_3\text{C}_2\text{T}_x$, while the Ti (II) and Ti (III) components arise from these mixed oxides and carboxides, and the Ti (IV) component arises from TiO_2 present on the surface of the grains as oxidation goes to completion. These spectra also include a component for Ti-F that becomes less prominent and merges with that for Ti (IV), likely as a result of the formation of a small amount of the intermediate, fluorinated TiO_2 , as hydroxyl groups replace the $-\text{F}$ termination during the oxidation of the outer surface of $\text{Ti}_3\text{C}_2\text{T}_x$. This region also indicates oxidation of the surface of the $\text{Ti}_3\text{C}_2\text{T}_x$ grains to Ti (IV) (TiO_2) for all modified $\text{Ti}_3\text{C}_2\text{T}_x$ samples. Accordingly, instead of F-termination, the $\text{KOH-Ti}_3\text{C}_2\text{T}_x$, $\text{KOAc-Ti}_3\text{C}_2\text{T}_x$ and $\text{d-Ti}_3\text{C}_2\text{T}_x$ surfaces are terminated with oxygen-containing groups. High-resolution

spectra of the samples in the K 1s region (Figure III.6.C) reveal two components, the first is for K^+ that is strongly electroadsorbed and the second component suggests that K^+ is present as salt, probably KF. The electroadsorbed K^+ is much more prevalent in KOAc- $Ti_3C_2T_x$ than in KOH- $Ti_3C_2T_x$. Figure III.6.D shows a schematic view summarizing these two chemical modification paths for $Ti_3C_2T_x$.

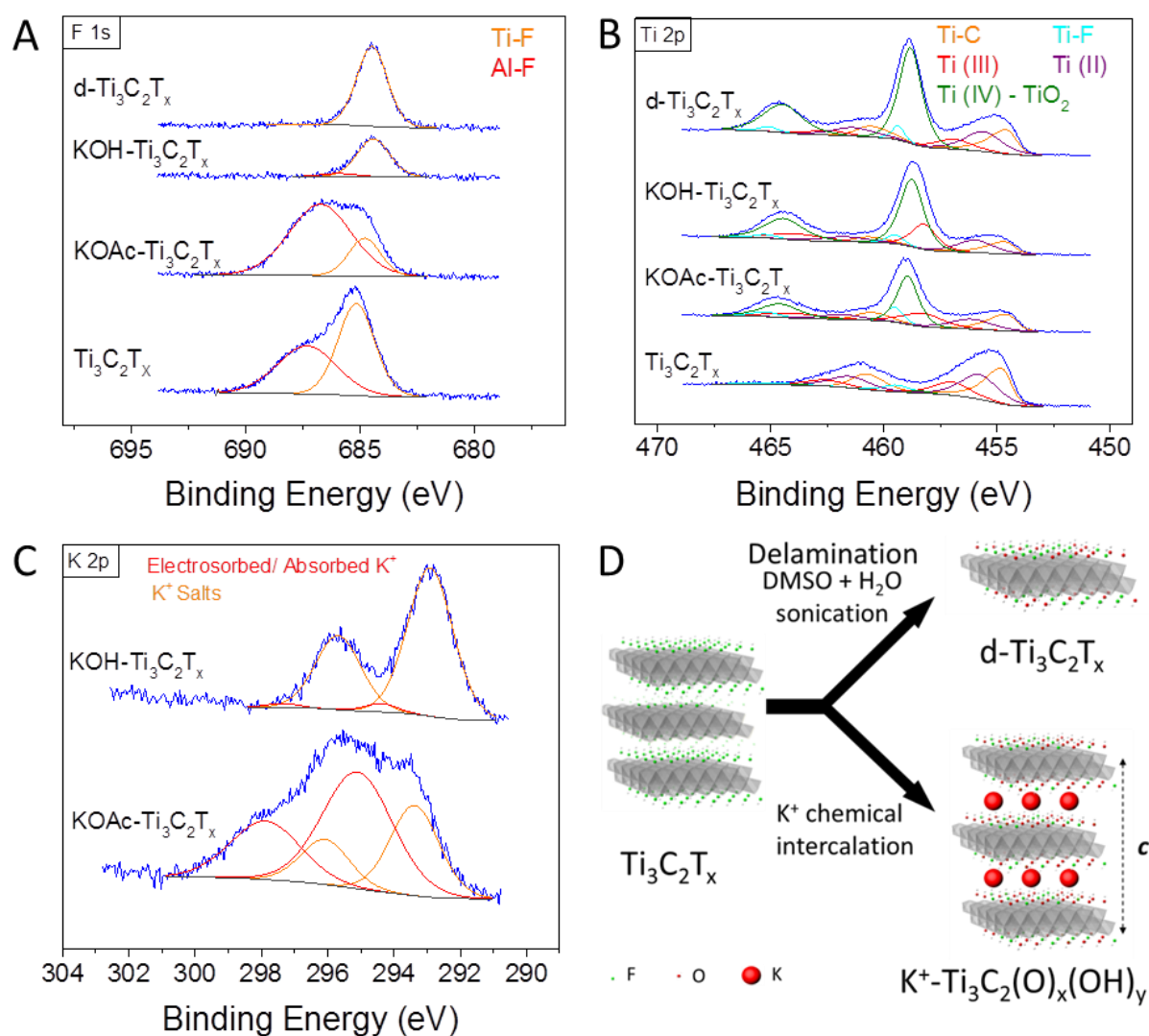


Figure III.6: Characterization data of Ti_3C_2 -based materials after surface modification in various intercalation agents. High-resolution X-ray photoelectron spectroscopy spectra in the F 1s region (A), the Ti 2p region (B), and K 2p region (C). Schematic illustration of the modifications of $Ti_3C_2T_x$; delamination and intercalation of K^+ (D) (adapted from (180)).

IV Electrochemical characterization

We demonstrated that a spontaneous intercalation reaction modifying the surface chemistry can occur when $\text{Ti}_3\text{C}_2\text{T}_x$ is in contact with different electrolytes. However the objective of this work is to investigate the electrochemical behavior of $\text{Ti}_3\text{C}_2\text{T}_x$. For this purpose, we prepared $\text{Ti}_3\text{C}_2\text{T}_x$ electrodes by mixing the dried powder in ethanol with 5 wt. % polytetrafluoroethylene binder (60 wt.% in H_2O , Aldrich) and 5 wt. % carbon black (Alfa Aesar), followed by rolling and cutting the electrode film into 7 mm diameter disks with thicknesses between 50 μm and 70 μm .

IV. 1 Results in various aqueous electrolytes

A large array of electrolytes were selected to observe the response to different electrolytes properties (stability window, pH, conductivity, cation and anion etc). The aqueous solutions selected were the same as used in previous tests: 1M sulfuric acid (H_2SO_4), 1M lithium hydroxide (LiOH), 1M sodium hydroxide (NaOH), 1M potassium hydroxide (KOH), 1M potassium acetate (KOAc), 1M potassium sulfate (K_2SO_4), 3M sodium acetate (NaOAc), 1M lithium sulfate (Li_2SO_4), 1M sodium sulfate (Na_2SO_4) and 1M magnesium sulfate (MgSO_4).

The resulting cyclic voltammograms using a three-electrode Swagelok cell with Ag wire as reference electrode and overcapacitive activated carbon as counter electrode at 20 mV/s are shown in Figure III.7. The main advantage of this electrochemical configuration is that the counter electrode potential is almost constant and therefore it allows to the study of the behavior of the working electrode over the total potential range.

Unlike what is observed for graphite, there was no irreversible capacitance loss during the first cycle for any of the studied electrolytes (181). The conductivities of all electrolytes are

presented in Table 6. As explained extensively in chapter 1 and 2 the rectangular shaped cyclic voltammograms indicate a capacitive behavior.

Rectangular shaped cyclic voltammograms were obtained in all electrolytes, with some broad peaks noticeable in some cases. Curiously the peaks are located at -0.2V vs. Ag in the following electrolytes; NaOAc, KOAc, Na_2SO_4 , K_2SO_4 , MgSO_4 , H_2SO_4 . Further work is needed to identify the reaction. As explained in detail in chapter 1, the presence of peaks in a cyclic voltammograms is due to redox reactions. The combination of an overall rectangular shaped cyclic voltammogram with few broad peaks is commonly observed in pseudocapacitive materials, such as RuO_2 that is described in detail in Figure I.12.

The performance of $\text{Ti}_3\text{C}_2\text{T}_x$ electrodes tested at different scan rates is summarized in Figure III.7.F. The specific capacitances were calculated by integrating the reduction portions of the cyclic voltammograms. The capacitances obtained at 2 mV/s were found between 45 F/g and 108 F/g . These results are quite high for such low specific surface area electrodes. Indeed, the capacitance due to the double layer is directly proportional to the specific surface area, as described by equation 5. However, $\text{Ti}_3\text{C}_2\text{T}_x$ electrodes have a moderate specific surface area of $23\text{ m}^2/\text{g}$ (160) which is very small compared to electrochemical double layer capacitor electrodes such as activated carbon ($2000\text{ m}^2/\text{g}$). If double layer capacitance were the only operative mechanism, the capacitance for this material should be lower than 6 F/g as the areal capacitance of double layer capacitor is up to $20\text{ }\mu\text{F}/\text{cm}^2$ (4). It is important to note that the capacitances obtained greatly depend of the electrolyte used.

To study the effect of a cation's size on the electrochemical behavior we analyzed the cyclic voltammograms obtained with electrolytes that have the same valence, the same anion and the same pH. No clear dependence on the cation size can be deduced since results with K^+ are

better than Na^+ with hydroxide anions (Figure III.7.A) but the opposite order appears with acetate anions (Figure III.7.B).

The responses in the Li_2SO_4 , Na_2SO_4 , K_2SO_4 and MgSO_4 (Figure III.7.C-D) are distinctively different. This is in agreement with the fact that the cations are intercalating, and not the anions. The best performance among sulfate electrolytes with close to neutral pH was obtained with MgSO_4 (up to 82 F/g). As the conductivity in MgSO_4 is the lowest, the better performance was suggested to be attributed to the bivalence of Mg^{2+} . However other electrolytes with multivalent cations (1M $\text{Al}_2(\text{SO}_4)_3$ and 1M $\text{Al}(\text{NO}_3)_3$) were investigated by Lukatskaya *et al.*, as seen in Annex 1 (174). Their performances were lower than with MgSO_4 even if $\text{Al}(\text{NO}_3)_3$ conductivity is higher (110 mS/cm²). Therefore no direct link between a cation's valence and electrochemical performance can be concluded.

The highest capacitances among all electrolytes studied were obtained in 1M H_2SO_4 with capacitance up to 108 F/g at 2 mV/s. This electrolyte has the best conductivity but the lowest potential window because of the low pH. Broad peaks at -0.2V vs. Ag are well defined. Recent work based on chronoamperometry at different potential suggests that these peaks in H_2SO_4 are associated with hydrogen storage but no study in the other electrolytes where this peak was observed has been performed to confirm it (182).

To conclude, the best performances were obtained with 1M H_2SO_4 and 1M MgSO_4 , which have very different physical properties (different cation sizes, different conductivities, different pH). In the following section, effort will be focused on understanding the energy storage mechanism.

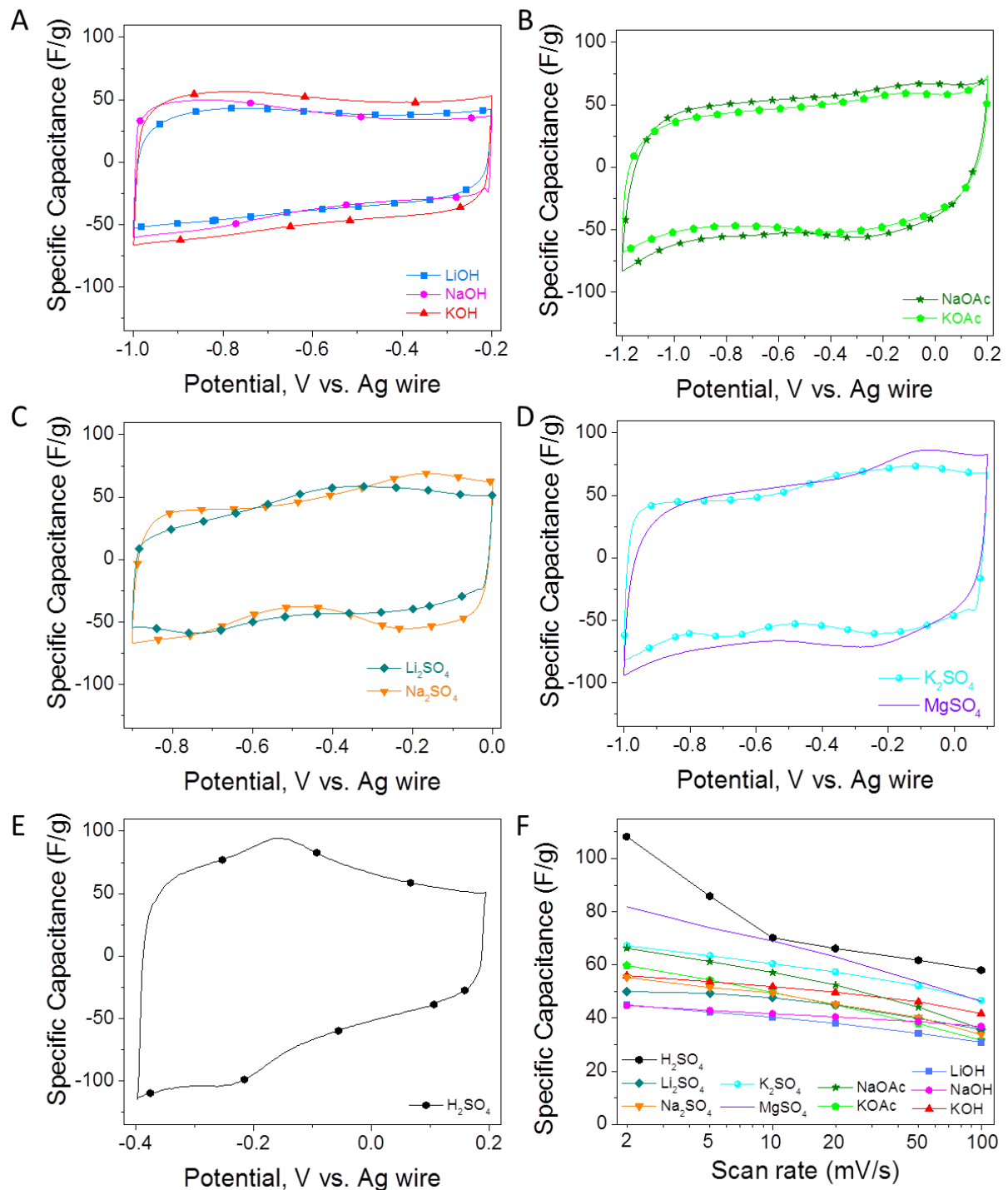


Figure III.7: Electrochemical performance of $\text{Ti}_3\text{C}_2\text{T}_x$ in various electrolytes; cyclic voltammograms at 20 mV/s in LiOH, NaOH and KOH (A) NaOAc and KOAc (B), Li_2SO_4 and Na_2SO_4 (C) K_2SO_4 and MgSO_4 (D) H_2SO_4 (E) Summary of rate performances in the different aqueous electrolytes (F).

Table 6: Ionic conductivities of the various aqueous electrolytes used in electrochemical experiments (183, 184).

Electrolyte	Conductivity, mS/cm
1 M H ₂ SO ₄	265
1 M KOH	191
1 M LiOH	150
1 M NaOH	141
1 M K ₂ SO ₄	100
1 M Na ₂ SO ₄	100
1 M KOAc	92
3 M NaOAc	79
1 M Li ₂ SO ₄	71
1 M MgSO ₄	51

IV. 2 Mechanism study by in situ X-ray diffraction

Electrodes that store charges through double layer capacitance have an areal capacitance up to 20 $\mu\text{F}/\text{cm}^2$ (4). It can be calculated that in order to reach a capacitance of 40 F/g based on double-layer, a specific surface area of 200 m^2/g is the minimum required, which is far above the value measured for $\text{Ti}_3\text{C}_2\text{T}_x$ electrodes. Therefore the double layer capacitance contribution to the total capacitance in this case is limited. To shed light on the energy storage mechanism, in-situ X-ray diffraction was performed using $\text{Ti}_3\text{C}_2\text{T}_x$ electrodes. It consists of recording the X-ray diffraction spectra at different potentials using the experimental set-up described in Chapter 2. Figure III.8 shows the results in the three different electrolytes that were selected for this study; 1M KOH, 1M MgSO₄ and 3M NaOAc.

Confirming the results shown previously, we observe that when $\text{Ti}_3\text{C}_2\text{T}_x$ is in contact with these aqueous electrolytes a (002) peak downshift was observed, demonstrating the spontaneous intercalation mentioned earlier. In the case of MgSO_4 the peaks appeared after 2 hours. The shift observed for NaOAc and MgSO_4 does not correspond perfectly to the values observed in Figure III.2. A possible explanation is that the materials used are slightly different, for example in one case the material used is a powder treated for 6 hours in the electrolytes and in the other case it is a film electrode of untreated $\text{Ti}_3\text{C}_2\text{T}_x$ with PTFE binder and carbon black that is soaked in the electrolyte.

In-situ X-ray diffraction studies during cycling showed that electrochemical cycling leads to small changes in the c-lattice parameters. This demonstrates that there is an intercalation process occurring. For example, when a $\text{Ti}_3\text{C}_2\text{T}_x$ electrode was cycled in a KOH containing electrolyte, the c values fluctuated within 0.33 \AA as the potential was scanned from -1 to -0.2 V, as shown Figure III.8.A. Interestingly, a slight shrinkage in c-lattice parameter was observed with increasing potential. The simplest explanation for this observation is that the positively charged ions incorporated in $\text{Ti}_3\text{C}_2\text{T}_x$ increase the electrostatic attraction between layers, in a manner analogous to what is observed for MnO_2 (185).

Similar behavior was observed when $\text{Ti}_3\text{C}_2\text{T}_x$ was cycled in 3M NaOAc as shown Figure III.8.B. The lattice expanded and shrank up to 0.22 \AA during oxidation and reduction which is smaller than in 1M KOH. Considering that acetate anions are larger than hydroxide anions and that the capacitance at low scan rate were better in 3M NaOAc than in 1M KOH, the lower change in the lattice is attributed to the smaller size of the cation. It also further supports the hypothesis that the anions do not intercalate.

Figure III.8.C shows the in-situ X-ray diffraction results in 1M MgSO_4 . When $\text{Ti}_3\text{C}_2\text{T}_x$ was electrochemically cycled, here again, a slight shrinkage in c values was observed with increasing V. The shift of the (002) peak almost doubled compared to the KOH and NaOAc

electrolytes (0.5 Å) and might either be due to the larger size of the cation and/or its bivalence. As the same phenomenon is demonstrated in these three very different electrolytes it can be generalized that $\text{Ti}_3\text{C}_2\text{T}_x$ stores energy through an intercalation capacitance mechanism.

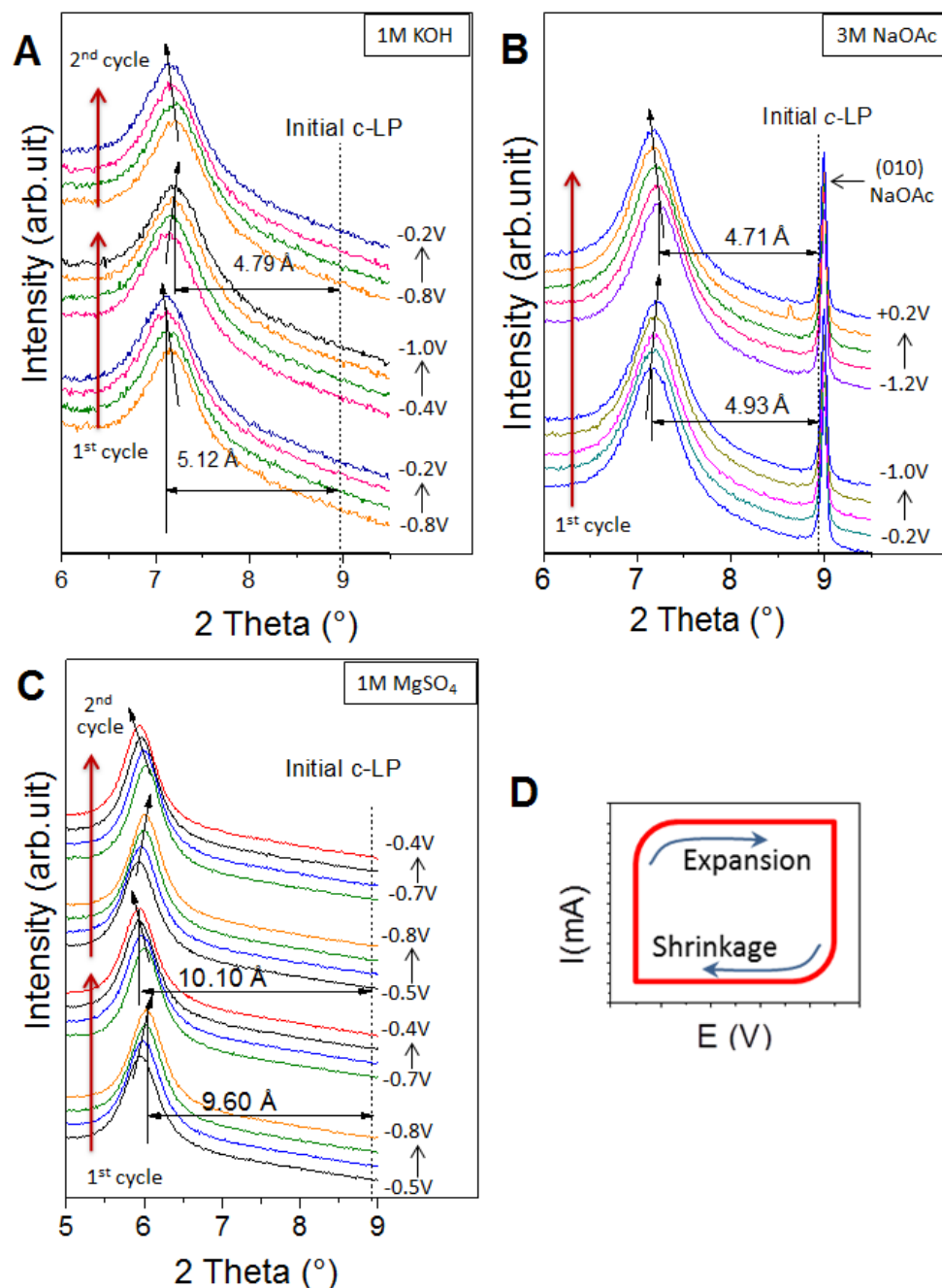


Figure III.8: Electrochemical in-situ X-ray diffraction study of $\text{Ti}_3\text{C}_2\text{T}_x$ in 1M KOH (A), 1M MgSO_4 (B) and 3M (NaOAc) (C). Vertical dashed lines indicate the original position of the (002) peak. Inclined arrows show the direction of the (002) peak shift. Illustration of cycling direction and concomitant change in c-lattice parameters (adapted from (174)).

IV. 3 Surface-modified $\text{Ti}_3\text{C}_2\text{T}_x$ performance

The effect of intercalation and delamination of the $\text{Ti}_3\text{C}_2\text{T}_x$ on its surface chemistry has been studied by X-ray photoelectron spectroscopy in part II.2.2. It was confirmed that terminal fluorine was successfully replaced with oxygen-containing functional groups after the chemical intercalation of potassium acetate ($\text{KOAc-Ti}_3\text{C}_2\text{T}_x$) and potassium hydroxide ($\text{KOH-Ti}_3\text{C}_2\text{T}_x$). Delamination of $\text{Ti}_3\text{C}_2\text{T}_x$ layers, denoted $\text{d-Ti}_3\text{C}_2\text{T}_x$, led to both an increase of the specific surface area of MXene films and the modification of the surface chemistry of $\text{d-Ti}_3\text{C}_2\text{T}_x$.

Theoretical calculations using first-principles simulation recently investigated the Li, Na, K, Mg, Ca, and Al storage on MXene nanosheets (177, 186). The effect of the surface chemistry on the electrochemical performance for use in batteries was systematically studied. The results demonstrated that bare MXenes have higher capacities and greater ion mobilities than the O-terminated MXenes. It is expected that the surface chemistry of MXene has an effect on the behavior in the case of supercapacitor as well because HF-synthesized MXene are terminated with $-\text{F}$ and $-\text{OH}/=\text{O}$ functional groups, where the $-\text{F}$ group may be a disadvantage to charge storage since F^- is not known to participate in any pseudocapacitive energy storage processes.

In the following, we investigated the influence of the surface chemistry of $\text{Ti}_3\text{C}_2\text{T}_x$ on its electrochemical performance in the acidic electrolyte sulfuric acid (H_2SO_4), this electrolyte was chosen because it had the best electrochemical performance.

Figure III.9.A shows the cyclic voltammograms of all samples tested at 10 mV/s sweep rate in aqueous 1 M H_2SO_4 . The best performances were achieved using $\text{d-Ti}_3\text{C}_2\text{T}_x$ electrodes, with an outstanding volumetric capacitance of 520 F/cm^3 and a gravimetric capacitance of 325 F/g

at 2 mV/s (Figure III.9.B). We believe the superior performance of d-Ti₃C₂T_x electrodes originate from several sources. First, it is a 6 times thinner electrode, leading to better charge transfer and improved mass transfer. It also has a higher specific surface area and is denser because of its morphology (aligned MXene flakes). Nonetheless, d-Ti₃C₂T_x has shown a stronger dependence of performance on scan rate, which is assumed to be caused by the flakes aligning parallel to the current collector and increasing the transport path for ions as the film thickness increases.

The Ti₃C₂T_x, KOH-Ti₃C₂T_x and KOAc-Ti₃C₂T_x electrodes have the same specific surface area, therefore the difference in electrochemical performance can only be related to the difference in surface chemistry. The moderate capacitances for Ti₃C₂T_x are consistent with the absence of redox activity of the F-termination. The KOAc-Ti₃C₂T_x and KOH-Ti₃C₂T_x electrodes exhibit similar behavior, with the latter having a higher gravimetric capacitance thanks to a lower content of F-groups (Figure III.6.A). Their surfaces are terminated by oxygen-containing groups, including –OOH, =O and –OH, which are known to be responsible for pseudocapacitive behavior seen in carbon in acidic electrolytes. This hypothesis is consistent with the shape of the cyclic voltammograms presented in Figure III.9.A, where the presence of a set of broad peaks at -0.2 and -0.1 V/Ref is observed. These peaks were assumed to originate from surface redox reactions of MXene leading to changes in the degree of oxidation of titanium in MXene, which is a transition metal capable of changing oxidation degree between +3 and +4.

Figure III.10.A shows the capacitance vs. cycle number dependencies obtained from galvanostatic charge-discharge curves shown in Figure III.10.B. Stable capacitances of 415 F/cm³ and 215 F/cm³ were obtained at 5 A/g for d-Ti₃C₂T_x and KOH-Ti₃C₂T_x, respectively. After 10 000 cycles, no significant degradation was observed. Similar electrochemical

performances improvements due to the delamination process were observed in some other electrolytes (KOH, NaOAc and MgSO_4) as seen in Annex 2.

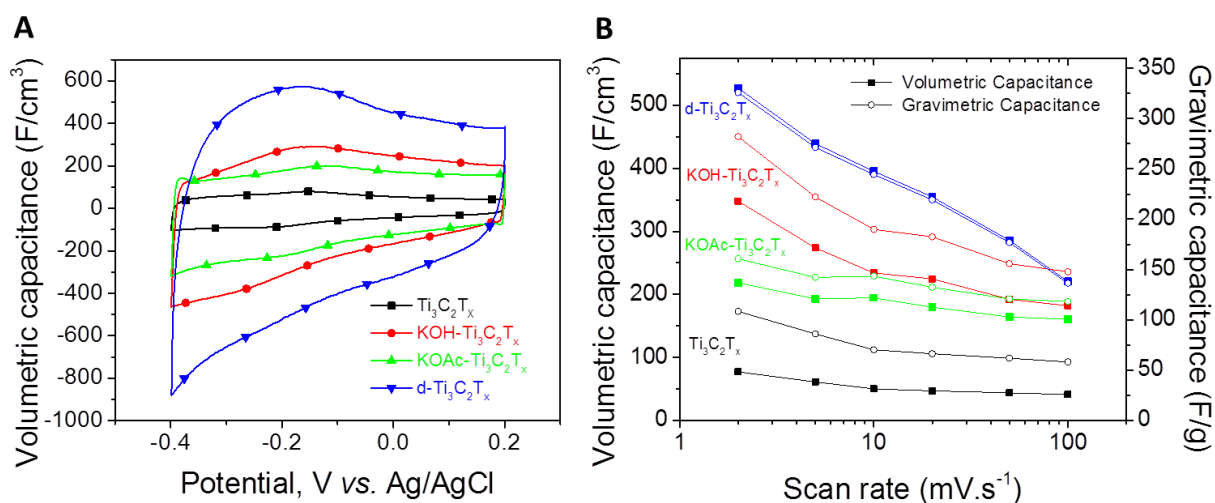


Figure III.9: Electrochemical performance of Ti_3C_2 -based electrodes in $1\text{M H}_2\text{SO}_4$: cyclic voltammograms profiles at 10 mV/s (A). Summary of rate performances (B) (adapted from (180)).

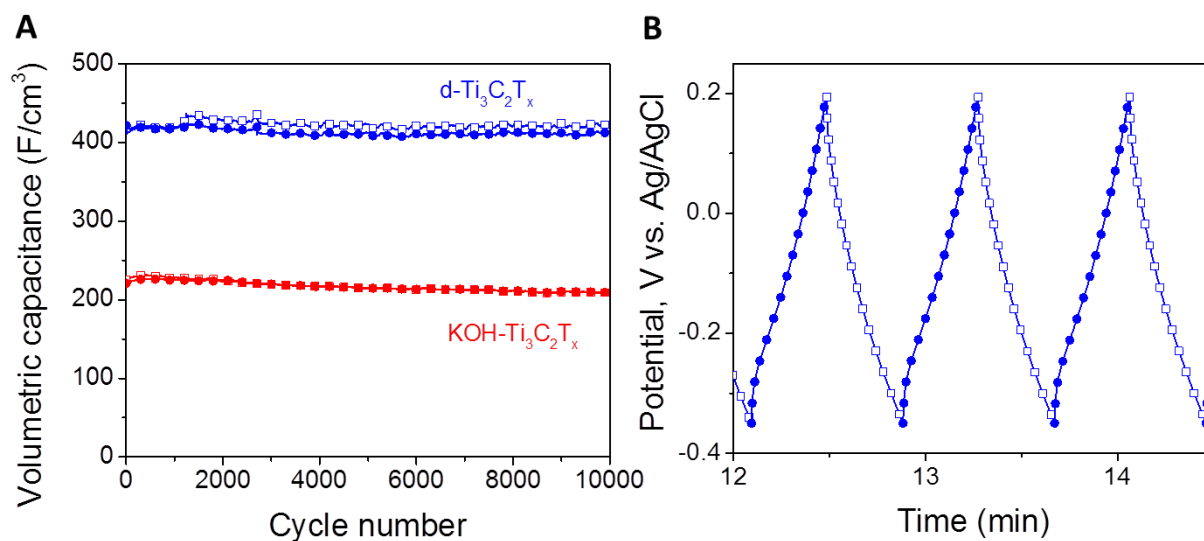


Figure III.10: Charge and discharge volumetric capacitance vs. cycle number of $\text{KOH-Ti}_3\text{C}_2\text{T}_x$ and $\text{d-Ti}_3\text{C}_2\text{T}_x$ electrodes from galvanostatic cycling in $1\text{M H}_2\text{SO}_4$ at 5 A/g (A). Galvanostatic charge-discharge profile of $\text{d-Ti}_3\text{C}_2\text{T}_x$ (B) (adapted from (180)).

V Conclusion

We have demonstrated the intercalation of a wide range of cations (Li^+ , Na^+ , K^+ and Mg^{2+}) between $\text{Ti}_3\text{C}_2\text{T}_x$ layers from various aqueous solutions. The mechanism depends on pH and the nature of the cations. The electrochemical behavior of $\text{Ti}_3\text{C}_2\text{T}_x$ was investigated in these aqueous electrolytes. The energy storage mechanism was identified to be intercalation capacitance by in-situ X-ray diffraction.

The best performance was observed in sulfuric acid electrolytes. The effect of intercalation and delamination of the two-dimensional titanium carbide, $\text{Ti}_3\text{C}_2\text{T}_x$ (MXene) on its surface chemistry and electrochemical capacitance has been demonstrated. The change in surface chemistry ($-\text{F}$ repaced by $-\text{O}$) led to a 4-fold increase in the capacitance in sulfuric acid, demonstrating a pseudocapacitive contribution to the electrochemical behavior of MXene. A recent study using in-situ X-ray absorption spectroscopy confirmed the change of oxidation state of Ti atoms in $\text{Ti}_3\text{C}_2\text{T}_x$ (182). Later, the performance of $\text{Ti}_3\text{C}_2\text{T}_x$ itself was improved by optimizing the d- $\text{Ti}_3\text{C}_2\text{T}_x$ electrode formulation (164) and a new synthesis route of $\text{Ti}_3\text{C}_2\text{T}_x$ (163).

The delamination process gave rise to an electrochemical capacitance of 520 F/cm^3 at 2 mV/s , the highest volumetric capacitance reported for this material. This value is dramatically higher than the $60\text{-}100 \text{ F/cm}^3$ for activated graphene (120, 187) or 180 F/cm^3 for micrometer-thin carbide-derived carbon electrodes (188, 189). Extreme values of 1200 F/cm^3 (190) and 640 F/cm^3 (191) for MnO_2 hybrid electrodes were obtained on *thin films* of supported nanoparticles and cannot be compared with our electrodes. Moreover, freestanding d- $\text{Ti}_3\text{C}_2\text{T}_x$ electrodes are highly flexible which is promising for wearable energy storage devices (192).

The fact that cations of different size and valence can be accommodated between the $\text{Ti}_3\text{C}_2\text{T}_x$ layers opens the door for the use of MXene in batteries going beyond Li-ions and metal-ion capacitors.

Chapter IV: MXene for Na-ion capacitors

Chapter IV : MXene for Na-ion capacitors

I Introduction

One of the most important applications of MXene are electrodes for lithium ion batteries. For example, Ti_3C_2 , V_2C and Nb_2C have recently shown better performance than Ti_2C , with reversible capacities about 400 mAh/g, 300 mAh/g and 200 mAh/g at 1C rate respectively (160, 193). Unfortunately, all data showed incompatible working potential window (from 0V to 2.5V) and a sloping charge-discharge which are drawbacks for batteries.

However, such a drawback becomes a key advantage for assembling hybrid devices, such as lithium and sodium ions capacitors. Ti_2C was proposed for Li-ion capacitors and exhibited 70 mAh/g at 10C rate (Figure I.26) (161). All MXene tested for lithium ion battery (Ti_3C_2 , Nb_2C and V_2C) are expected to be suitable for lithium ion capacitors. In particular, delaminated Ti_3C_2 electrodes have shown excellent power capability in batteries (Figure I.27) and a full cell could be assembled with a suitable battery-type counter electrode. However, the results shown in the previous chapter highlighted the innovative possibility to go beyond lithium with energy storage solutions based on the inexpensive sodium chemistry. Indeed, we demonstrated the fast intercalation of large cations between $Ti_3C_2T_x$ layers from various aqueous electrolytes, including sodium-based electrolytes.

Considering that Na^+ intercalation into $Ti_3C_2T_x$ from aqueous electrolytes lead to good performance, the Na^+ intercalation into MXene-based electrodes should be investigated for sodium-ion capacitors in organic electrolytes in order to increase the potential range. Herein we report our work to identify the most suitable MXene electrode to reach the highest energy and power densities for use in the assembly of a full sodium hybrid cell.

II Selection of suitable MXene electrode

Results in aqueous supercapacitors and lithium ion batteries emphasized that the electrochemical performance depend on the composition of MXene (M and X elements) as well as its surface chemistry. Therefore, before creating a full Na-ion capacitor we investigated the electrochemical behavior of all synthesized MXene in sodium based organic electrolyte. The synthesis conditions of MXenes are described in the chapter 2. Again reiterate that MXenes are terminated with functional groups (OH and F) and the formulas are annotated with T_x to account for these surface terminations.

Table 7 shows an estimated theoretical capacitance (Q) of MXene using the following equations:

$$M_{n+1}X_n + yNa^+ + ye^- \leftrightarrow Na_yM_{n+1}X_n$$

$$Q = \frac{yF}{3.6 \times M} \quad (\text{Eq. 4})$$

Where: y is the number of sodium intercalated, F is the Faraday constant (96485 C/mol) and M is the molar mass (g/mol).

Table 7: Capacitance estimation. Calculation did not take into account the surface chemistry and considered the intercalation of a single sodium per MXene formula.

$M_{n+1}X_n$	$Ti_3C_2T_x$	Ti_3CNT_x	Nb_2CT_x	Ti_2CT_x	$TiVCT_x$	$Ti_{1.5}V_{1.5}CT_x$	V_2CT_x
Q (mAh/g)	160	158	135	249	242	156	235

II. 1 Comparison of cyclic voltammograms

A two-electrode Swagelok cell was used for half-cells with metallic sodium as counter and reference electrode separated by a glass fiber separator (GFA). The working electrode was a given MXene powder mixed with 20 wt. % of carbon black (Alfa Aesar) to ensure good conductivity. The electrolyte used was 1M NaPF₆ in EC:DMC (1:1). Figure IV.1 shows the

cyclic voltammograms of carbon black and of all synthesized MXene materials. The result with carbon black shows that a reaction occurs below 0.5V vs. Na⁺/Na. The cell was cycled between 0 and 4V vs. Na⁺/Na in order to observe the electrolyte reaction occurring at high potential and determine the potential stability range (3.7 V). As expected the electrochemical behavior greatly varies according to the MXene composition.

The corresponding capacities are shown in Figure IV.2. Surprisingly the performance of Ti₂CT_x and Nb₂CT_x are the lowest observed whereas good performances were achieved for lithium ion batteries using the same materials. In all MXenes, an irreversibility was observed during first cycle, originating from the formation of the solid electrolyte interphase as well as irreversible processes, such as reactions between Na⁺ and residual water or unwashed etching products from the synthesis. A large degree of irreversibility was observed in particular for Ti₃CNT_x (70% capacity loss) lessening the interest of this material for commercial rechargeable energy storage application (5).

As the performance also depends on the surface chemistry it is difficult to attribute the electrochemical behaviors solely to the composition of M and X in MXenes. However, it appears that TiVCT_x and Ti_{1.5}V_{1.5}C₂T_x cyclic voltammograms are very similar, suggesting that there could be peaks characteristic to the composition.

The electrochemical performances of Ti₃C₂T_x, TiVCT_x, Ti_{1.5}V_{1.5}C₂T_x and V₂CT_x are in the same order of magnitude (150 mAh/g). But Ti₃C₂T_x and V₂CT_x could only be cycled in a limited potential range. Indeed, Ti₃C₂T_x capacitive behavior is achieved below 2.5 V, which is suitable for negative electrodes, while V₂CT_x has a redox peak above 3V, suitable for positive electrodes. To conclude, Ti₃C₂T_x and V₂CT_x were selected for further investigation because they have lower irreversibility, better defined redox peaks and their synthesis condition is better known.

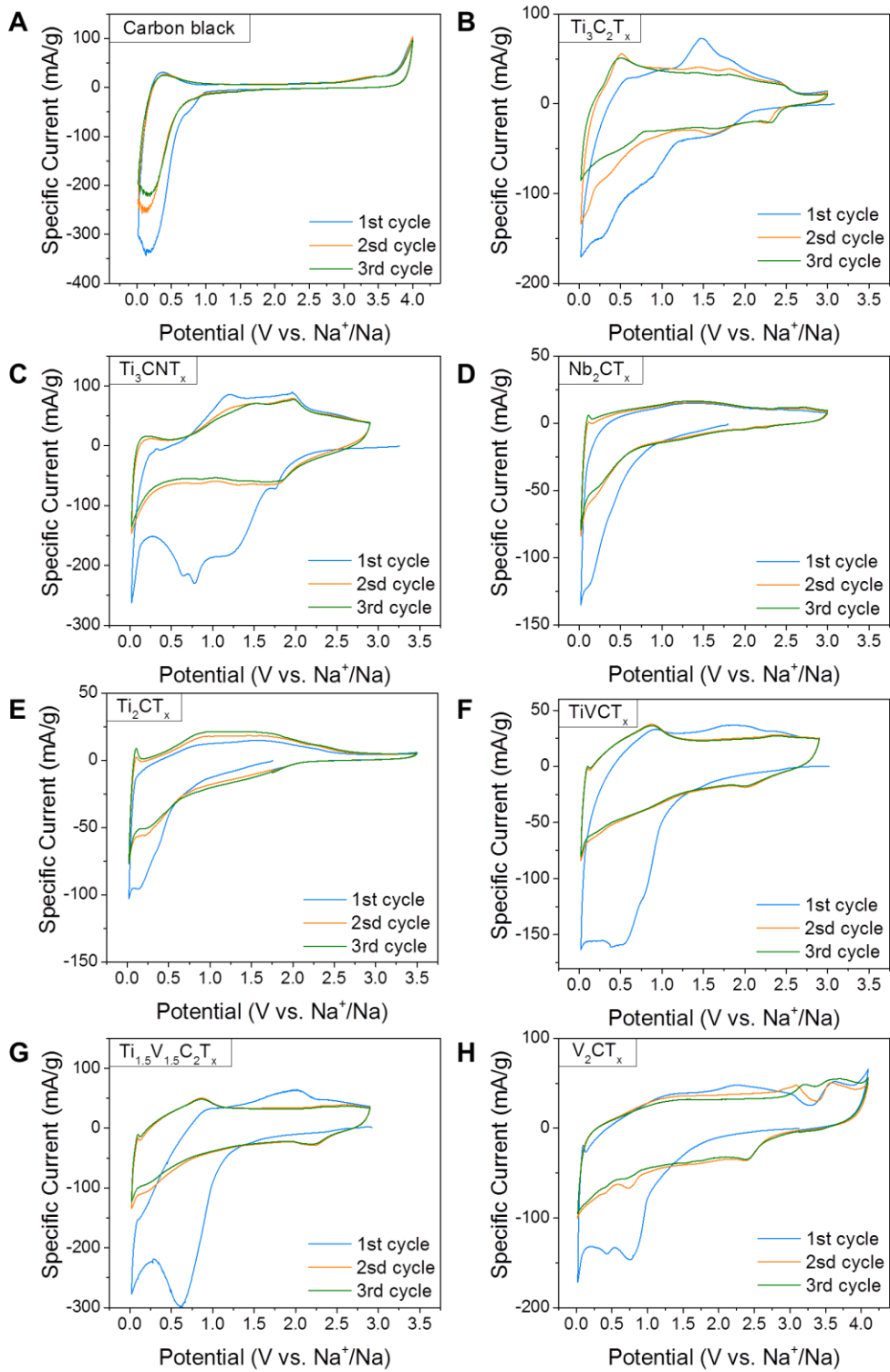


Figure IV.1: Cyclic voltammetry of Carbon black (A) and MXene (B-H) at 0.2 mV/s in 1 M NaPF₆ in EC:DMC.

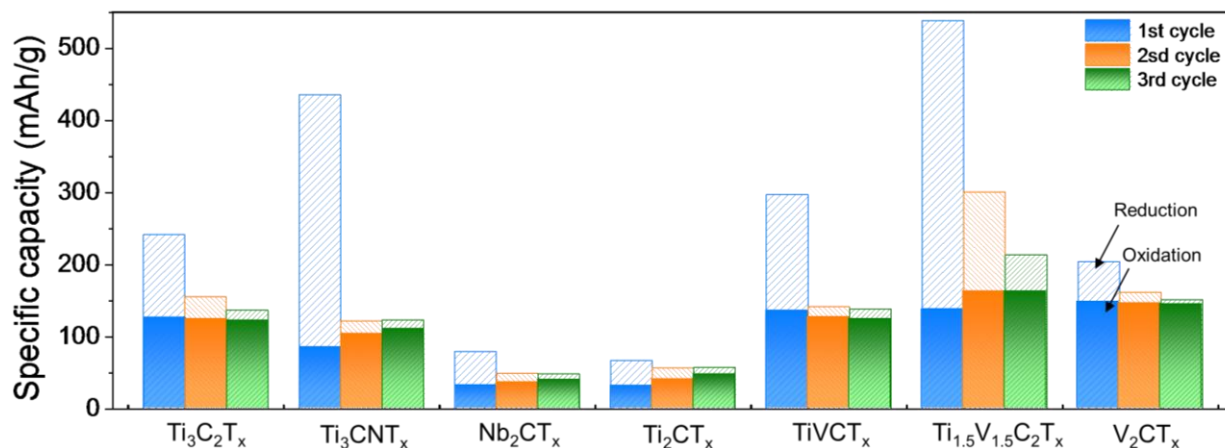


Figure IV.2: Capacity of all MXene calculated from cyclic voltammetry at 0.2 mV/s.

III Ti₃C₂T_x

Ti₃C₂T_x is the most studied MXene. In the previous chapter, we demonstrated that we could modify its electrochemical behavior in a given electrolyte by tuning its surface chemistry and morphology. Preliminary experiment in half-cell sodium ion batteries showed a capacity above 120 mAh/g, which is promising in the field of sodium ion battery. We first investigated the charge storage mechanism of Ti₃C₂T_x. Then, inspired by our previous results in supercapacitors, we attempted to improve the electrochemical performance by chemical treatment.

III. 1 Energy storage mechanism

In order to investigate the mechanism of energy storage mechanism, we again performed electrochemical in-situ X-ray diffraction experiments. We used the in-situ cell described in chapter 2 using a mixture of 80 wt. % of Ti₃C₂T_x and 20 wt. % of carbon black (Alfa Aesar) powder. Figure IV.3 shows the X-ray diffraction spectra during galvanostatic-charge discharge at 0.03 A/g.

During the first charge a downshift of the (00n) peaks, here (002) and (004), were recorded. This was attributed to sodium intercalation between Ti₃C₂T_x layers. According to equation 4,

the capacity was converted into the number of sodium intercalated and revealed that almost 3 cations are inserted into $\text{Ti}_3\text{C}_2\text{T}_x$ per formula unit, although the calculation overestimated this value because it did not take into account the solid electrolyte interphase formation nor the side reaction with impurities. Regardless, the c-lattice parameter expansion during the first charge is 1.4 Å, which is larger than the ionic radius of neat Na^+ . This suggests that more than 1 layer of sodium can be intercalated into $\text{Ti}_3\text{C}_2\text{T}_x$, but an effect of the solvation shell is not excluded.

During the next charge and discharge, a reversible cell expansion and shrinkage of 0.4 Å is observed. $\text{Ti}_3\text{C}_2\text{T}_x$ does not fully recover to its original lattice size. This phenomenon was previously observed upon cation intercalation from aqueous electrolytes and lithium intercalation in lithium ion capacitors (Figure I.26). It suggests that during the first reduction sodium cations are irreversibly intercalated and form a pillared structure, similar to what is seen in a other 2D materials (141, 194-196).

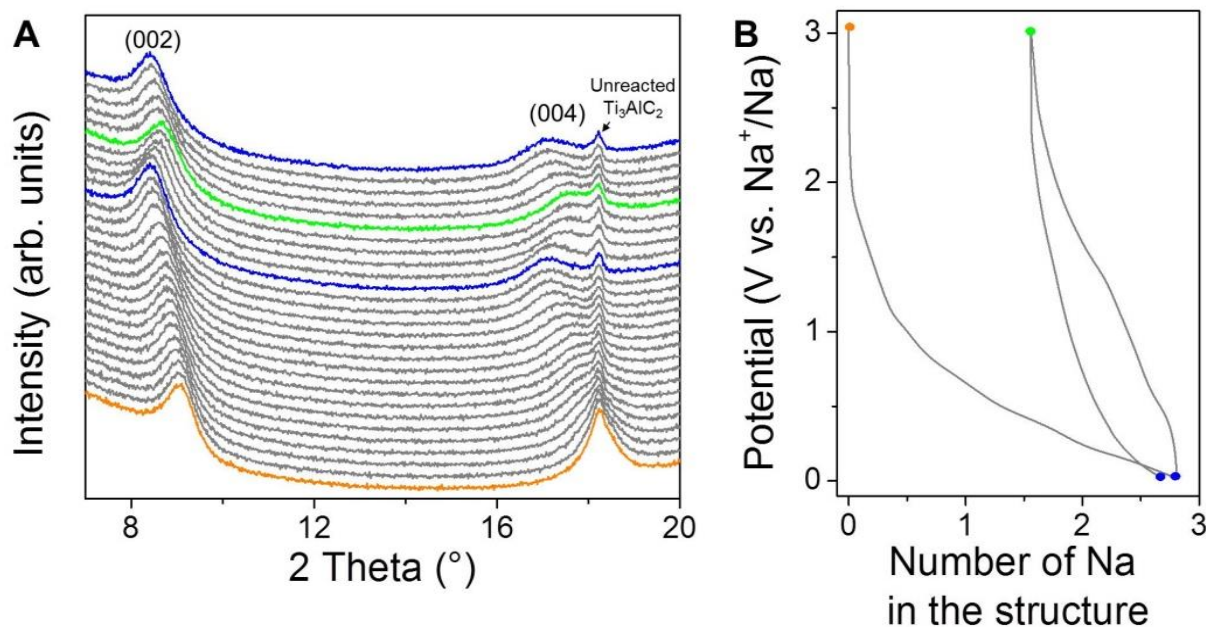


Figure IV.3: In-situ X-ray diffraction spectra (A) of $\text{Ti}_3\text{C}_2\text{T}_x$ during galvanostatic charge-discharge at 0.03 A/g and corresponding charge-discharge curves (B).

III. 2 Modification of $Ti_3C_2T_x$

As the results presented in Figure III.9 (capacitance improvement after chemical treatment in aqueous supercapacitors) suggest a valid strategy to improve the performance is to tune the surface chemistry of the MXene. For this purpose, $Ti_3C_2T_x$ was modified using the same treatment, described in chapter 3.II.1. In brief, $Ti_3C_2T_x$ was immersed and stirred for 6 hours in different electrolytes. Here, $Ti_3C_2T_x$ was immersed in 1M potassium hydroxide (KOH- $Ti_3C_2T_x$), 1M potassium acetate (KOAc- $Ti_3C_2T_x$), 1M lithium hydroxide (LiOH- $Ti_3C_2T_x$) and 1M sodium hydroxide (NaOH- $Ti_3C_2T_x$) replacing fluorine at the surface by oxygenated functional groups.

For comparison with the untreated $Ti_3C_2T_x$ in Figure IV.1.B, we performed cyclic voltammetry tests at 0.2 mV/s using modified- $Ti_3C_2T_x$ with 20 wt. % carbon black. The results, shown Figure IV.4.A-D, demonstrate that the various treatments greatly influenced the electrochemical response upon cycling.

The first cycle irreversibility was reduced in all modified- $Ti_3C_2T_x$. It can be attributed to the contribution of two phenomena. First, the chemical treatments removed impurities such as aluminum fluoride and therefore prevented irreversible side reaction. Second, cations were spontaneously pre-intercalated from the aqueous electrolyte during the chemical treatments (seen Figure III.2), resulting in an already pillared structure before cycling in the sodium ion battery half-cell.

The shape of the cyclic voltammograms was modified with a clear displacement of the redox peaks. For example, the oxidation peak at 0.5 V vs Na^+/Na in the untreated $Ti_3C_2T_x$ (Figure IV.1.B) disappeared in the others cases. Broad peaks at 1.2 V and 1V were observed in KOH- $Ti_3C_2T_x$ and KOAc- $Ti_3C_2T_x$, respectively. NaOH- $Ti_3C_2T_x$ exhibits well defined sharp redox peaks at 2.3 V while LiOH- $Ti_3C_2T_x$ redox peaks are at 2.3 V and 1.6 V.

Whereas a 4-fold increase in capacitance was achieved by KOH treatment in the case of aqueous supercapacitors, herein the capacities achieved were not greatly improved, as seen Figure IV.7. To conclude, we observed that it is possible to modify the $\text{Ti}_3\text{C}_2\text{T}_x$ behavior by chemical treatments. It is conceivable that one could be able to tune precisely a given MXene behavior by controlling the synthesis and post-treatment condition. This goal requires a separate extensive study.

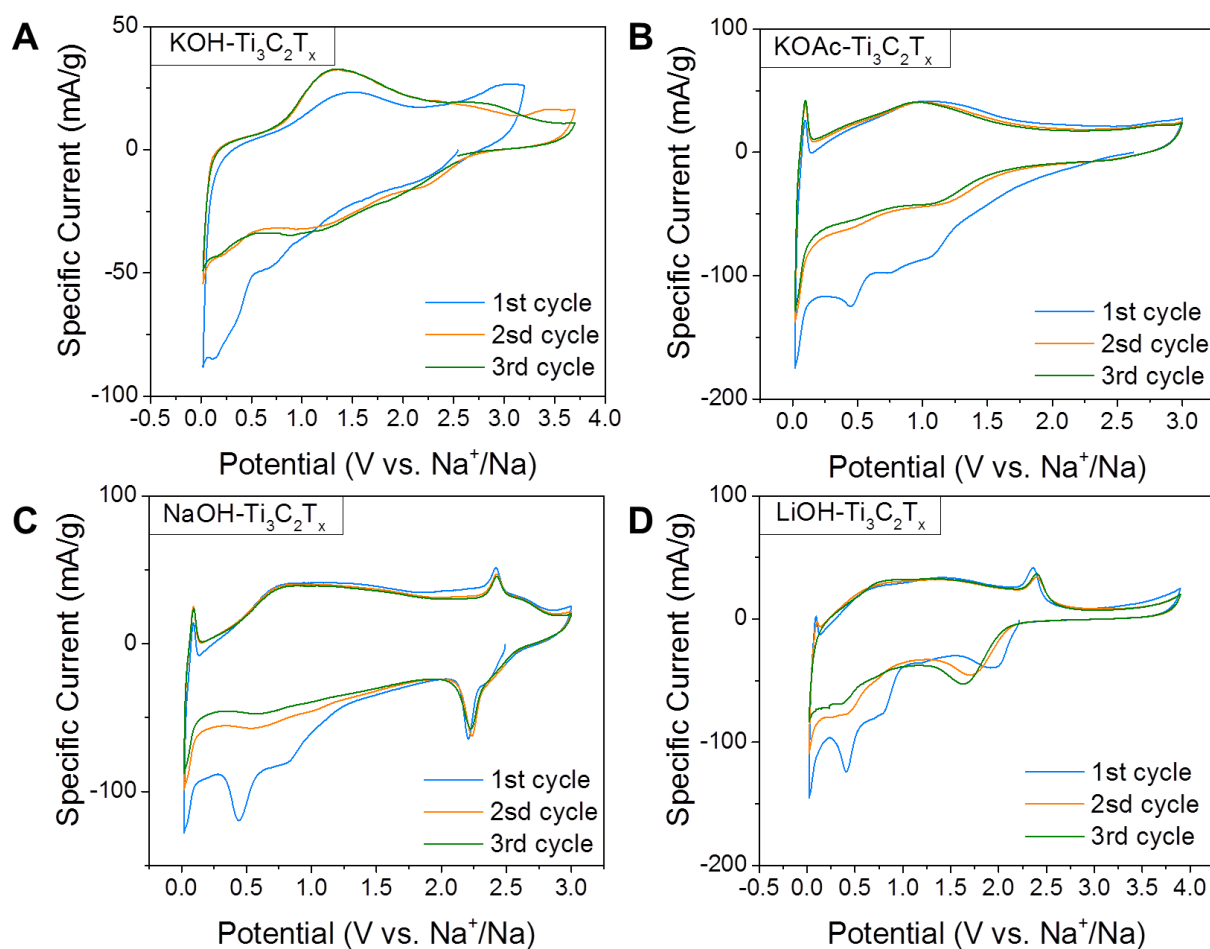


Figure IV.4: Cyclic voltammetry of $\text{Ti}_3\text{C}_2\text{T}_x$ treated in KOH (A) KOAc (B) NaOH (C) or LiOH (D) at 0.2 mV/s in 1 M NaPF_6 in EC:DMC.

III. 2-1 Delaminated $Ti_3C_2T_x$

The delamination process discovered by Mashtalir *et al.* (160) already led twice to energy storage improvement (shown Figure I.27 and Figure III.9). The experimental procedure to prepare a binder-free flexible film electrode is detailed in chapter 2.

The cyclic voltammograms obtained from this material are shown in Figure IV.5. The d- $Ti_3C_2T_x$ behavior is different than any $Ti_3C_2T_x$ -based electrode previously tested. Unexpectedly, the performance is worse than untreated $Ti_3C_2T_x$. Several possible reasons exist, such as ion accessibility hindered by residual DMSO or fast deterioration of the electrode in air, but none were investigated because a new synthesis method was discovered at Drexel University which quickly stole our attention. Recent research suggests that in-plane alignment of $Ti_3C_2T_x$ sheets limits the accessibility of electrolyte ions (164).

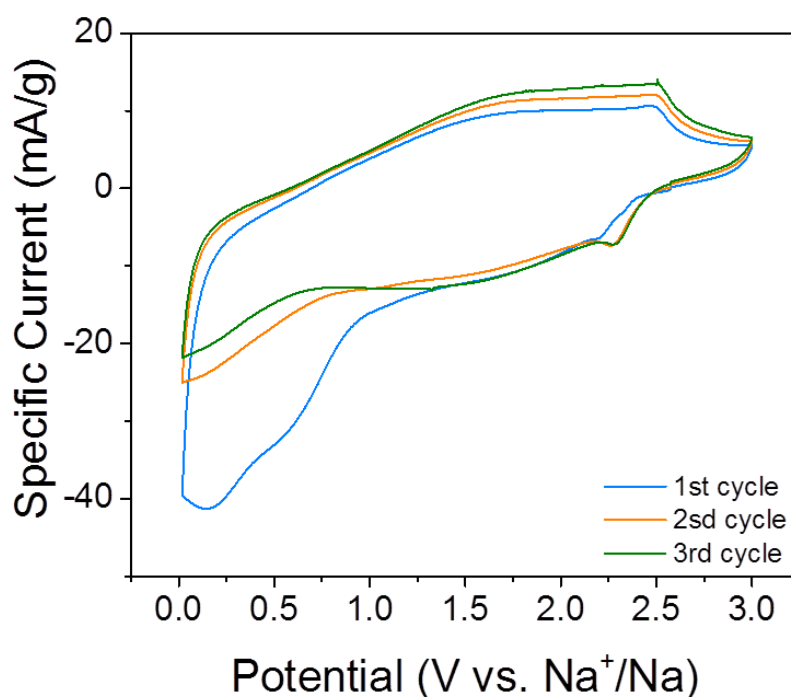


Figure IV.5: Cyclic voltammetry of d- $Ti_3C_2T_x$ at 0.2 mV s^{-1} in 1 M $NaPF_6$ in EC:DMC.

III. 2-2 Clay $Ti_3C_2T_x$

All the MXene results described previously were obtained from the selective etching of Al from MAX phases by a concentrated solution of hydrofluoric acid (HF). Handling HF is dangerous and new procedures were investigated for safer and easier manufacturing. Early in 2014, a new synthesis procedure has been proposed by Ghidui *et al.* (163), by replacing the hydrofluoric acid etching agent with a mixture of hydrochloric acid (HCl) and fluoride salt (LiF, etc.). This mixture produces in-situ HF that can react as previously described. The main advantage of this procedure is that it is easier to handle and uses safer and inexpensive chemicals. It consisted of mixing 2g of Ti_3AlC_2 in 100 mL of a 6M HCl/LiF at room temperature for 24 hours. With this mixture, the aluminum layer in Ti_3AlC_2 is still etched away but the produced $Ti_3C_2T_x$ behaves like clay that can be rolled by a glass tube to obtain a binder free flexible freestanding film electrode (163).

Figure IV.6.A shows the scanning electron microscopy image of the cross-section. We can observe that the film electrode is composed of multilayered $Ti_3C_2T_x$ and delaminated $Ti_3C_2T_x$ that created a network acting as binder and being responsible for the flexibility of the electrode. The electrochemical behavior of this material was investigated by cyclic voltammetry. In Figure IV. 6.B the cyclic voltammogram shape can be described as rectangular with a well-defined redox couple at 2.4V vs. Na^+/Na . Notably, the first cycle irreversibility is the lowest observed so far. Although the capacity is lower than in other $Ti_3C_2T_x$ its behavior is still attractive for sodium ion capacitor. Cyclic voltammetry at different rates has been performed to investigate the rate capability. The capacitance decreases quickly with increasing scan rate. At moderate rate 10 mV/s only 23 mAh/g remains which is too limited for real applications.

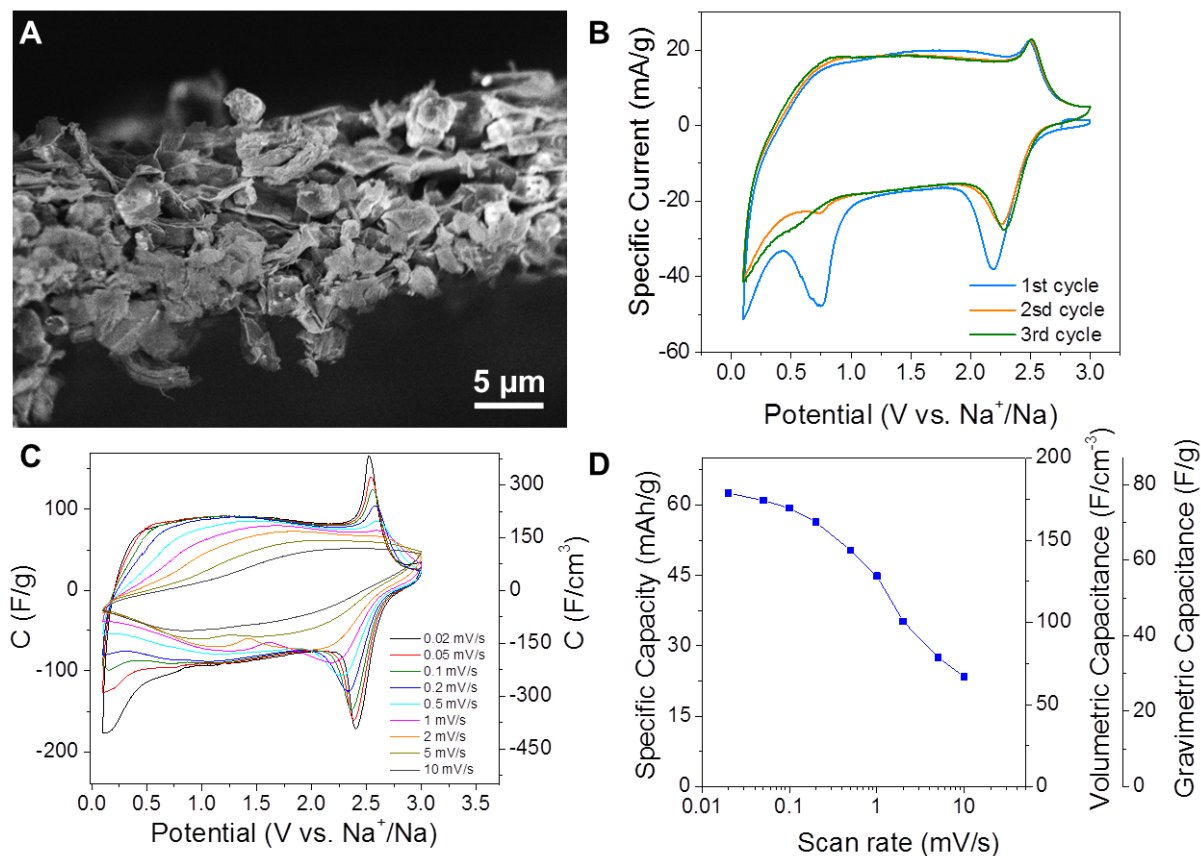


Figure IV.6: Scanning electron microscopy image of $\text{Ti}_3\text{C}_2\text{T}_x$ clay (A). Cyclic voltammetry of $\text{Ti}_3\text{C}_2\text{T}_x$ clay at $0.2\ \text{mV s}^{-1}$ (B) and at different rates (C) in $1\ \text{M NaPF}_6$ in EC:DMC. (A) Summary of rate performances (D).

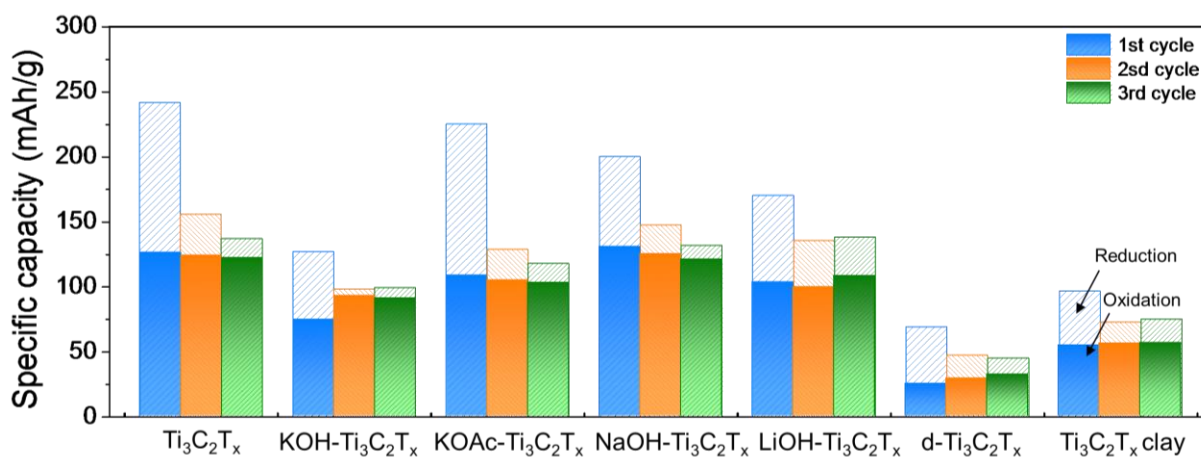


Figure IV.7: Capacity of all $\text{Ti}_3\text{C}_2\text{T}_x$ -based electrodes calculated from cyclic voltammetry at $0.2\ \text{mV/s}$.

Early in 2015, the first experimental investigation of sodium-ion capacitors using MXenes was published by Wang *et al.* (195), who used Ti_2C as the negative electrode and alluaudite $\text{Na}_2\text{Fe}_2(\text{SO}_4)_3$ as the positive electrode, as shown in Figure IV.8. The cyclic voltammetry of this Ti_2CT_x is very different than the one we observed in Figure IV.1, proving the influence of the synthesis conditions on the electrochemical performance. Interestingly it showed similarities to the clay $\text{Ti}_3\text{C}_2\text{T}_x$ (Figure IV.6), with redox peaks around 2.2 V vs. Na^+/Na . The mechanism was studied by ex situ X-ray diffraction and showed sodium intercalation only during the first charge. Surprisingly, this is a different mechanism than what was observed in Figure IV.3, despite this one could argue that ex-situ X-ray diffraction spectra could be irrelevant if extra care concerning reaction in air and electrode drying are not taken into account. The full cell showed a good rate capability and high specific power of 1.4 kW/kg with specific energy of 260 Wh per kg of Ti_2C .

Although promising results were shown with $\text{Ti}_3\text{C}_2\text{T}_x$, previous sodium ion battery studies demonstrated that it is not the best MXene in terms of performance. We decided to concentrate our effort on V_2CT_x .

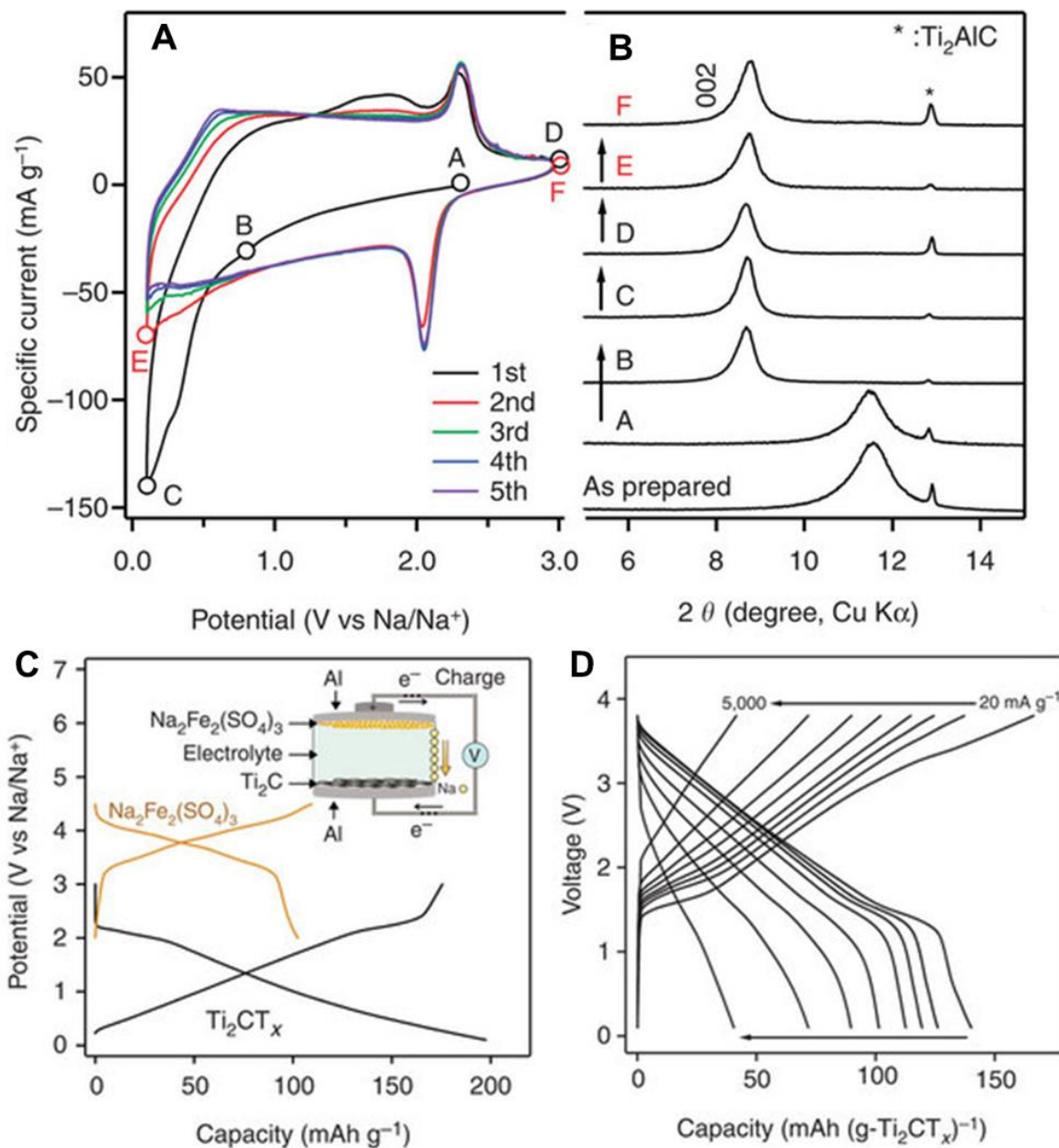


Figure IV.8: Cyclic voltammetry for Ti₂CT_x in a 1 M NaPF₆/EC–DEC electrolyte at a scan rate of 0.2 mV/s (A). Ex situ X-ray diffraction patterns during cycling (B). Charge/discharge curves of Ti₂CT_x and alluaudite Na₂Fe₂(SO₄)₃ versus Na/Na⁺; the specific currents are 30 and 6 mA/g, respectively. The inset is a schematic illustration of the Ti₂CT_x-alluaudite Na₂Fe₂(SO₄)₃ full cell (C). Charge/discharge profiles at various rates (D) (adapted from (196)).

IV V₂CT_x as positive electrode

In contrast with Ti₂C and Ti₃C₂ which can only be used as negative electrodes because of their operating potential window, V₂CT_x shows a potential window ranging from 1 V to 3.5 V vs Na⁺/Na. It is attractive as a positive electrode in Na sodium ion capacitors. Here, we extensively investigated the electrochemical behavior of two-dimensional vanadium carbide, V₂C, which has been identified as the most promising member from the MXene family for use as a positive electrode. We first performed further test in half cells, then we studied the energy storage mechanism and finally a full cell was assembled using a known negative electrode.

IV. 1 V₂CT_x vs Na

IV. 1-1 *Electrode preparation*

V₂CT_x electrodes were prepared with 5 wt.% polytetrafluoroethylene binder (60 wt.% in H₂O, Aldrich) and 15 wt.% carbon black (Alfa Aesar) to secure a sufficient electronic conductivity. The electrodes were rolled and cut into ≈30 μm thick disk with an average mass loading of 5 mg.cm². A two-electrode Swagelok cell was used for half-cells with metallic sodium as counter and reference electrode separated by a glass fiber separator (GFA).

IV. 1-2 *Cyclic voltammetry*

Figure IV.9.A shows the cyclic voltammetry results at different scan rates while the change of the capacitance with the scan rate is described in Figure IV.9.B. High capacitances of 100 F/g or 170 F/cm³ were obtained at slow scan rates and 50 F/g was still measured at 50 mV/s, evidence for good power performance of V₂CT_x for Na intercalation. At low scan rates, two different regions can be seen in the cyclic voltammograms, corresponding to two different electrochemical processes. From 1 V to 2.2 V, the rectangular shape of the voltammogram

describes pseudocapacitive behavior. A similar storage mechanism has been previously demonstrated in others MXenes. For example Ti_3C_2 cycled in aqueous electrolyte exhibits a rectangular-shaped voltammogram attributed to redox reactions and intercalation (174, 197). Redox peaks are identified at low scan rates, with an oxidation peak at 3 V (peak A), and a reduction peak at 2.5 V vs. Na^+/Na , (peak B). As the scan rate increases, the redox peaks tend to disappear, thus suggesting a diffusion limitation at scan rate beyond 2 mV/s. The large potential range and the absence of any 2-phase system plateaus make V_2C less suitable for sodium ion battery electrodes, but such features are attractive for sodium ion capacitors.

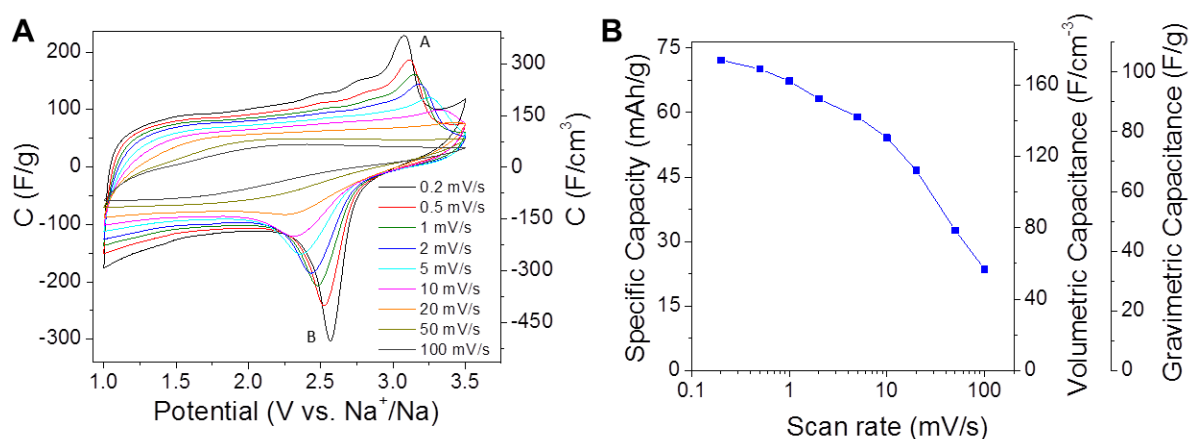


Figure IV.9: Cyclic voltammetry of V_2CT_x at different scan rate (A) and summary of rate performance (B) (adapted from (198)).

IV. 1-3 Galvanostatic charge discharge

V_2CT_x was cycled at current densities from 30 mA/g to 1 A/g corresponding to the rate from C/3 (3 hours discharge) to 20C (3 min discharge), as shown in Figure IV.10. At low charge/discharge rates, the faradic efficiency decreases, thus leading to a capacity fade with cycling. At a low rate (C/3), the capacity fading is more pronounced in the first 40 cycles. Good capacity up to 70 mAh/g was obtained, with remarkable stability at discharge rates beyond 3C. The performance achieved experimentally is lower than that predicted by first-principles simulations corresponding to the maximum theoretical capacity for a bare V_2C monolayer (335 mAh/g)(186). Experimentally, the capacity is limited by the presence of

MAX phase residue, functionalized layers and stacked layers. Thus, there is much room for further increases in the capacitance of this material.

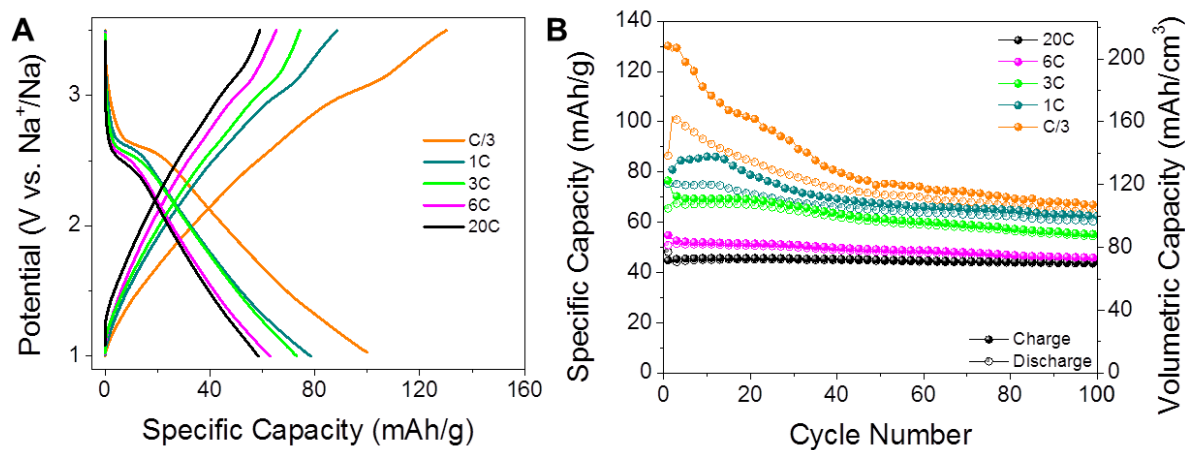


Figure IV.10: Charge-discharge profiles of V_2CT_x (A) and cycle life (B) from galvanostatic charge-discharge at different rates (adapted from (198)).

IV. 1-4 Mechanism

IV. 1-5 Electrochemical impedance spectroscopy

Characterization by electrochemical impedance spectroscopy was done at different potentials (Figure IV.11). The constant charge transfer resistance, as well as the improvement in the capacitive region at low frequencies, between 1 V to 2.5 V correlate well with a pseudo-capacitive intercalation mechanism. The charge transfer resistance ($200 \Omega/cm^2$) associated with the Na^+ pseudo-intercalation reaction explains the resistive behavior observed in the cyclic voltammetry curves. The increase of the charge transfer resistance and the semi-infinite diffusion limitation visible in the low-frequency region at 3.2 V is associated with the full desodiation of V_2CT_x , in agreement with the redox peaks observed in the voltammograms.

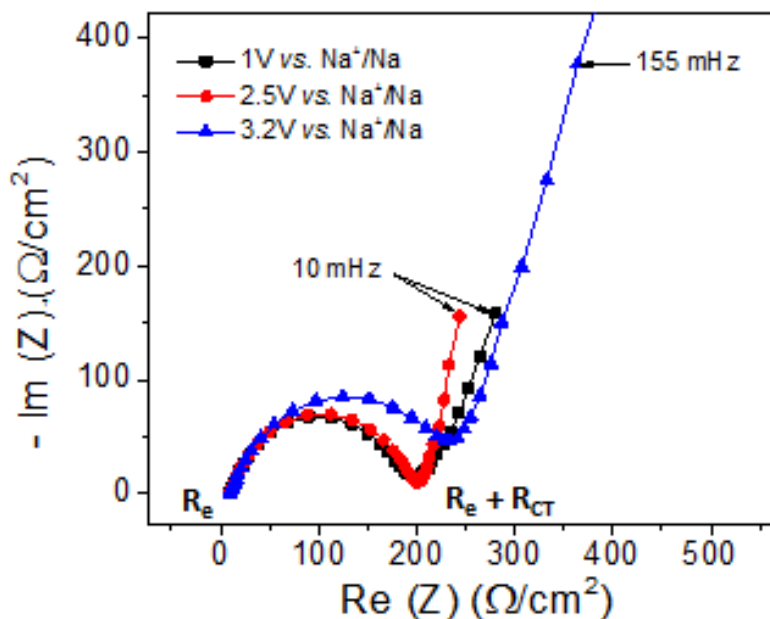


Figure IV.11: Nyquist plot from electrochemical impedance spectroscopy at different potentials (adapted from (198)).

IV. 1-6 X-ray diffraction

Figure IV.12 shows ex-situ X-ray diffraction patterns of V_2CT_x recorded at different voltages, where it can be observed that the (002) peak shifts continuously and reversibly from 9° to 12° during cycling between 1 and 3.5V vs Na^+/Na . In this potential range, the change is perfectly reversible, thus demonstrating that there are no undesired side reactions occurring. During sodiation, c-lattice parameter increases with the amount of Na^+ stored. This demonstrates that V_2CT_x stores energy through intercalation of Na^+ ions in between layers in a similar way to what was previously demonstrated for both, intercalation of Li^+ into $Ti_2C^{(161)}$ or $Ti_3C_2^{(177)}$ and Na^+ into $Ti_3C_2^{(196)}$. There is no new phase appearing at 3.5 V vs. Na^+/Na , thus the redox process identified by peaks A and B in the voltammogram do not modify the crystallographic structure of the material. A 4.6 \AA change in c-lattice parameter was observed, as calculated from Bragg's law. Taking into account that there are two interlayer gaps in a lattice unit, there is a 2.3 \AA expansion or shrinkage during sodiation and desodiation, respectively. This is a larger change than expected for a single layer of Na^+ ions, which indicates that a second layer of Na^+ could be intercalated, as shown for Ti_3C_2 intercalated by

Na^+ (196). The peak at 13° corresponds to V_2AlC from incomplete synthesis reaction. This peak does not move during cycling, demonstrating that the MAX phase is not electrochemically active and that the capacity could be increased by increasing V_2CT_x yield. Nevertheless, the presence of this peak is useful as a reference for the other peaks.

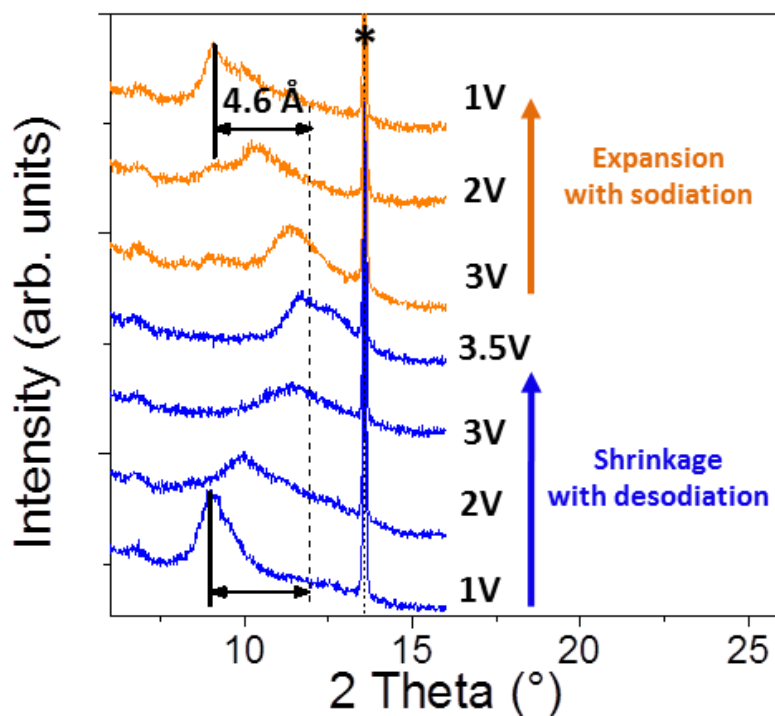


Figure IV.12: X-ray diffraction patterns at different potentials. (*) Peak of unreacted V_2AlC (adapted from (198)).

IV. 2 Full cell

IV. 2-1 Negative electrode Hard Carbon

The objective is to assemble a full cell using V_2CT_x as positive electrode and hard carbon (HC) as negative electrode for sodium intercalation (42). The hard carbon synthesized by pyrolysis of sugar under argon flow was selected because Ponrouch *et al.* demonstrated its low working potential (below 1V), good cycle life (>100cycles), and high specific capacity (230 mAh/g at 1C rate).

Galvanostatic charge-discharge cycling of hard carbon electrodes was done at the same C-rate as V_2CT_x in perspective to assemble the full cell. In Figure IV.13, the expected key features of a carbon intercalation electrode were observed, with an intercalation potential below 1 V vs Na^+/Na and a capacity beyond 200 mAh/g at low rates.

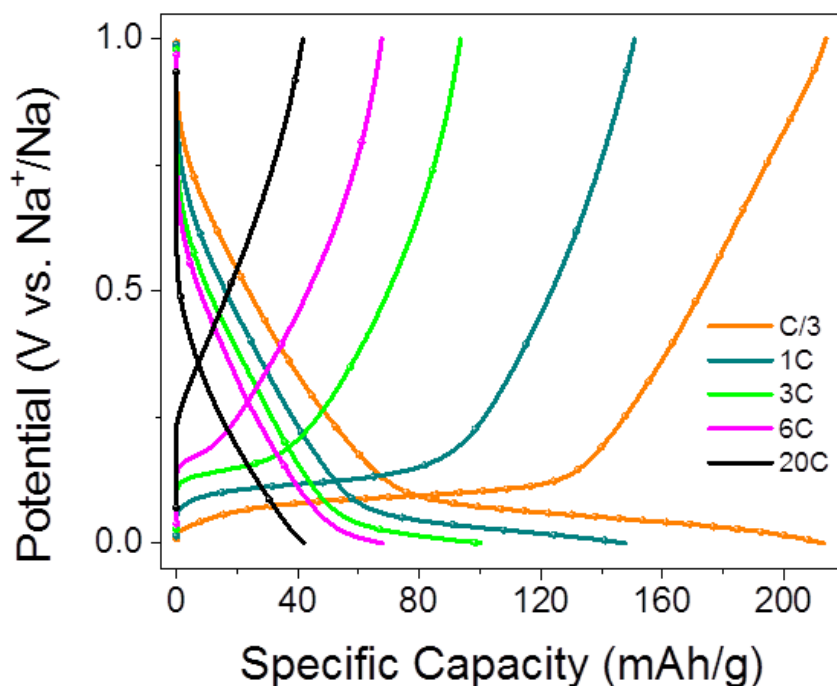


Figure IV.13: Charge-discharge profiles Hard Carbon electrode.

IV. 2-2 Full cell testing

Based on half-cell results, hybrid Na-ion capacitor full cells were assembled in three-electrode Swagelok® cells using an Ag wire as pseudo-reference electrode. The electrodes were pre-sodiated by immersing them in the electrolyte and short-circuited with metallic sodium. By anticipating the capacity decrease of V_2CT_x during the first cycles, we calculated a HC/ V_2CT_x weight ratio of 1:2.

In such conditions, the over-capacitive HC electrode allows a better potential stability for the negative electrode. The full cells were tested from C/3 to 20C rate. Figure IV.14.B shows the electrochemical performance obtained in a full cell configuration. All the gravimetric

capacities are calculated based on the total weight of both positive and negative electrodes in order to focus on the performances of the device. As the mass ratio of positive to negative electrode is 1:2, the equivalent capacities based on the mass of V_2CT_x are three times higher than those presented in Figure IV.14.

The charge/discharge galvanostatic profile is presented in Figure IV.14.A. During discharge, a sharp potential drop occurs from 3.5 V down to 2.6 V, followed by a small plateau at 2.5 V due to the redox reaction peaks observed in Figure IV.9.A. Figure IV.14.B shows that high-power performance could be achieved with 40% of the total capacity obtained at 20C, despite the use of a Na-ion intercalation HC negative electrode. The capacity decrease during the first cycles at the low rate (C/3) is associated with a decrease of the coulombic efficiency due to redox reactions occurring beyond 3V.

Figure IV.14.C shows the cycle life of the full cell at a high rate (20C). After 300 cycles, the capacity retention is 70%. Interestingly, the capacity slightly increases during the first 70 cycles. Afterward, the capacity decrease is associated with the decrease of the faradic efficiency down to 98%. In order to better understand this decrease, both electrodes were studied using a 3-electrode cell. Figure IV.14.D shows the 2^{sd} and 200th cycles. First, we can notice that the negative electrode potential range is smaller than 1 V because HC is in excess. As explained previously, a slightly overcapacitive negative electrode is necessary to ensure a good stability. Although the positive electrode has low irreversibility, it is sufficient to drive a shift of the negative electrode toward higher potentials after a large number of cycles. The potential of the V_2CT_x electrode goes slightly beyond the optimum operating potential range of 1 V to 3.5 V, which leads to irreversible redox reactions, thus explaining the capacity decrease upon cycling. An optimization of the electrode mass ratio should prevent the observed drift of the positive electrode potential, leading to an improvement in cyclability.

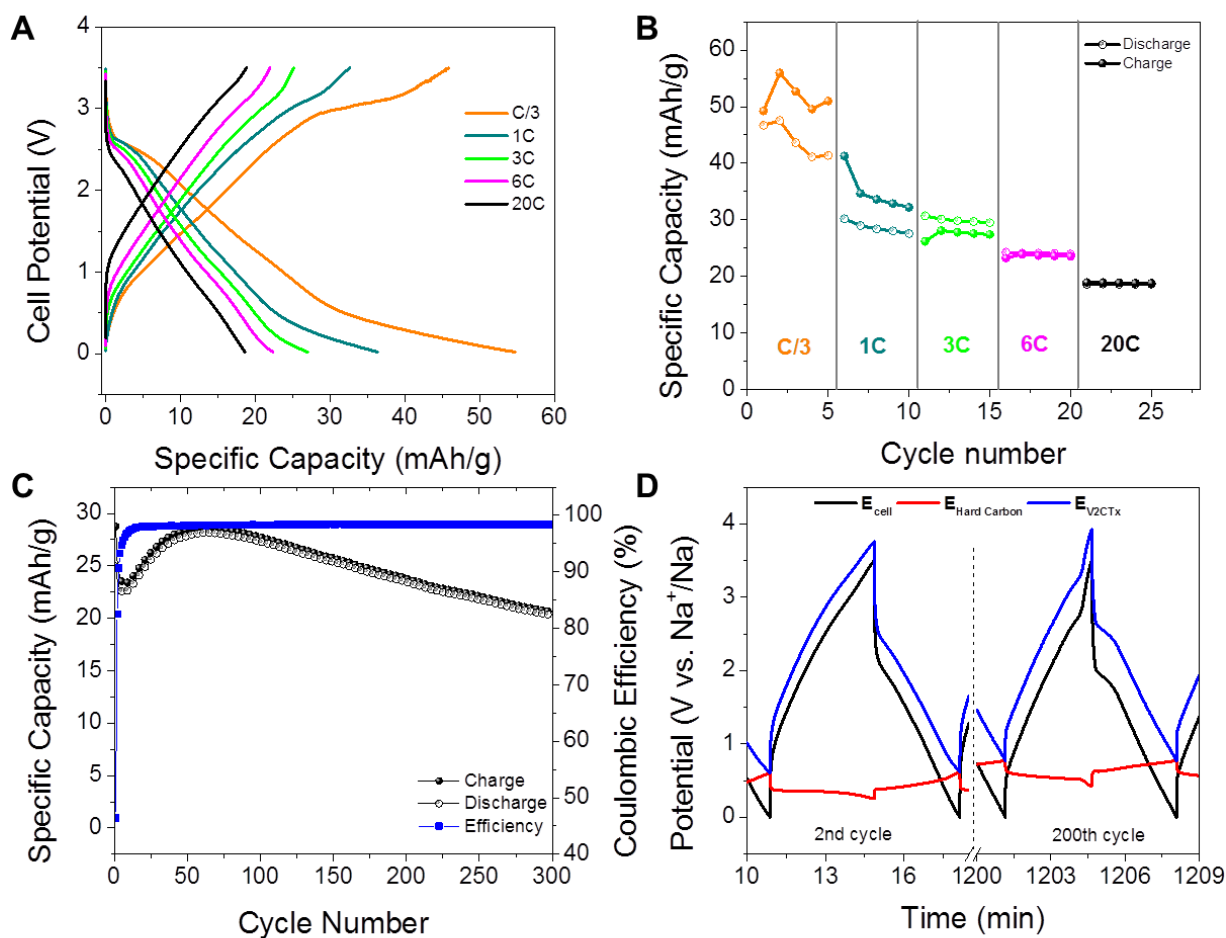


Figure IV.14: Charge-discharge profiles at various rates (A). Change of the capacity during galvanostatic charge-discharge at different rates (B). Capacity vs cycle number (C). Details of the potential range of positive and negative electrodes at 1A/g (D). Capacities were calculated for the total mass of both positive and negative active material, taken with the weight ratio as 1:2 (adapted from (198)).

V Conclusion

This work shows that at least one representative of the large family of MXenes, V_2CT_x , can serve as the positive electrode for a sodium ion capacitor. Investigation of the mechanism of sodiation and desodiation of V_2CT_x by X-ray diffraction shows continuous intercalation of sodium ions between the V_2CT_x layers in a wide range of potentials. Electrochemical testing in half-cells demonstrated that both capacitive (pseudocapacitive) and diffusion-limited redox processes take place. An asymmetric full cell was assembled using hard carbon, a known anode material for sodium ion battery. V_2CT_x/HC sodium-ion capacitor showed promising results, with a capacity of 50 mAh/g.

It is important to note that all results shown here were obtained on samples containing residual MAX phase, therefore decreasing the overall performances. The capacitance could be improved by tuning the surface chemistry by post-synthesis treatment or by the new synthesis route of MXene, via a fluoride salt and HCl etching, proposed for $Ti_3C_2T_x$. It may offer material of higher purity, which will also show improved performance in Na-ion capacitors. Finally, with just two MXenes studied in Na-ion capacitors to date and already showing promise for use as both, negative and positive electrodes, there is clear opportunity to create devices with both electrodes made of 2D carbides, but further studies of electrochemical behavior of those new materials are needed.

**Chapter V: MXene as a Supercapacitor
electrode in organic electrolytes**

Chapter V : MXene as a Supercapacitor electrode in organic electrolyte

I Introduction

MXene-based Ti_3C_2 electrodes have shown excellent capacitance in aqueous electrolytes in chapter 3, but in a narrow potential window which limits both the energy and power density. We have shown that the morphology and surface chemistry have a great impact on the electrochemical performance. New electrode formulation and synthesis routes have been explored by other researcher to continuously improve the performance of MXene electrodes in aqueous supercapacitors. Their recent discoveries are described in the following.

I. 1 Recent development in MXene electrode preparation

I. 1-1 *MXene composite*

The interest in composites has been demonstrated previously with the example of graphene composites. As MXene has comparable properties to graphene, the elaboration of MXene composites is a promising method to obtain new material properties.

Zhao *et al.* proposed the fabrication of various carbon material/ Ti_3C_2 composites (164). Tests with several carbon compounds (carbon nanotube, graphene or onion-like carbon) and different fabrication process (layer by layer sandwiched structure or mixed) were performed. The emphasis of the research was to obtain a flexible electrode for supercapacitors. 1M MgSO_4 electrolyte was used to compare the different composites. The impressive results were obtained with a sandwich-like composite of carbon nanotube/MXene fabricated as described in Figure V.1. As carbon nanotubes do not contribute significantly to the capacitance, the

improvement is attributed to the conductivity increase, to the increase of spacing between layers and to the well-organized layered structure that increase the diffusion rate. Capacitances up to 390 F/cm^3 were obtained for sandwich-like Ti_3C_2 /single-walled carbon nanotubes and up to 435 F/cm^3 for sandwich-like Ti_3C_2 /reduced graphene oxide. Liu *et al.* prepared a carbon nanotubes/ Ti_3C_2 composite for lithium ion batteries (199). The composite exhibited higher capacity (428 mAh/g) than individual Ti_3C_2 (96 mAh/g) and better rate capability.

Ling *et al.* investigated MXene composite with polymer (200). Charged polydiallyldimethylammonium chloride or an electrically neutral polyvinyl alcohol was mixed with Ti_3C_2 in solution then filtered to obtain free-standing composite films. The objective was also to investigate flexible electrode for aqueous supercapacitors. Capacitance up to 530 F/cm^3 was obtained with a gel electrolyte.

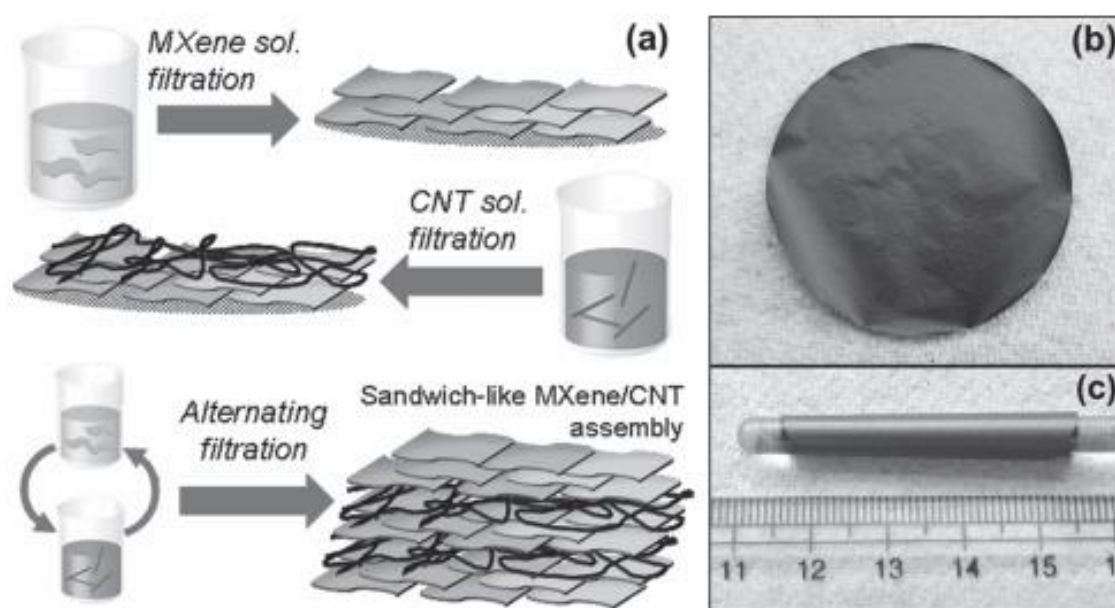


Figure V.1: Schematic showing the preparation of the sandwich-like MXene/Carbon nanotubes papers (A). Digital photographs showing a flexible and free-standing sandwich-like MXene/carbon nanotubes paper (B) and wrapping of latter around a 5-mm-diameter glass rod (C) (adapted from (164))

I. 1-2 Clay MXene

MXene synthesized with the new method proposed by Ghidui *et al.* (163) behaves differently than MXene synthesized by the concentrated HF method. The wet product behaves like clay and can be rolled as described on Figure V.2. In a single step (rolling) a conductive, flexible, and free-standing film can be prepared. In comparison, preparing the free-standing delaminated film previously described is laborious. Clay-like MXene did not show the graphite like (accordion-like) morphology. This was attributed to shearing of layers containing water acting as lubricant. The authors investigated the electrochemical behavior for aqueous supercapacitor using H_2SO_4 . They obtained excellent capacitance values up to 900 F/cm^3 and 245 F/g at 2 mV/s .

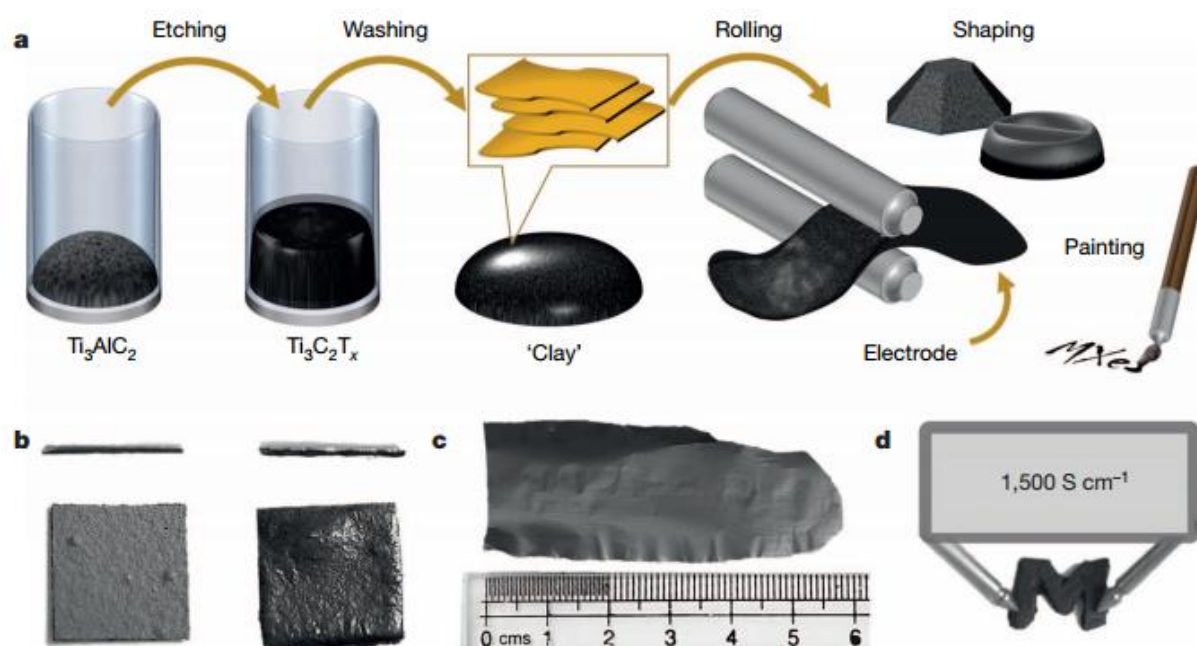


Figure V.2: Schematic of MXene clay synthesis and electrode preparation (adapted from (163)).

I. 2 Objectives

MXene has been investigated several times as electrode material for supercapacitors in aqueous electrolytes, but all the results reported showed a limited potential window due to water electrolysis. Moreover, oxidation of Ti_3C_2 under high anodic potentials in aqueous electrolytes further limits its use to cathodes of asymmetric devices. As both the energy and the power density increase with the square of the potential window, the expansion of the voltage window is one of the key challenges for designing supercapacitors with improved performance and organic electrolytes may expand the voltage window beyond 2-2.5 V.

Here, we investigated the electrochemical behavior of Ti_3C_2 MXene in 1M solution of 1-ethyl-3-methylimidazolium bis-(trifluoromethylsulfonyl)-imide (EMITFSI) in acetonitrile and two other common organic electrolytes. Both the addition of carbon nanotubes and the new synthesis procedure showed an increase in performance. The following describes the use of clay, delaminated, and composite Ti_3C_2 electrodes with carbon nanotubes in order to understand the effect of the electrode architecture and composition on the electrochemical performance.

II Electrode preparation

$\text{Ti}_3\text{C}_2\text{T}_x$ was synthesized by selectively etching the aluminum layer out of the Ti_3AlC_2 MAX phase in a 6M HCl/LiF solution at 35°C for 24h (163). The obtained material was then washed with distilled water. Full delamination of $\text{Ti}_3\text{C}_2\text{T}_x$ was obtained by ultrasonication for 1h in distilled water. A composite material was prepared by mixing the colloidal solution of delaminated Ti_3C_2 with 20 wt. % of multiwalled carbon nanotubes (MWCNT C100, Graphistrength) which have specific surface area of 175 m^2/g . The as-synthesized $\text{Ti}_3\text{C}_2\text{T}_x$, the delaminated $\text{Ti}_3\text{C}_2\text{T}_x$, and the CNT/ $\text{Ti}_3\text{C}_2\text{T}_x$ composite were filtered on polypropylene membranes then rolled into film electrodes on Teflon membranes using a glass tube. Once dried, the films were easily removed from the membrane to obtain the freestanding flexible $\text{Ti}_3\text{C}_2\text{T}_x$, d- $\text{Ti}_3\text{C}_2\text{T}_x$, and CNT- $\text{Ti}_3\text{C}_2\text{T}_x$ films without binder. The electrodes were prepared by cutting the films into $\sim 25 \text{ mm}^2$ rectangles with a razor blade, with mass loadings of 1.5 mg/cm^2 , 1.8 mg/cm^2 and 2.8 mg/cm^2 respectively, for $\text{Ti}_3\text{C}_2\text{T}_x$, d- $\text{Ti}_3\text{C}_2\text{T}_x$ and CNT- $\text{Ti}_3\text{C}_2\text{T}_x$ electrodes. The thicknesses were measured from scanning electron microscope observations and $\text{Ti}_3\text{C}_2\text{T}_x$, d- $\text{Ti}_3\text{C}_2\text{T}_x$ and CNT- $\text{Ti}_3\text{C}_2\text{T}_x$ film densities were calculated to be 2.3 g/cm^3 , 3.0 g/cm^3 and 2.9 g/cm^3 , respectively.

III Materials characterization

A scanning electron microscope JSM-6700F (JEOL, Japan) was used to investigate the morphology of the samples. Figure V.3 shows cross-section scanning electron microscopy images of electrode materials. The as-prepared MXene clay, denoted as $\text{Ti}_3\text{C}_2\text{T}_x$, is shown in Figure V.3.A-B. MXene layers can be rolled and sheared, forming a freestanding flexible electrode (163, 180). Fully delaminated MXene electrodes, denoted as d- $\text{Ti}_3\text{C}_2\text{T}_x$ (Figure V.3.C-D), were prepared for improving the electrochemical performance by taking advantage

of a higher specific surface area resulting from delamination. The specific surface areas values were 23 m²/g for multilayered Ti₃C₂ and 98 m²/g for delaminated Ti₃C₂ measured elsewhere by nitrogen gas sorption analysis (160) while 128 m²/g was estimated for CNT-Ti₃C₂T_x.

However, previous studies demonstrated that restacking of delaminated MXene layers forming a dense MXene “paper” with in-plane alignment of MXene sheets limits the accessibility of electrolyte ions. Such restacking issue can be prevented by addition of carbon nanoparticles (164, 199). Accordingly, composite electrodes were prepared by mixing appropriate amounts of d-Ti₃C₂T_x and MWCNTs. The specific surface area obtained by nitrogen gas sorption analysis was 70 m²/g for the CNT-Ti₃C₂T_x. Figure V.3.E-F show scanning electron microscopy images of a cross-section of the CNT-Ti₃C₂T_x composite electrode, where CNTs are homogeneously spread between the Ti₃C₂ layers since no aggregates can be seen. Aside from preventing restacking, CNT addition is known to increase the conductivity of the electrodes (164, 199, 201-203).

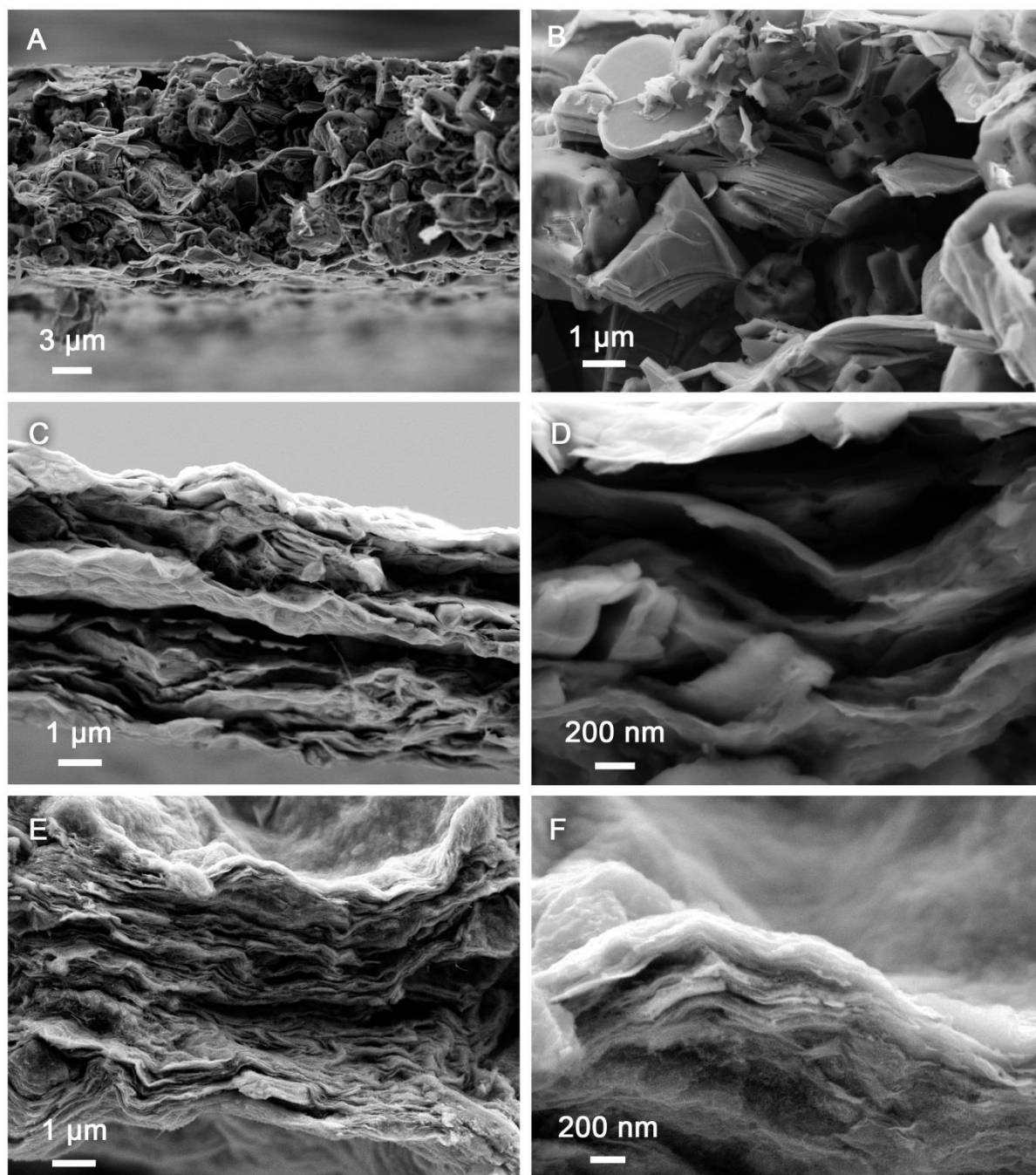


Figure V.3: Scanning electron microscope images of rolled $\text{Ti}_3\text{C}_2\text{T}_x$ “clay” (A-B), $\text{d-Ti}_3\text{C}_2\text{T}_x$ (C-D) and $\text{CNT-Ti}_3\text{C}_2\text{T}_x$ (E-F) electrode films (adapted from (204)).

IV Electrochemical behavior

Most pseudocapacitive materials, such as RuO₂, have high capacitance values in aqueous electrolytes (720 F/g for RuO₂ (88)) but very low in organic electrolytes. The reason for this important difference could be found in redox mechanisms in aqueous electrolytes that do not work in organic solutions. However Ti₃C₂T_x is promising because it can store the charge through intercalation capacitance even in organic electrolytes as it was demonstrated previously by Come *et al.* (161) and in chapter 4. In this part the study focused on the electrochemical behavior in a common organic electrolyte; 1M EMITFSI (Solvionic) dissolved in acetonitrile (Acros Organics). Three-electrode Swagelok© cells were used with Ti₃C₂ as working electrode, an Ag wire as a pseudo-reference electrode and a commercial activated carbon (YP17 Kuraray, Japan) overcapacitive counter electrode prepared by mixing 5 wt.% polytetrafluoroethylene binder (60 wt.% in H₂O, Aldrich) to 95 wt.% of YP17. A polypropylene membrane (GH Polypro, Pall) was used as a separator.

IV. 1 Characterization of carbon nanotube

Since we prepared a composite electrode with carbon nanotubes it was important to determine the capacitance contribution of this additive. In the first chapter we reported that carbon nanotubes capacitances are estimated at 60 F/g in the literature. However the performance depends on various parameters and we need to test the exact carbon nanotube that we selected.

Figure V.4 shows the cyclic voltammetry results at different scan rates of the multiwalled carbon nanotube C100 from Graphistrength © tested as powder in a three-electrode Swagelok cell with a Ag wire reference and overcapacitive activated carbon counter electrode. Gravimetric capacitance up to 36 F/g was obtained. This value is lower than what is reported for some other carbon nanotubes, but the cyclic voltammograms exhibits a rectangular shaped

response characteristic to double layer capacitance. A good rate capability highlights the good conductivity of this material. The capacitance contribution of 20 wt. % of these carbon nanotubes in the composite can be assumed to not exceed 7.2 F/g and will be taken into account.

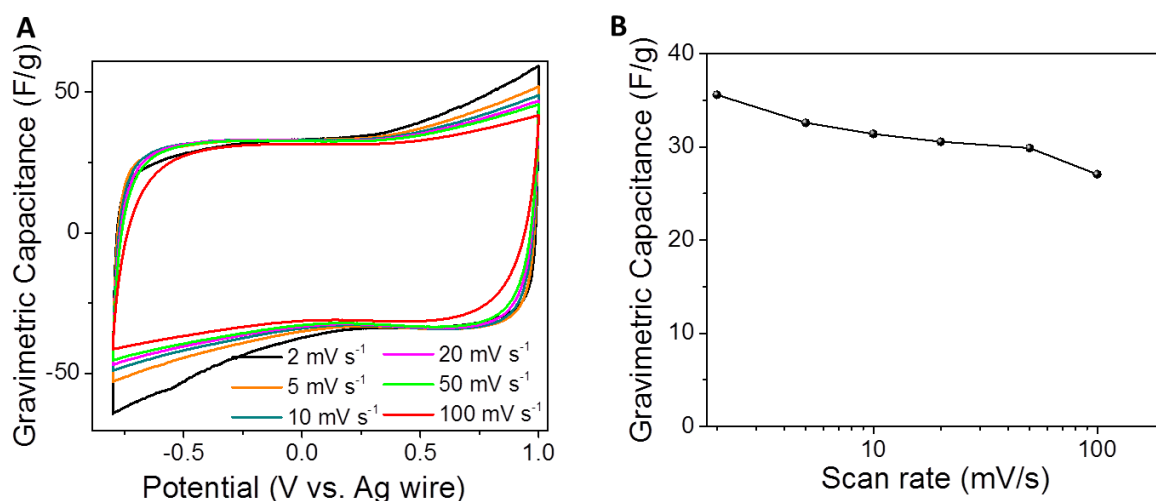


Figure V.4: Electrochemical performance of multiwalled carbon nanotubes in 1M EMITFSI in acetonitrile; cyclic voltammograms at different scan rates (A) and summary of capacitance with the potential scan rate (B).

IV. 2 Cyclic voltammetry

Figure V.5 shows cyclic voltammograms of the three Ti₃C₂-based electrodes at 20 mV/s in 1M EMITFSI in acetonitrile. The electrochemical signatures of the three samples appear to be similar, characterized by a capacitive envelope and a set of redox peaks around -0.2 V and -0.4 V vs. Ag. The potential difference between the oxidation and the reduction peaks, associated with kinetics and ohmic limitations, changes from one electrode to another. The smallest difference is observed for CNT-Ti₃C₂T_x, which can be associated with a first approach to a faster diffusion path, thanks to the addition of CNTs. Ti₃C₂T_x shows a similar electrochemical signature with a slightly larger overpotential. d-Ti₃C₂T_x shows the largest overpotential and most resistive behavior, possibly due to the restacking of delaminated layers during electrode preparation. The potential range (1.8V) is narrower than expected from this

electrolyte but could be explained by water trapped between Ti_3C_2 layers, responsible for electrolyte reaction at the extrema of the potential range visible at low scan rates.

The change of the capacitance (calculated from the integration of the charge during cyclic voltammograms measurements) with the potential scan rate is shown Figure V.5.D. Capacitance up to 245 F/cm^3 (85 F/g) was obtained at 2 mV/s for $\text{CNT-Ti}_3\text{C}_2$, with 75% capacitance retention at 100 mV/s (50% for $\text{d-Ti}_3\text{C}_2\text{T}_x$). This performance highlights a fairly high power capability of the electrodes, which is assumed to originate from the open 2D structure of the material and the associated high accessibility of the surface to ions. The lower rate performance of $\text{d-Ti}_3\text{C}_2\text{T}_x$ could be attributed to poor charge percolation.

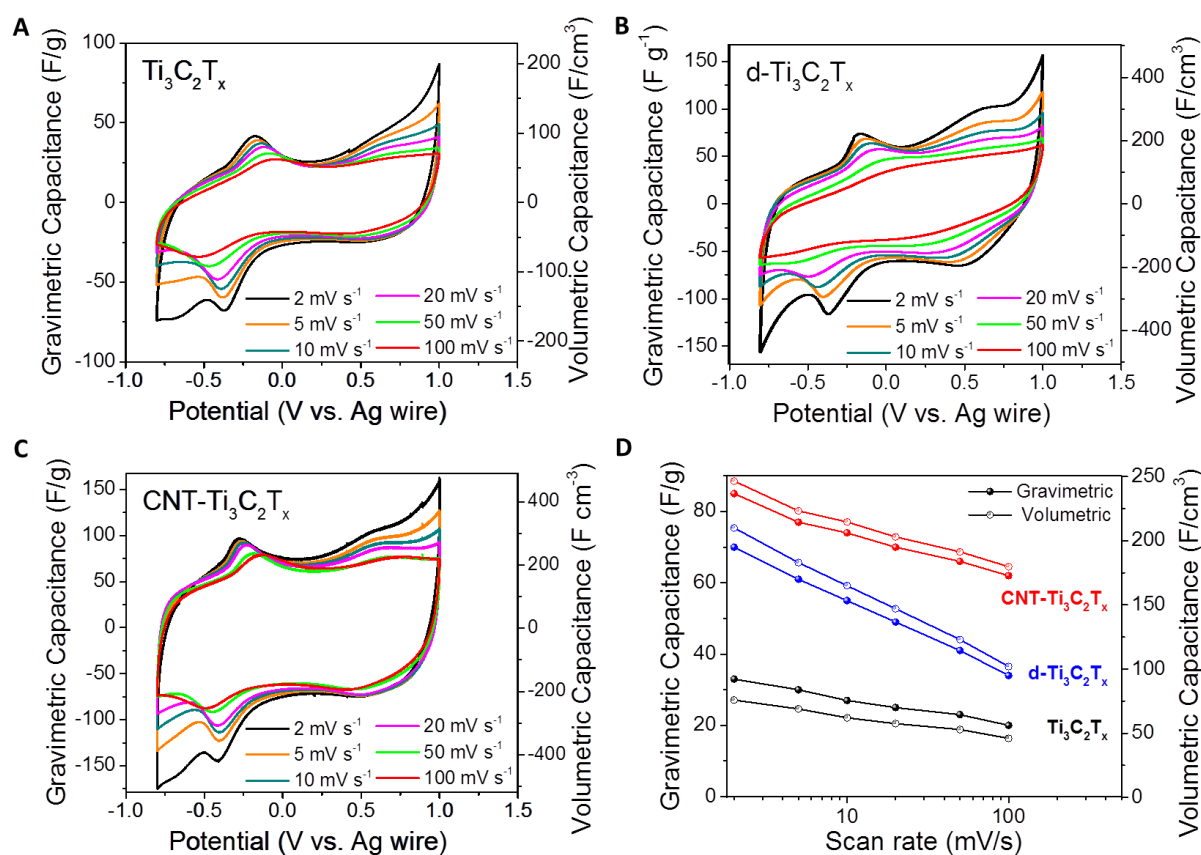


Figure V.5: Cyclic voltammograms of $\text{Ti}_3\text{C}_2\text{T}_x$ (A), $\text{d-Ti}_3\text{C}_2\text{T}_x$ (B) and $\text{CNT-Ti}_3\text{C}_2\text{T}_x$ (C) in 1M EMITFSI in acetonitrile electrolyte at different scan rates and summary of the change of capacitance with the potential scan rate (D). These measurements were done using a three-electrode Swagelok cell (adapted from (204)).

IV. 3 Electrochemical impedance spectroscopy

The electrochemical impedance spectroscopy measurements (Figure V.6) on the three different samples were performed between 200 kHz and 100 mHz in two-electrode configuration after polarization at 0.5 V vs. Ag (open circuit voltage) using three-electrode setup. The smaller semi-circle suggests that the addition of MWCNT greatly improves the charge percolation of the electrode. Additionally, there is little to no influence of MWCNTs on the electronic conductivity of the electrode, as can be seen from the constant value of the high-frequency resistance. This can be explained by a much higher conductivity of metallic $\text{Ti}_3\text{C}_2\text{T}_x$ electrode films ($\sim 2000 \text{ S/cm}$ (200)) compared to conventional activated carbon, oxide or even graphene electrodes.

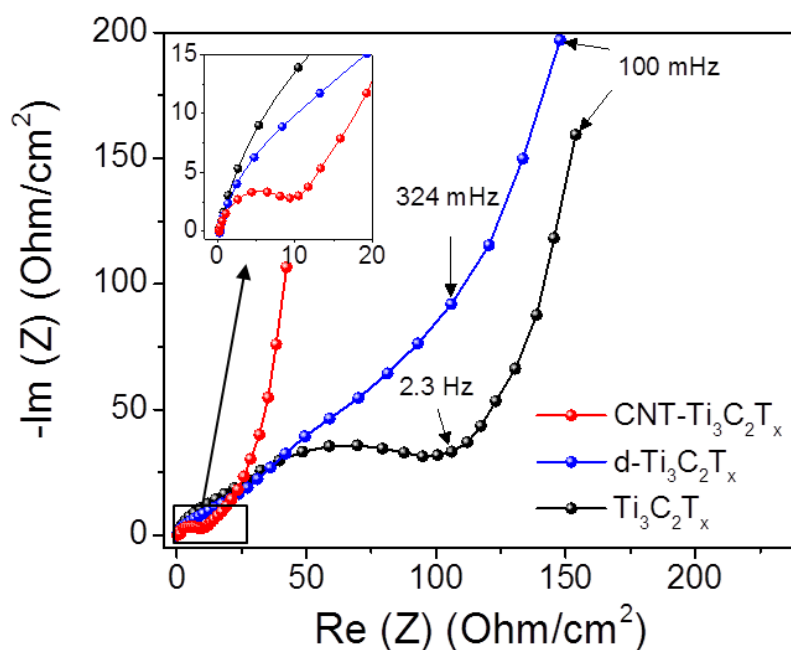


Figure V.6: Nyquist plot at 0.5 V vs. Ag reference obtained using a two-electrode setup (adapted from (204)).

IV. 4 Galvanostatic charge-discharge measurement

Figure V.7.A-C shows the galvanostatic charge-discharge curves obtained at 1A/g for the three electrodes. Gravimetric capacitances were calculated from the total mass of the composite electrode; associated volumetric capacitances were obtained using the density of

the respective electrodes. The curves are almost linear but contain a slight change in their slopes which correspond to the redox peaks identified previously. It appears that the electrodes exhibit pseudo-capacitive behavior. Also, a 5-10 times lower specific surface area of MXene (174) compared to activated carbons (4) would lead to a very low capacitance without contribution of charge-transfer processes. Figure V.7.D shows the cycle life for the different electrodes at 1A/g. CNT-Ti₃C₂T_x shows a good stability, with 90% capacitance retention after 1,000 cycles. Ti₃C₂T_x and d-Ti₃C₂T_x show a lower stability and faster capacitance decrease during cycling, as well as a lower coulombic efficiency.

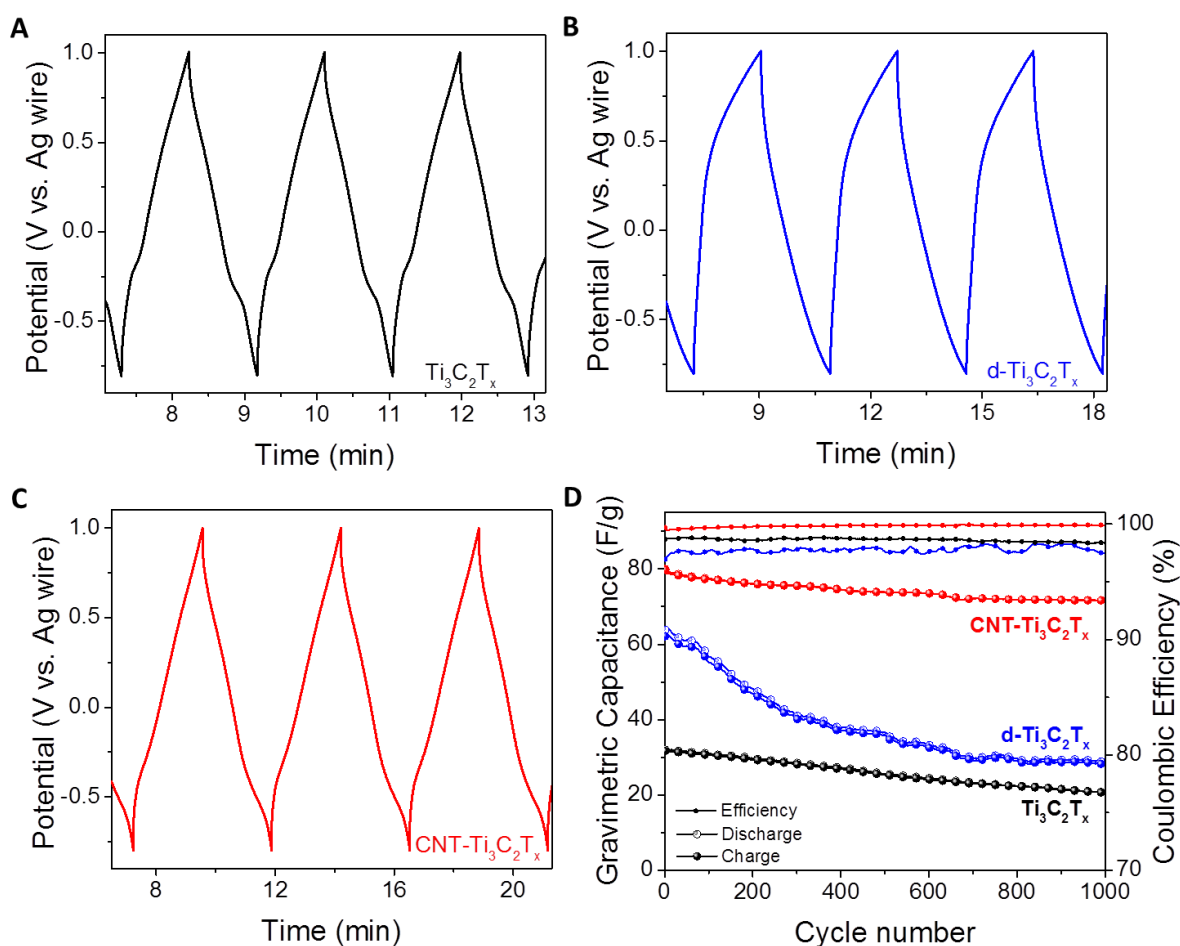


Figure V.7: Galvanostatic charge-discharge curves of Ti₃C₂T_x (A), d-Ti₃C₂T_x (B) and CNT-Ti₃C₂T_x (C) in 1M EMITFSI in acetonitrile electrolyte obtained at 1 A/g and the corresponding cycle life of those electrodes (D). These measurements were done using a three-electrode Swagelok cell (adapted from (204)).

V Charge storage mechanism

V.1 In-situ X-ray diffraction

The energy storage mechanism was investigated by recording *in situ* X-ray diffraction patterns at different potentials (Figure V.8). Each set of Bragg peaks can be indexed using the (00n) diffraction planes of Ti_3C_2 which are characteristic of the interlayer spacing. Interestingly at the open current voltage before cycling (open circuit voltage is 0.15 V vs. Ag) a (00n) downshift was observed, demonstrating a spontaneous intercalation similar to what was than previously observed in aqueous electrolytes.

The comparison of patterns indicates that depending on the applied potential two different sets of Bragg peaks are observed and that the phase change occurs at the same potential where the set of redox peaks appears in the cyclic voltammetry (Figure V.5.C). This shows that the intercalation / deintercalation processes follow a reversible two-phase mechanism. On the basis of the diffraction angle of (002) Bragg peaks (Figure V.8.B), it can be deduced that in the -0.8 V to -0.5 V potential range, the interlayer distance is 1.3 Å larger than at potentials above -0.5 V and should correspond to the intercalation and de-intercalation of ions from the electrolyte into $\text{Ti}_3\text{C}_2\text{T}_x$.

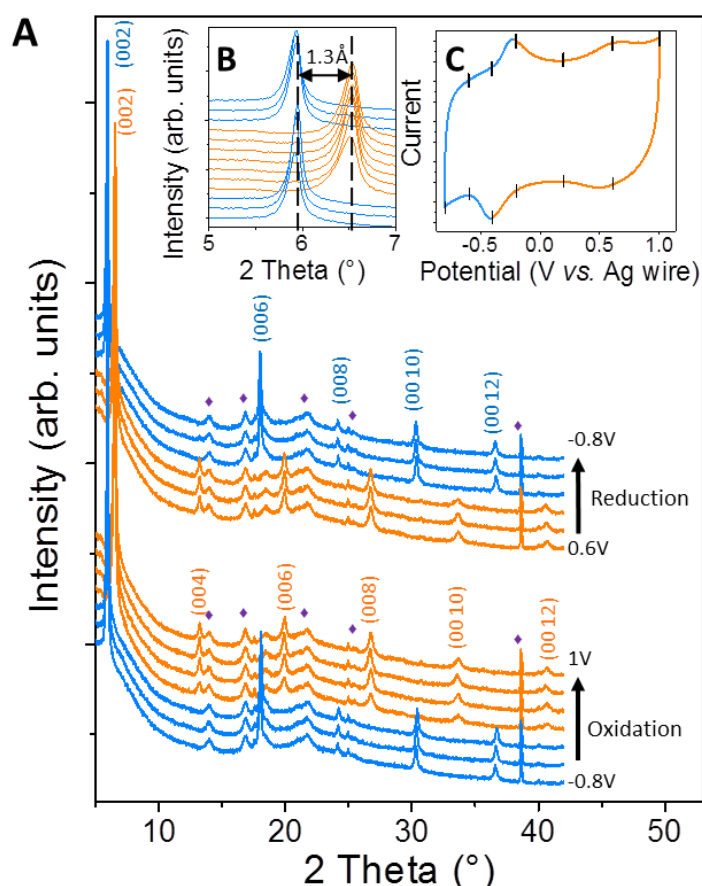


Figure V.8: In-situ X-ray diffraction patterns of CNT-Ti₃C₂T_x at different potentials in the 5-50° 2θ range (A). Purple diamonds indicate peaks coming from the cell for *in situ* measurements. Inset (B) shows a zoom in the 5-7° 2θ range and cycle voltammograms recorded at 20 mV/s (C) (adapted from (204)).

This charge storage mechanism was not expected for Ti₃C₂T_x because it differs from the progressive and continuous intercalation process previously observed for MXenes materials in aqueous supercapacitors (chapter 3) and metal-ions capacitors (Figure I.26 and chapter 4). Another method to reveal this fast and reversible two-phase transformation is to record the X-ray diffraction spectra during the electrochemical cycling over the total potential range instead of at fixed potential. For this purpose the in-situ cell was cycled at fast scan rate (50 mV/s) while the X-ray diffraction spectra was recorded slowly, as shown Figure V.9. The two set of peak were identifiable clearly demonstrating that this two-phase transformation is not limited by diffusion or kinetics.

Taking into account that the EMI^+ spontaneously intercalated between $\text{Ti}_3\text{C}_2\text{T}_x$ layers, a reasonable hypothesis for the intercalation/deintercalation mechanism observed is the formation of a second EMI^+ layer. This hypothesis, represented in the inset of Figure V.9 is supported by a recent in-situ aberration-corrected scanning transmission electron microscope experiment that demonstrated the formation of 2 layers of Na^+ between $\text{Ti}_3\text{C}_2\text{T}_x$ layers (196).

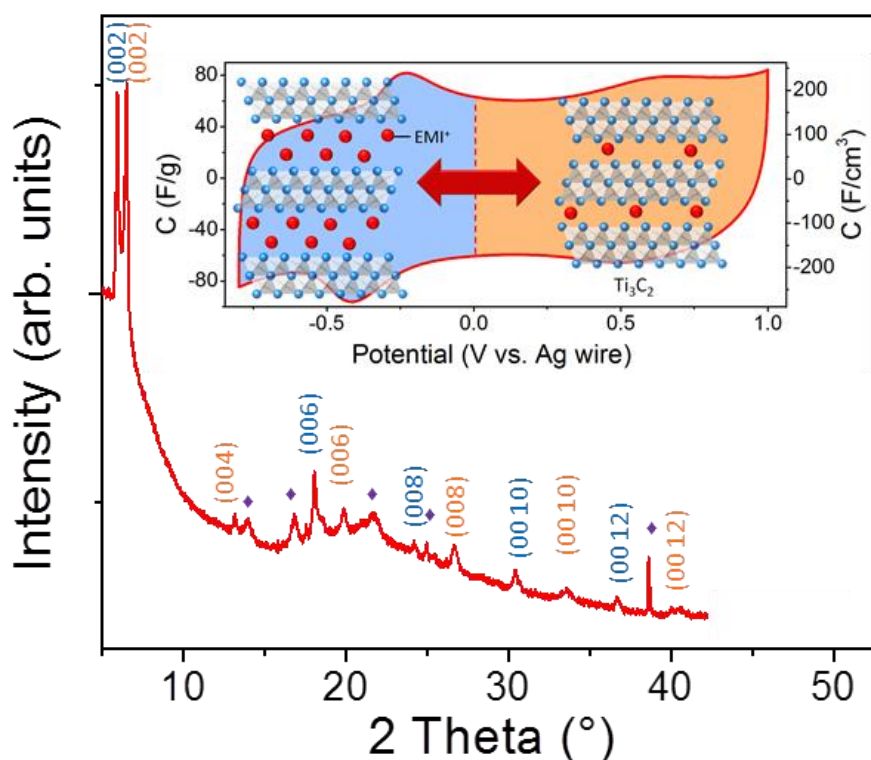


Figure V.9: In-situ X-ray diffraction patterns of CNT- $\text{Ti}_3\text{C}_2\text{T}_x$ during cycling at 50 mV/s. Purple diamonds indicate peaks corresponding to the *in situ* cell. Inset: Schematic of the two-phase transformation.

V.2 Cyclic voltammetry

Considering the low value of the intercalation potential, one can assume in a first approximation that the expansion is due to the intercalation of the EMI^+ cations between Ti_3C_2 layers and the shrinkage is attributed to its de-intercalation. Reversible intercalation of organic ions accompanied by peaks in the cyclic voltammograms, was observed for porous carbon electrodes when the ion size was somewhat larger than the pore size (205). Interestingly when cycled within the 0.1 V to 1 V potential range, $\text{Ti}_3\text{C}_2\text{T}_x$ capacitance

quickly decreases with the cycle number, while it is more stable when cycled between -0.8 V and 0.1 V, as shown Figure V.10. This suggests that the capacitive behavior observed above 0 V is associated with a redox process at negative potentials. In other 2D materials, it is observed that the intercalation of ions can form a pillared structure (141, 194-196). It is possible that cycling exclusively in the positive region causes the structure to collapse.

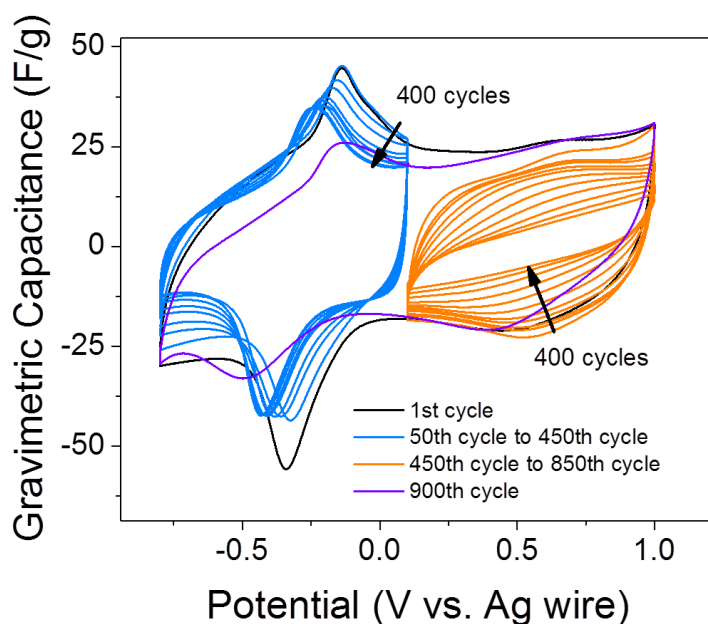


Figure V.10: Cyclic voltammograms of $\text{Ti}_3\text{C}_2\text{T}_x$ in different potential ranges at 20 mV/s (adapted from (204)).

VI Other organic electrolytes

The electrochemical performance of $\text{Ti}_3\text{C}_2\text{T}_x$ electrodes in aqueous electrolytes greatly depended on the electrolytes used. This was demonstrated in chapter 3 by performing extensive electrochemical tests in a wide variety of electrolytes. Herein, the behavior of CNT- $\text{Ti}_3\text{C}_2\text{T}_x$ in two other commonly used organic electrolytes, 1M EMIBF₄ (1-ethyl-3-methylimidazolium tetrafluoroborate, Fluka) and 1M TEABF₄ (tetraethylammonium tetrafluoroborate, Acros Organics), was tested by cyclic voltammetry at 20 mV/s.

Figure V.11.A shows the cyclic voltammogram of the CNT-Ti₃C₂T_x electrode in 1 M EMIBF₄ in acetonitrile electrolyte (a smaller anion but the same cation as in Figure V.5). The electrochemical signature is similar to that obtained in 1M EMITFSI in acetonitrile electrolyte (Figure V.5); more specifically, we note the presence of a set of redox peaks at the same potential. Figure V.11.B shows the cyclic voltammogram of the CNT-Ti₃C₂T_x electrode in 1 M TEABF₄ in acetonitrile electrolyte. When replacing the “planar” EMI⁺ cation with the larger and more “spherical” TEA⁺ cation, the electrochemical response is drastically changed. The reduction (intercalation) peak is present at a lower potential (-1 V vs Ag wire), but the reaction seems irreversible with an oxidation wave shifted to about 0.5 V. It is probable that the large TEA⁺ ions are stuck between MXene sheets after intercalation, decreasing the reversibility of the process, but also contributing to pillaring. The comparison of the cyclic voltammograms of CNT-Ti₃C₂T_x in 1M solutions of EMITFSI, EMIBF₄ and TEABF₄ in acetonitrile provides further evidence that the redox reaction is due to the intercalation of cations. These measurements suggest that the intercalation/deintercalation of the EMI⁺ cation is responsible for the reversible redox process occurring at -0.4 V vs. Ag. This hypothesis should be further confirmed by other *in situ* characterization techniques, such as electrochemical quartz crystal microbalance (206) or nuclear magnetic resonance (207).

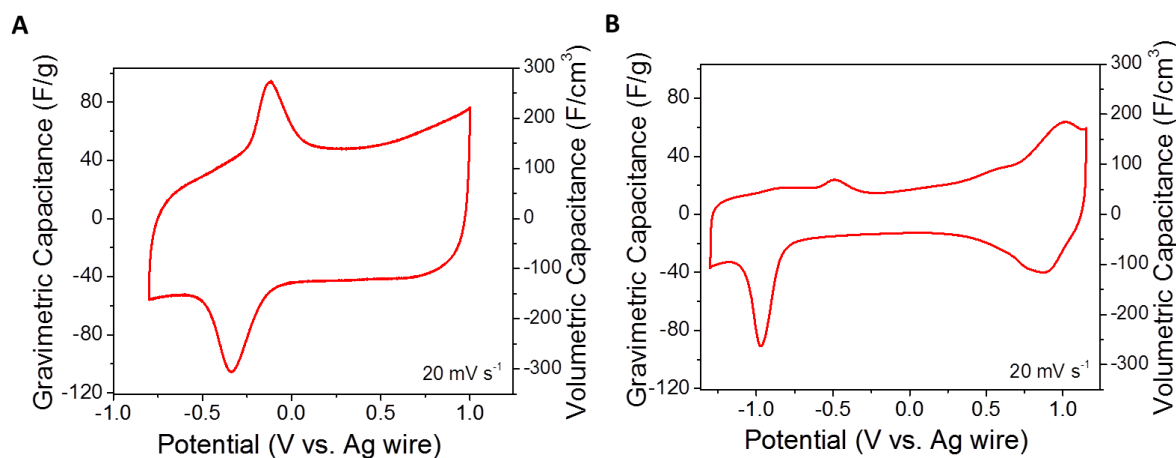


Figure V.11: Cyclic voltammetry of CNT-Ti₃C₂T_x at 20 mV/s in 1 M solutions of EMIBF₄ (A) and TEABF₄ (B) in acetonitrile (adapted from (204)).

VII Conclusions

The electrochemical behavior of $\text{Ti}_3\text{C}_2\text{T}_x$ as an electrochemical capacitor electrode in organic electrolytes has been investigated. Capacitance up to 32 F g^{-1} was obtained for as-produced $\text{Ti}_3\text{C}_2\text{T}_x$ -MXene clay and improved up to 85 F g^{-1} by delamination and addition of carbon nanotubes. Intercalation of large EMI^+ cations between the layers of Ti_3C_2 has been demonstrated suggesting that other large or multivalent cations may be similarly intercalated into MXenes from organic electrolyte solutions. $\text{Ti}_3\text{C}_2\text{T}_x$ capacitance was increased 3-fold, up to 85 F g^{-1} and 245 F cm^{-3} at 2 mV s^{-1} by using carbon nanotubes as an additive to improve ion accessibility to the active material. The CNT/ $\text{Ti}_3\text{C}_2\text{T}_x$ electrodes show a good rate performance and good cycle life stability.

Considering that this is the first report on capacitance of Ti_3C_2 in organic electrolytes used in supercapacitors and that Ti_3C_2 is only one of more than a dozen of already synthesized MXenes, there are good reasons to expect further improvement in capacitance as the optimal MXene-electrolyte couples have been identified and their performance optimized. It took less than two years to increase capacitance of Ti_3C_2 -MXene in aqueous electrolyte from about 100 F g^{-1} (174) to 320 F g^{-1} (180) and we expect fast improvement of capacitance in organic electrolytes as well.

General Conclusion

and

Future Work

General Conclusion

The objective of this thesis was to investigate the electrochemical behavior of a new family of two-dimensional materials called MXenes for designing high energy and power electrochemical storage. In this context, various MXenes were prepared and tested as electrodes for supercapacitors in aqueous electrolytes, for sodium-ion hybrid capacitors, and for supercapacitors in organic electrolytes.

A bibliographic review has introduced the principles of supercapacitors and intercalation batteries in the first chapter. Then, the interest of 2D materials for energy storages was discussed with examples of graphene and transition metal dichalcogenides which have both shown drawbacks and performance limitations. Finally, the state-of-the-art new 2D family of transition metal carbide, MXene, was presented. They have better conductivity than transition metal dichalcogenides and more diverse chemical compositions than graphene. The first results as electrodes materials for lithium ion batteries and lithium ion capacitors demonstrated the possibility to use MXene for energy storage and led us to start further investigation.

The second chapter describes the synthesis conditions of 7 MXenes, but it is only a few members of a large family of materials. Electrochemical setups and tests were presented. The experimental material characterization techniques used in this thesis were explained.

In the third chapter, we investigated Ti_3C_2 -based electrodes in various aqueous electrolytes. The spontaneous intercalation of few cations was demonstrated. The lattice expansion observed by X-ray diffraction could not be directly linked to the size of the cation, but rather to the contribution of both ion valence and pH. Using chemical modification of the MXene materials, we highlighted the effect of the surface chemistry and the morphology. The electrochemical performances greatly depended on the electrolytes used and we demonstrated

that the energy storage mechanism was the pseudo-intercalation reaction mechanism. The best performance in terms of capacitance was obtained in 1M H₂SO₄ with capacitances up to 520 F/cm³ or 325 F/g. The volumetric capacitance in particular is higher compared to similar materials. The corresponding maximum energy density of 16Wh per kg with a power density of 200 W per Kg of MXene was obtained. Although these values are higher than conventional carbon-based supercapacitors, they were limited by the small potential ranges.

As the intercalation of Na⁺ was demonstrated from aqueous electrolyte, we focused our work on the design of organic sodium-ion capacitors, in the fourth chapter. All synthesized MXenes were considered to be potentially attractive for this application, but only V₂C was studied as positive electrode. The intercalation mechanism was studied. The secondary objective of this part was to assemble a complete hybrid cell. For this purpose, hard carbon has used as the negative electrode. The full cell assembled shows capacity up to 50 mAh/g. Unfortunately, the performances at higher rate were lower than other materials proposed for this application.

Finally, in the last chapter, our research work focused on supercapacitors in organic electrolyte using Ti₃C₂ electrode synthesized by a new method which is more environmentally friendly and scalable. Using a carbon nanotube/MXene composite, a gravimetric capacitance of 85 F/g was obtained which is less than activated carbons. However, the volumetric capacitance, up to 245 F/cm³, is higher than other electrodes cycled in organic electrolytes. The high energy density of 8.10⁻² Wh/cm³ obtained at a power density of 16 W/cm³ highlighted the interest of MXene for applications where the volume is the main concern. A different storage mechanism than the two previous cases was demonstrated consisting of a two phase reaction based on the intercalation of the EMI⁺ cation. Preliminary results suggest that the size of the cation has an influence on the electrochemical behavior.

To conclude, this thesis highlights the need to develop new electrode materials and shows that MXenes are promising candidates for supercapacitor electrodes, but that further work is needed to better understand and optimize these materials.

Future Work

We have demonstrated that the surface chemistry of MXene can be modified by chemical treatment in various electrolytes and that it plays an important role in the electrochemical behavior of MXene. To further investigate these phenomena, work focusing on controlling the surface chemistry by other treatment (such as hydrogenation at high temperature) and using other analytical techniques will be performed. Besides, the spontaneous and electrochemical ions intercalation, demonstrated by X-ray diffraction, is not totally understood. The use of a broader variety of electrolytes could reveal more of the intercalation mechanism.

After investigating Ti_3C_2 -based electrodes in aqueous electrolytes and organic electrolytes, which showed promising results, it sounds appealing to investigate their electrochemical behavior in ionic liquids to increase the energy and power densities by increasing the potential range. Indeed, EMITFSI dissolved in acetonitrile has a smaller potential stability window than its pure ionic liquid phase. We have demonstrated that EMI^+ dissolved in acetonitrile could be reversibly intercalated into $\text{Ti}_3\text{C}_2\text{T}_x$, but the physicochemical properties in ionic liquid are different therefore a new study will take place.

Moreover, MXenes could be investigated in other energy storage applications. One of the most promising technologies under development are multivalent batteries based on Mg^{2+} , Ca^{2+} and Al^{3+} . The interest is that redox reactions with such ions exchange more electrons than with Li^+ or Na^+ . We demonstrated that at least Mg^{2+} spontaneously intercalates from aqueous electrolyte into Ti_3C_2 layers, which strongly encourages us to pursue in that direction.

Finally, in this thesis we mainly focused on Ti_3C_2 and V_2C , but they are members of a large family of two-dimensional transition metal carbides/nitrides. The synthesis work leading to new MXenes family needs to be continued. There is high probability that, if their composition and surface chemistry are properly controlled, other MXenes can achieve even higher electrochemical performances for the applications proposed here.

Annexes

Annexes

Annex 1

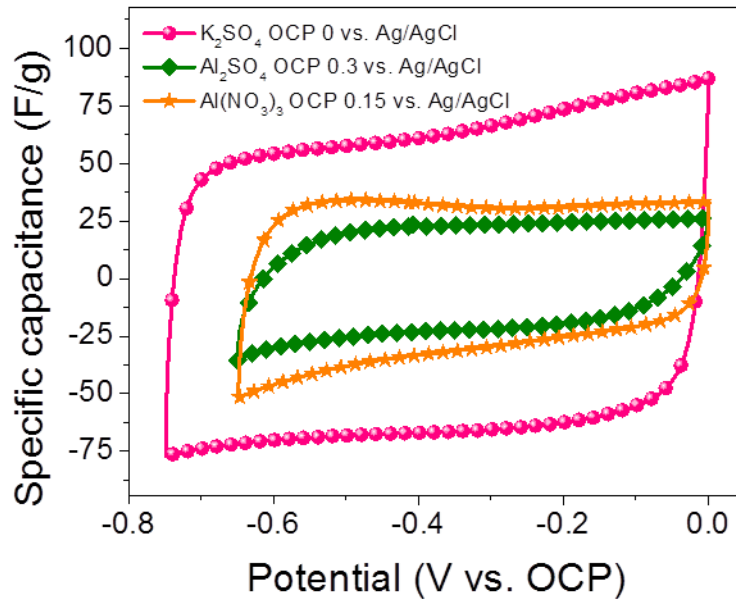


Figure A.1: Cyclic voltammetry for $\text{Ti}_3\text{C}_2\text{T}_x$ in a K_2SO_4 , Al_2SO_4 and $\text{Al}(\text{NO}_3)_3$ electrolytes at a scan rate of 10 mV/s (adapted from (174)).

Annex 2

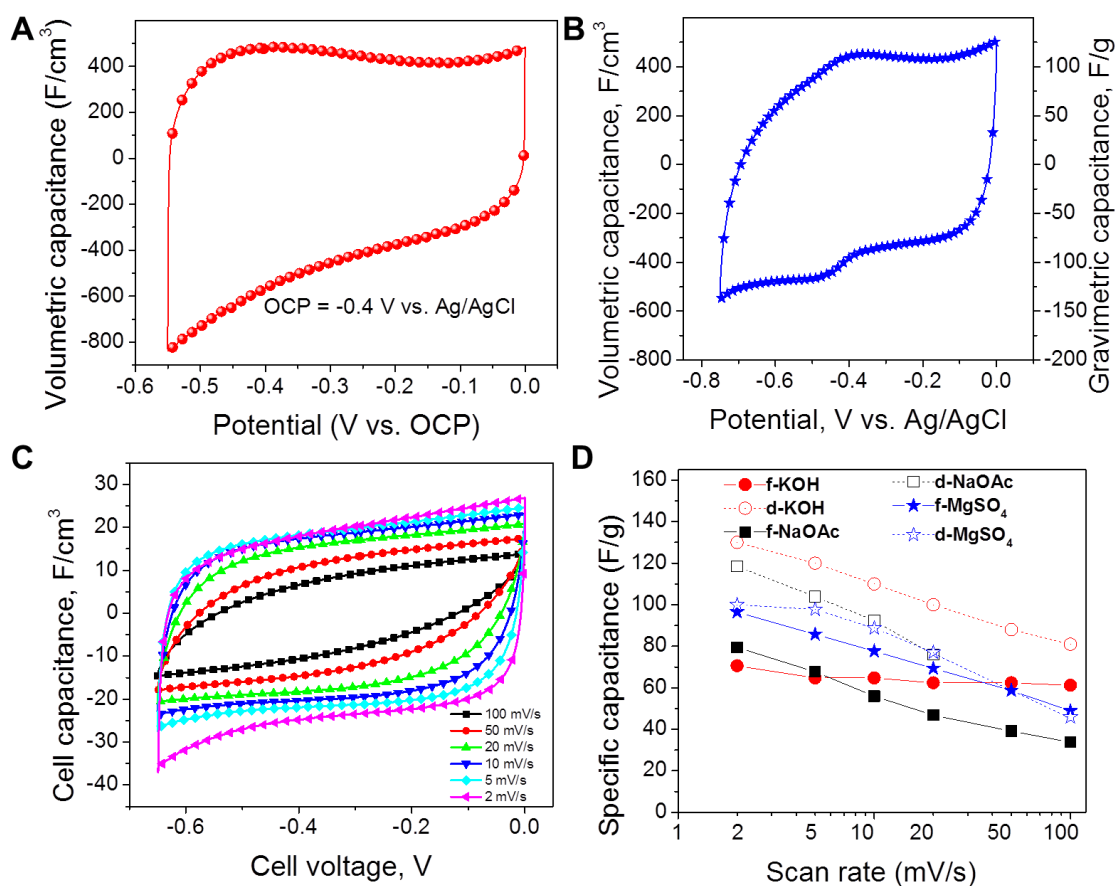


Figure A.2: Electrochemical performance of the binder-free delaminated d-Ti₃C₂

electrodes: Cyclic voltammetry 1M KOH (A) 1M MgSO₄ (B) and 0.5M K₂SO₄ (C)

electrolytes at a scan rate of 10 mV/s. Rate performance of the d-Ti₃C₂ (open symbols) vs. f-

Ti₃C₂ (solid symbols) in KOH, MgSO₄ and NaOAc electrolytes (D) (adapted from (174)).

List of Figure

List of Figures

Figure I.1: Ragone plot (specific power vs. specific energy) (adapted from (4)).....	7
Figure I.2: Schematic representation of a battery during discharge (A) and charge (B).....	8
Figure I.3: Typical behavior of a lithium-ion battery material during cyclic voltammetry (A) and galvanostatic charge-discharge measurement (B).	9
Figure I.4: Schematic representation of a Li-ion battery during discharge (A) and charge (B).	10
Figure I.5: Voltage vs. Capacity of relevant positive and negative electrodes materials for lithium-ion battery (adapted from (1)).....	11
Figure I.6: Electrochemical performance of hard carbon with different synthesis methods cycled in 1M NaClO ₄ in EC:PC vs. metallic Na: first cycle galvanostatic charge-discharge curves (A) and capacities vs. cycle number (B) (adapted from (42)).....	14
Figure I.7: Voltage vs. Capacity of relevant positive and negative electrodes materials for sodium ion battery. All materials can be found in the text.	16
Figure I.8: Schematic representation of an electrochemical double layer capacitor (A) and the Stern model (B).	17
Figure I.9: Typical behavior of electrochemical double layer capacitors during cyclic voltammetry (A) and galvanostatic charge-discharge measurement (B).	19
Figure I.10: Different types of reversible redox mechanisms that give rise to pseudocapacitance: underpotential deposition (A), redox pseudocapacitance (B) and intercalation pseudocapacitance (C) (adapted from (16)).....	21
Figure I.11: Typical behavior of pseudocapacitive material during cyclic voltammetry (A) and galvanostatic charge-discharge measurement (B).....	22
Figure I.12: Cycle voltammetry of RuO ₂ in H ₂ SO ₄ at 50 mV/s (adapted from (3)).....	23
Figure I.13: Cycle voltammetry of activated carbon at 5 mV/s in different electrolytes (adapted from (94)).....	25
Figure I.14: Electrode potentials vs. specific capacity of each electrode in a symmetric carbon/carbon supercapacitor and an asymmetric Li-ion hybrid during charge (A). Cell potential vs. specific capacity based on the total mass of the two electrodes (B).....	26
Figure I.15: Discharge profile as function of rate (A) and three-electrode measurement (B) of an asymmetric hybrid cell utilizing an activated carbon positive electrode and Li ₄ Ti ₅ O ₁₂ negative electrode in LiPF ₆ EC/DMC electrolyte (adapted from (101)).....	27

Figure I.16: Design of a flexible supercapacitor based on laser-scribed graphene. (inset) A digital photograph showing the flexibility of the device (A) Cyclic voltammograms and the effect of the bending at 1000 mV/s (adapted from (121)).30

Figure I.17: Structure of several typical layered transition metal sulfides: (A) MoS₂ or WS₂, (B) ZrS₂ or VS₂, (C) VS₄ and (D) SnS₂ (adapted from (149)).33

Figure I.18: Performances of the in-plan supercapacitor based on VS₂; cyclic voltammetry (A) and cycle life (B) (adapted from (155)).35

Figure I.19: Charge–discharge curves (A) and rate capability (B) of TiS₂ (adapted from (156)).35

Figure I.20: Repartition of M, A and X elements on the periodic table (adapted from (159)).36

Figure I.21: Crystalline structure of MAX phases M₂AX, M₃AX₂ and M₄AX₃ (adapted from (159)).37

Figure I.22: Schematic synthesis of MXene from MAX phases.39

Figure I.23: Secondary electron micrographs for (A) Ti₃AlC₂ particle before treatment. Particles after HF treatment of (B) Ti₃AlC₂, (C) Ti₂C, (D) Ta₄AlC₃, (E) TiNbAlC and (F) Ti₃AlCN (adapted from (158)).39

Figure I.24: Schematic representation of the intercalation mechanism (A). Particle size distribution in aqueous colloidal solution; inset shows Tyndall scattering effect in the solution (B). Scanning electron microscope image of d-Ti₃C₂ single flake on alumina membrane (C) (adapted from (160)).40

Figure I.25: Cyclic voltammetry at a constant scan rate of 0.2 mV/s. The solid arrows refer to main peaks positions during lithiation and delithiation cycles (A) and capacities vs cycle number at different scan rates (B) (adapted from (9)).42

Figure I.26: In-situ X-ray diffraction patterns during charge and discharge of Ti₂C (A) Charge and discharge specific capacity vs. cycle number of a Ti₂C/activated carbon asymmetric cell at 10C rate. Inset: corresponding curves at different cycles (B) (adapted from (161)).42

Figure I.27: Comparison of the performance of exfoliated and delaminated Ti₃C₂ as anode material in Li-ion batteries. Inset shows scanning electron microscope image of an additive-free film of delaminated f-Ti₃C₂ filtered through the membrane. (A) The galvanostatic charge/discharge curves at a 1C rate. The “y” value shown on top x-axis was calculated assuming a MXene chemistry of Ti₃C₂(OH)₂ (B) (adapted from (160)).43

Figure II.1: Schematic illustration of the delamination process.51

Figure II.2: Picture of a 2-electrode Swagelok cell.52

Figure II.3: Picture of a 3-electrode Swagelok cell.53

Figure II.4: Typical cyclic voltammograms of redox (A) and double layer (B) materials.54

Figure II.5: Typical galvanostatic charge-discharge curves of lithium ion intercalation (A) and double layer (B) materials.....	56
Figure II.6: Typical Nyquist plots of a battery-type materials ($\text{Li}_x\text{Mn}_2\text{O}_4$) (A) and carbon double layer material (B). Inset: equivalent circuit (adapted from (169) (173)).	59
Figure II.7: Schematic representation of Bragg's diffraction.	60
Figure II.8: Photography of the electrochemical in-situ X-ray diffraction cell.	61
Figure III.1: X-ray diffraction pattern of $\text{Ti}_3\text{C}_2\text{T}_x$ and $\text{LiOH-Ti}_3\text{C}_2\text{T}_x$. Purple diamond indicates peak coming from measurement set-up. Inset is a schematic of the intercalation process.	69
Figure III.2: X-ray diffraction patterns of $\text{Ti}_3\text{C}_2\text{T}_x$ after treatment in electrolytes with different anions (A-B) and different cations (C-D).	71
Figure III.3: X-ray diffraction patterns of $\text{Ti}_3\text{C}_2\text{T}_x$ during intercalation from 1M MgSO_4 . Each pattern took 20 min to be recorded. Vertical dashed lines indicate the original position of the (002) peak.	73
Figure III.4: X-ray diffraction patterns of $\text{Ti}_3\text{C}_2\text{T}_x$, $\text{DMSO-Ti}_3\text{C}_2\text{T}_x$ and $\text{d-Ti}_3\text{C}_2\text{T}_x$	74
Figure III.5: Scanning-electron microscope images of $\text{Ti}_3\text{C}_2\text{T}_x$ (A), $\text{KOH-Ti}_3\text{C}_2\text{T}_x$ (B) and $\text{d-Ti}_3\text{C}_2\text{T}_x$ (C) (adapted from (180)).	76
Figure III.6: Characterization data of Ti_3C_2 -based materials after surface modification in various intercalation agents. High-resolution X-ray photoelectron spectroscopy spectra in the F 1s region (A), the Ti 2p region (B), and K 2p region (C). Schematic illustration of the modifications of $\text{Ti}_3\text{C}_2\text{T}_x$; delamination and intercalation of K^+ (D) (adapted from (180)).	78
Figure III.7: Electrochemical performance of $\text{Ti}_3\text{C}_2\text{T}_x$ in various electrolytes; cyclic voltammograms at 20 mV/s in LiOH, NaOH and KOH (A) NaOAc and KOAc (B), Li_2SO_4 and Na_2SO_4 (C) K_2SO_4 and MgSO_4 (D) H_2SO_4 (E) Summary of rate performances in the different aqueous electrolytes (F).	82
Figure III.8: Electrochemical in-situ X-ray diffraction study of $\text{Ti}_3\text{C}_2\text{T}_x$ in 1M KOH (A), 1M MgSO_4 (B) and 3M (NaOAc) (C). Vertical dashed lines indicate the original position of the (002) peak. Inclined arrows show the direction of the (002) peak shift. Illustration of cycling direction and concomitant change in c-lattice parameters (adapted from (174)).	85
Figure III.9: Electrochemical performance of Ti_3C_2 -based electrodes in 1M H_2SO_4 : cyclic voltammograms profiles at 10 mV/s(A). Summary of rate performances (B) (adapted from (180)).	88
Figure III.10: Charge and discharge volumetric capacitance vs. cycle number of $\text{KOH-Ti}_3\text{C}_2\text{T}_x$ and $\text{d-Ti}_3\text{C}_2\text{T}_x$ electrodes from galvanostatic cycling in 1M H_2SO_4 at 5 A/g (A). Galvanostatic charge-discharge profile of $\text{d-Ti}_3\text{C}_2\text{T}_x$ (B) (adapted from (180)).	88
Figure IV.1: Cyclic voltammetry of Carbon black (A) and MXene (B-H) at 0.2 mV/s in 1 M NaPF_6 in EC:DMC.	96

Figure IV.2: Capacity of all MXene calculated from cyclic voltammetry at 0.2 mV/s.	97
Figure IV.3: In-situ X-ray diffraction spectra (A) of $Ti_3C_2T_x$ during galvanostatic charge-discharge at 0.03 A/g and corresponding charge-discharge curves (B).	98
Figure IV.4: Cyclic voltammetry of $Ti_3C_2T_x$ treated in KOH (A) KOAc (B) NaOH (C) or LiOH (D) at 0.2 mV/s in 1 M $NaPF_6$ in EC:DMC.	100
Figure IV.5: Cyclic voltammetry of d- $Ti_3C_2T_x$ at 0.2 mV s ⁻¹ in 1 M $NaPF_6$ in EC:DMC.	101
Figure IV.6: Scanning electron microscopy image of $Ti_3C_2T_x$ clay (A). Cyclic voltammetry of $Ti_3C_2T_x$ clay at 0.2 mV s ⁻¹ (B) and at different rates (C) in 1 M $NaPF_6$ in EC:DMC. (A) Summary of rate performances (D).	103
Figure IV.7: Capacity of all $Ti_3C_2T_x$ -based electrodes calculated from cyclic voltammetry at 0.2 mV/s.	103
Figure IV.8: Cyclic voltammetry for Ti_2CT_x in a 1 M $NaPF_6/EC-DEC$ electrolyte at a scan rate of 0.2 mV/s (A). Ex situ X-ray diffraction patterns during cycling (B). Charge/discharge curves of Ti_2CT_x and alluaudite $Na_2Fe_2(SO_4)_3$ versus Na/Na^+ ; the specific currents are 30 and 6 mA/g, respectively. The inset is a schematic illustration of the Ti_2CT_x -alluaudite $Na_2Fe_2(SO_4)_3$ full cell (C). Charge/discharge profiles at various rates (D) (adapted from (196)).	105
Figure IV.9: Cyclic voltammetry of V_2CT_x at different scan rate (A) and summary of rate performance (B) (adapted from (198)).	107
Figure IV.10: Charge-discharge profiles of V_2CT_x (A) and cycle life (B) from galvanostatic charge-discharge at different rates (adapted from (198)).	108
Figure IV.11: Nyquist plot from electrochemical impedance spectroscopy at different potentials (adapted from (198)).	109
Figure IV.12: X-ray diffraction patterns at different potentials. (*) Peak of unreacted V_2AlC (adapted from (198)).	110
Figure IV.13: Charge-discharge profiles Hard Carbon electrode.	111
Figure IV.14: Charge-discharge profiles at various rates (A). Change of the capacity during galvanostatic charge-discharge at different rates (B). Capacity vs cycle number (C). Details of the potential range of positive and negative electrodes at 1A/g (D). Capacities were calculated for the total mass of both positive and negative active material, taken with the weight ratio as 1:2 (adapted from (198)).	113
Figure V.1: Schematic showing the preparation of the sandwich-like MXene/Carbon nanotubes papers (A). Digital photographs showing a flexible and free-standing sandwich-like MXene/carbon nanotubes paper (B) and wrapping of latter around a 5-mm-diameter glass rod (C) (adapted from (164)).	118
Figure V.2: Schematic of MXene clay synthesis and electrode preparation (adapted from (163)).	119

Figure V.3: Scanning electron microscope images of rolled $\text{Ti}_3\text{C}_2\text{T}_x$ “clay” (A-B), $\text{d-Ti}_3\text{C}_2\text{T}_x$ (C-D) and CNT- $\text{Ti}_3\text{C}_2\text{T}_x$ (E-F) electrode films (adapted from (204))..... 123

Figure V.4: Electrochemical performance of multiwalled carbon nanotubes in 1M EMITFSI in acetonitrile; cyclic voltammograms at different scan rates (A) and summary of capacitance with the potential scan rate (B). 125

Figure V.5: Cyclic voltammograms of $\text{Ti}_3\text{C}_2\text{T}_x$ (A), $\text{d-Ti}_3\text{C}_2\text{T}_x$ (B) and CNT- $\text{Ti}_3\text{C}_2\text{T}_x$ (C) in 1M EMITFSI in acetonitrile electrolyte at different scan rates and summary of the change of capacitance with the potential scan rate (D). These measurements were done using a three-electrode Swagelok cell (adapted from (204))..... 126

Figure V.6: Nyquist plot at 0.5 V vs. Ag reference obtained using a two-electrode setup (adapted from (204))..... 127

Figure V.7: Galvanostatic charge-discharge curves of $\text{Ti}_3\text{C}_2\text{T}_x$ (A), $\text{d-Ti}_3\text{C}_2\text{T}_x$ (B) and CNT- $\text{Ti}_3\text{C}_2\text{T}_x$ (C) in 1M EMITFSI in acetonitrile electrolyte obtained at 1 A/g and the corresponding cycle life of those electrodes (D). These measurements were done using a three-electrode Swagelok cell (adapted from (204))..... 128

Figure V.8: In-situ X-ray diffraction patterns of CNT- $\text{Ti}_3\text{C}_2\text{T}_x$ at different potentials in the 5-50° 2θ range (A). Purple diamonds indicate peaks coming from the cell for *in situ* measurements. Inset (B) shows a zoom in the 5-7° 2θ range and cycle voltammograms recorded at 20 mV/s (C) (adapted from (204)). 130

Figure V.9: In-situ X-ray diffraction patterns of CNT- $\text{Ti}_3\text{C}_2\text{T}_x$ during cycling at 50 mV/s. Purple diamonds indicate peaks corresponding to the *in situ* cell. Inset: Schematic of the two-phase transformation..... 131

Figure V.10: Cyclic voltammograms of $\text{Ti}_3\text{C}_2\text{T}_x$ in different potential ranges at 20 mV/s (adapted from (204))..... 132

Figure V.11: Cyclic voltammetry of CNT- $\text{Ti}_3\text{C}_2\text{T}_x$ at 20 mV/s in 1 M solutions of EMIBF₄ (A) and TEABF₄ (B) in acetonitrile (adapted from (204))..... 133

Figure A.1: Cyclic voltammetry for $\text{Ti}_3\text{C}_2\text{T}_x$ in a K_2SO_4 , Al_2SO_4 and $\text{Al}(\text{NO}_3)_3$ electrolytes at a scan rate of 10 mV/s (adapted from (174))..... 143

Figure A.2: Electrochemical performance of the binder-free delaminated $\text{d-Ti}_3\text{C}_2$ electrodes: Cyclic voltammetry 1M KOH (A) 1M MgSO_4 (B) and 0.5M K_2SO_4 (C) electrolytes at a scan rate of 10 mV/s. Rate performance of the $\text{d-Ti}_3\text{C}_2$ (open symbols) vs. $\text{f-Ti}_3\text{C}_2$ (solid symbols) in KOH, MgSO_4 and NaOAc electrolytes (D) (adapted from (174)).144

Table List

List of Tables

Table 1: Comparison of lithium and sodium properties.	13
Table 2: Comparison of different carbon materials electrochemical performances (75).	20
Table 3: Properties of electrolytes (72, 92, 93).	24
Table 4: Synthesis condition of MXene.	50
Table 5: Energy-dispersive X-ray spectroscopy analysis of $Ti_3C_2T_x$ -based powder.	72
Table 6: Ionic conductivities of the various aqueous electrolytes used in electrochemical experiments (183, 184).	83
Table 7: Capacitance estimation. Calculation did not take into account the surface chemistry and considered the intercalation of a single sodium per MXene formula.	94

References

References

1. J. M. Tarascon, M. Armand, Issues and challenges facing rechargeable lithium batteries. *Nature* **414**, 359 (Nov, 2001).
2. J. R. Miller, P. Simon, Materials science - Electrochemical capacitors for energy management. *Science* **321**, 651 (Aug, 2008).
3. B. E. Conway, *Electrochemical supercapacitors: scientific fundamentals and technological applications*. (Springer Science & Business Media, 2013).
4. P. Simon, Y. Gogotsi, Materials for electrochemical capacitors. *Nat. Mater.* **7**, 845 (Nov, 2008).
5. M. Armand, J. M. Tarascon, Building better batteries. *Nature* **451**, 652 (02/07/print, 2008).
6. M. Winter, R. J. Brodd, What Are Batteries, Fuel Cells, and Supercapacitors? *Chemical Reviews* **104**, 4245 (2004/10/01, 2004).
7. A. S. Arico, P. Bruce, B. Scrosati, J. M. Tarascon, W. Van Schalkwijk, Nanostructured materials for advanced energy conversion and storage devices. *Nat. Mater.* **4**, 366 (May, 2005).
8. M. Naguib *et al.*, Two-Dimensional Nanocrystals Produced by Exfoliation of Ti_3AlC_2 . *Advanced Materials* **23**, 4248 (2011).
9. M. Naguib *et al.*, MXene: a promising transition metal carbide anode for lithium-ion batteries. *Electrochemistry Communications* **16**, 61 (3//, 2012).
10. A. Volta, On the Electricity Excited by the Mere Contact of Conducting Substances of Different Kinds. In a Letter from Mr. Alexander Volta, F. R. S. Professor of Natural Philosophy in the University of Pavia, to the Rt. Hon. Sir Joseph Banks, Bart. K. B. P. R. S. *Philosophical Transactions of the Royal Society of London* **90**, 403 (January 1, 1800, 1800).
11. K. Mizushima, P. C. Jones, P. J. Wiseman, J. B. Goodenough, Li_xCoO_2 ($0 < x < 1$): A new cathode material for batteries of high energy density. *Materials Research Bulletin* **15**, 783 (1980/06/01, 1980).
12. B. Di Pietro, M. Patriarca, B. Scrosati, On the use of rocking chair configurations for cyclable lithium organic electrolyte batteries. *Journal of Power Sources* **8**, 289 (1982/01/01, 1982).
13. H. I. Becker. (U.S. Patent 2800616 1957).
14. R. A. Rightmire. (U.S. Patent 3288641, 1966).
15. H. Helmholtz, Studien über elektrische Grenzschichten. *Annalen der Physik* **243**, 337 (1879).
16. V. Augustyn, P. Simon, B. Dunn, Pseudocapacitive oxide materials for high-rate electrochemical energy storage. *Energy & Environmental Science* **7**, 1597 (2014).
17. T. Brousse, D. Bélanger, J. W. Long, To Be or Not To Be Pseudocapacitive? *Journal of The Electrochemical Society* **162**, A5185 (January 1, 2015, 2015).
18. M. S. Whittingham, Chemistry of intercalation compounds: Metal guests in chalcogenide hosts. *Progress in Solid State Chemistry* **12**, 41 (1978/01/01, 1978).
19. M. R. Palacin, Recent advances in rechargeable battery materials: a chemist's perspective. *Chemical Society Reviews* **38**, 2565 (2009).
20. M. M. Doeff, Y. Ma, S. J. Visco, L. C. De Jonghe, Electrochemical Insertion of Sodium into Carbon. *Journal of The Electrochemical Society* **140**, L169 (December 1, 1993, 1993).
21. Y. P. Ma, M. M. Doeff, S. J. Visco, L. C. Dejonghe, Rechargeable Na_xCoO_2 and $Na_{15}Pb_4Na_xCoO_2$ polymer electrolyte cells. *Journal of the Electrochemical Society* **140**, 2726 (Oct, 1993).
22. J. B. Goodenough, K.-S. Park, The Li-Ion Rechargeable Battery: A Perspective. *Journal of the American Chemical Society* **135**, 1167 (2013/01/30, 2013).
23. D. Liu, G. Cao, Engineering nanostructured electrodes and fabrication of film electrodes for efficient lithium ion intercalation. *Energy & Environmental Science* **3**, 1218 (2010).
24. P. G. Bruce, B. Scrosati, J.-M. Tarascon, Nanomaterials for Rechargeable Lithium Batteries. *Angewandte Chemie International Edition* **47**, 2930 (2008).

25. F. Risacher, B. Fritz, Origin of Salts and Brine Evolution of Bolivian and Chilean Salars. *Aquat Geochem* **15**, 123 (2009/02/01, 2009).
26. A. Yaksic, J. E. Tilton, Using the cumulative availability curve to assess the threat of mineral depletion: The case of lithium. *Resources Policy* **34**, 185 (12//, 2009).
27. P. Ge, M. Foulletier, Electrochemical intercalation of sodium in graphite. *Solid State Ionics* **28**, 1172 (1988/09/01, 1988).
28. D. A. Stevens, J. R. Dahn, The Mechanisms of Lithium and Sodium Insertion in Carbon Materials. *Journal of The Electrochemical Society* **148**, A803 (August 1, 2001, 2001).
29. R. C. Asher, A lamellar compound of sodium and graphite. *Journal of Inorganic and Nuclear Chemistry* **10**, 238 (5//, 1959).
30. S.-W. Kim, D.-H. Seo, X. Ma, G. Ceder, K. Kang, Electrode Materials for Rechargeable Sodium-Ion Batteries: Potential Alternatives to Current Lithium-Ion Batteries. *Advanced Energy Materials* **2**, 710 (2012).
31. B. L. Ellis, L. F. Nazar, Sodium and sodium-ion energy storage batteries. *Current Opinion in Solid State and Materials Science* **16**, 168 (8//, 2012).
32. V. Palomares *et al.*, Na-ion batteries, recent advances and present challenges to become low cost energy storage systems. *Energy & Environmental Science* **5**, 5884 (Mar, 2012).
33. V. Palomares, M. Casas-Cabanas, E. Castillo-Martinez, M. H. Han, T. Rojo, Update on Na-based battery materials. A growing research path. *Energy & Environmental Science* **6**, 2312 (2013).
34. C. Masquelier, L. Croguennec, Polyanionic (Phosphates, Silicates, Sulfates) Frameworks as Electrode Materials for Rechargeable Li (or Na) Batteries. *Chemical Reviews* **113**, 6552 (2013/08/14, 2013).
35. C. Delmas, F. Cherkaoui, A. Nadiri, P. Hagenmuller, A nasicon-type phase as intercalation electrode - $\text{NaTi}_2(\text{PO}_4)_3$. *Materials Research Bulletin* **22**, 631 (May, 1987).
36. M. M. Doeff, M. Y. Peng, Y. P. Ma, L. C. Dejonghe, Orthorhombic Na_xMnO_2 as a cathode material for secondary sodium and lithium polymer batteries. *Journal of the Electrochemical Society* **141**, L145 (Nov, 1994).
37. J. Morales, J. Santos, J. L. Tirado, Electrochemical studies of lithium and sodium intercalation in MoSe_2 . *Solid State Ionics* **83**, 57 (Jan, 1996).
38. M. M. Doeff *et al.*, Thin-film solid-state sodium batteries for electric vehicles. *Electrochim. Acta* **40**, 2205 (Oct, 1995).
39. D. A. Stevens, J. R. Dahn, High Capacity Anode Materials for Rechargeable Sodium-Ion Batteries. *Journal of The Electrochemical Society* **147**, 1271 (April 1, 2000, 2000).
40. P. Thomas, D. Billaud, Electrochemical insertion of sodium into hard carbons. *Electrochim. Acta* **47**, 3303 (Aug, 2002).
41. S. Komaba *et al.*, Electrochemical Na Insertion and Solid Electrolyte Interphase for Hard-Carbon Electrodes and Application to Na-Ion Batteries. *Adv. Funct. Mater.* **21**, 3859 (Oct, 2011).
42. A. Ponrouch, A. R. Goñi, M. R. Palacín, High capacity hard carbon anodes for sodium ion batteries in additive free electrolyte. *Electrochemistry Communications* **27**, 85 (2//, 2013).
43. H. Xiong, M. D. Slater, M. Balasubramanian, C. S. Johnson, T. Rajh, Amorphous TiO_2 Nanotube Anode for Rechargeable Sodium Ion Batteries. *The Journal of Physical Chemistry Letters* **2**, 2560 (2011/10/20, 2011).
44. P. Senguttuvan, G. Rouse, V. Seznec, J. M. Tarascon, M. R. Palacin, $\text{Na}_2\text{Ti}_3\text{O}_7$: Lowest Voltage Ever Reported Oxide Insertion Electrode for Sodium Ion Batteries. *Chem. Mat.* **23**, 4109 (Sep, 2011).
45. C. Delmas, C. Fouassier, P. Hagenmuller, Structural classification and properties of the layered oxides. *Physica B+C* **99**, 81 (1//, 1980).
46. Y. Cao *et al.*, Reversible Sodium Ion Insertion in Single Crystalline Manganese Oxide Nanowires with Long Cycle Life. *Advanced Materials* **23**, 3155 (2011).

47. S. Komaba *et al.*, Fluorinated Ethylene Carbonate as Electrolyte Additive for Rechargeable Na Batteries. *ACS Appl. Mater. Interfaces* **3**, 4165 (Nov, 2011).
48. R. Berthelot, D. Carlier, C. Delmas, Electrochemical investigation of the P2–Na_xCoO₂ phase diagram. *Nat. Mater.* **10**, 74 (01//print, 2011).
49. X. H. Ma, H. L. Chen, G. Ceder, Electrochemical Properties of Monoclinic NaMnO₂. *Journal of the Electrochemical Society* **158**, A1307 (2011).
50. J. Billaud *et al.*, beta-NaMnO₂: A High-Performance Cathode for Sodium-Ion Batteries. *Journal of the American Chemical Society* **136**, 17243 (Dec, 2014).
51. H. Yoshida, N. Yabuuchi, S. Komaba, NaFe_{0.5}Co_{0.5}O₂ as high energy and power positive electrode for Na-ion batteries. *Electrochemistry Communications* **34**, 60 (Sep, 2013).
52. A. Mendiboure, C. Delmas, P. Hagenmuller, Electrochemical intercalation and deintercalation of Na_xMnO₂ bronzes. *J. Solid State Chem.* **57**, 323 (1985).
53. A. Bhide, K. Hariharan, Physicochemical properties of Na_xCoO₂ as a cathode for solid state sodium battery. *Solid State Ionics* **192**, 360 (Jun, 2011).
54. A. K. Padhi, K. S. Nanjundaswamy, J. B. Goodenough, Phospho-olivines as Positive-Electrode Materials for Rechargeable Lithium Batteries. *Journal of The Electrochemical Society* **144**, 1188 (April 1, 1997, 1997).
55. T. Shiratsuchi, S. Okada, J. Yamaki, T. Nishida, FePO₄ cathode properties for Li and Na secondary cells. *Journal of Power Sources* **159**, 268 (Sep, 2006).
56. S. M. Oh, S. T. Myung, J. Hassoun, B. Scrosati, Y. K. Sun, Reversible NaFePO₄ electrode for sodium secondary batteries. *Electrochemistry Communications* **22**, 149 (Aug, 2012).
57. P. Moreau, D. Guyomard, J. Gaubicher, F. Boucher, Structure and Stability of Sodium Intercalated Phases in Olivine FePO₄. *Chem. Mat.* **22**, 4126 (Jul, 2010).
58. K. Zaghib *et al.*, Characterization of Na-based phosphate as electrode materials for electrochemical cells. *Journal of Power Sources* **196**, 9612 (Nov, 2011).
59. J. Gopalakrishnan, K. K. Rangan, V₂(PO₄)₃ - a novel nasicon-type vanadium phosphate synthesized by oxidative deintercalation of sodium from Na₃V₂(PO₄)₃ *Chem. Mat.* **4**, 745 (Jul-Aug, 1992).
60. S. Patoux, G. Rousse, J. B. Leriche, C. Masquelier, Structural and electrochemical studies of rhombohedral Na₂TiM(PO₄)₍₃₎ and Li_{1.6}Na_{0.4}TiM(PO₄)₍₃₎ (M = Fe, Cr) phosphates. *Chem. Mat.* **15**, 2084 (May, 2003).
61. Z. L. Jian *et al.*, Carbon coated Na₃V₂(PO₄)₃ as novel electrode material for sodium ion batteries. *Electrochemistry Communications* **14**, 86 (Jan, 2012).
62. J. Kang *et al.*, High rate performance of a Na₃V₂(PO₄)₃/C cathode prepared by pyro-synthesis for sodium-ion batteries. *Journal of Materials Chemistry* **22**, 20857 (2012).
63. K. Saravanan, C. W. Mason, A. Rudola, K. H. Wong, P. Balaya, The First Report on Excellent Cycling Stability and Superior Rate Capability of Na₃V₂(PO₄)₃ for Sodium Ion Batteries. *Advanced Energy Materials* **3**, 444 (Apr, 2013).
64. H. Li, Y. Bai, F. Wu, Q. Ni, C. Wu, Na₃V₂(PO₄)₃/C nanorods as advanced cathode material for sodium ion batteries. *Solid State Ionics* **278**, 281 (Oct, 2015).
65. F. Sauvage, L. Laffont, J. M. Tarascon, E. Baudrin, Study of the insertion/deinsertion mechanism of sodium into Na_{0.44}MnO₂. *Inorg. Chem.* **46**, 3289 (Apr, 2007).
66. A. Ponrouch, E. Marchante, M. Courty, J. M. Tarascon, M. R. Palacin, In search of an optimized electrolyte for Na-ion batteries. *Energy & Environmental Science* **5**, 8572 (Sep, 2012).
67. C. Vidal-Abarca *et al.*, Improving the cyclability of sodium-ion cathodes by selection of electrolyte solvent. *Journal of Power Sources* **197**, 314 (1/1/, 2012).
68. R. Kotz, M. Carlen, Principles and applications of electrochemical capacitors. *Electrochim. Acta* **45**, 2483 (2000).
69. G. P. Wang, L. Zhang, J. J. Zhang, A review of electrode materials for electrochemical supercapacitors. *Chemical Society Reviews* **41**, 797 (2012).

70. D. L. Chapman, L.I. A contribution to the theory of electrocapillarity. *Philosophical Magazine Series 6* **25**, 475 (1913/04/01, 1913).
71. D. C. Grahame, The Electrical Double Layer and the Theory of Electrocapillarity. *Chemical Reviews* **41**, 441 (1947/12/01, 1947).
72. A. G. Pandolfo, A. F. Hollenkamp, Carbon properties and their role in supercapacitors. *Journal of Power Sources* **157**, 11 (Jun, 2006).
73. J. Gamby, P. L. Taberna, P. Simon, J. F. Fauvarque, M. Chesneau, Studies and characterisations of various activated carbons used for carbon/carbon supercapacitors. *Journal of Power Sources* **101**, 109 (Oct, 2001).
74. L. L. Zhang, X. S. Zhao, Carbon-based materials as supercapacitor electrodes. *Chemical Society Reviews* **38**, 2520 (2009).
75. W. Gu, G. Yushin, Review of nanostructured carbon materials for electrochemical capacitor applications: advantages and limitations of activated carbon, carbide-derived carbon, zeolite-templated carbon, carbon aerogels, carbon nanotubes, onion-like carbon, and graphene. *Wiley Interdisciplinary Reviews: Energy and Environment* **3**, 424 (2014).
76. N. Mohamad Nor, L. C. Lau, K. T. Lee, A. R. Mohamed, Synthesis of activated carbon from lignocellulosic biomass and its applications in air pollution control—a review. *Journal of Environmental Chemical Engineering* **1**, 658 (12//, 2013).
77. O. Barbieri, M. Hahn, A. Herzog, R. Kötz, Capacitance limits of high surface area activated carbons for double layer capacitors. *Carbon* **43**, 1303 (5//, 2005).
78. J. Chmiola, G. Yushin, R. Dash, Y. Gogotsi, Effect of pore size and surface area of carbide derived carbons on specific capacitance. *Journal of Power Sources* **158**, 765 (2006).
79. R. Dash *et al.*, Titanium carbide derived nanoporous carbon for energy-related applications. *Carbon* **44**, 2489 (2006).
80. J. Chmiola, C. Largeot, P. L. Taberna, P. Simon, Y. Gogotsi, Desolvation of Ions in Subnanometer Pores and Its Effect on Capacitance and Double-Layer Theory. *Angewandte Chemie* **120**, 3440 (2008).
81. B. E. Conway, V. Birss, J. Wojtowicz, The role and utilization of pseudocapacitance for energy storage by supercapacitors. *Journal of Power Sources* **66**, 1 (5//, 1997).
82. P. Simon, Y. Gogotsi, B. Dunn, Where Do Batteries End and Supercapacitors Begin? *Science* **343**, 1210 (Mar, 2014).
83. B. E. Conway, E. Gileadi, Kinetic theory of pseudo-capacitance and electrode reactions at appreciable surface coverage. *Transactions of the Faraday Society* **58**, 2493 (1962).
84. W. Sugimoto, H. Iwata, K. Yokoshima, Y. Murakami, Y. Takasu, Proton and Electron Conductivity in Hydrrous Ruthenium Oxides Evaluated by Electrochemical Impedance Spectroscopy: The Origin of Large Capacitance. *The Journal of Physical Chemistry B* **109**, 7330 (2005/04/01, 2005).
85. W. Sugimoto, T. Kizaki, K. Yokoshima, Y. Murakami, Y. Takasu, Evaluation of the pseudocapacitance in RuO₂ with a RuO₂/GC thin film electrode. *Electrochim. Acta* **49**, 313 (1/15/, 2004).
86. J. M. Miller, B. Dunn, Morphology and electrochemistry of ruthenium/carbon aerogel nanostructures. *Langmuir* **15**, 799 (Feb, 1999).
87. W. Sugimoto, H. Iwata, Y. Yasunaga, Y. Murakami, Y. Takasu, Preparation of ruthenic acid nanosheets and utilization of its interlayer surface for electrochemical energy storage. *Angew. Chem.-Int. Edit.* **42**, 4092 (2003).
88. B. E. Conway, Transition from supercapacitor to battery behavior in electrochemical energy-storage. *Journal of the Electrochemical Society* **138**, 1539 (Jun, 1991).
89. J. P. Zheng, P. J. Cygan, T. R. Jow, Hydrrous Ruthenium Oxide as an Electrode Material for Electrochemical Capacitors. *Journal of The Electrochemical Society* **142**, 2699 (August 1, 1995, 1995).
90. N. L. Wu, Nanocrystalline oxide supercapacitors. *Mater. Chem. Phys.* **75**, 6 (Apr, 2002).

91. X.-h. Yang, Y.-g. Wang, H.-m. Xiong, Y.-y. Xia, Interfacial synthesis of porous MnO₂ and its application in electrochemical capacitor. *Electrochim. Acta* **53**, 752 (2007).
92. M. Galiński, A. Lewandowski, I. Stępnia, Ionic liquids as electrolytes. *Electrochim. Acta* **51**, 5567 (8/15/, 2006).
93. M. Ue, M. Takeda, M. Takehara, S. Mori, Electrochemical Properties of Quaternary Ammonium Salts for Electrochemical Capacitors. *Journal of The Electrochemical Society* **144**, 2684 (August 1, 1997, 1997).
94. E. Frackowiak, G. Lota, J. Pernak, Room-temperature phosphonium ionic liquids for supercapacitor application. *Appl. Phys. Lett.* **86**, (Apr, 2005).
95. J. R. Miller, Proceedings of the Fifth International Seminar on Double-Layer Capacitors and Similar Energy Storage Devices. S. P. Wolsky, N. Marincic, eds., *Florida Educational Seminars, Boca Raton, Fla (1995)*. (1995).
96. K. Naoi, P. Simon, New Materials and New Configurations for Advanced Electrochemical Capacitors. *Journal of the Electrochemical Society*, 34 (2008).
97. K. Naoi, S. Ishimoto, J. Miyamoto, W. Naoi, Second generation 'nanohybrid supercapacitor': Evolution of capacitive energy storage devices. *Energy & Environmental Science* **5**, 9363 (Nov, 2012).
98. J. H. Park, O. O. Park, K. H. Shin, C. S. Jin, J. H. Kim, An electrochemical capacitor based on a Ni(OH)₂/activated carbon composite electrode. *Electrochemical and Solid-State Letters* **5**, H7 (2002).
99. AxionPower, <http://www.axionpower.com/>.
100. T. Brousse *et al.*, Long-term cycling behavior of asymmetric activated carbon/MnO₂ aqueous electrochemical supercapacitor. *Journal of Power Sources* **173**, 633 (11/8/, 2007).
101. G. G. Amatucci, F. Badway, A. Du Pasquier, T. Zheng, An asymmetric hybrid nonaqueous energy storage cell. *Journal of the Electrochemical Society* **148**, A930 (Aug, 2001).
102. A. Du Pasquier, I. Plitz, S. Menocal, G. Amatucci, A comparative study of Li-ion battery, supercapacitor and nonaqueous asymmetric hybrid devices for automotive applications. *Journal of Power Sources* **115**, 171 (3/27/, 2003).
103. K. Naoi, S. Ishimoto, N. Ogihara, Y. Nakagawa, S. Hatta, Encapsulation of Nanodot Ruthenium Oxide into KB for Electrochemical Capacitors. *Journal of The Electrochemical Society* **156**, A52 (January 1, 2009, 2009).
104. K. Naoi, S. Ishimoto, Y. Isobe, S. Aoyagi, High-rate nano-crystalline Li₄Ti₅O₁₂ attached on carbon nano-fibers for hybrid supercapacitors. *Journal of Power Sources* **195**, 6250 (9/15/, 2010).
105. V. Khomenko, E. Raymundo-Piñero, F. Béguin, High-energy density graphite/AC capacitor in organic electrolyte. *Journal of Power Sources* **177**, 643 (3/1/, 2008).
106. JMEnergy, <http://jmenergy.co.jp/en/profile.html>.
107. R. Ding, L. Qi, H. Wang, An investigation of spinel NiCo₂O₄ as anode for Na-ion capacitors. *Electrochim. Acta* **114**, 726 (12/30/, 2013).
108. K. Kuratani *et al.*, Na-ion capacitor using sodium pre-doped hard carbon and activated carbon. *Electrochim. Acta* **76**, 320 (8/1/, 2012).
109. J. Yin, L. Qi, H. Wang, Sodium Titanate Nanotubes as Negative Electrode Materials for Sodium-Ion Capacitors. *ACS Appl. Mater. Interfaces* **4**, 2762 (2012/05/23, 2012).
110. Z. Chen *et al.*, High-Performance Sodium-Ion Pseudocapacitors Based on Hierarchically Porous Nanowire Composites. *ACS Nano* **6**, 4319 (2012/05/22, 2012).
111. Z. Yu, L. Tetard, L. Zhai, J. Thomas, Supercapacitor electrode materials: nanostructures from 0 to 3 dimensions. *Energy & Environmental Science* **8**, 702 (2015).
112. A. K. Geim, K. S. Novoselov, The rise of graphene. *Nat. Mater.* **6**, 183 (03//print, 2007).
113. K. S. Novoselov *et al.*, Electric Field Effect in Atomically Thin Carbon Films. *Science* **306**, 666 (October 22, 2004, 2004).
114. J.-H. Chen, C. Jang, S. Xiao, M. Ishigami, M. S. Fuhrer, Intrinsic and extrinsic performance limits of graphene devices on SiO₂. *Nat Nano* **3**, 206 (04//print, 2008).

115. A. A. Balandin *et al.*, Superior Thermal Conductivity of Single-Layer Graphene. *Nano Letters* **8**, 902 (2008/03/01, 2008).
116. M. D. Stoller, S. Park, Y. Zhu, J. An, R. S. Ruoff, Graphene-Based Ultracapacitors. *Nano Letters* **8**, 3498 (2008/10/08, 2008).
117. W. Hong, Y. Xu, G. Lu, C. Li, G. Shi, Transparent graphene/PEDOT–PSS composite films as counter electrodes of dye-sensitized solar cells. *Electrochemistry Communications* **10**, 1555 (10//, 2008).
118. J. Yan *et al.*, Preparation of a graphene nanosheet/polyaniline composite with high specific capacitance. *Carbon* **48**, 487 (2//, 2010).
119. S. Chen, J. Zhu, X. Wu, Q. Han, X. Wang, Graphene Oxide–MnO₂ Nanocomposites for Supercapacitors. *ACS Nano* **4**, 2822 (2010/05/25, 2010).
120. Y. Zhu *et al.*, Carbon-Based Supercapacitors Produced by Activation of Graphene. *Science* **332**, 1537 (June 24, 2011, 2011).
121. M. F. El-Kady, V. Strong, S. Dubin, R. B. Kaner, Laser Scribing of High-Performance and Flexible Graphene-Based Electrochemical Capacitors. *Science* **335**, 1326 (March 16, 2012, 2012).
122. Y. Sun, Q. Wu, G. Shi, Graphene based new energy materials. *Energy & Environmental Science* **4**, 1113 (2011).
123. X. Yang, C. Cheng, Y. Wang, L. Qiu, D. Li, Liquid-Mediated Dense Integration of Graphene Materials for Compact Capacitive Energy Storage. *Science* **341**, 534 (2013).
124. E. Yoo *et al.*, Large Reversible Li Storage of Graphene Nanosheet Families for Use in Rechargeable Lithium Ion Batteries. *Nano Letters* **8**, 2277 (2008/08/01, 2008).
125. P. Guo, H. Song, X. Chen, Hollow graphene oxide spheres self-assembled by W/O emulsion. *Journal of Materials Chemistry* **20**, 4867 (2010).
126. D. S. Su, R. Schlögl, Nanostructured Carbon and Carbon Nanocomposites for Electrochemical Energy Storage Applications. *ChemSusChem* **3**, 136 (2010).
127. D. Pan *et al.*, Li Storage Properties of Disordered Graphene Nanosheets. *Chem. Mat.* **21**, 3136 (2009/07/28, 2009).
128. P. Lian *et al.*, Large reversible capacity of high quality graphene sheets as an anode material for lithium-ion batteries. *Electrochim. Acta* **55**, 3909 (4/30/, 2010).
129. P. Guo, H. Song, X. Chen, Electrochemical performance of graphene nanosheets as anode material for lithium-ion batteries. *Electrochemistry Communications* **11**, 1320 (6//, 2009).
130. E. Pollak *et al.*, The Interaction of Li⁺ with Single-Layer and Few-Layer Graphene. *Nano Letters* **10**, 3386 (2010/09/08, 2010).
131. C. Uthaisar, V. Barone, Edge Effects on the Characteristics of Li Diffusion in Graphene. *Nano Letters* **10**, 2838 (2010/08/11, 2010).
132. J. Yan *et al.*, Fast and reversible surface redox reaction of graphene–MnO₂ composites as supercapacitor electrodes. *Carbon* **48**, 3825 (11//, 2010).
133. S. Chen, J. Zhu, X. Wang, One-Step Synthesis of Graphene–Cobalt Hydroxide Nanocomposites and Their Electrochemical Properties. *The Journal of Physical Chemistry C* **114**, 11829 (2010/07/15, 2010).
134. H. Wang, H. S. Casalongue, Y. Liang, H. Dai, Ni(OH)₂ Nanoplates Grown on Graphene as Advanced Electrochemical Pseudocapacitor Materials. *Journal of the American Chemical Society* **132**, 7472 (2010/06/02, 2010).
135. D. Wang *et al.*, Ternary Self-Assembly of Ordered Metal Oxide–Graphene Nanocomposites for Electrochemical Energy Storage. *ACS Nano* **4**, 1587 (2010/03/23, 2010).
136. S.-M. Paek, E. Yoo, I. Honma, Enhanced Cyclic Performance and Lithium Storage Capacity of SnO₂/Graphene Nanoporous Electrodes with Three-Dimensionally Delaminated Flexible Structure. *Nano Letters* **9**, 72 (2009/01/14, 2009).
137. L.-S. Zhang *et al.*, Mono dispersed SnO₂ nanoparticles on both sides of single layer graphene sheets as anode materials in Li-ion batteries. *Journal of Materials Chemistry* **20**, 5462 (2010).

138. J. Yao, X. Shen, B. Wang, H. Liu, G. Wang, In situ chemical synthesis of SnO₂-graphene nanocomposite as anode materials for lithium-ion batteries. *Electrochemistry Communications* **11**, 1849 (10//, 2009).
139. L. Wang *et al.*, A facile method of preparing mixed conducting LiFePO₄/graphene composites for lithium-ion batteries. *Solid State Ionics* **181**, 1685 (12/13/, 2010).
140. D. Wang *et al.*, Self-Assembled TiO₂-Graphene Hybrid Nanostructures for Enhanced Li-Ion Insertion. *ACS Nano* **3**, 907 (2009/04/28, 2009).
141. N. Zhu *et al.*, Graphene as a conductive additive to enhance the high-rate capabilities of electrospun Li₄Ti₅O₁₂ for lithium-ion batteries. *Electrochim. Acta* **55**, 5813 (8/1/, 2010).
142. Z.-S. Wu *et al.*, Graphene Anchored with Co₃O₄ Nanoparticles as Anode of Lithium Ion Batteries with Enhanced Reversible Capacity and Cyclic Performance. *ACS Nano* **4**, 3187 (2010/06/22, 2010).
143. S. Yang *et al.*, Fabrication of Cobalt and Cobalt Oxide/Graphene Composites: Towards High-Performance Anode Materials for Lithium Ion Batteries. *ChemSusChem* **3**, 236 (2010).
144. F.-Y. Su *et al.*, Flexible and planar graphene conductive additives for lithium-ion batteries. *Journal of Materials Chemistry* **20**, 9644 (2010).
145. Y. Ding *et al.*, Preparation of nano-structured LiFePO₄/graphene composites by co-precipitation method. *Electrochemistry Communications* **12**, 10 (1//, 2010).
146. G. Wang *et al.*, Sn/graphene nanocomposite with 3D architecture for enhanced reversible lithium storage in lithium ion batteries. *Journal of Materials Chemistry* **19**, 8378 (2009).
147. J. K. Lee, K. B. Smith, C. M. Hayner, H. H. Kung, Silicon nanoparticles-graphene paper composites for Li ion battery anodes. *Chemical Communications (Cambridge, United Kingdom)* **46**, 2025 (2010).
148. S.-L. Chou *et al.*, Enhanced reversible lithium storage in a nanosize silicon/graphene composite. *Electrochemistry Communications* **12**, 303 (2//, 2010).
149. X. Xu, W. Liu, Y. Kim, J. Cho, Nanostructured transition metal sulfides for lithium ion batteries: Progress and challenges. *Nano Today* **9**, 604 (10//, 2014).
150. H. Wang, H. B. Feng, J. H. Li, Graphene and Graphene-like Layered Transition Metal Dichalcogenides in Energy Conversion and Storage. *Small* **10**, 2165 (Jun, 2014).
151. J. Xiao *et al.*, Electrochemically Induced High Capacity Displacement Reaction of PEO/MoS₂/Graphene Nanocomposites with Lithium. *Adv. Funct. Mater.* **21**, 2840 (2011).
152. T. Stephenson, Z. Li, B. Olsen, D. Mitlin, Lithium ion battery applications of molybdenum disulfide (MoS₂) nanocomposites. *Energy & Environmental Science* **7**, 209 (2014).
153. T. Brousse, S. M. Lee, L. Pasquereau, D. Defives, D. M. Schleich, Composite negative electrodes for lithium ion cells. *Solid State Ionics* **113**, 51 (Dec, 1998).
154. Y. Kim, J. B. Goodenough, Lithium Insertion into Transition-Metal Monosulfides: Tuning the Position of the Metal 4s Band. *The Journal of Physical Chemistry C* **112**, 15060 (2008/09/25, 2008).
155. J. Feng *et al.*, Metallic Few-Layered VS₂ Ultrathin Nanosheets: High Two-Dimensional Conductivity for In-Plane Supercapacitors. *Journal of the American Chemical Society* **133**, 17832 (2011/11/09, 2011).
156. G. A. Muller, J. B. Cook, H.-S. Kim, S. H. Tolbert, B. Dunn, High Performance Pseudocapacitor Based on 2D Layered Metal Chalcogenide Nanocrystals. *Nano Letters* **15**, 1911 (2015/03/11, 2015).
157. M. Naguib *et al.*, Synthesis of a new nanocrystalline titanium aluminum fluoride phase by reaction of Ti₂AlC with hydrofluoric acid. *RSC Advances* **1**, 1493 (2011).
158. M. Naguib *et al.*, Two-Dimensional Transition Metal Carbides. *ACS Nano* **6**, 1322 (2012/02/28, 2012).
159. M. W. Barsoum, The M_{N+1}AX_N phases: A new class of solids: Thermodynamically stable nanolaminates. *Progress in Solid State Chemistry* **28**, 201 (2000).
160. O. Mashtalir *et al.*, Intercalation and delamination of layered carbides and carbonitrides. *Nat Commun* **4**, 1716 (04/16/online, 2013).

161. J. Come *et al.*, A Non-Aqueous Asymmetric Cell with a Ti₂C-Based Two-Dimensional Negative Electrode. *Journal of the Electrochemical Society* **159**, A1368 (2012).
162. Q. Tang, Z. Zhou, P. Shen, Are MXenes Promising Anode Materials for Li Ion Batteries? Computational Studies on Electronic Properties and Li Storage Capability of Ti₃C₂ and Ti₃C₂X₂ (X = F, OH) Monolayer. *Journal of the American Chemical Society* **134**, 16909 (2012/10/10, 2012).
163. M. Ghidui, M. R. Lukatskaya, M.-Q. Zhao, Y. Gogotsi, M. W. Barsoum, Conductive two-dimensional titanium carbide /'clay/' with high volumetric capacitance. *Nature* **516**, 78 (12/04/print, 2014).
164. M.-Q. Zhao *et al.*, Flexible MXene/Carbon Nanotube Composite Paper with High Volumetric Capacitance. *Advanced Materials* **27**, 339 (2015).
165. J. M. Tarascon *et al.*, First example of monodispersed (Mo₃Se₃)_{1∞} clusters. *J. Solid State Chem.* **58**, 290 (1985/07/15, 1985).
166. S. Goriparti *et al.*, Review on recent progress of nanostructured anode materials for Li-ion batteries. *Journal of Power Sources* **257**, 421 (7/1/, 2014).
167. M. Winter, J. O. Besenhard, M. E. Spahr, P. Novák, Insertion Electrode Materials for Rechargeable Lithium Batteries. *Advanced Materials* **10**, 725 (1998).
168. F. Nobili, F. Croce, B. Scrosati, R. Marassi, Electronic and Electrochemical Properties of Li_xNi_{1-y}Co_yO₂ Cathodes Studied by Impedance Spectroscopy. *Chem. Mat.* **13**, 1642 (2001/05/01, 2001).
169. W. Van Schalkwijk, B. Scrosati, *Advances in lithium-ion batteries*. (Springer Science & Business Media, 2002).
170. D. Aurbach, Review of selected electrode-solution interactions which determine the performance of Li and Li ion batteries. *Journal of Power Sources* **89**, 206 (Aug, 2000).
171. R. de Levie, On porous electrodes in electrolyte solutions. *Electrochim. Acta* **8**, 751 (1963/10/01, 1963).
172. J.-F. Fauvarque, P. Simon, Principles of Electrochemistry and Electrochemical Methods. *Carbons for Electrochemical Energy Storage and Conversion Systems*, RC Press/Taylor and Francis, 1 (2009).
173. P. L. Taberna, P. Simon, J. F. Fauvarque, Electrochemical characteristics and impedance spectroscopy studies of carbon-carbon supercapacitors. *Journal of the Electrochemical Society* **150**, A292 (Mar, 2003).
174. M. R. Lukatskaya *et al.*, Cation Intercalation and High Volumetric Capacitance of Two-Dimensional Titanium Carbide. *Science* **341**, 1502 (Sep, 2013).
175. V. Augustyn *et al.*, High-rate electrochemical energy storage through Li⁺ intercalation pseudocapacitance. *Nat. Mater.* **12**, 518 (06//print, 2013).
176. Z. Sun *et al.*, Microstructure and supercapacitive properties of buserite-type manganese oxide with a large basal spacing. *Journal of Power Sources* **216**, 425 (10/15/, 2012).
177. Y. Xie *et al.*, Role of Surface Structure on Li-Ion Energy Storage Capacity of Two-Dimensional Transition-Metal Carbides. *Journal of the American Chemical Society* **136**, 6385 (2014/04/30, 2014).
178. L. M. Viculis, J. J. Mack, O. M. Mayer, H. T. Hahn, R. B. Kaner, Intercalation and exfoliation routes to graphite nanoplatelets. *Journal of Materials Chemistry* **15**, 974 (2005).
179. Y. Hernandez *et al.*, High-yield production of graphene by liquid-phase exfoliation of graphite. *Nat Nano* **3**, 563 (09//print, 2008).
180. Y. Dall'Agnese *et al.*, High capacitance of surface-modified 2D titanium carbide in acidic electrolyte. *Electrochemistry Communications* **48**, 118 (11//, 2014).
181. P. W. Ruch *et al.*, A dilatometric and small-angle X-ray scattering study of the electrochemical activation of mesophase pitch-derived carbon in non-aqueous electrolyte solution. *Carbon* **48**, 1880 (2010).
182. M. R. Lukatskaya *et al.*, Probing the Mechanism of High Capacitance in 2D Titanium Carbide Using In Situ X-Ray Absorption Spectroscopy. *Advanced Energy Materials* **5**, n/a (2015).

183. R. C. Weast, CRC Handbook of Chemistry, and Physics, 70th Edition CRC Press, Boca Raton, FL, , D (1989).
184. A. V. Wolf, Aqueous Solutions and Body Fluids. Harper and Row, New York, (1966).
185. O. Ghodbane, F. Ataherian, N. L. Wu, F. Favier, In situ crystallographic investigations of charge storage mechanisms in MnO₂-based electrochemical capacitors. *Journal of Power Sources* **206**, 454 (May, 2012).
186. Y. Xie *et al.*, Prediction and Characterization of MXene Nanosheet Anodes for Non-Lithium-Ion Batteries. *ACS Nano* **8**, 9606 (2014/09/23, 2014).
187. S. Murali *et al.*, Volumetric capacitance of compressed activated microwave-expanded graphite oxide (a-MEGO) electrodes. *Nano Energy* **2**, 764 (9//, 2013).
188. J. Chmiola, C. Largeot, P.-L. Taberna, P. Simon, Y. Gogotsi, Monolithic Carbide-Derived Carbon Films for Micro-Supercapacitors. *Science* **328**, 480 (2010).
189. M. Heon *et al.*, Continuous carbide-derived carbon films with high volumetric capacitance. *Energy & Environmental Science* **4**, 135 (2011).
190. X. Lang, A. Hirata, T. Fujita, M. Chen, Nanoporous metal/oxide hybrid electrodes for electrochemical supercapacitors. *Nat Nano* **6**, 232 (04//print, 2011).
191. X. Zhao *et al.*, Incorporation of Manganese Dioxide within Ultraporous Activated Graphene for High-Performance Electrochemical Capacitors. *ACS Nano* **6**, 5404 (2012/06/26, 2012).
192. J. R. Miller, Valuing Reversible Energy Storage. *Science* **335**, 1312 (2012).
193. M. Naguib *et al.*, New Two-Dimensional Niobium and Vanadium Carbides as Promising Materials for Li-Ion Batteries. *Journal of the American Chemical Society* **135**, 15966 (2013/10/30, 2013).
194. M. M. Hantel, R. Nesper, A. Wokaun, R. Kötz, In-situ XRD and dilatometry investigation of the formation of pillared graphene via electrochemical activation of partially reduced graphite oxide. *Electrochim. Acta* **134**, 459 (7/10/, 2014).
195. Y. Dong *et al.*, Inhibiting effect of Na⁺ pre-intercalation in MoO₃ nanobelts with enhanced electrochemical performance. *Nano Energy* **15**, 145 (7//, 2015).
196. X. Wang *et al.*, Pseudocapacitance of MXene nanosheets for high-power sodium-ion hybrid capacitors. *Nat Commun* **6**, (04/02/online, 2015).
197. M. R. Lukatskaya *et al.*, Probing the Mechanism of High Capacitance in 2D Titanium Carbide Using In Situ X-Ray Absorption Spectroscopy. *Adv. Energy Mater.*, n/a (2015).
198. Y. Dall'Agnese, P.-L. Taberna, Y. Gogotsi, P. Simon, Two-Dimensional Vanadium Carbide (MXene) as Positive Electrode for Sodium-Ion Capacitors. *The Journal of Physical Chemistry Letters* **6**, 2305 (2015).
199. Y. Liu, W. Wang, Y. Ying, Y. Wang, X. Peng, Binder-free layered Ti₃C₂/CNTs nanocomposite anodes with enhanced capacity and long-cycle life for lithium-ion batteries. *Dalton Transactions* **44**, 7123 (2015).
200. Z. Ling *et al.*, Flexible and conductive MXene films and nanocomposites with high capacitance. *Proceedings of the National Academy of Sciences* **111**, 16676 (November 25, 2014, 2014).
201. Q. Cheng *et al.*, Graphene and carbon nanotube composite electrodes for supercapacitors with ultra-high energy density. *Physical Chemistry Chemical Physics* **13**, 17615 (2011).
202. X.-M. Liu *et al.*, Carbon nanotube (CNT)-based composites as electrode material for rechargeable Li-ion batteries: A review. *Composites Science and Technology* **72**, 121 (1/18/, 2012).
203. B. J. Landi, M. J. Ganter, C. D. Cress, R. A. DiLeo, R. P. Raffaele, Carbon nanotubes for lithium ion batteries. *Energy & Environmental Science* **2**, 638 (2009).
204. Y. Dall'Agnese, P. Rozier, P.-L. Taberna, Y. Gogotsi, P. Simon, Capacitance of two-dimensional titanium carbide (MXene) and MXene/carbon nanotube composites in organic electrolytes. *Journal of Power Sources* **306**, 510 (2016).
205. R. Lin *et al.*, Solvent effect on the ion adsorption from ionic liquid electrolyte into sub-nanometer carbon pores. *Electrochim. Acta* **54**, 7025 (11/30/, 2009).

206. M. D. Levi *et al.*, Solving the Capacitive Paradox of 2D MXene using Electrochemical Quartz-Crystal Admittance and In Situ Electronic Conductance Measurements. *Advanced Energy Materials* **5**, 1400815 (2015).
207. J. M. Griffin *et al.*, In situ NMR and electrochemical quartz crystal microbalance techniques reveal the structure of the electrical double layer in supercapacitors. *Nat Mater* **14**, 812 (2015).

Résumé de Thèse

Résumé de Thèse

Introduction générale

Les sources d'énergies majoritairement utilisées de nos jours sont le pétrole, le gaz, le charbon et le nucléaire, ce qui entraîne de nombreuses problématiques tant du point de vue économique (épuiement des ressources) qu'écologique (pollution et réchauffement climatique). La mise en place de sources d'énergies renouvelables, telle que les énergies solaire et éolienne, nécessite d'améliorer les technologies permettant de stocker cette énergie intermittente pour la distribuer de façon continue à grande échelle (1, 2). Le développement des systèmes de stockage de l'énergie est aussi motivé par la généralisation des dispositifs électroniques portables, tels que les smartphones et les ordinateurs, qui consomment de plus en plus d'énergie. Les systèmes de stockage électrochimiques tels que les batteries et les supercondensateurs sont des solutions énergétiques qui offrent l'avantage d'émissions nulles de dioxyde de carbone, de rendements énergétiques élevés ainsi que des tailles contrôlables (3-5).

La demande en énergie et puissance ne cesse d'augmenter. Les batteries et supercondensateurs commercialisés actuellement ne possèdent pas les caractéristiques techniques adaptées (densité d'énergie et/ou de puissance) pour subvenir aux besoins énergétiques des années futures (4-6). Ces dernières années, il a été mis en avant qu'une plus grande densité d'énergie peut être acquise par les supercondensateurs lorsqu'ils utilisent des matériaux pseudocapacitifs, c'est-à-dire lorsqu'ils stockent l'énergie grâce à des réactions d'oxydo-réductions rapides de surface, contrairement au stockage de charge électrostatique comme c'est le cas pour les supercondensateurs commercialisés à base de carbone.

L'objectif de cette thèse est d'étudier les performances électrochimiques d'une nouvelle famille de matériaux pseudocapacitifs, appelée MXène, afin d'obtenir de hautes densités

d'énergie et de puissance. Les MXènes sont une famille de matériaux carbonés métalliques bidimensionnels qui ont démontré des résultats prometteurs dans le domaine des batteries lithium-ion (7, 8). Ces matériaux possèdent une variété de compositions chimiques (non limité au carbone) et sont composés de métaux de transition qui peuvent participer à des réactions d'oxydo-réductions permettant d'obtenir de plus grandes densités d'énergie. Le manuscrit est structuré en cinq chapitres qui décrivent de manière détaillée les résultats présentés.

Chapitre I : Etude bibliographique

Le premier chapitre de cette thèse présente une étude bibliographique qui décrit les principes de fonctionnement des supercondensateurs et présente l'état de l'art des MXènes.

Les différents systèmes de stockage de l'énergie sont généralement complémentaires les uns des autres, comme on peut le voir lorsque l'on place les systèmes sur le diagramme de Ragone (Figure 1). Les batteries sont caractérisées par des charges lentes de l'ordre de plusieurs heures - ce qui leur confère une grande densité d'énergie - tandis que les condensateurs délivrent de grandes puissances et de faibles énergies en quelques millisecondes ; les supercondensateurs sont des systèmes aux performances intermédiaires entre les deux.

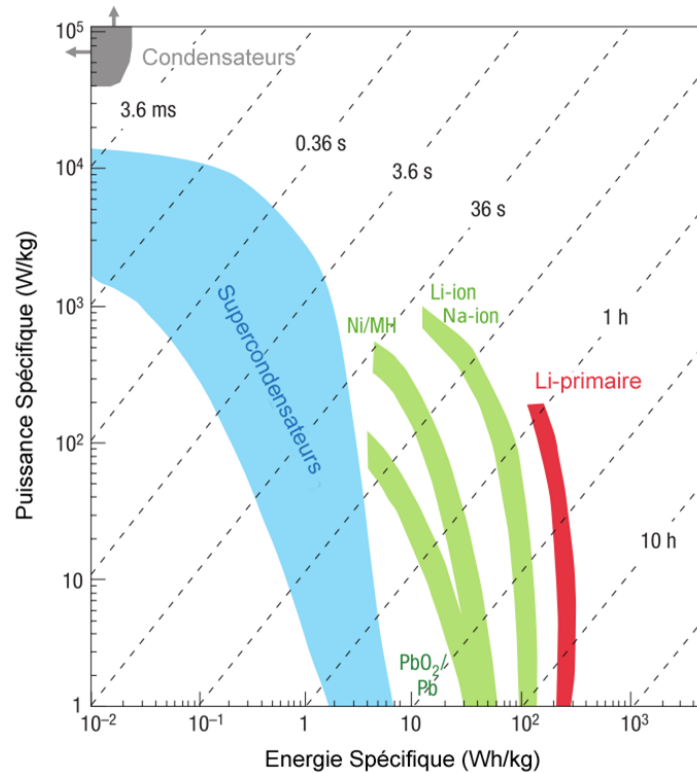


Figure I.1. Diagramme de Ragone (puissance vs. énergie spécifique) (adaptée de (4)).

I. Supercondensateurs

Il existe plusieurs types de supercondensateurs, distincts par la nature des matériaux utilisés, mais tous possèdent de grandes puissances, d'excellentes durées de vie et leurs signatures électrochimiques sont similaires. On distingue deux mécanismes de stockage de charge : le stockage capacitif avec les supercondensateurs à base de carbone de grande surface développée qui fait intervenir le phénomène d'interactions électrostatiques dans la double couche électrochimique, et le stockage faradique qui met en jeu des réactions d'oxydoréductions rapides de surface dans les supercondensateurs pseudo-capacitifs (3, 4, 9). La réponse électrochimique d'un supercondensateur idéal est représentée Figure I.2. A la différence des batteries, le mécanisme de stockage des charges ne se produit pas à un potentiel précis mais sur toute la plage de potentiel ; c'est pourquoi il n'y a pas de pic présent lors de la voltampérométrie cyclique, ni de plateau lors des tests galvanostatiques.

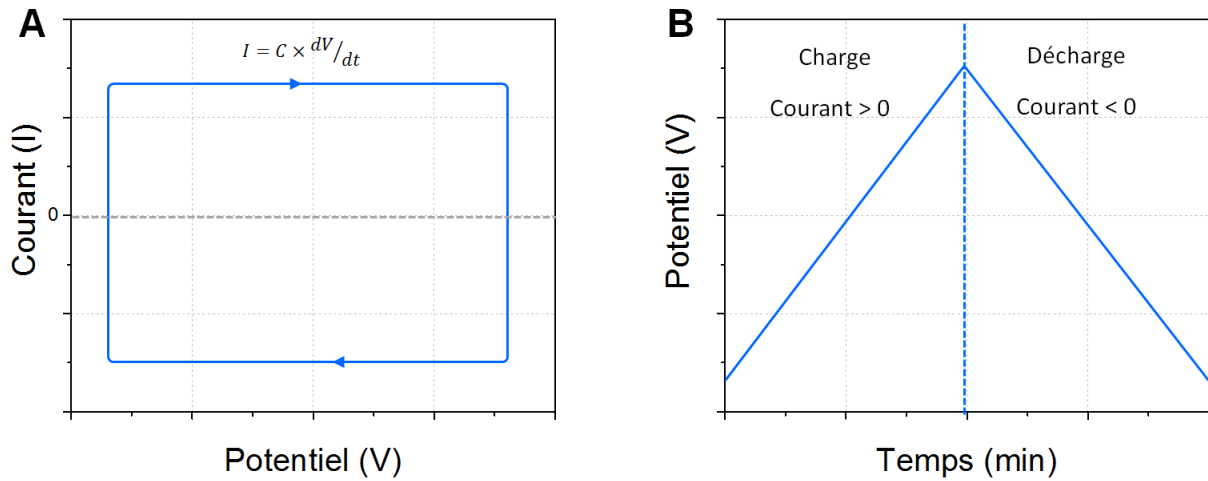


Figure I.2. Comportement électrochimique d'un supercondensateur au cours d'une voltampérométrie cyclique (A) et d'un cycle galvanostatique (B).

Les supercondensateurs à double couche électrochimique :

Dans les supercondensateurs à double couche électrochimique, le mécanisme de stockage des charges est purement électrostatique. Le comportement capacitif du matériau est causé par la séparation électrostatique des charges à l'interface électrode/ électrolyte qui forme la double couche électrochimique lorsqu'un potentiel est appliqué entre les deux électrodes, comme décrit schématiquement dans la Figure I.3.

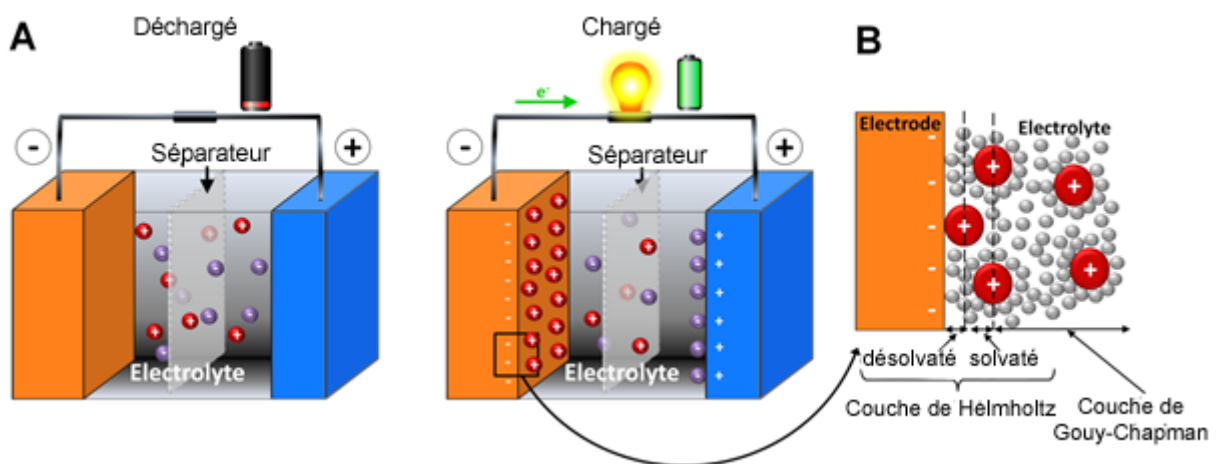


Figure I.3. Schéma représentant le fonctionnement d'un supercondensateur à double couche électrochimique (A) et le modèle de Stern de la double couche (B).

Les matériaux d'électrodes utilisés doivent être composés de matériaux actifs poreux de très grandes surfaces spécifiques, être conducteurs électriques et chimiquement stables. Les différentes formes du carbone, tels les nanotubes de carbone, le graphène et les charbons actifs sont de bons candidats (10-13). Les charbons actifs sont les plus fréquemment utilisés du fait de leurs bonnes propriétés de conductivité électrique, leurs faibles coûts et des capacités de 300 F/g. Ils sont synthétisés à partir de matériaux naturels peu coûteux (coquille de noix de coco, bois, charbon) par une étape de carbonisation puis une étape d'activation qui crée la porosité du matériau et augmente la surface spécifique jusqu'à 3000 m²/g (oxydation dans la vapeur d'eau ou réaction avec des bases) (14).

Les supercondensateurs pseudo-capacitifs :

Dans un supercondensateur pseudo-capacitif, le mécanisme de charge est une succession de réactions faradiques réversibles et rapides qui peuvent être distinguées des réactions faradiques des batteries car le temps de charge est plus rapide et la quantité de charge est linéaire au potentiel (15-17). La présence de réaction d'oxydoréduction a pour effet d'obtenir de plus hautes valeurs de capacité et d'énergie comparé aux supercondensateurs à double couche électrochimique.

Les oxydes métalliques, tels que MnO₂, RuO₂, Co₂O₃, TiO₂ et V₂O₅ (16), ont été les premiers étudiés. RuO₂ est l'un des plus étudiés car malgré son coût élevé, il a la meilleure conductivité et trois états d'oxydations stables sur 1.2V, ce qui permet d'obtenir des capacités de 720 F/g (18-22).

Les supercondensateurs hybrides :

Les systèmes hybrides sont une alternative par rapport aux supercondensateurs classiques (dits symétriques) car ils associent une électrode de supercondensateur à une électrode de

batterie. Ceci permet de bénéficier à la fois de la puissance du supercondensateur et de la densité d'énergie d'une batterie. La combinaison d'électrodes différentes permet d'augmenter la tension de cellule et de stocker une plus grande densité d'énergie par rapport aux supercondensateurs conventionnels.

Les électrolytes :

L'électrolyte est un facteur clé pour les performances électrochimiques d'un supercondensateur (23). L'énergie et la puissance sont en effet proportionnelles au carré de la tension de fonctionnement de la cellule qui est limitée par la stabilité électrochimique de l'électrolyte. Cependant, la conductivité ionique, la stabilité en température et la compatibilité avec les matériaux d'électrodes sont aussi importants. On distingue trois types d'électrolytes liquides : les électrolytes aqueux, les électrolytes organiques et les liquides ioniques. Le Tableau 1 présente les propriétés de ces électrolytes.

Tableau 1. Propriétés des électrolytes (10, 23, 24).

	Stabilité électrochimique (V)	Conductivité ionique (mS/cm)	Temperature (°C)
Aqueux	< 1.2	>400	-20 to +50
Organique	< 3	<100	-40 to +80
Liquide ionique	< 6	<15	-100 to +400

II. Les MXènes

Les phases MAX :

Une nouvelle famille de matériaux bidimensionnels, nommée MXène, a été découverte en 2011 à l'université de Drexel (Philadelphie, USA). Il s'agit de matériau synthétisé par

exfoliation d'une phase précurseur, la phase MAX, de formule $M_{n+1}AX_n$ où M est un métal de transition, A est un élément des groupes IIIA ou IVA et X est un atome de carbone et/ou d'azote, dont la structure est représentée Figure I.4 (7, 25, 26).

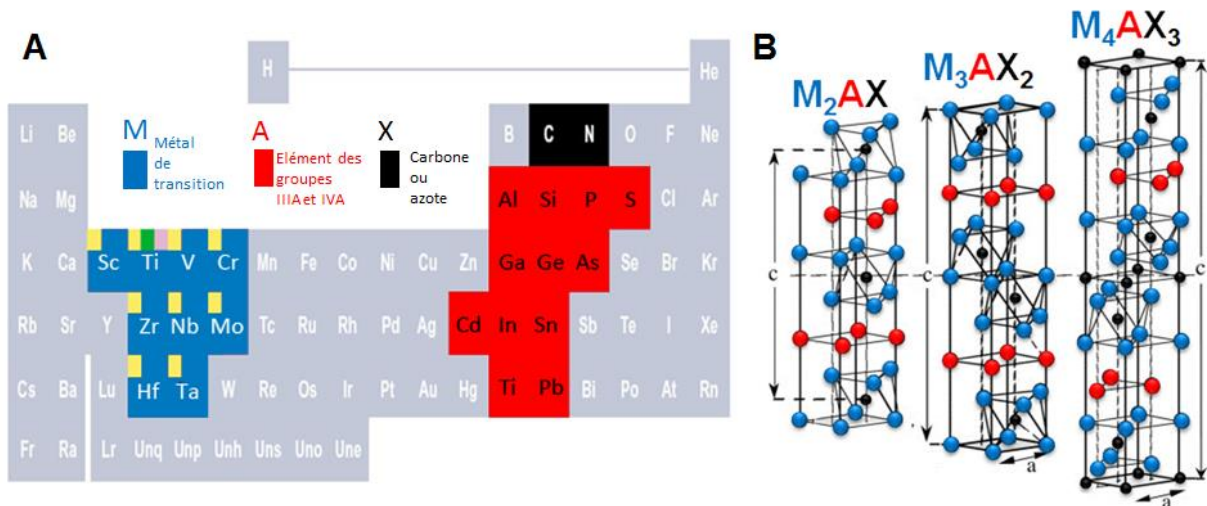


Figure I.4. Répartition des éléments M, A et X sur la table périodique et structure cristalline des phases MAX (adaptée de (26)).

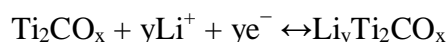
La synthèse des MXènes :

Les MXènes ont une structure bidimensionnelle formée de feuillets de $M_{n+1}X_n$ reliés entre eux par des liaisons faibles de Van der Waals. L'intérêt principal de ces matériaux est qu'ils sont composés d'une couche de carbure au cœur qui garantit une bonne conductivité électrique et une couche de métaux de transition à la surface qui peut participer à des réactions d'oxydo-réductions. De nombreux MXène sont envisageables (plus de soixante) mais les premiers composés synthétisés sont Ti_3C_2 , Ti_2C , Ta_4C_3 et $TiNbC$ par élimination de la couche d'aluminium des phases MAX correspondantes par réaction chimique avec l'acide fluorhydrique (27). Après réaction, la surface des MXènes est composée de groupes fonctionnels oxygénés et fluorés. La surface spécifique de ces matériaux est approximativement $20 \text{ m}^2/\text{g}$, ce qui est très faible comparé aux électrodes de carbone utilisés commercialement dans les supercondensateurs à double couche électrochimique.

Dans la majorité des matériaux bidimensionnels, tels que le graphène, une étape de délamination consistant à séparer complètement les feuillets les uns des autres est nécessaire afin d'améliorer les propriétés du matériau. En 2012, Mashtalir et al. ont réalisé la délamination de la MXène Ti_3C_2 en utilisant des ultrasons après l'intercalation de la MXène par du diméthylsulfoxyde (28). La surface spécifique de Ti_3C_2 après délamination a augmenté jusqu'à $98 \text{ m}^2/\text{g}$.

Les applications des MXènes :

La première application des MXènes étudiée a été pour les batteries lithium-ion, en choisissant la MXène Ti_2C car il s'agit de la plus légère (27). Les premiers résultats ont démontré une capacité stable de 225 mAh/g à une vitesse de $C/25$ (une charge ou décharge en 25 heures), ce qui correspond à la réaction d'un ion lithium par formule de Ti_2C lors de la réaction électrochimique proposée suivante:



Le Ti_2C a aussi été proposé en tant qu'électrode négative pour les supercondensateurs hybrides à ion lithium (29). Lors de cette étude, de bonnes performances à grande vitesse de charge ont été obtenues (70 mAh/g à $10C$ pour 1000 cycles). Le mécanisme de stockage de l'énergie a été étudié par diffraction des rayons X. Il a été démontré qu'il s'agit de l'intercalation des ions lithium entre les feuillets de Ti_2C .

Les performances obtenues avec le Ti_3C_2 après délamination en tant qu'électrode pour anode de batterie lithium-ion est de 410 mAh/g à $1C$ et 110 mAh/g à $36C$. Ces résultats sont prometteurs car supérieurs aux électrodes de graphite utilisées dans les batteries commerciales mais aussi car le Ti_3C_2 démontre une excellente rétention de capacité à grande vitesse de balayage. Grâce à ces performances, les MXènes semblent intéressantes pour des applications à haute puissance. Il est donc essentiel de continuer à étudier cette famille dans le cadre des supercondensateurs.

Chapitre II : Matériaux et techniques expérimentales

Les phases MAX utilisées au cours de ce travail sont soit commerciales (3-ONE-2, Voorhees, NJ), soit préparées par broyage à billes suivi d'un traitement thermique sous argon, à l'université de Drexel (groupes de M. Barsoum et Y. Gogotsi). Un total de sept phases MAX ont été choisies pour notre étude ; Ti_3AlC_2 , Ti_2AlC , Nb_2AlC , V_2AlC , $TiVAIC$, $Ti_{1.5}V_{1.5}AlC_2$ et Ti_3AlCN .

Le protocole de synthèse des MXènes par traitement des phases MAX dans l'acide fluorhydrique consiste à immerger 10g de la phase MAX sélectionnée dans 100 mL d'une solution de HF (Fisher Scientific, Fair Lawn, NJ) à température ambiante. Après plusieurs heures, la suspension obtenue est récupérée et rincée à l'eau distillée ; la phase MXène sous forme de poudre est ensuite séparée par centrifugation. La surface des MXènes obtenues est riche en groupes contenant des atomes d'oxygène et de fluor, c'est pourquoi le suffixe T_x est ajouté à la formule chimique. Le Tableau 2 résume les conditions expérimentales d'obtention de chaque MXène.

Tableau 2. Conditions de synthèse des MXènes

Phase MAX	Concentration HF	Temps	MXène
Ti_3AlC_2	50%	18h	$Ti_3C_2T_x$
Ti_2AlC	10%	10h	Ti_2CT_x
Nb_2AlC	50%	90h	Nb_2CT_x
V_2AlC	50%	8h	V_2CT_x
$TiVAIC$	50%	1h	$TiVCT_x$
$Ti_{1.5}V_{1.5}AlC_2$	50%	18h	$Ti_{1.5}V_{1.5}C_2T_x$
Ti_3AlCN	30%	18h	Ti_3CNT_x

Différentes techniques de caractérisations ont été utilisées dans cette thèse, en particulier la diffraction des rayons X, la microscopie électronique pour les caractérisations structurales et la voltampérométrie cyclique, le cyclage galvanostatique et la spectroscopie d'impédance pour les caractérisations électrochimiques.

Chapitre III : Etude électrochimique des MXènes pour les supercondensateurs en milieu aqueux

I. Introduction

L'objectif principal de ce chapitre est d'observer les performances électrochimiques des MXènes en tant qu'électrodes pour les supercondensateurs pour des applications de fortes puissances. Nous avons choisi d'étudier exclusivement la MXène Ti_3C_2 car elle présente les meilleures performances dans les batteries lithium-ion. Au vue de la faible surface spécifique du Ti_3C_2 ($23 \text{ m}^2/\text{g}$), de bonnes performances ne peuvent être expliquées que par l'existence de réactions électrochimiques de type pseudo-capacitives. Les électrolytes aqueux ont été choisis car ils possèdent de meilleures conductivités et sont compatibles avec les électrodes pseudo-capacitives trouvées dans la littérature.

II. L'intercalation spontanée des cations

Dans un premier temps, nous avons étudié la stabilité du $Ti_3C_2T_x$ dans les électrolytes aqueux. En utilisant l'analyse par diffraction des rayons X, nous avons mis en évidence que lorsque le $Ti_3C_2T_x$ est immergé pendant 5 heures dans les électrolytes aqueux aux pH basiques et neutres, la taille de la maille augmente. La Figure III.1.A montre le décalage du pic correspondant au paramètre de maille c après immersion dans de l'hydroxyde de potassium et de l'acétate de potassium. Ceci signifie qu'il y a une réaction d'intercalation spontanée d'ions

des électrolytes entre les feuillets de $Ti_3C_2T_x$. Les résultats d'analyse dispersive en énergie démontrent qu'il s'agit du cation de l'électrolyte.

La comparaison des différents résultats obtenus avec les 10 électrolytes sélectionnés n'ont pas permis de définir clairement les forces motrices de la réaction d'intercalation, mais il semble qu'il y ait une contribution du pH de l'électrolyte ainsi que de la valence du cation.

Grâce à l'étude par spectroscopie photoélectronique X, nous avons mis en évidence que les protocoles d'intercalations des cations et de délaminations modifient la chimie de surface du $Ti_3C_2T_x$. En effet, lors de ces deux traitements, les groupes fluorés sont plus ou moins remplacés par des groupes oxygénés, comme représenté schématiquement sur la Figure III.1.B.

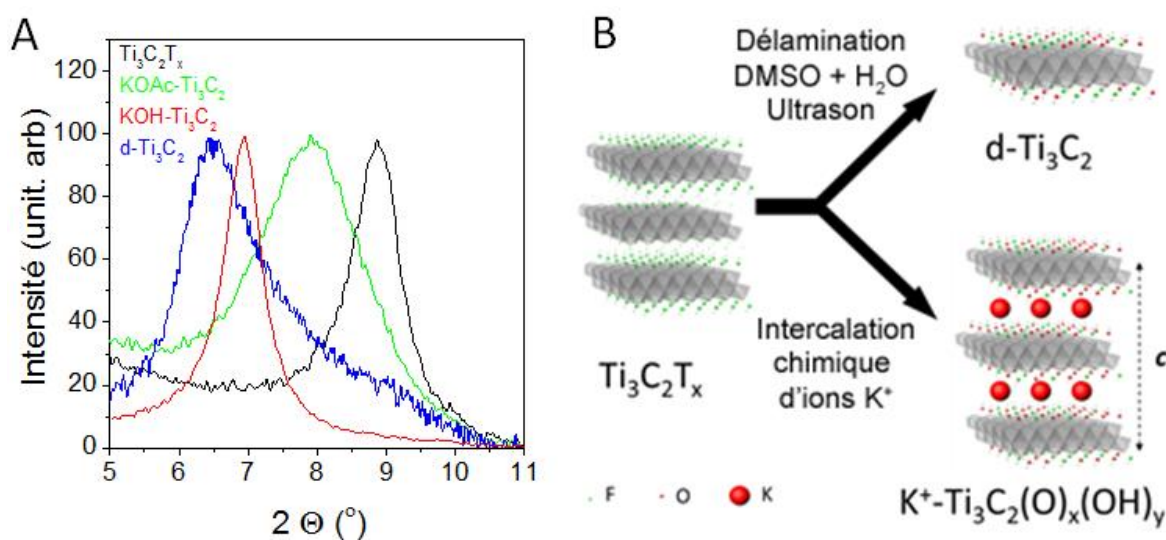


Figure III.1. Spectres de diffraction des rayons X (A) et schéma de la modification chimique de la surface du $Ti_3C_2T_x$ (B) après traitement dans des sels de potassium et délamination.

III. Caractérisation électrochimique

Nous avons testé les performances électrochimiques du $Ti_3C_2T_x$ en tant qu'électrode de supercondensateurs dans 10 électrolytes aqueux aux propriétés différentes (pH, cation, anion, conductivité et fenêtre de stabilité de potentiel). Le comportement dans chaque électrolyte est

différent, comme l'illustre la comparaison entre les voltampérogrammes obtenus dans trois électrolytes différents dans la Figure III.2.A. A faible vitesse de balayage (2 mV/s), les capacités obtenues vont de 45 F/g à 108 F/g. Ces valeurs sont élevées pour des matériaux à faible surface spécifique. En effet, si le mécanisme de stockage de l'énergie était électrostatique (adsorption d'ions à la surface des MXenes) comme dans les supercondensateurs à double couche, les capacités obtenues dans tous les électrolytes seraient très faibles et peu dépendantes de l'électrolyte. Ceci suggère qu'un autre mécanisme de charge doit avoir lieu.

Les voltampérogrammes dans les divers électrolytes sont rectangulaires mais dans certains cas des pics peuvent être présents. L'allure rectangulaire du signal avec la présence de pics larges ressemble à la signature électrochimique caractéristique des réactions d'oxydoréductions présentes dans les supercondensateurs pseudocapacitifs.

Nous avons étudié le mécanisme de charge dans l'acétate de sodium, l'hydroxyde de potassium et le sulfate de magnésium par une étude *in situ* de diffraction des rayons X, c'est-à-dire l'enregistrement des spectres de diffractions à différents états de charge du supercondensateur. La Figure III.2.B présente les résultats dans l'hydroxyde de potassium mais la même tendance a été observée dans les deux autres électrolytes étudiés. Les résultats démontrent que durant la charge, la maille se contracte (décalage du pic vers les petits angles) puis s'agrandit durant la décharge. Le paramètre de maille c fluctue de 0.33 Å lors du cycle. Ceci démontre que le mécanisme de stockage des charges est dû à l'intercalation des cations entre les feuillets de $Ti_3C_2T_x$ d'une manière semblable au MnO_2 (30).

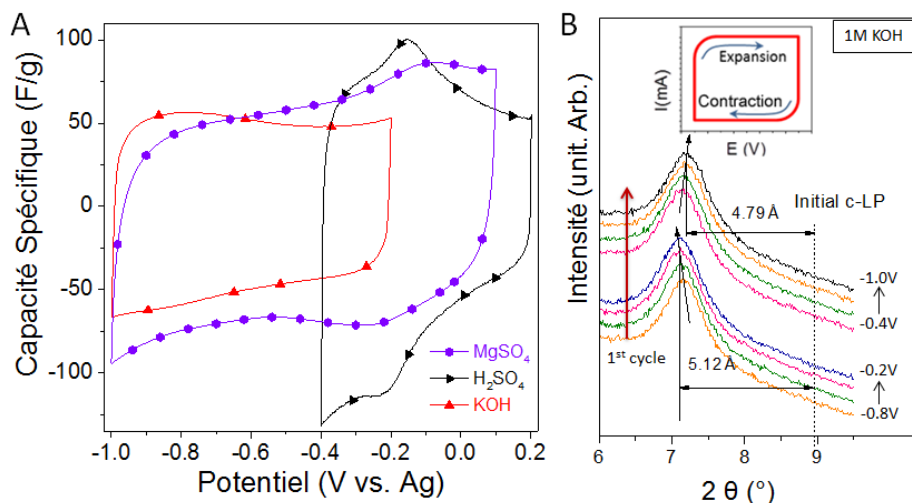


Figure III.2. Voltampérommes du $\text{Ti}_3\text{C}_2\text{T}_x$ dans MgSO_4 , H_2SO_4 et KOH (A).
Diffractogrammes obtenus pendant la charge et décharge dans du KOH (B).

Le rôle de la morphologie et de la chimie de surface du $\text{Ti}_3\text{C}_2\text{T}_x$ sur les performances électrochimiques a été observé par comparaison du comportement électrochimique de quatre échantillons dans le même électrolyte (1M H_2SO_4). Les quatre échantillons sont ; le $\text{Ti}_3\text{C}_2\text{T}_x$ non traité, le $\text{Ti}_3\text{C}_2\text{T}_x$ après intercalation spontanée dans de l'hydroxyde de potassium ($\text{KOH-Ti}_3\text{C}_2\text{T}_x$), le $\text{Ti}_3\text{C}_2\text{T}_x$ après intercalation spontanée dans du acétate de potassium ($\text{KOAc-Ti}_3\text{C}_2\text{T}_x$) et du $\text{Ti}_3\text{C}_2\text{T}_x$ après délamination ($\text{d-Ti}_3\text{C}_2\text{T}_x$). La Figure III.3 présente les résultats obtenus.

Comme $\text{Ti}_3\text{C}_2\text{T}_x$, $\text{KOH-Ti}_3\text{C}_2\text{T}_x$ et $\text{KOAc-Ti}_3\text{C}_2\text{T}_x$ ont la même valeur de surface spécifique, la différence de performance ne peut provenir que de leur différence de fonctions de surface. Il est donc possible de conclure que les groupes de fonctions oxygénés ($-\text{OOH}$, $=\text{O}$ et $-\text{OH}$) présents majoritairement dans $\text{KOH-Ti}_3\text{C}_2\text{T}_x$ et $\text{KOAc-Ti}_3\text{C}_2\text{T}_x$ sont responsables de l'amélioration de la capacité observée par le biais de réactions électrochimiques rapides à la surface du matériau. Le $\text{d-Ti}_3\text{C}_2\text{T}_x$ bénéficie à la fois de groupes oxygénés actifs et d'une surface spécifique quatre fois plus élevée. C'est pour cette raison que cet échantillon montre les meilleures performances avec 325 F/g et 520 F/cm^3 à 2 mV/s.

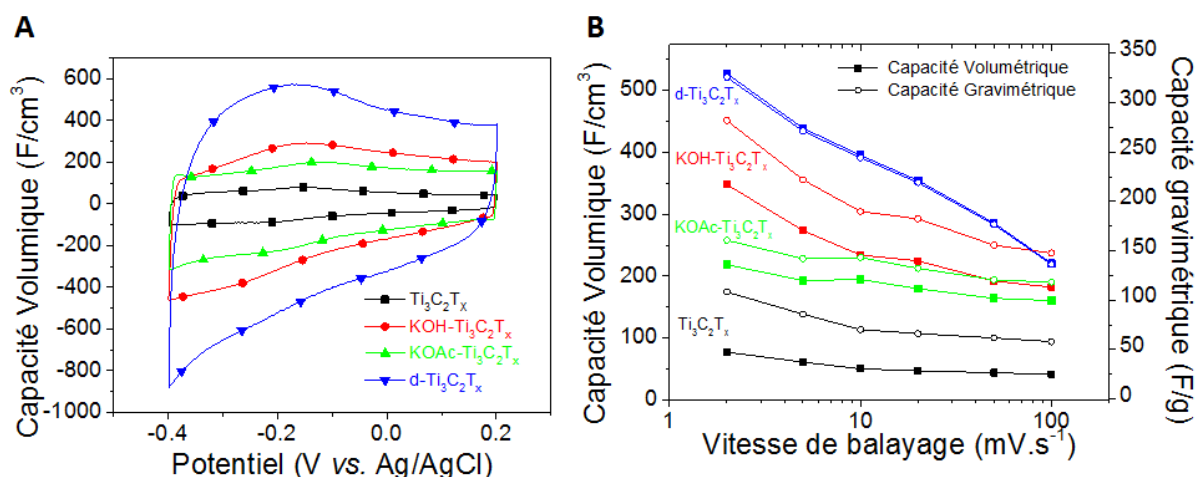


Figure III.3. Voltampérogrammes dans 1M H_2SO_4 à 10 mV/s (A) et capacités en fonction de la vitesse de balayage (B) (adaptée de (180)).

Chapitre IV : Etude électrochimique des MXènes pour les supercondensateurs hybrides à ion sodium

I. Introduction

Dans le chapitre précédent, nous avons démontré de bonnes performances électrochimiques grâce à l'intercalation de divers cation. Mais la tension de cellule est très faible dans tous les électrolytes aqueux. Afin d'augmenter les densités de puissance et d'énergie, il est possible d'utiliser des supercondensateurs hybrides dans des électrolytes organiques. Les résultats préliminaires du Ti_2C en tant qu'électrode pour supercondensateur hybride à ion lithium ont démontré la faisabilité d'un tel système (29).

D'un autre côté, nous venons d'observer que le phénomène d'intercalation dans le Ti_3C_2 ne se limite pas aux ions lithiums. Ces dernières années, il a été démontré qu'il y a un intérêt économique important à remplacer le lithium par le sodium dans les batteries et les supercondensateurs hybrides. En effet, les ressources en lithium sont limitées et situées dans peu de pays (principalement en Chine, Chili, Bolivie et Australie), ce qui crée des tensions économiques et politiques, alors que le sodium se trouve en abondance partout dans le monde.

Dans la suite de ce chapitre, nous avons étudié plusieurs MXènes dans des demi-cellules de batterie au sodium. Nous avons principalement étudié la MXène V_2CT_x en tant qu'électrode positive pour les supercondensateurs hybrides à ions sodium.

II. Etude électrochimique du V_2CT_x

Avant d'assembler une cellule hybride complète, composée du V_2CT_x et d'un matériau de type batteries, il est essentiel d'analyser le comportement électrochimique du V_2CT_x . Pour cela, des tests en demi-cellule, contenant une contre-électrode en sodium métallique, ont été effectués. La Figure IV.1 montre les résultats obtenus par voltampérométrie cyclique, à différentes vitesses de balayage. Des valeurs élevées de capacités ont été obtenues ; 100 F/g ou 170 F/cm^3 à faible vitesse et 50 F/g à 50 mV/s. Deux régions sont identifiables sur les voltampérogrammes à faible vitesse. Un comportement capacitif est observable entre 1 V et 2.2 V vs. Na^+/Na , caractérisé par une forme rectangulaire, alors qu'un couple de pics d'oxydo-réduction se situe à 3V et 2.5V (pics A et B). Lorsque la vitesse de balayage augmente au-delà de 2 mV/s, les pics disparaissent, démontrant ainsi que cette réaction électrochimique est limitée par la diffusion.

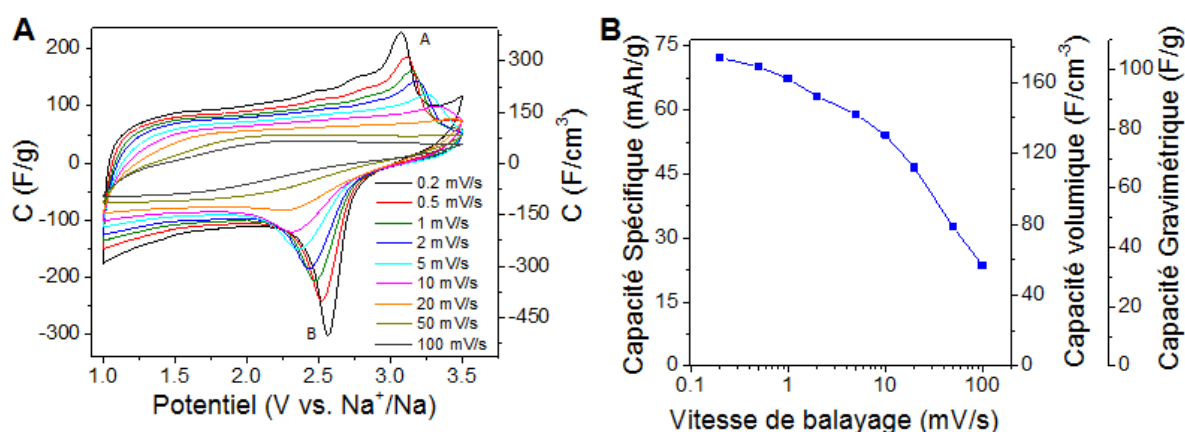


Figure IV.1. Voltampérométrie dans 1M $NaPF_6$ dans EC:DMC (A) et capacités en fonction de la vitesse de balayage (B) (adaptée de (198)).

La Figure IV.2 présente l'étude du mécanisme de stockage de charge par diffraction des rayons X à différents potentiels. Ces résultats démontrent qu'il s'agit de l'intercalation des ions sodium sur toute la plage de potentiel et non de deux zones de comportements différents. Une expansion/contraction réversible de 2.3 Å entre deux feuillets est observée. Contrairement aux résultats en milieu aqueux, ici nous observons que le paramètre de maille augmente pendant l'insertion de sodium.

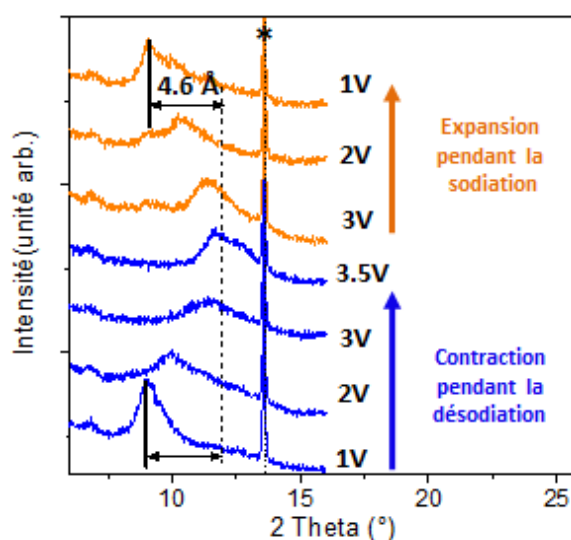


Figure IV.2. Diffractogrammes obtenus à différents potentiels. (*) Pics d'impureté du précurseur V₂AlC (adaptée de (198)).

III. Caractérisation électrochimique d'une cellule hybride Hard Carbon/V₂CT_x

Une électrode négative de batterie sodium-ion a été choisie, nommée hard carbon, dans le but d'assembler une cellule hybride complète. Etant donné les capacités respectives des deux électrodes, le ratio massique 1:2 pour hard carbon/ V₂CT_x a été choisi.

La Figure IV.3 présente les résultats électrochimiques de cette cellule à plusieurs vitesses de charge et décharge, entre C/3 et 20C. Les valeurs de capacités présentées sont calculées en tenant compte de la masse totale des deux électrodes. Lors de la décharge galvanostatique, il

est intéressant de noter qu'il y a une grande chute de potentiel de 3.5V à 2.6V ce qui réduit la fenêtre de potentiel réellement utilisable. Plus de 40% de la capacité est préservée lorsque la vitesse de charge est augmentée de C/3 à 20C. Ceci démontre de bonnes performances adaptées pour des applications en haute puissance. Après 300 cycles, une perte de capacité de 30% est observée. La durée de vie estimée pour cette cellule semble donc être courte comparée aux supercondensateurs à double couche électrochimique. La dégradation de capacité est liée au glissement de la fenêtre de potentiel, observable lorsqu'on compare la différence de potentiel de chaque électrode entre le deuxième et au deux-centième cycle. Une optimisation du rapport massique entre les deux électrodes pourrait améliorer la durée de vie.

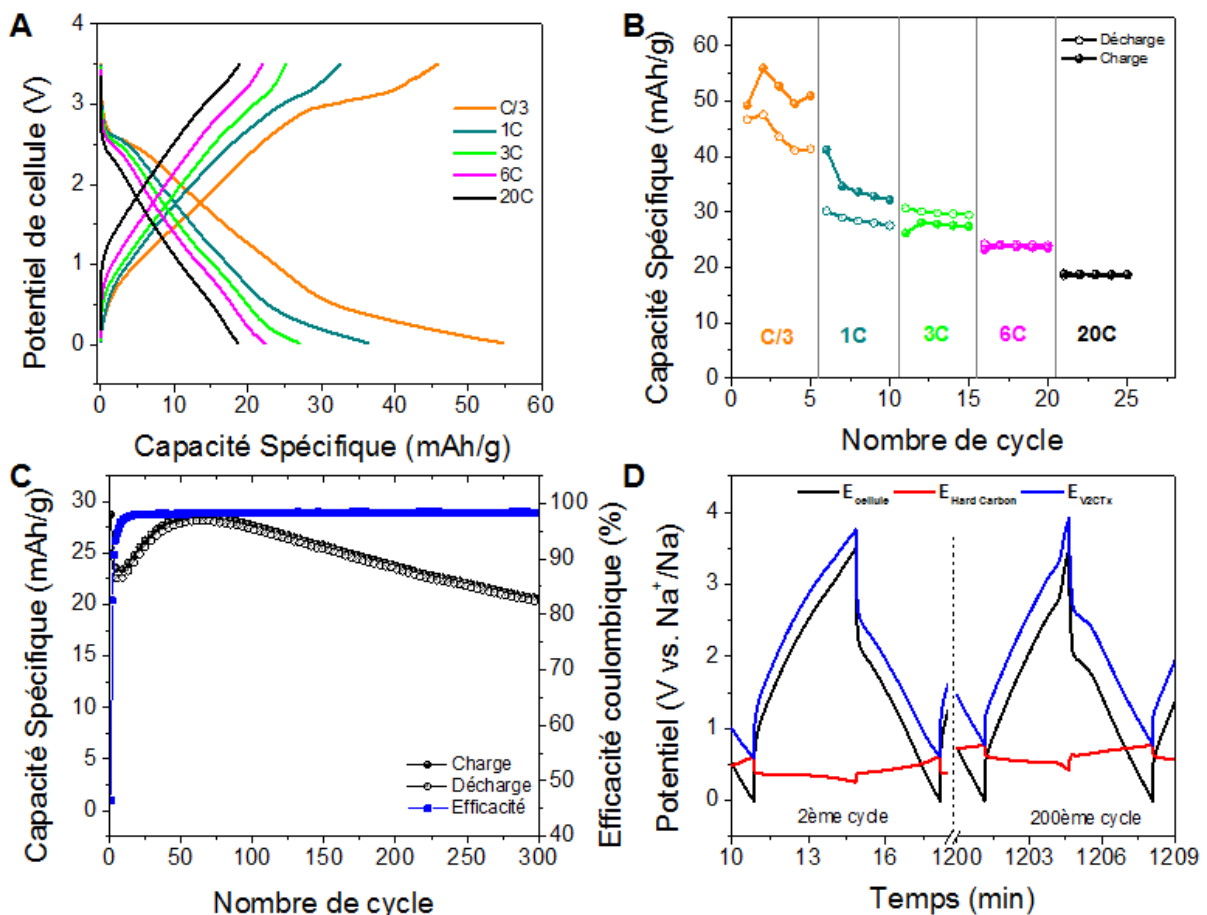


Figure IV.3. Courbes de charge et décharge galvanostatique (A) et capacités correspondantes en fonction du nombre de cycles (B). Capacités spécifiques en fonction du nombre de cycles à 1A/g (C) et détail des potentiels (D) (adaptée de (198)).

Chapitre V : Etude électrochimique des MXènes pour les supercondensateurs en milieu organique

I. Introduction

Les résultats obtenus dans le chapitre III dans divers électrolytes aqueux ont montré d'excellentes capacités. Cependant, la faible tension de cellule, due à l'électrolyse de l'eau, limite grandement les densités d'énergies et de puissances accessibles. Dans ce dernier chapitre, nous avons choisi d'étudier les performances électrochimiques des MXènes dans trois électrolytes organiques afin d'augmenter la tension de cellule. Tenant compte de l'importance de la chimie de surface et de la morphologie des électrodes sur les comportements électrochimiques, nous avons décidé d'utiliser une nouvelle voie de synthèse pour préparer l'électrode de MXène de façon optimale. Nous nous sommes inspirés de la méthode d'élimination de l'aluminium de $Ti_3AlC_2T_x$ par un mélange à 6 M de d'acide chlorhydrique et de fluorure de lithium élaborée par Ghidui *et al.* (31) et de l'amélioration que l'ajout de nanotubes de carbone apporte au MXène, comme démontré par Zhao *et al.* (32).

II. Etude électrochimique

Trois matériaux différents ont été étudiés ; le $Ti_3C_2T_x$, le $Ti_3C_2T_x$ délaminé par ultrason (noté d- $Ti_3C_2T_x$), et le composite contenant 20% de nanotube de carbone et 80% de $Ti_3C_2T_x$ (noté CNT- $Ti_3C_2T_x$). La Figure V.1 montre les voltampérogrammes obtenus à 20 mV/s et les capacités obtenues entre 2 mV/s et 100 mV/s dans une solution à 1M de 1-éthyl-3-méthylimidazolium bis-(trifluorométhylsulfonyl)-imide (EMITFSI) dans l'acétonitrile.

Les capacités obtenues sont différentes mais leurs comportements électrochimiques se ressemblent et peuvent être décrits par une enveloppe capacitive et des pics d'oxydo-réductions autour de -0.2 V et -0.4 V *vs.* Ag. La différence de potentiel entre le pic d'oxydation et le pic de réduction est associée à des limitations cinétiques et ohmiques. En

comparant la position des pics de chaque électrode, on observe que la plus faible différence de potentiel entre les pics est obtenue avec le CNT-Ti₃C₂T_x, ce qui confirme que l'ajout de nanotubes de carbone améliore la conductivité et la diffusion.

La capacité maximale, 245 F/cm³ ou 85 F/g, est obtenue avec CNT-Ti₃C₂T_x à 2 mV/s. Cette électrode démontre un bon comportement en puissance car 75% de cette capacité reste accessible à 100 mV/s (contre 50% dans le cas de d-Ti₃C₂T_x). Par analogie avec les résultats montrés dans le chapitre III, la différence de capacité entre les différentes électrodes est attribuée à la différence de morphologies qui peut modifier l'accessibilité des ions à la surface des feuillets.

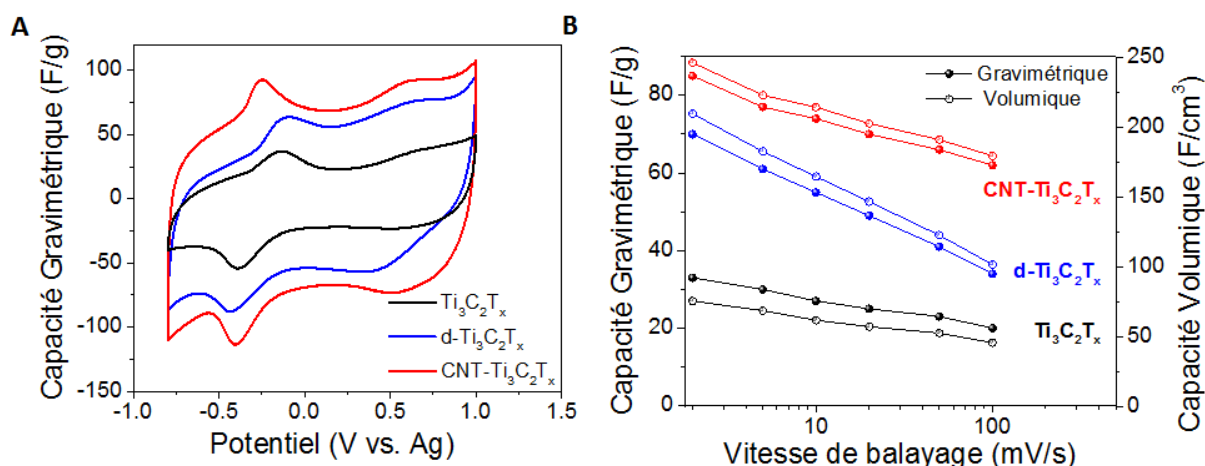


Figure V.1. Voltampérommes dans 1M EMITFSI dans l'acétonitrile à 20 mV/s (A) et capacités en fonction de la vitesse de balayage (B) (adaptée de (204)).

III. Etude du mécanisme de stockage des charges

Une étude du mécanisme de stockage des charges a été entreprise en utilisant la diffraction des rayons X *in-situ*. La Figure V.2 montre les diffractogrammes du CNT-Ti₃C₂T_x obtenus à différents potentiels. L'intercalation spontanée d'ions entre les feuillets a été observée par un décalage des pics avant de commencer les tests, comme c'était le cas dans certains électrolytes aqueux étudiés au chapitre III.

Les résultats de diffraction des rayons X démontrent qu'il y a deux jeux de pics distincts selon le potentiel appliqué. Le changement de pics s'effectue aux potentiels des pics d'oxydo-réduction observés sur le voltampérogramme. Ceci démontre qu'il y a un changement de phase associé à cette réaction électrochimique. La différence entre les deux phases peut s'expliquer par une différence de la distance entre feuillets de 1.3 Å. Ce comportement est différent de l'intercalation continue des ions observé dans les deux chapitres précédents.

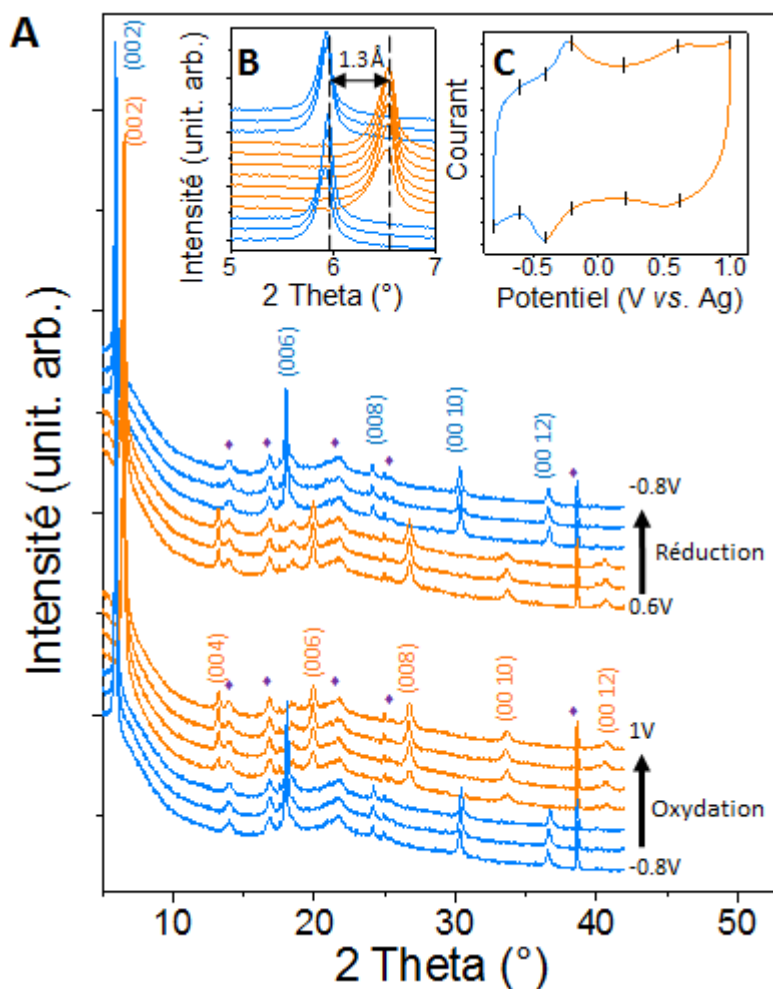


Figure V.2. Diffractogrammes obtenus pendant la réduction et l'oxydation du CNT-Ti₃C₂T_x

(A). Les pics notés par des losanges violets sont associés à la cellule de diffraction. Zoom entre 5 et 7° (B) et voltampérogrammes à 20 mV/s (C) (adaptée de (204)).

Conclusion générale

L'objectif de cette thèse était d'étudier le comportement électrochimique d'une nouvelle famille de matériaux bidimensionnels appelée MXène, dans le cadre d'application dans les supercondensateurs. Dans ce contexte, plusieurs MXènes ont été préparées et modifiées pour obtenir les meilleures performances électrochimiques, tout en analysant le mécanisme de stockage des charges mis en jeu.

Ces recherches ont permis, pour la première fois, i) de démontrer l'intercalation spontanée d'une grande variété de cations entre feuillets de MXène, ii) de modifier la chimie de surface et d'observer son effet sur le comportement électrochimique, iii) de mettre en évidence le mécanisme de stockage pseudo-capacitif liant de l'intercalation (continue ou à potentiel fixe, selon l'électrolyte) et des réactions d'oxydo-réduction de surface, et enfin iv) d'assembler un supercondensateur hybride à ions sodium complet utilisant une MXène en électrode positive, avec d'excellentes capacités volumiques (520 F/cm^3 dans l' H_2SO_4 et 245 F/cm^3 dans l'EMITFSI dans l'acétonitrile).

D'autre part, ces découvertes nous encouragent à poursuivre l'étude des MXènes dans le cadre du stockage de l'énergie. Il serait intéressant de poursuivre ces travaux en testant les performances dans les liquides ioniques et dans les batteries à cation multivalent, ainsi qu'étudier de nouvelles MXènes.

Références

1. J. M. Tarascon, M. Armand, Issues and challenges facing rechargeable lithium batteries. *Nature* 414, 359 (Nov, 2001).
2. J. R. Miller, P. Simon, Materials science - Electrochemical capacitors for energy management. *Science* 321, 651 (Aug, 2008).
3. B. E. Conway, *Electrochemical supercapacitors: scientific fundamentals and technological applications*. (Springer Science & Business Media, 2013).
4. P. Simon, Y. Gogotsi, Materials for electrochemical capacitors. *Nat. Mater.* 7, 845 (Nov, 2008).
5. M. Armand, J. M. Tarascon, Building better batteries. *Nature* 451, 652 (02/07/print, 2008).
6. A. S. Arico, P. Bruce, B. Scrosati, J. M. Tarascon, W. Van Schalkwijk, Nanostructured materials for advanced energy conversion and storage devices. *Nat. Mater.* 4, 366 (May, 2005).
7. M. Naguib et al., Two-Dimensional Nanocrystals Produced by Exfoliation of Ti_3AlC_2 . *Advanced Materials* 23, 4248 (2011).
8. M. Naguib et al., MXene: a promising transition metal carbide anode for lithium-ion batteries. *Electrochemistry Communications* 16, 61 (2012).
9. G. P. Wang, L. Zhang, J. J. Zhang, A review of electrode materials for electrochemical supercapacitors. *Chemical Society Reviews* 41, 797 (2012).
10. A. G. Pandolfo, A. F. Hollenkamp, Carbon properties and their role in supercapacitors. *Journal of Power Sources* 157, 11 (Jun, 2006).
11. J. Gamby, P. L. Taberna, P. Simon, J. F. Fauvarque, M. Chesneau, Studies and characterisations of various activated carbons used for carbon/carbon supercapacitors. *Journal of Power Sources* 101, 109 (Oct, 2001).

12. L. L. Zhang, X. S. Zhao, Carbon-based materials as supercapacitor electrodes. *Chemical Society Reviews* 38, 2520 (2009).
13. W. Gu, G. Yushin, Review of nanostructured carbon materials for electrochemical capacitor applications: advantages and limitations of activated carbon, carbide-derived carbon, zeolite-templated carbon, carbon aerogels, carbon nanotubes, onion-like carbon, and graphene. *Wiley Interdisciplinary Reviews: Energy and Environment* 3, 424 (2014).
14. N. Mohamad Nor, L. C. Lau, K. T. Lee, A. R. Mohamed, Synthesis of activated carbon from lignocellulosic biomass and its applications in air pollution control—a review. *Journal of Environmental Chemical Engineering* 1, 658 (12//, 2013).
15. B. E. Conway, V. Birss, J. Wojtowicz, The role and utilization of pseudocapacitance for energy storage by supercapacitors. *Journal of Power Sources* 66, 1 (5//, 1997).
16. V. Augustyn, P. Simon, B. Dunn, Pseudocapacitive oxide materials for high-rate electrochemical energy storage. *Energy & Environmental Science* 7, 1597 (2014).
17. T. Brousse, D. Bélanger, J. W. Long, To Be or Not To Be Pseudocapacitive? *Journal of the Electrochemical Society* 162, A5185 (January 1, 2015, 2015).
18. W. Sugimoto, H. Iwata, K. Yokoshima, Y. Murakami, Y. Takasu, Proton and Electron Conductivity in Hydrated Ruthenium Oxides Evaluated by Electrochemical Impedance Spectroscopy: The Origin of Large Capacitance. *The Journal of Physical Chemistry B* 109, 7330 (2005/04/01, 2005).
19. W. Sugimoto, T. Kizaki, K. Yokoshima, Y. Murakami, Y. Takasu, Evaluation of the pseudocapacitance in RuO₂ with a RuO₂/GC thin film electrode. *Electrochim. Acta* 49, 313 (1/15/, 2004).
20. J. M. Miller, B. Dunn, Morphology and electrochemistry of ruthenium/carbon aerogel nanostructures. *Langmuir* 15, 799 (Feb, 1999).

21. W. Sugimoto, H. Iwata, Y. Yasunaga, Y. Murakami, Y. Takasu, Preparation of ruthenic acid nanosheets and utilization of its interlayer surface for electrochemical energy storage. *Angew. Chem.-Int. Edit.* 42, 4092 (2003).
22. B. E. Conway, Transition From Supercapacitor To Battery Behavior In Electrochemical Energy-Storage. *Journal of the Electrochemical Society* 138, 1539 (Jun, 1991).
23. M. Galiński, A. Lewandowski, I. Stępnia, Ionic liquids as electrolytes. *Electrochim. Acta* 51, 5567 (8/15/, 2006).
24. M. Ue, M. Takeda, M. Takehara, S. Mori, Electrochemical Properties of Quaternary Ammonium Salts for Electrochemical Capacitors. *Journal of the Electrochemical Society* 144, 2684 (August 1, 1997, 1997).
25. M. Naguib et al., Synthesis of a new nanocrystalline titanium aluminum fluoride phase by reaction of Ti_2AlC with hydrofluoric acid. *RSC Advances* 1, 1493 (2011).
26. M. W. Barsoum, The $MN+1AX_n$ phases: A new class of solids: Thermodynamically stable nanolaminates. *Progress in Solid State Chemistry* 28, 201 (2000).
27. M. Naguib et al., Two-Dimensional Transition Metal Carbides. *ACS Nano* 6, 1322 (2012/02/28, 2012).
28. O. Mashtalir et al., Intercalation and delamination of layered carbides and carbonitrides. *Nat Commun* 4, 1716 (04/16/online, 2013).
29. J. Come et al., A Non-Aqueous Asymmetric Cell with a Ti_2C -Based Two-Dimensional Negative Electrode. *Journal of the Electrochemical Society* 159, A1368 (2012).
30. O. Ghodbane, F. Ataherian, N. L. Wu, F. Favier, In situ crystallographic investigations of charge storage mechanisms in MnO_2 -based electrochemical capacitors. *Journal of Power Sources* 206, 454 (May, 2012).

31. M. Ghidui, M. R. Lukatskaya, M.-Q. Zhao, Y. Gogotsi, M. W. Barsoum, Conductive two-dimensional titanium carbide /clay/ with high volumetric capacitance. *Nature* 516, 78 (12/04/print, 2014).
32. M.-Q. Zhao et al., Flexible MXene/Carbon Nanotube Composite Paper with High Volumetric Capacitance. *Advanced Materials* 27, 339 (2015).

Résumé

La demande urgente d'innovations dans le domaine du stockage de l'énergie est liée au développement récent de la production d'énergie renouvelable ainsi qu'à la diversification des produits électroniques portables qui consomment de plus en plus d'énergie. Il existe plusieurs technologies pour le stockage et la conversion électrochimique de l'énergie, les plus notables étant les batteries aux ions lithium, les piles à combustible et les supercondensateurs. Ces systèmes sont utilisés de façon complémentaire des uns aux autres dans des applications différentes. Par exemple, les batteries sont plus facilement transportables que les piles à combustible et ont de bonne densité d'énergie alors que les supercondensateurs ont des densités de puissance plus élevées et une meilleure durée de vie.

L'objectif principal de ces travaux est d'étudier les performances électrochimiques d'une nouvelle famille de matériaux bidimensionnel appelée MXène, en vue de proposer de nouvelles solutions pour le stockage de l'énergie. Pour y arriver, plusieurs directions ont été explorées. Dans un premier temps, la thèse se concentre sur les supercondensateurs dans des électrolytes aqueux et aux effets des groupes de surface. La seconde partie se concentre sur les systèmes de batterie et de capacités à ions sodium. Une cellule complète comportant une anode en carbone et une cathode de MXène a été développées. La dernière partie de la thèse présente l'étude des MXènes pour les supercondensateur en milieu organique.

Une attention particulière est apportée à l'étude du mécanisme d'intercalation des ions entre les feuillets de MXène. Différentes techniques de caractérisations ont été utilisées, en particulier la voltampérométrie cyclique, le cyclage galvanostatique, la spectroscopie d'impédance, la microscopie électronique et la diffraction des rayons X.

Mots clés: Supercondensateur ; batteries à ion sodium ; condensateur sodium-ion ; matériaux bidimensionnels ; MXene.

Abstract

An increase in energy and power densities is needed to match the growing energy storage demands linked with the development of renewable energy production and portable electronics. Several energy storage technologies exist including lithium ion batteries, sodium ion batteries, fuel cells and electrochemical capacitors. These systems are complementary to each other. For example, electrochemical capacitors can deliver high power densities whereas batteries are used for high energy densities applications.

The first objective of this work is to investigate the electrochemical performances of a new family of 2-D material called MXene and propose new solutions to tackle the energy storage concern. To achieve this goal, several directions have been explored. The first part of the research focuses on MXene behavior as electrode material for electrochemical capacitors in aqueous electrolytes. The next part starts with sodium-ion batteries, and a new hybrid system of sodium ion capacitor is proposed. The last part is the study of MXene electrodes for supercapacitors in organic electrolytes.

The energy storage mechanisms are thoroughly investigated. Different characterization techniques were used in this work, such as cyclic voltammetry, galvanostatic charge-discharge, electrochemical impedance spectroscopy, scanning electron microscopy and X-ray diffraction.

Keywords: Electrochemical capacitors; sodium-ion batteries; sodium ion-capacitors; two-dimensional materials; MXene